Attosecond dynamics of nano-localized fields probed by photoelectron spectroscopy

Frederik Süßmann

München 2013

Attosecond dynamics of nano-localized fields probed by photoelectron spectroscopy

Frederik Süßmann

Dissertation
an der Fakultät für Physik
der Ludwig–Maximilians–Universität
München

vorgelegt von
Frederik Süßmann
aus Bremen

München, den 31. Mai 2013

Erstgutachter: Prof. Dr. Matthias Kling
Zweitgutachter: Prof. Dr. Thomas Fennel
Tag der mündlichen Prüfung: 17.07.2013

Zusammenfassung

Im Mittelpunkt dieser Arbeit steht die Wechselwirkung von ultrakurzen Laserpulsen mit Nanosystemen wobei besonderes Augenmerk auf die örtlichen und zeitlichen Eigenschaften der erzeugten Nahfelder gelegt wird. Zur direkten und indirekten Bestimmung der Nahfeldentwicklung und -verteilung wird auf verschiedene Formen der Elektronenspektroskopie zurückgegriffen.

Zum einen wird die Photoemission von isolierten SiO_2 Nanokugeln mit Hilfe der Velocity-Map-Imaging-Methode bei gleichzeitiger Bestimmung der Träger-Einhüllenden-Phase der ultrakurzen Laserpulse gemessen. Die Impulsspektren zeigen eine starke Abhängigkeit von der Feldentwicklung des Laserfeldes und erstrecken sich zu unerwartet hohen Energien. Mit Hilfe numerischer Simulationen kann gezeigt werden, dass photoionisierte Elektronen eine hochdynamische Ladungsverteilung an der Oberfläche erzeugen, welche für eine zusätzliche Beschleunigung für ausgewählte Elektronentrajektorien verantwortlich ist. Messungen an Nanokugeln mit verschiedener Größe zeigen, dass die durch Propagationseffekte erzeugte asymmetrische Feldverteilung direkt auf die Impulsprojektionen übertragen wird. Die Korrelation zwischen Orts- und Impulsraum der Photoelektronen und eine mögliche Rekonstruktion der Feldverteilung an der Oberfläche werden diskutiert.

Mit weiteren Experimenten an einem Stereo-Flugzeitspektrometer wird die Photoemission von Nanoteilchen unterschiedlicher Zusammensetzung (SiO_2, ZrO_2, TiO_2, Si, Au) bei hohen Intensitäten oberhalb von $10^{14}\,\mathrm{W/cm^2}$ untersucht. Diese zeigen eine nichtlineare Abhängigkeit der höchsten Elektronenenergien von der Intensität. Die Gesetzmäßigkeit aller Materialien konvergiert, was ein starkes Indiz für eine drastische Änderung der optischen Eigenschaften noch während des Laserpulses ist. Die verfügbaren theoretischen Modelle zur Erzeugung freier Ladungsträger, die zu einem solchen transienten Effekt führen können, werden diskutiert.

Zeitaufgelöste Messungen der Nahfeldoszillationen an Nanoteilchen würden ein tiefgreifenderes Verständnis und Charakterisierung der kollektiven Elektronendynamik ermöglichen. Die Anwendung von Attosekundenpulsen zu diesem Zweck wird diskutiert wobei besonderes Augenmerk auf die inhomogene örtliche Verteilung der Felder an Nanostrukturen gelegt wird. Erste experimentelle Resultate zur Messung der Nahfeldoszillationen an Gold-Nanospitzen werden präsentiert. Die Ergebnisse zeigen einen deutlichen Phasenversatz zu Referenzmessungen. Die örtliche Herkunft des Signals und mögliche Verbesserungen des Experiments werden aufgezeigt.

Abstract

This work focuses on the interaction of few-cycle laser pulses with nanosystems. Special emphasis is placed on the spatio-temporal evolution of the induced near-fields. Measurements on carrier-envelope-phase (CEP) controlled photoemission from isolated SiO_2 nanospheres are taken by single-shot velocity map imaging (VMI) combined with CEP tagging. The obtained photoelectron spectra show a pronounced dependence on the CEP and extend to unexpectedly high energies. Comparison with numerical simulations identify the additional Coulomb forces of the liberated electron cloud as an effective additional acceleration mechanism for distinct trajectories. For larger spheres, an asymmetry in the field distribution is classically predicted. This asymmetry is also observed in the photoelectron momentum distributions. The mapping between position and momentum space in the VMI approach are investigated by analyzing the correlation of the photoelectron's birth and detection position.

In a second set of experiments, photoemission at intensities exceeding $10^{14}\,\mathrm{W/cm^2}$ from isolated nanospheres of different composition (SiO_2, ZrO_2, TiO_2, Si, Au) is examined by stereo time-of-flight spectroscopy. It is found that the measured cutoff energies scale nonlinearly with laser intensity depending on the material properties of the nanosystem. A trend towards a unified behavior for high intensities is observed indicating a drastic change in optical properties within the duration of the few-cycle laser pulse. The charge carrier generation mechanisms that could lead to such a transient effect are discussed.

For a better understanding of the interaction of few-cycle fields with nanosystems, a direct access to the temporal evolution of (plasmonic) near-fields is highly desirable. The efforts on the realization of nanoplasmonic attosecond streaking spectroscopy are presented. Numerical simulations are used to identify the influence of the inhomogeneous near-field distributions on the streaking process. First experimental results obtained from Au nanotips show clear streaking features of sub-micron localized near-fields. The near-field oscillations are found to be phase offset as compared to reference measurements. The exact origin of the streaking features of the Au tip and possible improvements of the experimental approach are discussed.

Contents

Summary v

1 Introduction 1

2 Theoretical background 7
- 2.1 Interaction of strong laser fields with matter . . . 7
  - 2.1.1 Few-cycle laser fields . . . 7
  - 2.1.2 Interaction of few-cycle laser fields with nanosize objects . . . 8
  - 2.1.3 Plasmons as collective electron excitations . . . 10
  - 2.1.4 Mie theory for spherical particles . . . 12
  - 2.1.5 Quasistatic dipole approximation . . . 14
  - 2.1.6 Numerical methods for arbitrary geometries . . . 16
  - 2.1.7 Multipole expansion of charge distributions . . . 16
- 2.2 Ionization of atoms and solids by strong light fields . . . 19
  - 2.2.1 Above threshold ionization . . . 19
  - 2.2.2 HHG and attosecond pulse generation . . . 21
  - 2.2.3 Photoionization processes in the solid state . . . 23
  - 2.2.4 Optical breakdown and metallization effects . . . 24

3 Experimental techniques 27
- 3.1 Generation of few-cycle laser pulses . . . 27
- 3.2 CEP stabilization and measurement . . . 30
  - 3.2.1 Active phase stabilization . . . 30
  - 3.2.2 Stereo-ATI phasemeter . . . 32
  - 3.2.3 Statistical rebinning for exact phase retrieval . . . 33
- 3.3 Nanoparticle samples . . . 34
  - 3.3.1 Sample preparation and characterization . . . 34
  - 3.3.2 Aerodynamic lensing . . . 35
- 3.4 Velocity map imaging . . . 36
  - 3.4.1 Implementation of single-shot VMI . . . 38
  - 3.4.2 Asymmetry parameters . . . 40
  - 3.4.3 CEP resolved photoemission from Xe gas . . . 42
  - 3.4.4 VMI of nanoparticles - background suppression . . . 42

3.4.5 Stability of CEP tagging for long acquisition times 44
3.5 Stereo time-of-flight setup 45
3.5.1 Setup 45
3.5.2 Data acquisition and analysis 46
3.6 AS-5 attosecond beamline 48
3.6.1 Attosecond streak camera 48
3.6.2 Beamline layout 50

4 CEP resolved photoemission from dielectric nanospheres 53
4.1 Introduction 53
4.2 M^3C simulation model 54
4.2.1 Overview 54
4.2.2 External laser field 55
4.2.3 Modeling mutual electron interaction by mean field approach 56
4.2.4 Electron emission, scattering and impact ionization 56
4.3 Microscopic analysis 57
4.4 Comparison to experimental VMI data 61
4.5 Propagation effects at large SiO_2 nanospheres 68
4.5.1 Spatial reconstruction of the near-fields 68
4.5.2 Field distribution at large SiO_2 nanospheres 70
4.5.3 Size-dependent VMI data 72
4.5.4 Correlation analysis and reconstruction of field profiles 74
4.6 Conclusions and outlook 77

5 Nonlinear regime of photoemission near optical breakdown 79
5.1 STOF measurements 80
5.1.1 Samples 80
5.1.2 Intensity dependence of spectral cutoffs 80
5.1.3 CEP dependence at high intensities 84
5.2 Theoretical predictions 87
5.2.1 M^3C model 87
5.2.2 Free charge density approximations 87
5.2.3 Interpretation 89
5.3 Conclusions and outlook 90

6 Direct measurement of near-fields by attosecond streaking 93
6.1 Introduction 93
6.2 General considerations 94
6.2.1 The regimes of near-field streaking 96
6.2.2 Simulated streaking spectrograms for Au spheres 98
6.2.3 Target density and count rate approximations 102
6.3 Attosecond streaking from Au nano-tips 103
6.3.1 Plasmonic properties 103

6.3.2 Streaking experiments 105
6.3.3 Interpretation 112
6.4 Conclusions and outlook 116

A Data analysis 117
A.1 Calibration of velocity map images 117
A.2 Statistical rebinning of single shot CE measurements 118
A.3 Calibration of the AS-5 TOF 118

B Data Archiving 121

Bibliography 127

Acknowledgements 140

List of Figures

2.1 Few-cycle laser pulses 8
2.2 Dielectric function of metal systems 9
2.3 SPPs and LSPs 11
2.4 Mie theory 12
2.5 Near-field distributions of spherical particles 15
2.6 Multipole expansion of charge distributions 18
2.7 Ionization regimes 19
2.8 Simple man's model for ATI and HHG 20
2.9 Illustration of the HHG process during a single half-cycle 22
2.10 High-harmonic generation process 23

3.1 Overview of the AS-5/PFS laser system 28
3.2 Laser pulse properties 29
3.3 Active phase stabilization 31
3.4 Schematic of the phasemeter setup 32
3.5 Phasemeter working principle 33
3.6 Aerodynamic lensing 34
3.7 Velocity map imaging technique 37
3.8 Schematic of single-shot VMI data acquisition 39
3.9 Asymmetry parameters 40
3.10 VMI measurements of Xe gas 41
3.11 ATI background suppression 43
3.12 Long term stability of VMI measurements 44
3.13 Schematic of the STOF setup 45
3.14 Examples of S-TOF measurements 46
3.15 Attosecond streak camera 47
3.16 Attosecond streaking measurements 49
3.17 Overview of the AS-5 beamline 50
3.18 Experimentally obtained XUV pulse properties 52

4.1 Simulated spectra from SiO_2 nanoparticles 58
4.2 Energy vs birth time analysis 59
4.3 Phase space snapshots for simulated SiO_2 spheres 60

4.4 Experimental and simulated VMI projections for 95 nm SiO_2 62
4.5 Asymmetry maps for 95 nm SiO_2 64
4.6 Comparison of cutoff energy and phase shift 65
4.7 CEP modulation map $1.3 \times 10^{13}\,\mathrm{W/cm^2}$ 66
4.8 CEP modulation map $3.7 \times 10^{13}\,\mathrm{W/cm^2}$ 67
4.9 Spatial reconstruction 69
4.10 Field enhancement maps for large SiO_2 nanoparticles 70
4.11 Propagation effects at 400 nm SiO_2 spheres 71
4.12 VMI projections and CEP dependence of large SiO_2 spheres 73
4.13 Comparison to M^3C simulations (400 nm) 74
4.14 Correlation between birth and detection angle 75
4.15 Polar modulation plots 76
4.16 Center of mass comparison with Mie theory 77

5.1 Photoelectron energy spectra and cutoff dependence for SiO_2 81
5.2 Cutoff dependence of 60 nm TiO_2 and ZrO_2 nanospheres 82
5.3 Comparison of rescaled cutoff laws 83
5.4 CEP dependency of 95 nm SiO_2 nanospheres 85
5.5 CEP dependency of 60 nm ZrO_2, Si and TiO_2 nanospheres 86
5.6 Free electron density approximations 88

6.1 Working principle of nanoplasmonic streaking 95
6.2 Regimes of plasmonic streaking 97
6.3 Au sphere field maps 99
6.4 Streaking trajectory analysis from Au spheres 100
6.5 Simulated streaking spectrograms for Au spheres 101
6.6 Near-fields of Au nanotips 104
6.7 SEM images of the Au tip 105
6.8 XUV spectra of Au tip, position scan 106
6.9 Relative difference spectrogram 107
6.10 Experimental results of Au tip streaking 109
6.11 Superimposed experimental data 111
6.12 Simulated streaking from Au nanotips 112
6.13 Comparison of experimental and simulated streaking spectrograms 114

A.1 VMI calibration 117
A.2 AS-5 TOF calibration 119

List of Tables

3.1 Geometry of aerodynamic lens 36

5.1 List of samples used for STOF experiments 80

6.1 Results of streaking measurements 110

Chapter 1

Introduction

In 1908, Gustav Mie could theoretically explain the light scattering by small spherical particles [1]. His work extended the Rayleigh scattering theory as it was capable to predict material and size specific resonances. At this time, it could not be foreseen that the formulation of Mie already contained the essential physics that govern nanoplasmonics. The observation of grating anomalies by Wood in 1902 was essentially the discovery of surface-plasmon polaritons [2]. Equally spaced features in electron energy loss spectra at metal foils and films were observed by Ritchie and served as another cornerstone for understanding the interaction of photons and electrons in metals [3, 4]. It was found that the electron oscillations show quasiparticle character which were named plasmons.

For a long time, no particular interest was attributed to the near-field properties of nanoparticles. At the end of the 20th century, this situation drastically changed and the two principal characteristics, namely extreme field enhancement and spatial confinement were systematically studied and utilized. The confinement of light at micro- and even nanosystems was successfully employed in surface-enhanced Raman spectroscopy [5]. The rising interest in nanoplasmonics was even more fueled by the advent of optical communication networks and the desire to build even more compact and faster opto-electronic components. Progress in new fabrication techniques such as nano-lithography made it now possible to design and build antennas for visible light for a variety of purposes. The possible applications of nanosystems range over the whole spectrum of technology from the mentioned electronic devices. The field enhancement can be utilized to build miniaturized light sources [6] as well as to enhance the efficiency of solar cells [7]. Medical applications can benefit from the resonant absorption of light [8].

Part of the rapid progress in nanoscience can also be attributed to the invention of the laser in the mid 1960s as a highly coherent light source. Only a few years later, first pulsed laser light sources helped pushing the experimentally achievable temporal resolution to new (sub-nanosecond) time scales [9]. With such pulsed lasers, pump-probe measurement techniques offered access to ultrafast phenomena in all physical areas and the trend to ever shorter pulses and higher temporal resolution has been continuing until today. Studies on heat transfer in solids [10], ultrafast demagnetization [11] and transient absorption spectroscopy of valence electron motion [12] illustrate how science is today already tackling the most fundamental constituents of matter, namely the real-time observation of electronic motion. Laser pulse lengths have been shortened to a few femtoseconds while intensities are reaching the Petawatt level. For such short pulses, it was found that the field evolution can be characterized and controlled by the carrier envelope phase (CEP). At the beginning of this century, the combination of high intensity and short pulse duration has enabled to even break the femtosecond barrier. By now, attosecond science has become a standard technique for the time-resolved measurement of electron dynamics with pulse lengths well below 100 as [13, 14].

The goal of this work is to investigate the combination of these two major developments, namely the application of femto- and attosecond laser science in the nanoworld. One key subject is the interaction of intense few-cycle laser fields with (dielectric) nanosystems. For single atoms in intense light fields, there is today a basic understanding of the ionization and subsequent processes [15] which serves as the backbone of modern attosecond science. A number of studies extend these concepts to many body systems. It was found that the ionization dynamics of molecules can also be controlled by the laser waveform [16]. The interaction of atomic clusters with intense laser fields creates essentially a nanoplasma, which challenges the theoretical models [17]. A first question that will be addressed in this work is to what extent the ionization dynamics will be modified by the near-field localization of light at the nanoparticle surface and the collective response of ionized electrons. Compared to atoms or molecules the potential landscape differs strongly, being highly asymmetric at the surface and likely to be further influenced by free charges. These issues are addressed in this work by studying the photoemission from dielectric silicon dioxide nanoparticles. Special emphasis is placed on the carrier-envelope-phase of the driving laser field. Knowledge of the waveform defined by the CEP greatly enhances the information obtained from the experiment as one can directly identify the field driven processes.

Passig *et al.* showed that the optical response of silver clusters can well be controlled by optical pumping and subsequent expansion of the clusters [18]. The decreasing charge carrier densities are imprinted in the photoelectron spectra obtained from a time-delayed fs-laser pulse. This raises the interesting question whether the optical properties of nanosystems can also be instantaneously controlled by a light field. Recent experimental work on bulk dielectric samples could prove that charge creation by few-cycle light fields can be limited to sub-fs time scales and a CEP-dependent current can be driven through the samples [19]. Such experiments target the question to what extent one can control electronic motion on attosecond time scales in a (possibly even insulating) medium using short enough driving fields, such that electronic relaxation and scattering processes only play a minor role. From a technical viewpoint, coherent control of electrons on the nanoscale will pave the way for a further speed-up and miniaturization of opto-electronic devices. In such devices, information will be encoded and transferred in the waveform of light fields. Driving currents with electric fields will push the clock speeds into the PHz regime. The application of high intensities to nanoparticles might reveal how the photoionization and rescattering process is modified as it is heavily dependent on the near-field evolution. The use of nanoparticles has the major advantage that the system can still be considered a bulk while propagation effects are minimized, such that a possible transient modification of the material properties is more evident.

As the intrinsic time scale of electronic processes is in the attosecond regime, the question arises whether this motion can not only be excited but also directly measured by employing attosecond pulses. Such a time-resolved measurement can in future experiments be a valuable tool for further progress in nanoscience. The electron dynamics and elementary processes leading to the creation and decay of plasmonic oscillations can be studied with this approach. The experiments on nanoparticles will extend sub-cycle attosecond measurements on surfaces and thin films to resonant processes. As the nanoplasmonic attosecond streaking approach has up to now not been implemented, this work focuses on the question is to what extent the concepts of attosecond science can be transferred to nanosystems.

The presented work is organized as follows. In chapter 2 the most central theoretical concepts for describing the classical interaction of laser light with matter are discussed. A detailed description of the experimental techniques is presented in chapter 3. Chapter 4 contains the results of photoemission experiments from SiO_2 nanospheres of various sizes illustrating the strong coherence and correlation of electrons ionized from the surface. The high intensity regime of photoemission from nanoparticles is discussed in chapter 5. These measurements focus on the phase transition from unperturbed to highly ionized state of the nanoparticle's electronic state and its implications on the photoemission process. A first successful implementation of a sub-cycle, time-resolved measurement of plasmonic oscillations by attosecond streaking spectroscopy is presented in chapter 6 along with a theoretical analysis of the nanoplasmonic streaking process.

List of publications with relevance to the work presented in this thesis

[1] F. Süßmann, T. Fennel, L. Seiffert, V. Mondes, J. Stierle, M. Arbeiter, A. Kessel, J. Plenge, P. Rupp, C. Peltz, B. Ahn, S. Trushin, D. E. Kim, F. Krausz, C. Graf, E. Rühl, S. Zherebtsov, M. F. Kling, "Optical near-field mapping at isolated nanosystems ", *in preparation*, 2013.

[2] F. Süßmann, S. L. Stebbings, S. Zherebtsov, S. H. Chew, M. I. Stockman, E. Rühl, U. Kleineberg, T. Fennel, and M. F. Kling, "Attosecond control and tracing of collective electron motion in nanostructures", *Attosecond and XUV Physics: Ultrafast Dynamics and Spectroscopy*, Wiley-VCH, in press, 2013.

[3] T. Rathje, N. G. Johnson, M. Möller, F. Süßmann, D. Adolph, M. Kübel, R. Kienberger, M. F. Kling, G. G. Paulus, and A. M. Sayler, “Review of attosecond resolved measurement and control via carrier-envelope phase tagging with above-threshold ionization”, *Journal of Physics B: Atomic, Molecular and Optical Physics*, vol. 45, no. 7, p. 074003, 2012.

[4] S. Zherebtsov, F. Süßmann, C. Peltz, J. Plenge, K. J. Betsch, I. Znakovskaya, A. S. Alnaser, N. G. Johnson, M. Kübel, A. Horn, V. Mondes, C. Graf, S. A. Trushin, A. Azzeer, M. J. J. Vrakking, G. G. Paulus, F. Krausz, E. Rühl, T. Fennel, and M. F. Kling, “Carrier-envelope phase-tagged imaging of the controlled electron acceleration from SiO_2 nanospheres in intense few-cycle laser fields”, *New Journal of Physics*, vol. 14, no. 7, p. 075010, 2012.

[5] S. H. Chew, F. Süßmann, C. Späth, A. Wirth, J. Schmidt, S. Zherebtsov, A. Guggenmos, A. Oelsner, N. Weber, J. Kapaldo, A. Gliserin, M. I. Stockman, M. F. Kling, and U. Kleineberg, “Time-of-flight-photoelectron emission microscopy on plasmonic structures using attosecond extreme ultraviolet pulses”, *Applied Physics Letters*, vol. 100, no. 5, p. 051904, 2012.

[6] F. Süßmann, S. Zherebtsov, J. Plenge, N. G. Johnson, M. Kübel, A. M. Sayler, V. Mondes, C. Graf, E. Rühl, G. G. Paulus, D. Schmischke, P. Swrschek, and M. F. Kling, “Single-shot velocity-map imaging of attosecond light-field control at kilohertz rate”, *Review of Scientific Instruments*, vol. 82, no. 9, p. 093109, 2011.

[7] F. Süßmann and M. Kling, “Attosecond nanoplasmonic streaking of localized fields near metal nanospheres”, *Physical Review B*, vol. 84, no. 12, p. 121406(R), 2011.

[8] S. Zherebtsov, T. Fennel, J. Plenge, E. Antonsson, I. Znakovskaya, A. Wirth, O. Herrwerth, F. Süßmann, C. Peltz, I. Ahmad, S. A. Trushin, V. Pervak, S. Karsch, M. J. J. Vrakking, B. Langer, C. Graf, M. I. Stockman, F. Krausz, E. Rühl, and M. F. Kling, “Controlled near-field enhanced electron acceleration from dielectric nanospheres with intense few-cycle laser fields”, *Nature Physics*, vol. 7, pp. 656-662, 2011.

Other publications

[9] Y. Yang, A. Scrinzi, A. Husakou, Q. Li, S. L. Stebbings, F. Süßmann, H. Yu, S. Kim, E. Rühl, J. Herrmann, X. Lin, and M. F. Kling, “High-harmonic and single attosecond pulse generation using plasmonic field enhancement in ordered arrays of gold nanoparticles with chirped laser pulses”, *Optics Express*, vol. 21, no. 2, p. 2195, 2013.

[**10**] S. L. Stebbings, F. Süßmann, Y. Yang, A. Scrinzi, M. Durach, A. Rusina, M. I. Stockman, and M. F. Kling, "Generation of isolated attosecond extreme ultraviolet pulses employing nanoplasmonic field enhancement: optimization of coupled ellipsoids", *New Journal of Physics*, vol. 13, no. 7, p. 073010, 2011.

[**11**] Y. Yang, F. Süßmann, S. Zherebtsov, I. Pupeza, J. Kaster, D. Lehr, H. Fuchs, E. Kley, E. Fill, X. Duan, Z. Zhao, F. Krausz, S. L. Stebbings, and M. F. Kling, "Optimization and characterization of a highly-efficient diffraction nanograting for MHz XUV pulses", *Optics Express*, vol. 19, no. 3, p. 1954, 2011.

[**12**] Y. Yang, E. Csapó, Y. Zhang, F. Süßmann, S. L. Stebbings, X. Duan, Z. Zhao, I. Dékány, and M. F. Kling, "Optimization of the field enhancement and spectral bandwidth of single and coupled bimetal core-shell nanoparticles for few-cycle laser applications", *Plasmonics*, vol. 7, no. 1, p. 99-106, 2012.

Major conference proceedings

[**13**] F. Süßmann and M. F. Kling, "Attosecond measurement of petahertz plasmonic near-fields", *Proc. SPIE* 8096, Plasmonics: Metallic Nanostructures and Their Optical Properties IX, pp. 80961C, 2011.

[**14**] S. L. Stebbings, Y.-Y. Yang, F. Süßmann, R. Graf, A. Apolonskiy, A. Weber-Bargioni, M. Durach, M. I. Stockman, A. Scrinzi, F. Krausz, M. F. Kling "Probing ultrafast nano-localized plasmonic fields via XUV light generation", *Proc. SPIE* 7757, Plasmonics: Metallic Nanostructures and Their Optical Properties VIII, 77571F, 2010.

Chapter 2

Theoretical background

2.1 Interaction of strong laser fields with matter

2.1.1 Few-cycle laser fields

The principle of superposition that governs classical electrodynamics enables the creation of pulsed light fields by superimposing waves with different optical frequencies and appropriate relative phases. In order to obtain a few-cycle field, one requires an octave-spanning spectrum and a flat phase, i.e. no higher order dependency of the spectral phase. The light field can be decomposed into the harmonic oscillation of the carrier and an envelope function $f(t)$, which yields for a transform-limited Gaussian laser pulse:

$$\mathbf{E}_\mathrm{l}(t) = \mathbf{E}_0 \cos(\omega t + \phi_\mathrm{ce}) f(t) = \mathbf{E}_0 \cos(\omega t + \phi_\mathrm{ce}) \exp\left[-2\ln 2 \left(\frac{t}{\tau}\right)^2\right]. \tag{2.1}$$

Here E_0 is the peak electric field amplitude, τ the pulse length (intensity full-width-half-maximum) and ω the carrier frequency. If the pulse length approaches the period of an optical cycle $T = 2\pi/\omega$, the carrier-envelope offset phase ϕ_ce (CEP) becomes an important parameter as it governs the field evolution during the pulse. The CEP relates the temporal offset of the electric field oscillations with respect to the pulse envelope. Figure 2.1 shows the electric field for a CEP of $\phi_\mathrm{ce} = 0$ and $\pi/2$.

For strong field applications another important characteristic of a laser field is the ponderomotive potential U_p which is the average classical kinetic energy of an electron in the laser field

$$U_p = \frac{e^2 E_0^2}{4 m_e \omega^2} \approx 9.33^{-14} I_0 \lambda^2 \left[\frac{\mathrm{eV\ cm}^2}{\mu\mathrm{m\ W}}\right]. \tag{2.2}$$

Here, e denotes the elementary charge, m_e the electron mass, E_0 and I_0 the peak electric field and intensity, respectively. The dependence on the wavelength λ comes about as the the effective time the electron is accelerated is directly proportional to the optical period.

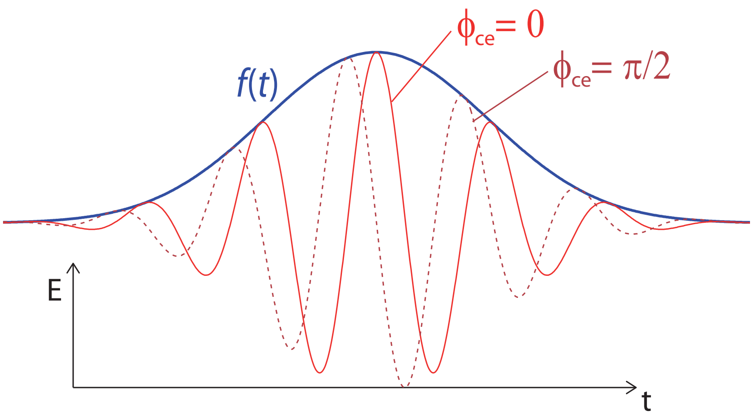

Figure 2.1: Illustration of a 4 fs few-cycle light field. The electric field oscillations are plotted for two different carrier envelope phases.

2.1.2 Interaction of few-cycle laser fields with nanosize objects

As the penetration depth of optical radiation into the medium is typically much larger than the inter-atomic distance, the macroscopic Maxwell equations govern the dynamics [20]. The equations read [21]:

$$\nabla \cdot \mathbf{D} = \rho_{\text{ext}} \tag{2.3a}$$

$$\nabla \cdot \mathbf{B} = 0 \tag{2.3b}$$

$$\nabla \times \mathbf{E} = -\frac{\partial \mathbf{B}}{\partial t} \tag{2.3c}$$

$$\nabla \times \mathbf{H} = \mathbf{J}_{\text{ext}} + \frac{\partial \mathbf{D}}{\partial t}. \tag{2.3d}$$

This set of differential equations couples the dielectric displacement **D**, the electric field **E**, the magnetic field **H** and the magnetic induction **B** to the external charge density ρ_{ext} and current $\mathbf{J}_{\text{ext}}$.

The electric field will cause an effective separation of the charge carriers in a medium and a polarization **P** will build up. For isotropic, linear and non-magnetic materials the field quantities are linked by:

$$\mathbf{D} = \epsilon_0 \mathbf{E} + \mathbf{P} = \epsilon_0 \epsilon_r \mathbf{E} \tag{2.4a}$$

$$\mathbf{B} = \mu_0 \mathbf{H}. \tag{2.4b}$$

The linearity of the medium enables the introduction of the relative permittivity (or dielectric function) $\epsilon_r = \epsilon/\epsilon_0$. Another important relation is the proportionality of the local current in the medium to the electric field:

$$\mathbf{J} = \frac{\partial \mathbf{P}}{\partial t} = \sigma \mathbf{E}, \tag{2.5}$$

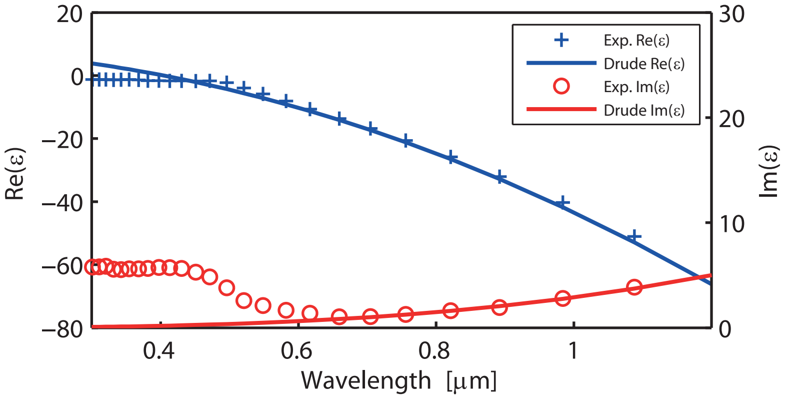

Figure 2.2: Dielectric function of Au. The experimental data was taken from [22]. The Drude fit parameters were taken from [23].

where σ is the conductivity. A crucial aspect, that needs to be considered is that equations (2.4a) and (2.5) are only valid for homogeneous fields and currents. In general, the displacement and current is given by a spatial and temporal convolution [21]:

$$\mathbf{D}(\mathbf{r},t) = \epsilon_0 \iint dt'\mathbf{dr}'\epsilon_r(\mathbf{r}-\mathbf{r}',t-t')\mathbf{E}(\mathbf{r}',t') \tag{2.6a}$$

$$\mathbf{J}(\mathbf{r},t) = \iint dt'\mathbf{dr}'\sigma(\mathbf{r}-\mathbf{r}',t-t')\mathbf{E}(\mathbf{r}',t') \tag{2.6b}$$

The physical interpretation is that the response of the system at a position $\mathbf{r}$ and time t is in principle composed of contributions from all parts of the medium that might originate also at earlier times t'. With respect to nanosystems, it was shown that such effects have to be considered if extremely small structures with sub-nanometer spacing are under investigation [24]. A Fourier transform of equations (2.6a) and (2.6b) both in space and time gives

$$\mathbf{D}(\mathbf{k},\omega) = \epsilon_0\epsilon_r(\mathbf{k},\omega)\mathbf{E}(\mathbf{k},\omega) \tag{2.7a}$$

$$\mathbf{J}(\mathbf{k},\omega) = \sigma(\mathbf{k},\omega)\mathbf{E}(\mathbf{k},\omega) \tag{2.7b}$$

where $\mathbf{k}$ is the wavevector and ω the angular frequency. In frequency space, a direct relation of the dielectric function to the conductivity can be obtained:

$$\epsilon_r(\mathbf{k},\omega) = 1 + \frac{i\sigma(\mathbf{k},\omega)}{\epsilon_0\omega}. \tag{2.8}$$

Note that in Eq. (2.8) any response to external fields is modeled by the (complex) conductivity that includes polarization effects due to the definition given by (2.5). It is also possible to distinguish between bound (polarization) and free charges (conductivity). This results in a different notation $\epsilon_r = \epsilon_p + i\sigma_c/(\epsilon_0\omega)$. Assuming a spatial local and homogeneous response there is no dependence on $\mathbf{k}$ such that the only relevant wavevector is $\mathbf{k} = \mathbf{0}$ which simplifies the Eq. (2.8) to $\epsilon_r(\mathbf{k}, \omega) = \epsilon_r(\omega)$.

For many dielectric materials (such as SiO_2) $\epsilon_r(\omega)$ does not vary drastically in the optical frequency range and can be approximated to be constant at least when nanosystems are under consideration. For metals one can employ the Drude model. This model treats the conducting electrons of a metal as a free electron gas. For this simple picture the dielectric function can be derived for a harmonic external driving field $\mathbf{E}(t) = \mathbf{E}_0 e^{-i\omega t}$ [20]:

$$\epsilon_r(\omega) = 1 - \frac{\omega_p^2}{\omega^2 + i\gamma_e\omega}. \tag{2.9}$$

Here γ_e is the collision frequency of the electrons and ω_p is the plasma frequency which is defined as

$$\omega_p = \sqrt{\frac{n_e e^2}{\epsilon_0 m_{\text{eff}}}}. \tag{2.10}$$

n_e is the density of electrons in the medium with an effective mass of m_{eff}. The Drude model usually reproduces the main characteristics of the interaction of metals with light. For real systems inter- and intraband transitions have to be taken into account as well. Figure 2.2 shows the experimentally obtained dielectric function of gold [22] in addition to a fit according to the Drude model , where $\omega_p = 1.36 \times 10^{16}$ rad s^{-1} and $\gamma_e = 1.05 \times 10^{14}$ rad s^{-1} [23]. The deviations at small wavelength are a result of inter- and intraband transitions which are not included in the Drude model.

2.1.3 Plasmons as collective electron excitations

The term plasmon polariton refers to a quantized excitation of the electron charge distribution in bulk media. It is often exclusively used for the (resonant) response of the conduction band electrons in a metal. This leads to the common misconception that plasmons only exist in metallic system, i.e. systems that show a noticeable dc-conductivity. As the frequency-dependent dielectric function $\epsilon_r(\omega)$ is governing the system's response to a time varying electro-magnetic field, the response for e.g. optical frequencies might be completely unrelated to the behavior at $\omega \approx 0$. Therefore, even isolating dielectrics might show a metal-like response for optical frequencies. Such a behavior was theoretically predicted for thin dielectric films in intense electric fields [25].

In general, one can distinguish between surface plasmon polaritons (SPP) and localized surface plasmons (LSP). An SPP denotes a confined traveling electromagnetic wave at a metal-dielectric interface [21]. Such a wave needs to be TM-polarized and is depicted in Fig. 2.3 a). If the size of the system becomes smaller and falls below the wavelength of the SPP, the surface wave can of course not propagate. In this limiting case, one speaks about localized surface plasmons (see Fig. 2.3 b)). Given the right material properties, a sub-wavelength nanoplasmonic particle can be imagined as an antenna for optical light.

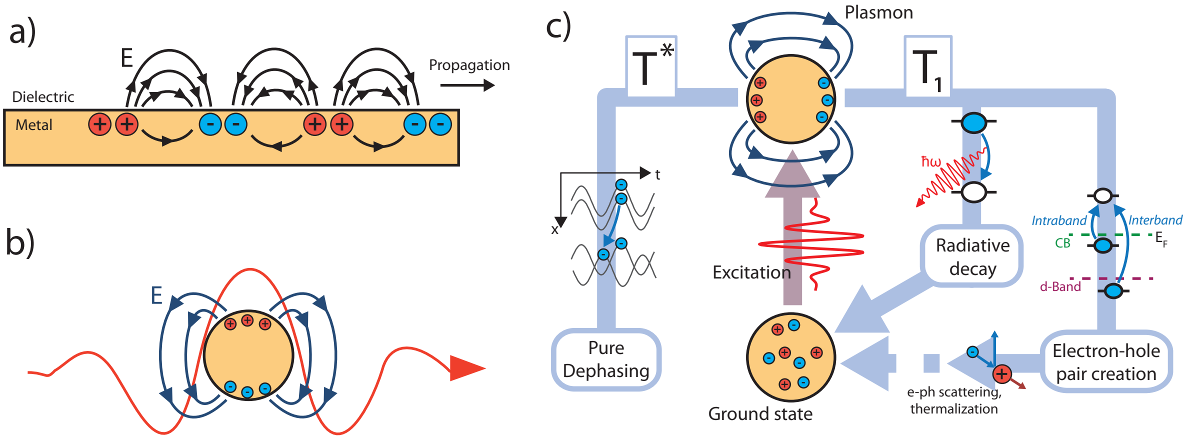

Figure 2.3: a) Surface plasmon polariton. b) Localized surface plasmon. c) Decay channels of excited plasmons. As published in [27].

The response of the system usually leads to a pronounced near-field enhancement and resonant oscillations of the electronic polarization. It is possible to couple two or more of these antennas leading to even stronger near-field enhancement and sharper resonances [26].

The lifetime of a plasmonic oscillation usually lies in the femtosecond regime [28]. The possible decay channels are indicated in Fig. 2.3 c). After excitation, the elastic dephasing due to local inhomogeneities is causing an effective decrease in oscillation amplitude. A second pathway are inelastic scattering processes causing intra- and interband transitions and a thermalization of the electron gas. The final equilibration with the lattice via electron-phonon scattering takes place on a much longer time scale in the ps regime [29]. A direct decay channel is the re-emission of photons referred to as radiative decay. Its influence is determined by the coupling strength to the far field. It was shown that the situation for nanoplasmonic systems can be treated with the tools of radio antenna physics [30]. From the elastic and inelastic decay channels an effective decay time constant can be defined:

$$\frac{1}{T_2} = \frac{1}{T^*} + \frac{1}{T_1}. \tag{2.11}$$

Here T^* quantifies the elastic phase loss and T_1 includes the inelastic phase loss and radiative decay. The imaginary part of the dielectric function includes the influence of elastic dephasing and electron-electron scattering.

As will be shown in the next sections, field enhancement and near-field localization can also be observed for dielectric particles where $Re[\epsilon_r(\omega)] > 0$. This is why in this work, it will not be distinguished between metals, semiconductors and dielectrics. The term ”plasmon” will be avoided in such cases. As the unified notation of Eq. (2.8) suggests this work will focus on collective electron excitations in general regardless whether they can be

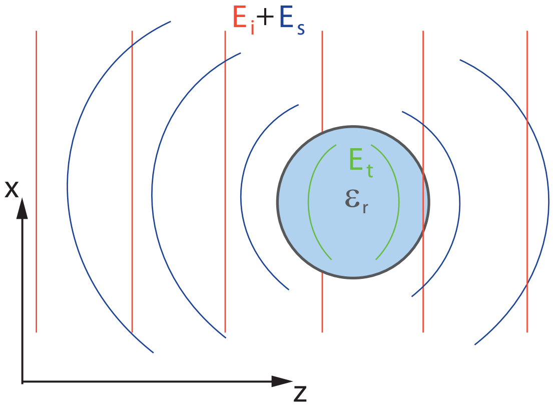

Figure 2.4: Conventions used for the Mie solution. The field outside the sphere is composed of incident field $\mathbf{E}_i$ (wavefronts indicated by red lines) polarized in x-direction and scattered field $\mathbf{E}_s$ (blue lines). The field inside the sphere is the transmitted wave $\mathbf{E}_t$ (green).

attributed to a free electron gas or a polarization response of bound electrons.

2.1.4 Mie theory for spherical particles

Due to the symmetry of a spherical system, it is possible to derive an analytic exact solution of the Maxwell equations [1, 31]. Without loss of generality, the sphere with a permittivity of ϵ and a radius of R can be placed at the origin. Furthermore assuming a linear response of the medium, the Mie solution spectrally decomposes the incident field by considering only monochromatic plane waves. The incident wave shall be polarized along the x axis and can be written as:

$$\mathbf{E}_i(\mathbf{r},\omega) = E_0 e^{-ikrcos\theta}\mathbf{e}_x. \tag{2.12}$$

The field at any point outside the sphere is constructed by a superposition of incident field $\mathbf{E}_i$ and a contribution by the scattered fields $\mathbf{E}_s$ (see Fig. 2.4). The fields inside the sphere will be denoted $\mathbf{E}_t$. The expressions for $\mathbf{E}_i$, $\mathbf{E}_s$ and $\mathbf{E}_t$ and their corresponding magnetic fields ($\mathbf{H}_i$, $\mathbf{H}_s$ and $\mathbf{H}_t$) must satisfy the wave equations. These wave equations can be derived from Maxwell's equations in Fourier space and read [32]:

$$\nabla^2\mathbf{E} + k^2\mathbf{E} = 0\ , \tag{2.13a}$$

$$\nabla^2\mathbf{H} + k^2\mathbf{H} = 0\ . \tag{2.13b}$$

$k = |\mathbf{k}| = \sqrt{\omega^2\epsilon\mu}$ represents the wavevector. Both $\mathbf{E}$ and $\mathbf{H}$ are required to be divergence-free:

$$\nabla\cdot\mathbf{E} = 0, \qquad \nabla\cdot\mathbf{H} = 0. \tag{2.14}$$

The field quantities are linked (in analogy to equations (2.3a) and (2.3b)) by

$$\nabla\times\mathbf{E} = i\omega\mu\mathbf{H}, \qquad \nabla\times\mathbf{H} = -i\omega\epsilon\mathbf{E}. \tag{2.15}$$

Given the spherical symmetry of the problem, finding the solution to the wave equation is the simplest in spherical coordinates. This can be done by constructing two vector functions

$$\mathbf{M} = \nabla \times (\mathbf{r}\psi), \qquad \mathbf{N} = \frac{\nabla \times \mathbf{M}}{k}, \tag{2.16}$$

where $\mathbf{r}$ is a (in principle arbitrary) vector and ψ is a scalar function. By the use of vector identities one can show that the vector functions $\mathbf{M}$ and $\mathbf{N}$ satisfy the requirements imposed by equations (2.13a), (2.14) and (2.15). Furthermore, as $\mathbf{r}$ denotes the spatial coordinate, $\mathbf{M}$ and $\mathbf{N}$ are only solutions to the wave equation if ψ is a solution to the scalar wave equation in spherical coordinates:

$$\frac{1}{r^2}\frac{\partial}{\partial r}\Big(r^2\frac{\partial\psi}{\partial r}\Big) + \frac{1}{r^2\sin(\theta)}\frac{\partial}{\partial\theta}\Big(\sin(\theta)\frac{\partial\psi}{\partial\theta}\Big) + \frac{1}{\sin^2(\theta)}\frac{\partial^2\psi}{\partial\phi^2} + k^2\psi = 0. \tag{2.17}$$

The problem has now been simplified considerably as only the solution of a single scalar wave equation needs to be determined from which the complete set of vector harmonics $\mathbf{M}$ and $\mathbf{N}$ can be constructed. After a separation of variables the general solution to the (orthogonal) generating functions read

$$\psi_{emn} = \cos(m\phi)P_n^m(\cos\theta)z_n(kr) \tag{2.18a}$$

$$\psi_{omn} = \sin(m\phi)P_n^m(\cos\theta)z_n(kr). \tag{2.18b}$$

Here P_n^m are the associated Legendre functions of the first kind, while z_n is any of the four spherical Bessel functions. The next step in solving the problem is the expansion of the incident wave given by equation (2.12). Here one finds

$$\mathbf{E}_i = \sum_{n=1}^{\infty}\big(B_{o1n}\mathbf{M}^j_{o1n} + A_{e1n}\mathbf{N}^j_{e1n}\big) = E_0\sum_{n=1}^{\infty} i^n\frac{2n+1}{n(n+1)}\big(\mathbf{M}^j_{o1n} + \mathbf{N}^j_{e1n}\big). \tag{2.19}$$

The superscripts (j) denote that only the Bessel functions which are finite at the origin need to be taken into account. The continuity of the normal components of both $\mathbf{E}$ and $\mathbf{H}$ demand that

$$(\mathbf{E}_i + \mathbf{E}_s - \mathbf{E}_t) \times \mathbf{e}_r = 0, \qquad (\mathbf{H}_i + \mathbf{H}_s - \mathbf{H}_t) \times \mathbf{e}_r = 0. \tag{2.20}$$

With these boundary conditions it is possible to derive expressions for the scattered and transmitted field:

$$\mathbf{E}_s = \sum_{n=1}^{\infty} E_n\big(i^n a_n\mathbf{N}^h_{e1n} - b_n\mathbf{M}^h_{o1n}\big) \tag{2.21a}$$

$$\mathbf{E}_t = \sum_{n=1}^{\infty} E_n\big(c_n\mathbf{M}^j_{o1n} - id_n\mathbf{N}^j_{e1n}\big) \tag{2.21b}$$

with $E_n = i^nE_0(2n{+}1)/n(n{+}1)$. The superscript h demands the use of the spherical Bessel function of the third kind (Hankel function). The expansion coefficients a_n, b_n, c_n and d_n

are referred to as scattering or Mie coefficients. Scattering cross section and absorption coefficients can be directly calculated from these scattering coefficients. Similar expressions are also found for the magnetic field components **H**. By using the orthogonality of the generating functions one can find analytic expressions for the scattering coefficients:

$$a_n = \frac{m^2 j_n(m\rho)\big(\rho j_n(\rho)\big)' - j_n(\rho)\big(m\rho j_n(m\rho)\big)'}{m^2 j_n(m\rho)\big(\rho h_n(\rho)\big)' - h_n(\rho)\big(m\rho j_n(m\rho)\big)'}, \tag{2.22a}$$

$$b_n = \frac{j_n(m\rho)\big(\rho j_n(\rho)\big)' - j_n(\rho)\big(m\rho j_n(m\rho)\big)'}{j_n(m\rho)\big(\rho h_n(\rho)\big)' - h_n(\rho)\big(m\rho j_n(m\rho)\big)'}, \tag{2.22b}$$

$$c_n = \frac{j_n(\rho)\big(\rho h_n(\rho)\big)' - h_n(\rho)\big(\rho j_n(\rho)\big)'}{j_n(m\rho)\big(\rho h_n(\rho)\big)' - h_n(\rho)\big(m\rho j_n(m\rho)\big)'}, \tag{2.22c}$$

$$d_n = \frac{m j_n(\rho)\big(\rho h_n(\rho)\big)' - m h_n(\rho)\big(\rho j_n(\rho)\big)'}{m^2 j_n(m\rho)\big(\rho h_n(\rho)\big)' - h_n(\rho)\big(m\rho j_n(m\rho)\big)'}. \tag{2.22d}$$

Here j_n is the nth spherical Bessel function of the first kind, while h_n is the spherical Hankel function of the first kind. m denotes the relative refractive index which is in the case of a sphere in vacuum $m = \sqrt{\epsilon_r}$, and ρ is the size parameter $\rho = kR$. Note, that the sphere material is assumed to be non-magnetic. Figure 2.5 a) shows examples of field distributions around nanospheres (E_y-component). The fields were calculated for a wavelength of 720 nm for 60 nm diameter SiO_2, Si, Au and TiO_2 spheres. The superposition of incident and scattered fields leads to a significant field enhancement at the poles of the spheres. As can be seen, the magnitude of this enhancement depends on the dielectric function which also affects the shielding of the interior fields. Due to the small size of the spheres, the relative field distributions are comparable for all materials. Figure 2.5 b) shows the field enhancement of Au spheres (E_y) for different wavelengths and sphere diameters sampled at the pole. One can see that for small diameters, the enhancement is dominated by the material properties. Above 100 nm higher order modes are excited leading to an effective red shift and broadening of the plasmonic resonance for increasing diameter.

2.1.5 Quasistatic dipole approximation

The number of Mie coefficients that are taken into account in equation (2.21) has to be adapted to the size parameter ρ. In principle, this compares the size of the sphere to the wavelength. If the sphere is much smaller than the wavelength, propagation effects over the sphere can be neglected and only low order vector harmonics contribute. The field distributions shown in Fig. 2.5 a) resemble the one of a dipole. Indeed, for sizes much smaller than the wavelength $R \ll \lambda$, it turns out that the only relevant expansion coefficients in Eq. (2.21) are of the first order ($n = 1$). For such a condition the derivation of the fields can also be obtained under the assumption of a spatial homogeneous incident field $\mathbf{E}_i(\mathbf{r}) = \mathbf{E}_i$ (the time dependence is omitted here) [21]. Solving the electrostatic

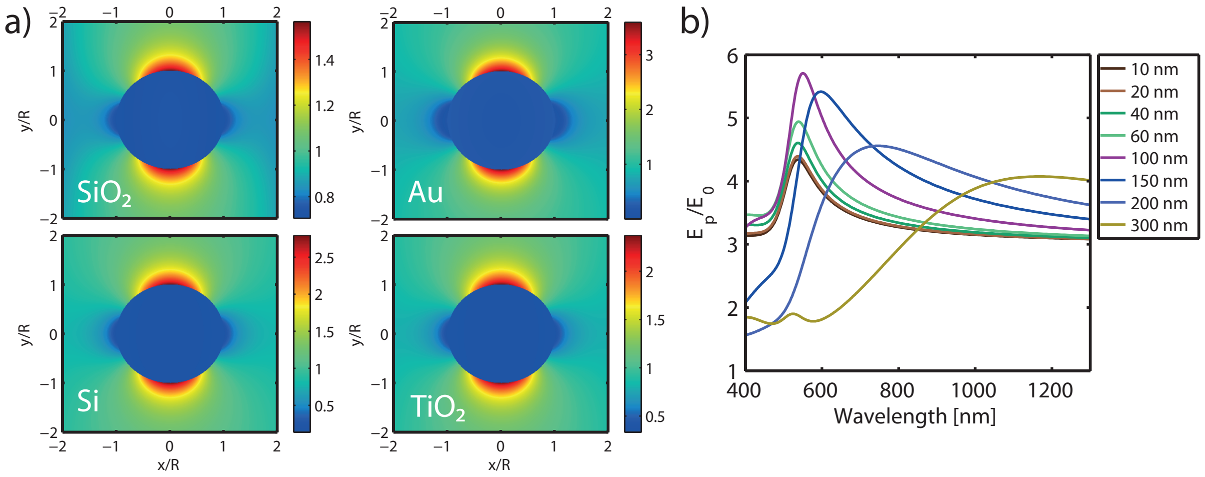

Figure 2.5: a) Field distributions for SiO_2, Si and Au nanoparticles. b) Enhancement as a function of wavelength for various sphere diameters.

problem yields simple expressions for the fields inside and outside of the sphere [31, 21]:

$$\mathbf{E}_{\text{in}}(\mathbf{r}) = \frac{3\epsilon_m}{\epsilon_r + 2\epsilon_m}\mathbf{E}_0 \tag{2.23a}$$

$$\mathbf{E}_{\text{out}}(\mathbf{r}) = \mathbf{E}_0 + \frac{3\hat{\mathbf{r}}(\hat{\mathbf{r}} \cdot \mathbf{p}) - \mathbf{p}}{4\pi\epsilon_0\epsilon_m}\frac{1}{r^3} \tag{2.23b}$$

Here $\hat{\mathbf{r}}$ is the normal vector of $\mathbf{r}$ and ϵ_m is the relative permittivity of the surrounding medium. The effective polarization of the sphere is given by

$$\mathbf{p} = 4\pi\epsilon_0\epsilon_m R^3 \frac{\epsilon_r - \epsilon_m}{\epsilon_r + 2\epsilon_m}\mathbf{E}_0. \tag{2.24}$$

With these simple solutions, important characteristics such as field enhancement at the surface can easily be obtained. For dielectrics, an increase in ϵ_r leads to a higher field enhancement factor reaching a limiting value of 3 for $\epsilon_r \gg \epsilon_m$. The interior of the sphere is shielded from the incident field. A higher index of refraction results in more efficient shielding. In case of metals, the real part of the relative permittivity is usually negative. This can lead to a resonant behavior if the denominators in (2.23a) and (2.24) go to zero which is also referred to as the Fröhlich condition [33]. For a small, metallic sphere in vacuum this condition is equivalent to

$$Re[\epsilon_r(\omega)] = -2. \tag{2.25}$$

For real metals the imaginary part of $\epsilon_r(\omega)$ is usually non-zero and positive assuring finiteness of the fields. Comparing the dispersion relation for Au shown in Fig. 2.2 one can see that the Fröhlich condition is fulfilled for frequencies in the visible. In combination with the small damping factor in this wavelength region the resonant behavior makes gold thus a popular system for nanoplasmonics. The quasi-static treatment and the Fröhlich condition is only valid for very small spheres well below 100 nm. For larger spheres, geometric effects and wave propagation will excite higher field modes in the sphere and therefore also result in a modified resonance condition. Usually, the resonance shifts to longer wavelengths for increasing sphere size, which can be seen in Fig. 2.5 b).

2.1.6 Numerical methods for arbitrary geometries

For a system with a more complex geometry (other than sphere, ellipsoid or infinite cylinder) finding an analytic expression is usually not feasible. In these cases one has to employ numerical methods to obtain the field distributions. One of the most popular techniques is the finite-difference-time-domain method. This grid based approach discretizes the Maxwell equations in space and time using a central-difference approximation [34]. Other methods which work in the spectral domain include finite-element method (FEM), boundary-element methods (BEM) and discrete dipole scattering approximations.

A major advantage of FDTD is its simplicity, as only the geometry and material properties need to be assigned to the simulation grid. The incident light field can be directly specified in the time domain and a single simulation run yields the field evolution in the simulation volume. Material dispersion can be included by employing polarization terms. The drawbacks are diffraction effects due to the limited simulation volume and numerical dispersion, which make the simulation of few-cycle pulses challenging. Also, the limitation to a rectangular grid poses problems if the surfaces are not parallel to the grid resulting in hotspot-like artifacts.

2.1.7 Multipole expansion of charge distributions

Multipole expansions can be used for an efficient calculation of the Coulomb potential created by an arbitrary charge distribution. Such an expansion can include the presence of a spherical medium. The following derivation is given here as a courtesy of Prof. Thomas Fennel, Universität Rostock.

The potential of a free charge q_i at position $\mathbf{r}_i$ in a medium with relative permittivity ϵ_r is given by Coulomb's law

$$\Phi_i(\mathbf{r}) = \frac{1}{4\pi\epsilon_0\epsilon_r}\frac{q_i}{|\mathbf{r}-\mathbf{r}_i|} = \frac{1}{4\pi\epsilon_0\epsilon_r}\frac{q_i}{|\mathbf{r}_> - \mathbf{r}_<|} \tag{2.26}$$

Here, $r_>$ is the larger value of the two absolute values $|\mathbf{r}|$ and $|\mathbf{r}_i|$, while $r_<$ is the smaller value. At all position $\mathbf{r} \neq \mathbf{r}_i$, the Laplace equation must be fulfilled:

$$\triangle\Phi_i(\mathbf{r}) = 0 \quad \forall\mathbf{r} \neq \mathbf{r}_i \tag{2.27}$$

Rewriting this differential in spherical coordinates yields [20]:

$$\frac{1}{r}\frac{\partial}{\partial r}(r\Phi) + \frac{1}{r^2\sin(\theta)}\frac{\partial}{\partial\theta}\Big(\sin(\theta)\frac{\partial\Phi}{\partial\theta}\Big) + \frac{1}{\sin^2(\theta)}\frac{\partial^2\Phi}{\partial\phi^2} = 0 \tag{2.28}$$

After a separation of variables the solution can be written as a product of functions of the spherical coordinates:

$$\Phi = \sum_{l=0}^{\infty} \sum_{m=-\infty}^{\infty} \frac{U_l(r)}{r} P_l(\cos\theta) Q_m(\phi) \tag{2.29}$$

with

$$U_l(r) = A_l r^{l+1} + B_l r^{-l} \tag{2.30a}$$

$$Q_m(\phi) = C_m e^{im\phi} \tag{2.30b}$$

$$P_l(x) = \frac{1}{2^l l!} \frac{\partial^l}{\partial x^l} (x^2 - 1)^2 \tag{2.30c}$$

$P_l(x)$ are the well-known Legendre polynomials. The coefficients A_l, B_l and C_m have to be determined from the boundary conditions. For finding these coefficients for a single charge at $\mathbf{r}_i$, a trick can be used by rotating the coordinate system such the z-axis aligns with $\mathbf{r}_i$. Now the problem has cylindrical symmetry around this axis, which implicates the problem does no more depend on ϕ ($C_0 = 1, C_m = 0 \quad \forall m \neq 0$). This yields

$$\Phi_i(\mathbf{r}) = \sum_{l=0}^{\infty} [A_l r^l + B_l r^{-(l+1)}] P_l(\cos(\theta)) \tag{2.31}$$

A Taylor expansion of (2.26) around $r_< = 0$ and a comparison of coefficients yields expressions for the A_l and B_l resulting in

$$\Phi_i(\mathbf{r}) = \frac{q_i}{4\pi\epsilon_0\epsilon_r} \sum_{l=0}^{\infty} \frac{r_<^l}{r_>^{l+1}} P_l(\cos(\theta_{\mathbf{r}\mathbf{r}_i})), \tag{2.32}$$

where $\theta_{\mathbf{r}\mathbf{r}_i}$ is the angle between $\mathbf{r}$ and $\mathbf{r}_i$. Equation (2.32) is equivalent to (2.26). The potential of multiple charges can be obtained by simply superimposing the individual contributions.

We will now assume a sphere with a relative permittivity ϵ_r and a radius R to be placed at $\mathbf{r} = \mathbf{0}$. The conventions are shown in Fig. 2.6 a) and b) for the potential outside Φ_i^{out} and inside of the sphere Φ_i^{in}, respectively. Both solutions have to obey the boundary conditions on the surface. At first, one has to distinguish whether a charge is placed inside the sphere or outside. As the solution has to be finite, this leads to an ansatz for the case $r_i < R$:

$$\Phi_i^{\text{in}}(\mathbf{r}) = \frac{q_i}{4\pi\epsilon_0\epsilon_r} \sum_l \frac{r_<^l}{r_>^{l+1}} P_l(\cos\theta_{\mathbf{r}\mathbf{r}_i}) + \sum_l A_l r^l P_l(\cos\theta_{\mathbf{r}\mathbf{r}_i}) \qquad r < R \tag{2.33a}$$

$$\Phi_i^{\text{out}}(\mathbf{r}) = \sum_l B_l r^{-(l+1)} P_l(\cos\theta_{\mathbf{r}\mathbf{r}_i}) \qquad r > R \tag{2.33b}$$

while for $r_i > R$

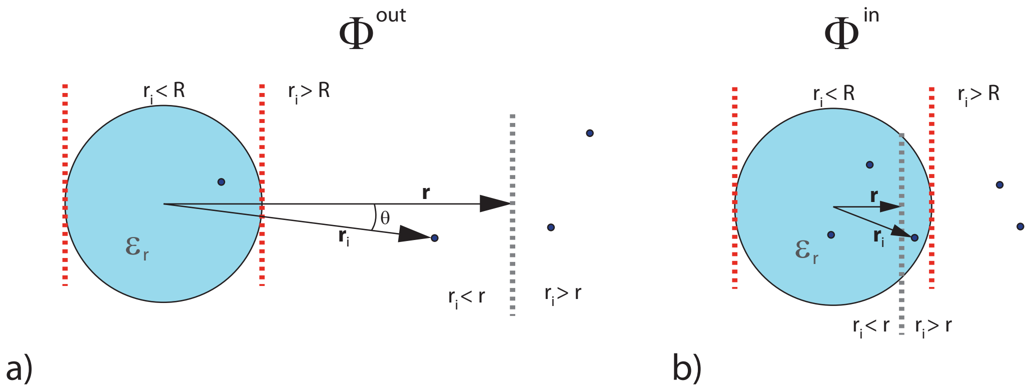

Figure 2.6: Illustration of the multipole expansion of charges located in and outside of a dielectric sphere. a) Summing convention for the potential outside the sphere and b) inside the sphere.

$$\Phi_i^{\text{in}}(\mathbf{r}) = \sum_l C_l r^l P_l(\cos\theta_{\mathbf{r}\mathbf{r}_i}) \qquad r < R \tag{2.34a}$$

$$\Phi_i^{\text{out}}(\mathbf{r}) = \frac{q_i}{4\pi\epsilon_0} \sum_l \frac{r_<^l}{r_>^{l+1}} P_l(\cos\theta_{\mathbf{r}\mathbf{r}_i}) + \sum_l D_l r^{-(l+1)} P_l(\cos\theta_{\mathbf{r}\mathbf{r}_i}) \qquad r > R \tag{2.34b}$$

The boundary conditions at the sphere surface demand for a continuity of the potential itself and the normal component of the dielectric displacement $\mathbf{D}$ [20]:

$$\Phi^{\text{in}}(\mathbf{R}) = \Phi^{\text{out}}(\mathbf{R}) \tag{2.35a}$$

$$\mathbf{D}_\perp^{\text{in}}(\mathbf{R}) = \epsilon_r \frac{\partial \Phi^{\text{in}}}{\partial r}(\mathbf{R}) = \epsilon_r \frac{\partial \Phi^{\text{out}}}{\partial r}(\mathbf{R}) = \mathbf{D}_\perp^{\text{out}}(\mathbf{R}) \tag{2.35b}$$

Inserting equations (2.33) and (2.34) into these boundary conditions again gives solutions for the coefficients A_l, B_l, C_l and D_l. The final solution for a all charges i inside the sphere reads

$$\Phi^{\text{in}}(\mathbf{r}) = \frac{1}{4\pi\epsilon_0\epsilon_r} \sum_l \left[\sum_{\substack{r_i<R \\ r_i<r}} \frac{q_i r_i^l}{r^{l+1}} P_l(\alpha_i) + \sum_{\substack{r_i<R \\ r_i>r}} \frac{q_i r^l}{r_i^{l+1}} P_l(\alpha_i) + \sum_{r_i<R} a_l r^l q_i r_i^l P_l(\alpha_i) \right] \tag{2.36a}$$

$$\Phi^{\text{out}}(\mathbf{r}) = \frac{1}{4\pi\epsilon_0} \left[\sum_l \sum_{r_i<R} b_l \frac{q_i r_i^l}{r^{r+1}} P_l(\alpha_i) \right] \tag{2.36b}$$

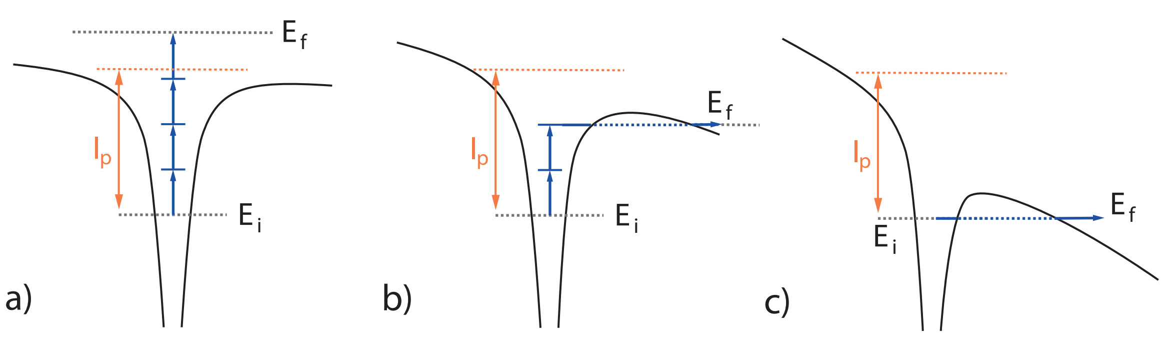

Figure 2.7: Transition of the ionization process from multi-photon to tunneling regime. a) MPI at low intensities. b) Intermediate regime. c) Tunnel regime at high intensities. Adapted from [32].

while for charges outside the sphere

$$\Phi^{\text{in}}(\mathbf{r}) = \frac{1}{4\pi\epsilon_0}\left[\sum_l \sum_{r_i<R} q_i \frac{c_l r^l}{r_i^{r+1}} P_l(\alpha_i)\right] \tag{2.37a}$$

$$\Phi^{\text{out}}(\mathbf{r}) = \frac{1}{4\pi\epsilon_0\epsilon_r}\sum_l\left[\sum_{\substack{r_i>R\\ r_i<r}} \frac{q_i r_i^l}{r^{l+1}} P_l(\alpha_i) + \sum_{\substack{r_i>R\\ r_i>r}} \frac{q_i r^l}{r_i^{l+1}} P_l(\alpha_i) + \sum_{r_i>R} q_i \frac{d_l q_i}{r_i^{l+1} r^{l+1}} P_l(\alpha_i)\right] \tag{2.37b}$$

The coefficients a_l, b_l, c_l and d_l can again be determined from the boundary conditions.

2.2 Ionization of atoms and solids by strong light fields

2.2.1 Above threshold ionization

Ionization of matter, i.e. the liberation of bound electrons by a laser field, is strongly dependent on the peak amplitude of the light field oscillation. Not only the ionization yield increases with intensity but also the dominant process changes for higher intensities. Figure 2.7 visualizes these different ionization regimes. For low intensities, ionization of a medium can be understood in terms of multiphoton ionization (MPI), where the absorption of n photons is required to overcome the binding potential $n\hbar\omega > I_p$ (as illustrated in Fig. 2.7 a)). Perturbation theory predicts that the rate of multi-photon ionization scales with the corresponding power of the laser intensity $w_{\text{MPI}} \propto I_0^n$, where n is the number of absorbed photons. As the electric field strength approaches or even overcomes the Coulomb field which binds the electron to the parent ion, the ionization will take place in a distinctively different manner. As schematically shown in Fig. 2.7 b) and c), the atomic potential is strongly bent by the laser field enabling either a mixture of MPI and tunneling ionization or pure tunneling.

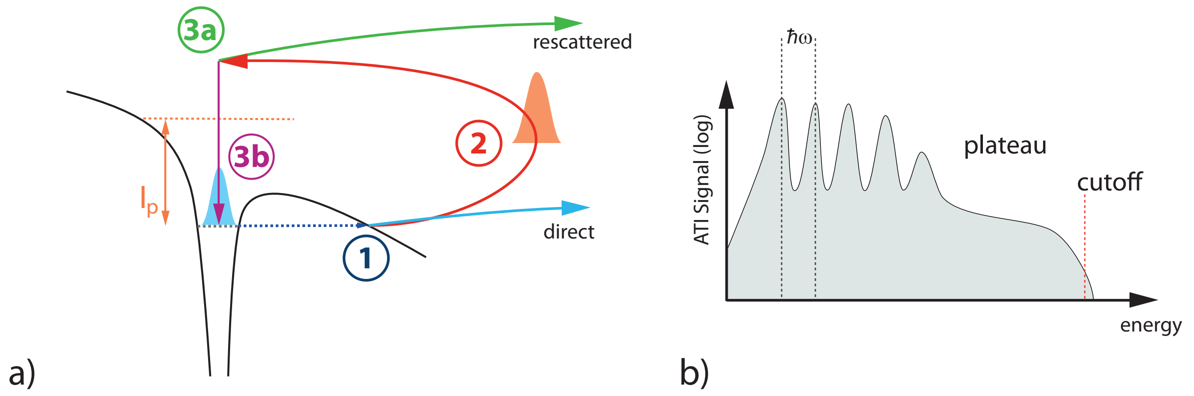

Figure 2.8: a) Illustration of the simple man's model for ATI and HHG. The electron is ionized by the laser field (1). The electron is accelerated in the laser field (2). Upon recollision the electron can either scatter (3a) or recombine (3b). b) Schematic ATI energy spectrum for a few-cycle laser pulse.

Ionization by intense laser fields is referred to as above-threshold-ionization (ATI). The name already suggests that the laser field can transfer more energy to the liberated electron than necessary for ionization. Under such conditions the electron has an appreciable probability to tunnel through the effective potential barrier (tunnel regime) or can even leave the atom freely (above the barrier regime). To characterize the dynamics the Keldysh parameter is usually employed which relates the strength of the atomic potential to the driving field [35]:

$$\gamma = \frac{\omega\sqrt{m_e I_p}}{|eE|} = \sqrt{\frac{I_p}{2U_p}}. \tag{2.38}$$

Here m_e and e denote the electron's mass and charge, while I_p is the ionization potential and U_p the ponderomotive potential. At high intensities $\gamma < 1$ and tunneling ionization is usually the dominant process, while for $\gamma > 1$ multi-photon ionization needs to be taken into account. There are a number of theoretical approaches to model the ionization rate. Often Keldysh-like theories like the Ammosov-Delone-Krainov (ADK) model are employed in the tunneling regime [35, 36]. This ADK model is derived for linearly polarized laser light in which the pulse length is assumed to be much longer than an optical cycle. The ionization rate is given by:

$$w = N \exp\left(-\frac{4\sqrt{2m_e}I_p^{3/2}}{3\hbar e E_0}\right). \tag{2.39}$$

Here e and m_e is the electron charge and mass, respectively. N is a slowly varying function, which depends on the ionization potential I_p and average laser intensity.

The dynamics of the ionized electron wave packet will clearly depend on the time of birth as it is subject to the (time-dependent) electric fields. This is the realm of the so called three-step or simple man's model [37]. The main assumption of this model is that the acceleration of the electron is dominated by the external laser field. This can be justified by the strong laser field itself and furthermore by a large enough distance between tunneled electron and parent ion. Fig. 2.8 a) shows an illustration of the processes. Integrating the classical equation of motion with only the external laser field as a driving force, one finds that there are two types of trajectories. Direct electrons leave the atom without return. Varying the emission time, classical mechanics predict a maximum kinetic energy of 2 U_p of such direct electrons. All other trajectories will return to the parent ion. Here they can either be scattered or recombine. The recombination will produce high energetic photons which will be described in the next section. If the electron scatters, it will be further accelerated in the laser field potentially gaining more energy. Taking into account only the acceleration in the laser field, the highest kinetic energy of a back-scattered photoelectron was found to be $E_\mathrm{c} = 10.0007\ U_p$ by integration of the classical equations of motion [38]. Busuladžić *et al.* proposed a modified version of this cutoff law which takes the influence of the atomic potential into account and therefore yields more accurate results especially for lower intensities [39]:

$$E_\mathrm{c} = 10.0007\ U_p + 0.538\ I_p. \tag{2.40}$$

The shape of an ATI-photoelectron spectrum heavily depends on intensity, wavelength and laser pulse length. The occurrence of trajectories yielding the same final kinetic energy results in interference. Sub- and intercycle interferences create the typical ATI peaks in the spectrum being more pronounced for long pulses. For few-cycle laser fields, the highest energetic trajectories will only occur once during a single pulse. Thus, the high-energy part of the spectrum usually features a plateau which extends up to the highest observable energies (cutoff). Fig. 2.8 b) shows such a spectrum schematically.

2.2.2 HHG and attosecond pulse generation

Within the simple man's model the recolliding electron has a probability for recombination into the initial ground state. This process is referred to as high-harmonic generation (HHG). Due to energy conservation the recombination is only possible under the emission of a photon which carries the binding energy of the final state in addition to the energy the electron has acquired from the laser field. The maximum energy an electron gains in the laser field before returning to the core is 3.17 U_p [40]. Therefore the maximum photon energy can easily lie in the extreme-ultraviolet (XUV) spectral region and is given classically by

$$E_\mathrm{xuv} = \hbar\omega_\mathrm{xuv} = 3.17\ U_p + I_p. \tag{2.41}$$

In a quantum mechanical treatment, the picture is slightly different as only a fraction of the electronic wavefunction appears at the tunnel exit [41, 15]. The other part remains in the ground state. The ionized portion will be accelerated by the laser field and returns to the core, where it overlaps with the localized parts of the wavefunction. This interference causes a modulation of the electronic probability distribution which was shown to be equivalent to a rapidly oscillating dipole creating the high energetic radiation.

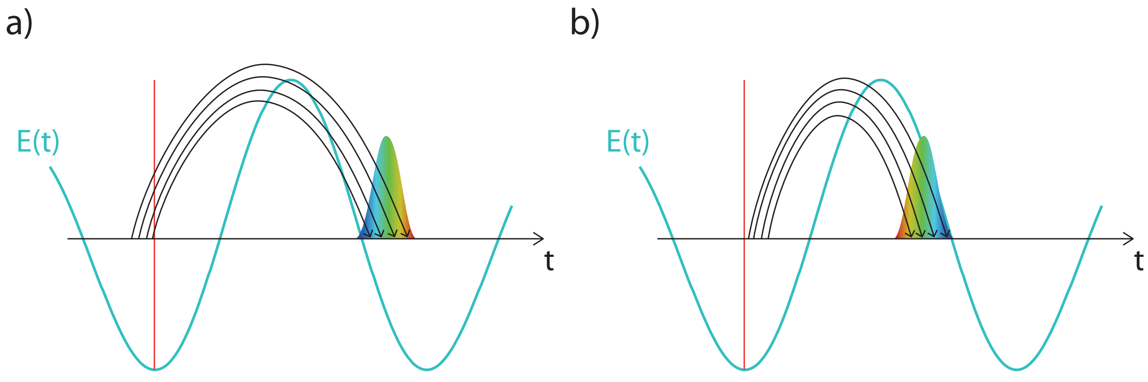

Figure 2.9: Illustration of the HHG process during a single half-cycle. a) If ionization occurs before the field crest, the electrons travel on long trajectories resulting in an XUV pulse with negative chirp. b) Electrons ionized after the field crest run on short trajectories which results in a positively chirped pulse.

An very important feature of the HHG process is the temporal confinement of the photon emission. As the times of emission and recombination of the electrons are limited to a fraction of an optical period, the resulting radiation has a similar short pulse length. This makes HHG the key experimental technique for the generation of attosecond light pulses [42, 13]. Fig. 2.9 illustrates the classical picture of the HHG process for a single half-cycle. The black arrows indicate the electron trajectories. Depending on its emission time with respect to the oscillation peaks, the electron can run on long and short trajectories. If an electron is emitted before the field peaks, it will run on a long trajectory and experience two zero crossings of the electric field before it recollides. Emission after the field crests results in short trajectories and the electron will experience only a single crossing of the driving field. When independently analyzing the emitted XUV radiation one finds that the short trajectories produce positively chirped pulses, while long trajectories result in a negative chirp. Preference of either short or long trajectories depend on the phase matching conditions of driving NIR field and harmonics in the medium, which can in practice be controlled by varying the focus position of the driving laser [43]. As there is usually a higher efficiency and preference of short trajectories, the experimental realization of a strong XUV source usually target on the optimization of short trajectories.

The process for a complete few-cycle pulse is shown in 2.10 a). Depending on the laser intensity electron emission can take place at multiple half-cycles. Therefore the HHG spectrum will exhibit similar features as discussed for the ATI process. Lower photon energies can be emitted multiple times during one laser pulse. This will generate a train of attosecond pulses which exhibits a significantly modulated spectrum. Unlike ATI, the peaks will be spaced by double the fundamental photon energy as emission can take place at each half-cycle. For few-cycle laser fields the highest energetic trajectories are limited to emission during a few or even one half-cycle. This generates a plateau in the spectrum.

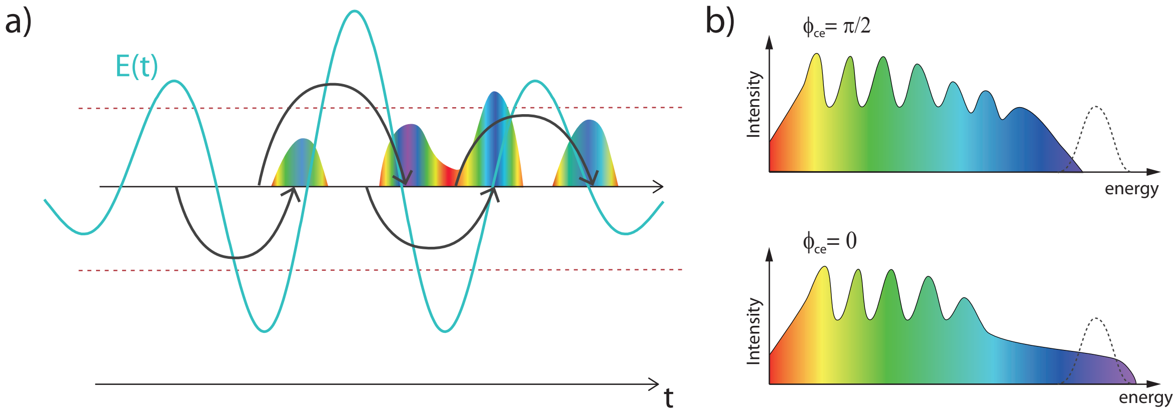

Figure 2.10: a) Illustration of the HHG process by a few-cycle laser pulse ($\phi_{\mathrm{ce}} = 0$). The ionization takes place at the center peaks of the electric field. The trajectories of the ionized electrons are indicated by the grey arrows. Upon return the recombination process leads to the generation of high energetic photons. The maximum photon energies are indicated by the color map. b) Schematic XUV spectra for a carrier envelope phase $\phi_{\mathrm{ce}} = \pi/2$ and $\phi_{\mathrm{ce}} = 0$. For a cosine-shape laser field, the highest photon energies are only generated for a single half-cycle. By spectral filtering (indicated by the grey dotted curve), isolated attosecond pulses can be generated. Adapted from [15].

In general, the shape of the HHG spectrum is heavily dependent on the carrier-envelope phase [44]. Figure 2.10 b) shows schematic spectra for a CEP of $\phi_{\mathrm{ce}} = 0$ and $\phi_{\mathrm{ce}} = \pi/2$. When choosing the appropriate CEP of $\phi_{\mathrm{ce}} \approx 0$, the highest energetic photons are only created during a single half-cycle of the driving laser field. Therefore, when applying spectral filtering such that only this highest energy region is left, one obtains an isolated attosecond pulse. With such a few-cycle approach pulse lengths of 80 as could be created [13]. Other methods for the generation of isolated XUV pulse include polarization gating where the high dependence of HHG efficiency on the laser ellipticity is employed. Zhao *et al.* could generate XUV pulses as short as 67 as using a double-optical-gating method [14].

2.2.3 Photoionization processes in the solid state

Due to the complex potential landscape, ionization in bulk media differs from single atoms. In his original publication Keldysh also presented a solution for the ionization yield for a solid [35]. The Keldysh parameter is modified $\gamma = \omega\sqrt{m_{\mathrm{eff}}\Delta}/|eE|$ such that the band gap Δ now enters as the effective potential barrier and the electron mass is given by the reduced effective mass m_{eff}. Both multi-photon ionization as well tunnel ionization are included as limiting cases. The ionization rate is given by:

$$W_\gamma = \frac{2\omega}{9\pi}\left(\frac{m_e\omega}{\phi\hbar}\right) Q_{\mathrm{np}}\left(\gamma, \frac{\Delta_{\mathrm{eff}}}{\hbar\omega}\right) \exp\left[-\pi\left\langle\frac{\Delta_{\mathrm{eff}}}{\hbar\omega}+1\right\rangle \cdot \frac{K(\phi)-E(\phi)}{E(\theta)}\right], \qquad (2.42)$$

where K and E are the complete elliptic integrals of the first and second kind with the arguments $\phi = \gamma/\sqrt{1+\gamma^2}$ and $\theta = 1/\sqrt{1+\gamma^2}$. Δ_{eff} can be interpreted as an effective band gap and reads:

$$\Delta_{\text{eff}} = \frac{2\Delta}{\pi} \cdot \frac{E(\theta)}{\phi}. \tag{2.43}$$

Q_{np} is a slowly-varying function and given by

$$Q_{\text{np}}(\gamma, x) = \sqrt{\frac{\pi}{2 \cdot K(\theta)}} \sum_{n=0}^{\infty} \exp\left[-\pi \frac{K(\phi) - E(\phi)}{K(\theta)}\right] \cdot \Phi\left(\sqrt{\frac{\pi^2 \left(2\langle x+1\rangle - 2x + n\right)}{2 \cdot K(\theta) \cdot E(\theta)}}\right). \tag{2.44}$$

Here $\langle x+1\rangle$ denotes the integer part of $x+1$. The function $\Phi(z) = \int_0^z \exp\left(y^2 - z^2\right) dy$ is the Dawson integral.

Of course the Keldysh model is generalizing the situation, especially as it assumes a non-parabolic band structure. It was shown that the theoretically obtained ionization rates differ drastically at high intensities if a different band model is used [45]. Nevertheless it is still one of the most popular models to quantify ionization rates in bulk media. A comparison of the limiting cases of MPI and tunnel ionization with the Keldysh rate equation shows that for typical materials tunnel ionization is the dominant mechanism for intensities above $3 \times 10^{13}\,\text{W/cm}^2$ [32].

Besides MPI and tunneling ionization, another pathway for a transfer of valence band electrons to the conduction band (CB) is impact ionization. The underlying mechanism is inelastic scattering of a high energetic electron, that transfers momentum to an electron at rest. In strong laser fields the classical picture predicts the onset of impact ionization to occur as soon as the ponderomotive energy of free electrons in the material reach the band gap. As the electrons created by impact ionization can itself ionize more electrons once they are accelerated, this process is also referred to as avalanche ionization [29]. The initial seed electron population in the conduction band is either excited by MPI or already existent before the laser pulse due to a non-zero temperature. As it scales non-linearly with time, the relative influence of impact ionization depends on the number of oscillations of the laser pulse and is therefore most efficient for laser pulses longer than tens of femtoseconds [46].

2.2.4 Optical breakdown and metallization effects

Considering a bulk, dielectric material under intense laser radiation, it is obvious that the number of free charge carriers might exceed a critical value. In a simple approach, the change in optical properties can be calculated by employing the Drude model [29]

$$\epsilon_r(\omega) = \epsilon_r^0(\omega) + \Delta\epsilon_r(\omega) = \epsilon_r^0(\omega) - \frac{\omega_p^2}{\omega^2 + i\gamma_e\omega}, \tag{2.45}$$

where $\epsilon_r^0(\omega)$ is the dielectric function of the unperturbed medium. The plasma frequency $\omega_p^2 = n_e e^2/(\epsilon_0 m_{\text{eff}})$, will lie at very low frequencies before the laser pulse. As charge carriers are generated by the laser pulse, ω_p will grow. The critical density n_c is reached when the plasma frequency equals the laser frequency $\omega_p = \omega$. At this point, the electromagnetic wave becomes evanescent as $Re[\epsilon_r(\omega)]$ turns negative. This process is referred to as optical breakdown. Due to the large amount of energy deposited in the system it is usually equivalent to the damage threshold of dielectric materials. The critical electron density is in the range of $n_c \approx 10^{21} - 10^{22}\,\mathrm{cm}^{-3}$ [47, 48]. Through subsequent electron-phonon scattering the energy is transferred to the lattice resulting in localized melting of the material and laser ablation [46, 47].

To model the temporal evolution of the conduction band population n_e, classical rate equations can be employed [48, 49, 50]

$$\frac{dn_e}{dt} = (W_\gamma + \beta n_e I)\left(1 - \frac{n_e}{n_0}\right) - \frac{n_e}{\tau_r}, \tag{2.46}$$

where W_γ describes the charge creation by tunnel and multi-photon ionization given by equation (2.42), while the term $\beta n_e I$ models the electron avalanche process. To take saturation into account, a maximum number density of CB electrons n_0 is introduced. The saturation is reflected by the scaling term $1 - n_e/n_0$. The relaxation term n_e/τ_r accounts for recombination of free charge carriers. For increasing electron densities, also the relaxation time τ_r can be expected to change.

Considering few-cycle laser fields, it is obvious that the peak intensities have to be chosen higher to reach the conditions for optical breakdown. Then electron excitation is highly non-linear and confined to a few half-cycles of the laser field. For such conditions, a simple modeling of electron population by equation (2.46) is questionable. Nevertheless, it is to be expected that for high pulse energies the system will be disturbed heavily ultimately leading to the creation of a free, dense plasma. A number of simulation models have been developed and extended to cope with such high intensities. A particle-in-cell (PIC) code that include microscopic collision events and the propagation of the electro-magnetic wave was used to study the non-linear plasma wave dynamics in resonant hydrogen-like clusters [51, 52]. Otobe *et al.* showed by time-dependent density functional theory (TDFT) simulations that the number of electrons in the conduction band reaches $5 \times 10^{22}\,\mathrm{cm}^{-3}$ in α-SiO_2 when subject to a $2.5 \times 10^{15}\,\mathrm{W/cm}^2$ laser pulse of 16 fs duration [53]. Apalkov *et al.* proposed that a reversible CB population is excited by a mixing of valence and conduction band state imposed by the external laser field (Stark effect) [54]. This model predicts optical breakdown to occur for SiO_2 at an inner intensity of $1.7 \times 10^{14}\,\mathrm{W/cm}^2$.

Chapter 3

Experimental techniques

3.1 Generation of few-cycle laser pulses

The key component for all experiments described in this work are intense, waveform controlled few-cycle laser fields. The generation and characterization of such laser pulses has become a routine experimental technique over the past years. Nevertheless, it still requires a variety of complex optical and electronic equipment. The key components of the laser system used in this work at the AS-5 beamline are outlined in Fig. 3.1.

The laser pulses are generated by a commercial chirped-pulse amplification (CPA) laser system (FemtoPower Compact PRO) working at a repetition rate of 1 kHz. The system is shared with the Petawatt Field Synthesizer (PFS) group, where it is used mainly for seed generation [55, 56]. An ultra-broadband Ti:Sa oscillator pumped by a diode-pumped solid state laser generates seed pulses with a repetition rate of 70 MHz and a pulse energy of 3.5 nJ. The oscillator spectrum extends from 620 nm to 1000 nm with a pulse duration shorter than 7 fs. Before entering the amplifier the seed pulse is stretched to a pulse duration of approximately 10 ps by a SF-57 glass stretcher. In addition, the beam passes an Acousto-Optic Programmable Dispersive Filter (AOPDF, Fastlite DAZZLER) for fine dispersion control. After 10 amplification passes through the Ti:Sa amplifier, the laser pulse energy now reaches 2 mJ with a spectral bandwidth of approximately 100 nm centered at a wavelength of 800 nm (see Fig. 3.2 a)). The beam passes a triggered Pockels cell and a Glan-Thompson prism, which enable the generation of two 500 Hz beams for simultaneous operation of PFS and AS-5. From here the laser beam is guided through tubes and beam cubes to the experimental laboratory. As the distance from laser system to experimental lab exceeds 10 m, the beam profile has now increased to about 2.5 cm diameter due to its intrinsic divergence. Therefore it has to be resized by a 1:2.5 telescope. It now enters the hybrid pulse compressor (HPC). The first stage of such a HPC is a double-prism pulse compressor. The prism compressor is set such that a rest of positive dispersion is left in the pulse when it leaves the last prism. Final compression of the pulse to its Fourier limit is achieved by a set of 16 high dispersive mirrors (HDM), each of which adds $-500\,\mathrm{fs}^2$ [55, 57]. The advantage of this hybrid approach is that self-phase modulation especially in the glass

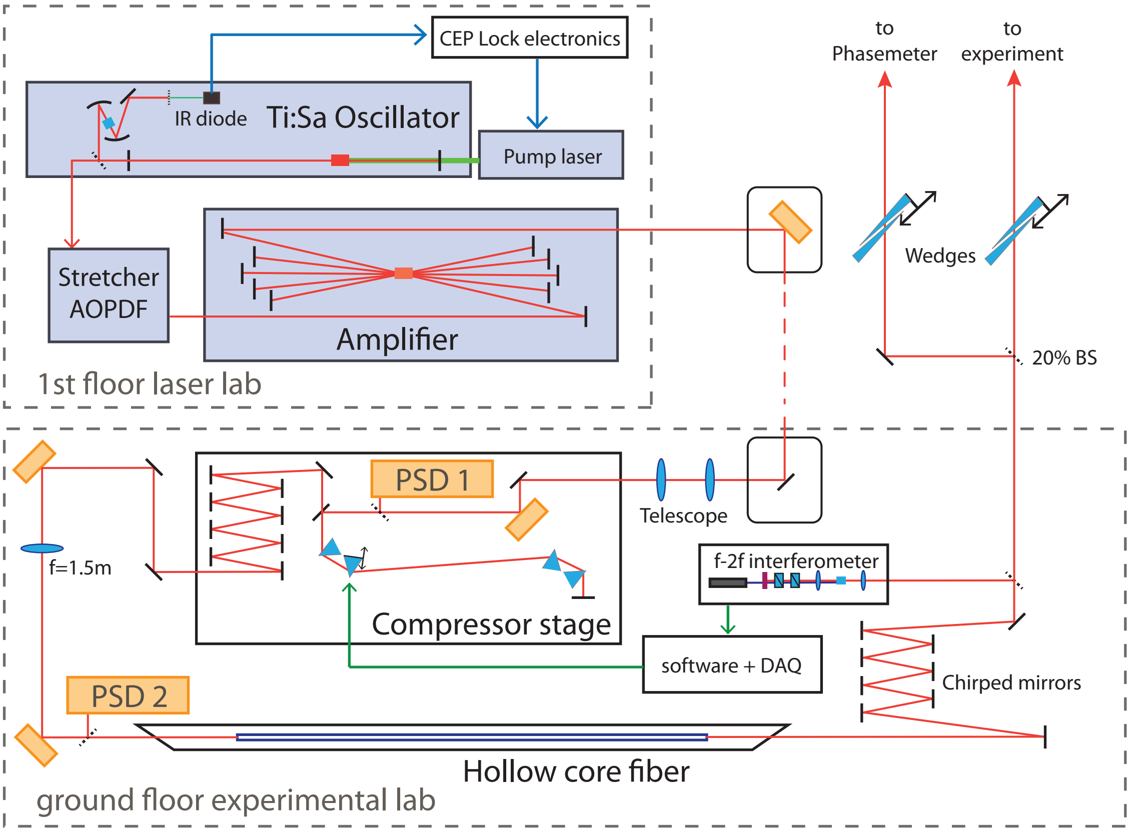
CEP Lock electronics
to Phasemeter
to experiment
IR diode
Ti:Sa Oscillator
Pump laser
Wedges
Stretcher AOPDF
Amplifier
20% BS
1st floor laser lab
PSD 1
Telescope
f=1.5m
f-2f interferometer
Compressor stage
software + DAQ
Chirped mirrors
PSD 2
Hollow core fiber
ground floor experimental lab

Figure 3.1: Overview of the AS-5 laser system.

prisms can be avoided [55]. Drifts of the beam pointing and mechanical instabilities are compensated by a commercial beam lock system, which stabilizes pointing and position of the beam before entering the compressor stage. After the compressor stage, the pulses have a duration of 26 fs and a pulse energy of 1.4 mJ. The beam is now focused into a hollow core fiber (HCF) for spectral broadening. The HCF is mounted in a tube with Brewster entrance and exit windows (thickness 1 mm, material SF-57). The inner diameter of the HCF is 275 μm at a length of 1 m. The focal length of the lens is 1.5 m. A second beam stabilization system ensures a constant position of the beam on the fiber entrance. The tube containing the HCF is filled with Ne gas at a pressure $p \approx 2.8 - 3$ bar. The high intensity of the focused laser pulse induces self-phase modulation due to the change in refractive index, which results from the optical Kerr effect:

$$\Delta n(t) = n_2 I(t) = p\psi_2 I(t). \tag{3.1}$$

Here $I(t)$ is the laser intensity and n_2 the non-linear index of refraction, which can be assumed to be proportional to the gas pressure p [32]. The use of noble gases with high ionization potentials reduces the influence of excessive ionization which would result in a

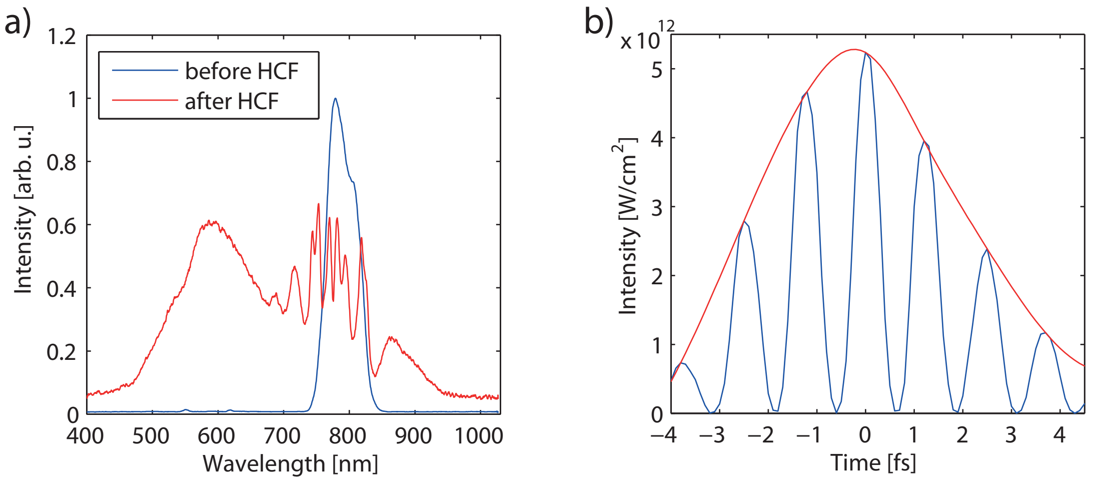

Figure 3.2: a) Spectra of the laser pulses in before (blue) and after the the hollow core fiber. b) Intensity profile after the HCF and compression obtained by attosecond streaking spectroscopy.

distortion of the pulse. In addition to self-phase modulation, the pulse experiences self-steepening which results in a flatter leading edge and a spectrum that extends more to the blue side with respect to the central wavelength [58].

The laser spectrum measured behind the hollow-core fiber is shown in Fig. 3.2 a). It now extends over a full octave from slightly below 500 nm up to 1000 nm. The Fourier transform limited pulse duration of such a spectrum is below 3 fs well in the few-cycle regime. Due to the huge bandwidth, an effective compression and dispersion management is a challenge. Broadband negatively chirped mirrors provide an efficient tool for compressing a spectrum exceeding one octave [59]. The design of these mirrors is optimized such that two reflections under angles of 5° and 19° yield a homogeneous GDD. At the AS-5, the number of chirped mirrors in the beam path varies from 4 to 8 pairs depending on the experiment and its amount of positive dispersion to compensate. Fine tuning of the laser pulse length is achieved with a set of motorized glass wedges. One reflection from the wedges is sent to an f-2f interferometer for CEP stabilization (see next subsection). At the AS-5 beamline, the NIR laser pulses could be compressed to about $4-4.5$ fs, depending on laser settings. The intensity profile obtained by an attosecond streaking measurement is shown in figure 3.2 b). For the velocity-map-imaging and stereo time-of-flight experiments a 20% broadband beam splitter can be inserted to branch off a portion of the beam to the phasemeter setup. This channel is equipped with its own pair of wedges such that pulse durations can be optimized for both phasemeter and experiment separately.

3.2 CEP stabilization and measurement

3.2.1 Active phase stabilization

With advances in laser science, today there is the possibility to either actively stabilize the laser carrier-envelope phase (CEP) or to measure it for every single laser shot (CEP tagging). The choice will depend on the experimental requirements. Isolated attosecond pulse generation relies on a fixed waveform and therefore active CEP locking is required for efficient measurements. Experiments which study the CEP dependence of a process will on the other side benefit from CEP tagging.

The CEP locking system relies on a fast loop, which stabilizes the output of the oscillator and a slow loop which compensates drifts in the amplifier system, beam path and compressor. For stabilization of the oscillator, an f-to-0 technique is used. From analysis of the frequency comb, one learns that the individual lines of the comb are equally spaced but also have a common offset [60, 61]

$$f_n = n f_{\mathrm{rep}} + f_0. \tag{3.2}$$

Here f_{rep} is the repetition rate of the oscillator. It was found that f_0 is proportional to a change in the CE phase $\Delta\phi_{\mathrm{ce}} = 2\pi f_0 / f_{\mathrm{rep}}$ [60]. If f_0 can be fixed to zero, all laser pulses would have the same CEP. In practice, locking f_0 to a fixed value of $f_{\mathrm{rep}}/4$ is sufficient as then every fourth laser pulse has the same CEP and it just needs to be ensured that only these are picked for amplification. The measurement of f_0 is accomplished by a highly non-linear periodically poled lithium niobate crystal (PPLN). A fraction of the oscillator output is focused into this crystal where difference frequency generation of the individual frequency comb lines takes place:

$$f_{\mathrm{diff}} = (n f_{\mathrm{rep}} + f_0) - (m f_{\mathrm{rep}} + f_0) = (n - m) f_{\mathrm{rep}}. \tag{3.3}$$

Further mixing of difference frequencies $(n - m) f_{\mathrm{rep}}$ with long wavelength components f_k of the frequency comb results in an effective beating (for $n - m - k = 0$)

$$f_{\mathrm{beat}} = f_{\mathrm{diff}} - f_k = (n - m - k) f_{\mathrm{rep}} + f_0 = f_0. \tag{3.4}$$

Fig. 3.3 a) illustrates the process. The imprint of f_{beat} is most pronounced in the IR part of the spectrum. The output of the PPLN is thus filtered with a long-pass filter before being detected by a fast photodiode. The signal is sent into locking electronics which detect the beat frequency f_0. Deviations from the desired value $f_{\mathrm{rep}}/4$ generates an error signal. The control and compensation of errors is achieved by an acousto-optic modulator (AOM) in the pump laser beam of the oscillator. By variation of the laser pump power with the AOM it is possible to influence the CEP [62, 61].

An additional phase-locking loop is necessary, because any drift in the following beam path will alter the CEP as well. This final stabilization system is installed after the hollow core fiber. Main component is an f-to-$2f$ interferometer [63, 64]. The experimental implementation is illustrated in Fig. 3.3 b). A small portion of the beam is focused into a

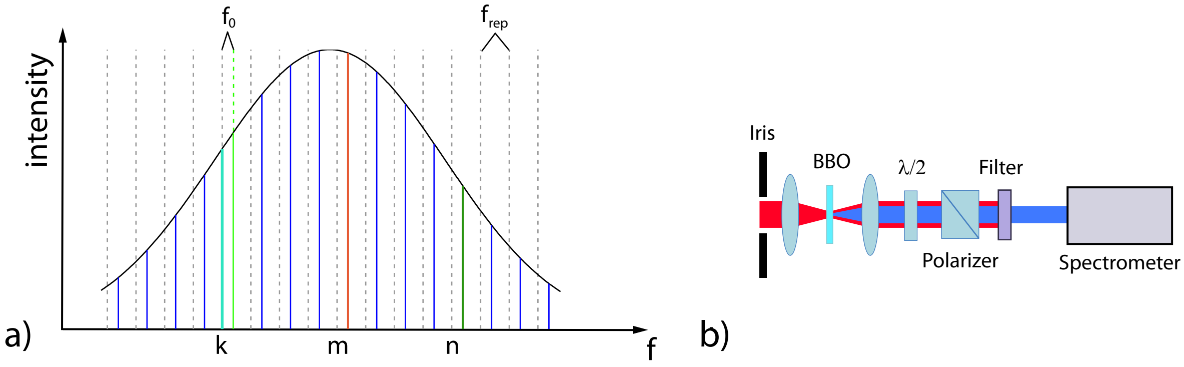

Figure 3.3: a) Working principle of the f-to-0 technique. Mixing of three frequency comb lines (indicated by the green, red and orange line) result in a f_0-modulation. b) Slow-loop phase lock detector.

BBO crystal where the second harmonic is generated. The polarization of the fundamental beam is rotated by a half-wave plate to be parallel to the second harmonic. As the spectrum of the laser pulse here extends over a whole octave, the long wavelength region of the frequency doubled beam will overlap with the short wavelengths of the fundamental. The spectral intensity of the superposition of fundamental and second harmonic is given by [63]:

$$I(\omega) = I_f(\omega) + I_{2f}(\omega) + 2\sqrt{I_f(\omega) I_{2f}(\omega)} \cos\big(\phi_f(\omega) - \phi_{2f}(\omega) + \omega\tau + \phi_{\text{ce}}\big). \tag{3.5}$$

Here $I_f(\omega)$ and $I_{2f}(\omega)$ denote the spectral intensity of the fundamental and second harmonic beam. The third term causes a modulation of the spectrum as a function of the individual spectral phases of fundamental ϕ_f and second harmonic ϕ_{2f}. The temporal delay τ between ω- and 2ω-components due to chirp and walk off also results in a modulation. Most important for phase stabilization is that the pattern is shifted by the CEP ϕ_{ce}. The relative strength of the interference pattern can be maximized by a rotatable polarizer. A computer program calculates the phase offset of the modulation pattern by Fourier transforming the spectrum and actively stabilizes the CEP by moving one of the prism in the compressor system.

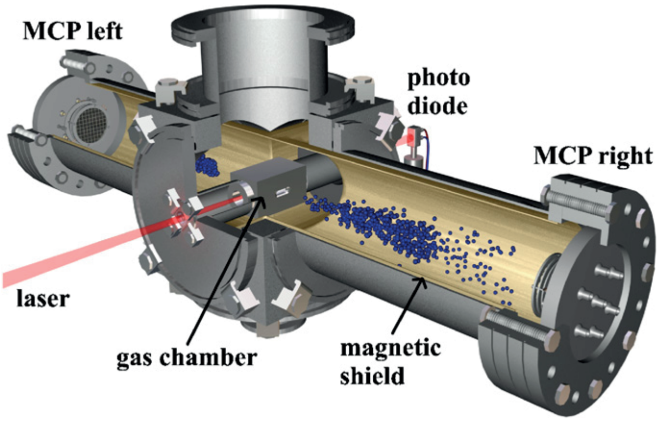

Figure 3.4: Schematic of the phasemeter setup. The laser is focused into the center of a stereo time-of-flight detector. The polarization lies parallel to the detector axes. The ATI spectrum is detected on both sides by MCPs and further amplified. Taken from [65].

3.2.2 Stereo-ATI phasemeter

Although active CEP stabilization is a well established technique, it still has its shortcomings. A first limitation is the stabilization time which is usually less than two to three hours. Secondly, any drifts caused by pointing instabilities or small changes in the spectrum will affect especially the slow loop stabilization. If one is interested in the CE phase dependence of a process, the intrinsic randomness of the laser CEP combined with a direct measurement for each single laser shot is a more accurate and comfortable alternative. Paulus *et al.* observed an influence of ϕ_{ce} on the direction of ATI photoemission from noble gases [66]. Based upon this work it was found that the ATI-spectra show characteristic asymmetries with different phase offsets for different energy intervals [67]. Sayler *et al.* then demonstrated that the CEP of amplified laser pulses can be retrieved from single laser shots at a kHz repetition rate [68].

The design of the phasemeter is depicted in Fig. 3.4. A fraction of the laser pulse is focused into the center of a stereo time-of-flight spectrometer. Here the laser interacts with a dense Xenon gas target. Emitted electrons are detected by multi-channel plates (MCP) on both sides in polarization direction after passing a μ-metal shielded drift tube with a length of 30 cm. The signal of direct electrons is suppressed by retardation grids on 30 V negative potential. Thus only the signals from the ATI-plateau of the MCPs are capacitively coupled out and amplified. Figure 3.5 a) shows these spectra schematically for different carrier-envelope phases. A fast circuitry integrates both signals in the two depicted energy regions 1 and 2. From these four intervals R_1, R_2, L_1 and L_2 two asymmetry parameters are calculated for each single laser shot:

$$A_1 = \frac{L_1 - R_1}{L_1 + R_1}, \qquad A_2 = \frac{L_2 - R_2}{L_2 + R_2}. \tag{3.6}$$

The integration regions can be chosen such that A_1 and A_2 are nearly harmonic functions

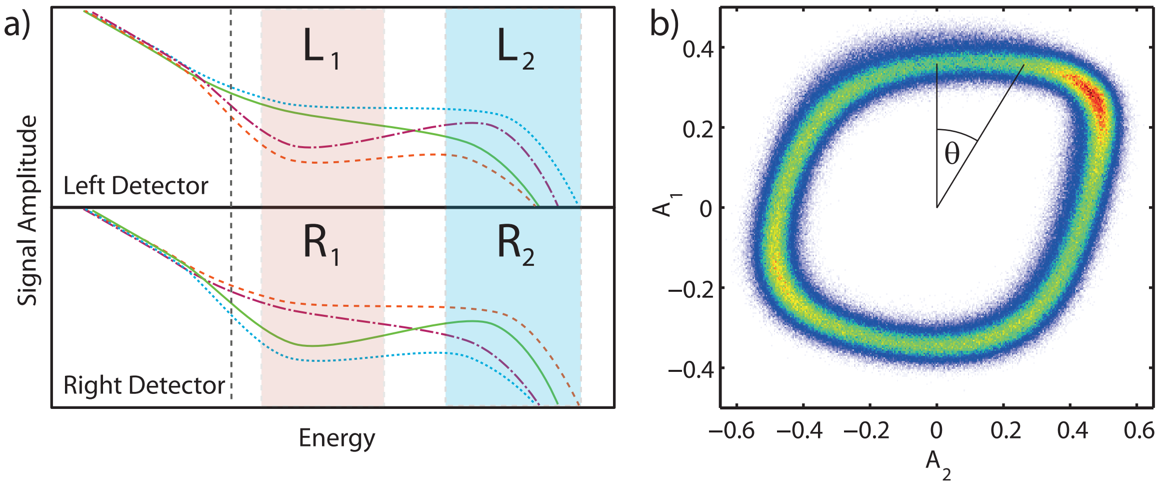

Figure 3.5: a) Illustration of the working principle of the ATI phasemeter. The signal in the left and right detector is shown schematically for four different phases with emphasis on the rescattering plateau. The low energy MPI contribution can be filtered out using a retarding field. Both left and right signals are integrated in two spectral regions as indicated by L$_1$, L$_2$, R$_1$ and R$_2$. From these four integrals the two asymmetry values can be calculated. b) Asymmetry values A_1 and A_2 for 10^6 laser shots.

of ϕ_{ce}:

$$A_1 \approx A_1^0 \sin(\phi_{\mathrm{ce}} + \phi_1) \qquad A_2 \approx A_2^0 \sin(\phi_{\mathrm{ce}} + \phi_2). \tag{3.7}$$

The ideal condition is that the phase offsets ϕ_1 and ϕ_2 differ by 90°. Then A_1 and A_2 will lie on a circle from which the laser CEP can be directly retrieved from the angle between A_1 and A_2:

$$\theta = \arctan(A_1/A_2). \tag{3.8}$$

3.2.3 Statistical rebinning for exact phase retrieval

Figure 3.5 b) shows a parametric asymmetry plot (PAP) of the A_1 and A_2 distribution obtained from 10^6 consecutive laser shots. One can see that it indeed has a circular character. But even after optimizing the integration gates, a distortion remains which stems in parts from an unbalanced detector response. Also the harmonic dependence given by equation (3.7) cannot be exactly realized. It is obvious that a direct calculation of ϕ_{ce} from the angle between A_1 and A_2 would result in a rather large error. The angles with strong signal in the PAP would occur more often than those with a weak signal which is not physical. Given a large enough statistics ϕ_{ce} should show a homogeneous distribution between 0 and 2π as the CEP of a single shot is expected to be random [65]. This assumption can be used to make the phase measurement more accurate, as one can create a mapping $\phi_{\mathrm{ce}} = F(\theta)$ which compensates the non-homogeneous distribution of θ

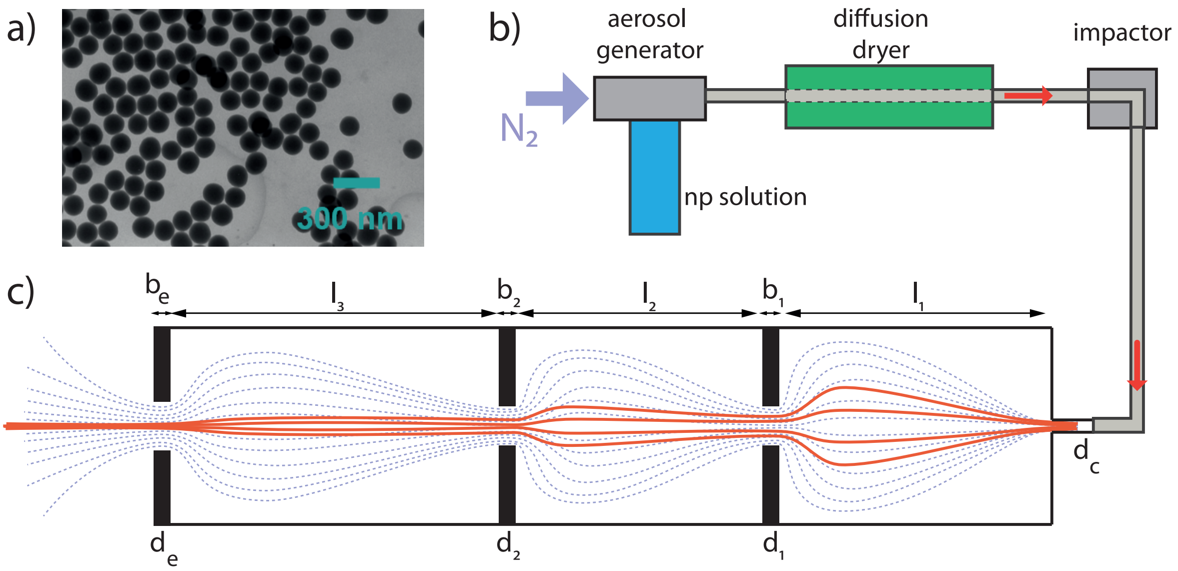

Figure 3.6: a) TEM image of SiO_2 nanoparticles with a diameter of 147 nm. b) Flow diagram for the generation of the nanoparticle aerosol. c) Working principle of an aerodynamic nanoparticle lens. The trajectories of gas molecules are schematically indicated by the blue dashed lines. The nanoparticle trajectories are shown in red. Adapted from [70].

[68], which is explained in appendix A.2. The size of the statistics necessary to obtain a reliable redistribution function F can typically be chosen between 10^4 and 10^5 laser shots. In order to prevent a wrong mapping of CE phases, the phase redistribution function needs to be updated depending on laser stability and acquisition time [69].

3.3 Nanoparticle samples

3.3.1 Sample preparation and characterization

The preparation of single nanoparticles is achieved by chemical synthesis. Spherical SiO_2 nanoparticles can be grown by the use of the Stöber procedure [71]. Here the reaction of tetraalkyl silicate in a solution of water and bases can form a mono-disperse solution of nanoparticles given the right mixture and reaction parameters. The size deviation of these chemically grown spheres is usually below 5%. The SiO_2 samples used for this work were produced by the groups of Prof. Eckart Rühl, FU Berlin, and Prof. Christina Graf, FU Berlin. Figure 3.6 a) shows a transmission-electron microscope (TEM) image of a sample with 147 nm average diameter. The spheres show a high surface quality without noticeable roughness.

3.3.2 Aerodynamic lensing

All the presented photoemission experiments take place in ultra-high vacuum. Therefore a method for depositing isolated nanoparticles in the interaction region of the respective experiment is required. So far the most efficient method for this task is an aerodynamic lens system used to create a narrow particle beam. The technique was invented by Liu *et al.* [70], who could show with numerical flow simulations that a set of simple apertures (called "aerodynamic lenses") can be used to efficiently compress the flow of nanoparticles in a carrier gas. Such an aerodynamic lens system is schematically shown in Fig. 3.6 c). A pressure gradient between inlet (right side) and outlet of the lens system results in the flow of carrier gas through the lens system which has a cylindrical geometry. The gas molecules have to pass the apertures placed in the tube. Their trajectories are indicated by the blue dashed lines. Nanoparticles in the carrier gas are accelerated by aerodynamic drag forces. It was shown that, given the right particle size and gas flow properties, the nanoparticles efficiently follow the convergent gas stream in front of an aperture while they are less affected by the gas expansion after passing the aperture [70]. In a simple picture, one can just assume that at the (radial) center there are not enough gas molecules capable of transferring radial momentum to the nanoparticles. This leads to an efficient compression of the nanoparticle beam. One can define a contraction factor $\nu = r_b/r_a$, where r_b and r_a are the distance to the center of the nanoparticle trajectory. This contraction factor depends on the particle size and gas flow properties. In the ideal case, a particle would end up in the center of the lens system after passing an aperture, which is usually not true due to rest perpendicular momentum [70]. The design of a aerodynamic lens system thus usually employs a set of several apertures. This leads to a successive compression of the beam. By varying the aperture diameters an efficient compression over a broad range of sizes can be achieved. Numerical tools for the optimization of the lens design have been developed by Wang *et al.* [72].

The experimental realization starts with a nanoparticle suspension as described above. From this suspension an aerosol is created by a commercial aerosol generator (TSI 3076) using nitrogen as a carrier gas. This aerosol contains up to 10^6 particles per cm^3 depending on the nanoparticle concentration in the suspension. The aerosol is sent through a diffusion drier to remove rests of solvent from the aerosol and from the nanoparticle surface. A further device is the so called impactor, where the aerosol has to pass a sharp 90° turn. Clusters of nanoparticles and eventual contaminations of the sample will be deposited on the wall of this turn due to their high mass. Now the actual aerodynamic lens system is reached. The initial orifice determines the gas flow through the lens system. Thus its diameter is a crucial parameter for the efficiency of the focusing. In the current setup a critical orifice of 180 μm is installed. Now the aerosol passes a set of five apertures followed by the final aperture. Behind the lens system three stages of differential pumping remove the carrier gas. With the differential pumping system the pressure in the experimental chambers can be kept at around 10^{-7} mbar. As most of the particles size of interest lie between 60 and 500 nm, the design proposed by Bresch was used [73]. The inner diameter of the lens is 10 mm. The aperture sizes and distances are shown in table 3.3.2. With this

Lens nr	inner diameter d_n	aperture length b_n	distance l_n
inlet	180 μm	-	-
ap 1	5.3 mm	10 mm	40 mm
ap 2	5.0 mm	2 mm	50 mm
ap 3	4.7 mm	2 mm	50 mm
ap 4	4.44 mm	2 mm	50 mm
ap 5	4.24 mm	10 mm	50 mm
exit	3.94 mm	10 mm	65 mm

Table 3.1: Geometry of the aerodynamic lens used in this work. The lens is optimized for nanoparticle diameters around 100 nm [73].

lens design it was shown that NaCl particles ($d \approx 120\,\mathrm{nm}$) could be focused to a beam diameter of about 480 μm (FWHM) at 14 cm distance from the exit aperture [73].

Another important parameter governing the density of nanoparticles in the interaction region is the concentration of nanoparticles in the solution feeding the aerosol generator. This has to be carefully chosen. If too high, a single droplet created by the aerosol generator can contain two or more nanoparticles. As the solvent evaporates, the nanoparticles are likely to form a cluster. The number of such clusters that reach the lens will be reduced by the impactor device. Also, as clusters have a significant higher mass, the transmission through the aerodynamic lens will be smaller and the focusing will be less efficient. A last possibility to actively remove the cluster signal from the measurement is the discrimination by count rates (see section 3.4.4). The suppression of clusters in the beam of course depends on the size of the single nanospheres. It was found that for small nanoparticles clustering was more pronounced as for larger particles. By tests with different nanoparticle concentrations and comparison of the individual spectra the highest possible concentration not showing clustering was determined.

3.4 Velocity map imaging

In experiments that study ionization and molecular dissociation usually the energy and momentum of the reaction products (ions and electrons) are detected. Time-of-flight techniques like reaction microscopy (REMI) can reconstruct the full information about momenta of electrons and ions but due to detector dead times they are limited to a low count rate [75]. Velocity-map-imaging (VMI) is an alternative that overcomes these count rate limitations. It also offers access to the full 2D and 3D momentum distributions of ions and electrons [76, 77]. VMI does not rely on temporal measurements but rather a spatial mapping of the electron (or ion) momentum. The typical design of a VMI device is shown in figure 3.7 a). The ionization takes place in a nearly homogeneous, static electric field **F**. The laser light is polarized parallel to the detector plane. The strong electric field bends the photoelectron trajectories towards an imaging detector at a distance L, which is usually a MCP/phosphor screen combination. If the electron's initial velocity lies in

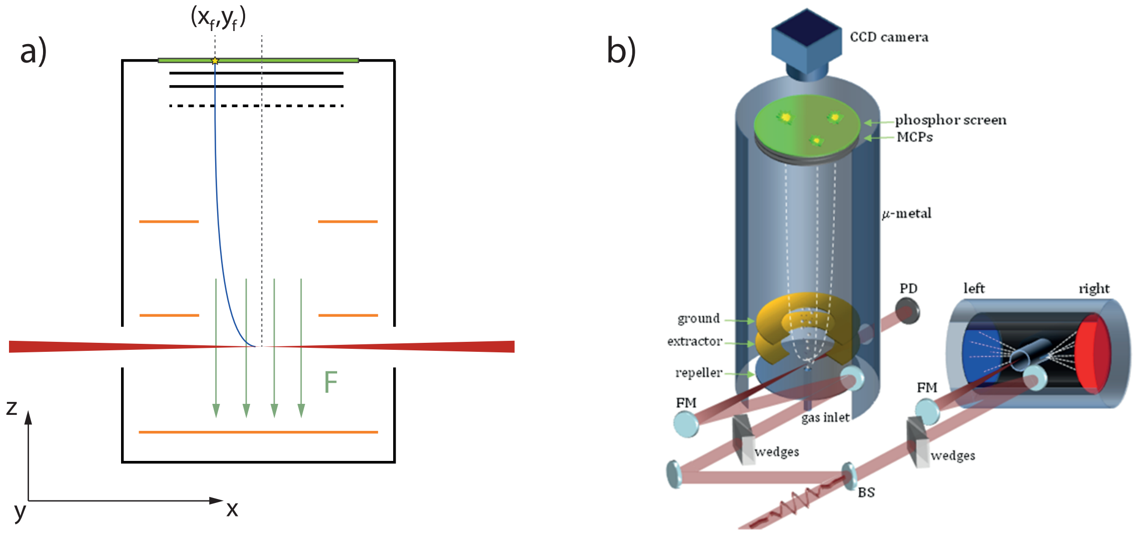

Figure 3.7: a) Working principle of VMI. The laser is polarized in y-direction. Emitted electrons are accelerated to the detector by the extraction field, which is parallel to the z-axis. b) VMI setup used for this work. A portion of the beam is split off and sent to the phasemeter. As published in [74].

the plane of the detector, the final hit position will be approximately proportional to this initial velocity. In general the position is given by [78]:

$$x_f = \frac{2L\cos\phi\sin\theta}{\rho}\Big(\sqrt{\sin^2\phi\sin^2\theta+\rho}-\sin\phi\sin\theta\Big), \tag{3.9a}$$

$$y_f = \frac{2L\cos\theta}{\rho}\Big(\sqrt{\sin^2\phi\sin^2\theta+\rho}-\sin\phi\sin\theta\Big). \tag{3.9b}$$

Here $\rho = eFL/E_{\mathrm{kin}}$ is the ratio between the energy acquired in the dc-field to the initial kinetic energy E_{kin}. In order to achieve the same mapping for the whole interaction volume defined by the laser focus size, the projecting electric field is usually not homogeneous. Depending on the energy region under consideration a set of multiple electrodes can be used. The geometry can be optimized using numerical tools such as SIMION.

The raw images obtained by the VMI technique are composed by a superposition of all emission angles θ and thus all momenta p_z. Therefore these raw images will be referred to as VMI projections. For atomic systems, the emission will be cylindrically symmetric with respect to the laser polarization axis. The symmetry originates from dipole selection rules and the fact that rescattering occurs at a spherically symmetric potential. This enables an Abel inversion of the obtained VMI projections from which the full 3D momentum distribution can be obtained [78, 79].

The VMI setup at the AS-5 beamline, is outlined in Fig. 3.7 b). The VMI design consists of the electrostatic lens system consisting of repeller, extractor and ground electrode. The electrons are imaged onto an MCP/phosphor screen combination with an active diameter of 8 cm. The MCP supply voltage is gated by a fast high voltage switch with a gate width of 100 ns synchronized to the laser pulse. This efficiently reduces the dark count signal picked up by the camera. For measurements on gases, the repeller has a small hole of 100 μm diameter in the center through which the gas can be injected into the interaction region. The density of gas atoms in the laser focus can be adjusted by the backing pressure in the gas supply line. For nanoparticle measurements, the aerodynamic lens system can be attached to the VMI apparatus. The nanoparticle beam then intersects the laser beam perpendicular to both polarization and VMI detection axis. As single-shot phase detection is employed, a fraction of the laser pulse is split off and sent to the phasemeter. The remaining beam is then focused by a $f = 40\,\text{cm}$ spherical mirror through the entrance window into the interaction region. Its intensity can be adjusted by a rotatable neutral density filter wheel. The focus position and camera orientation can be optimized in the spatial imaging mode.

3.4.1 Implementation of single-shot VMI

During this work, the VMI apparatus at the AS-5 beamline was upgraded making it capable to record in single-shot mode in combination with a CE phasemeter [74]. This has a variety of advantages. First of all, measuring the CE phase usually gives a higher accuracy as compared to the traditional CEP locking method [65]. Long acquisition times can easily be realized and are in practice only limited by laser stability. Furthermore the single-shot approach also brings a number of benefits with respect to the VMI measurement itself. It was shown by Horio *et al.* that single-shot acquisition enhances the image quality of multiphoton ionization of NO molecules [80]. In the following sections, it will be demonstrated that not only image quality but also species selectivity and background reduction are a key benefit when studying nanosystems.

Figure 3.8 a) outlines the data acquisition process of the single-shot VMI. The camera used for single-shot acquisition employs a high-speed complementary metal oxide semiconductor (CMOS) chip (GS-Vitec Marathon Ultra). The chip and data bus to the host computer allows for recording up to 1000 frames/s with a resolution of 800x600 pixels. The camera is synchronized to the laser with a TTL trigger signal. The intensity of each pixel is represented by a 16-bit integer number. This results in a data rate of about 1 GB/s. While this data rate can be handled by the bus from the camera to the host computer, the bottleneck lies in the final storage of the data. Using large hard-drive arrays saving the data would be feasible but also result in high costs and limited acquisition time. In a normal VMI experiment, this complete information is also not necessary, as the electron rates reaching the detector are low enough that a single frame consists mainly of "dark" pixels. This limitation in count rates is also beneficial for an accurate experiment, as multiple, simultaneous electron hits on the MCP/phosphor screen might result in a saturated response. A reduction of the data rate is thus feasible using a special version of the camera software (GS-Vitec Marathon Pro), which was developed for these purposes. Here it is possible to define a threshold intensity above which the pixel data is kept for saving while those below it are discarded. Each "bright" pixel is represented in memory by its position and its intensity value (3*2 = 6 bytes in total). The maximum number of above threshold

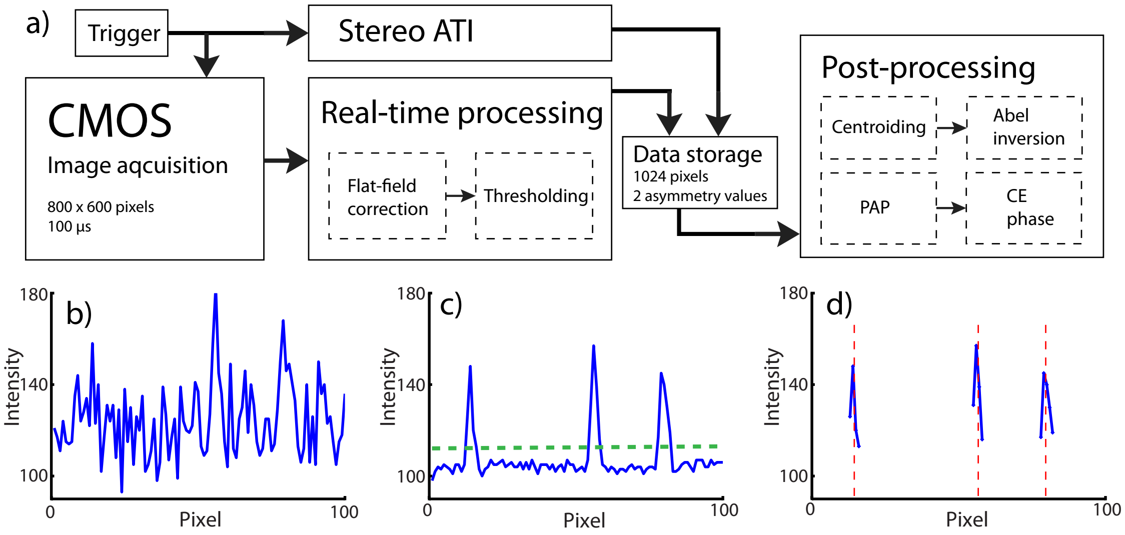
a)
Trigger
Stereo ATI
CMOS
Image aqcuisition
800 x 600 pixels
100 µs
Real-time processing
Flat-field correction
Thresholding
Data storage
1024 pixels
2 asymmetry values
Post-processing
Centroiding
Abel inversion
PAP
CE phase
b)
c)
d)
Intensity
180
140
100
0
Pixel
100

Figure 3.8: a) Schematic of single-shot VMI data acquisition. b) Single CMOS line signal before and c) after flat field correction. The green dashed line corresponds to the intensity threshold. d) Signal above threshold. The red lines indicate the center of intensity of isolated electron events. Taken from [74].

pixels that could be processed is limited by the available computing power. In the current setup, a safe operation at 1024 active pixels per shot is achievable without artifacts and drop outs. A flat-field correction algorithm eliminates the inhomogeneous response and offsets across the CMOS chip. This results in a drastically enhanced signal-to-noise ratio. Figure 3.8 b) and c) shows a single pixel line once without and with the flat-field correction for the same image, respectively. One can see that the three electron events are now much clearer visible above the noise floor and intensity threshold (green dashed line). Figure 3.8 d) shows the information that is stored for this image for later analysis.

After a completed measurement the raw VMI and phasemeter data is merged. The measured asymmetry values from the phasemeter are statistically redistributed to get the exact value of the CEP ϕ_{ce}. The single VMI frames are read in series and assigned the corresponding value of ϕ_{ce} for that laser shot. The image data is then summed in a number of phase bins. The bin size is usually set to $\pi/10$ resulting in 20 images. This phase bin size usually gives the best trade-off between information contained in the data and statistics. Depending on the magnification settings and electron count rates of the VMI and camera system, it is also possible to centroid single electron events. If one electron event extends over several pixels, selecting only the center of intensities of these pixels results in a resolution higher than that of the CMOS chip. This centroiding method was employed for the Xe measurements presented in this section. For the nanoparticle scans where the maximum momentum/energy range of the VMI (up to 100 eV) was used, the electron events usually occur so close to each other on the detector screen that the centroiding approach cannot be used.

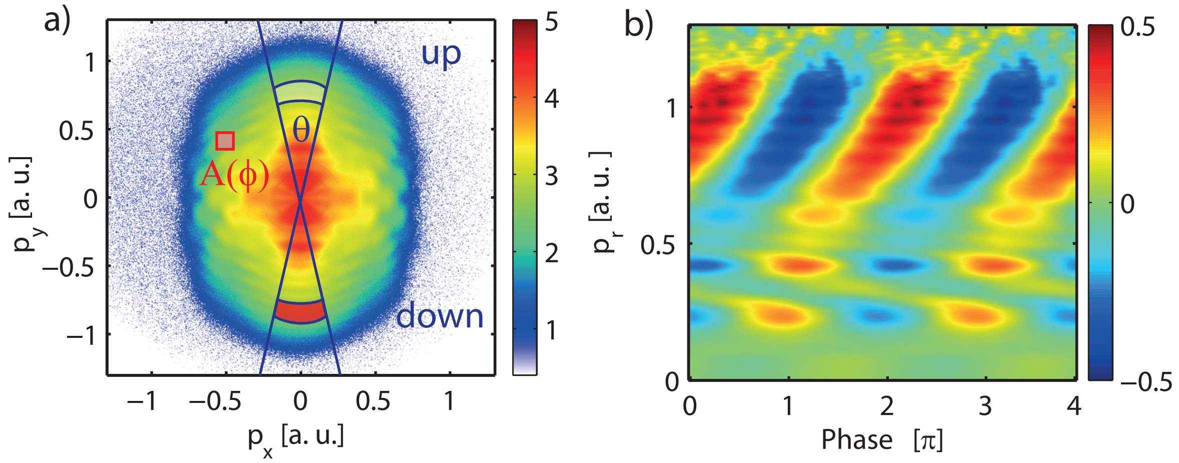

Figure 3.9: a) Illustration of the two methods for obtaining the CE-phase dependence. The radial asymmetry is indicated in blue, while the single momentum asymmetry is indicated in red. b) Relative radial asymmetry for a Xe scan at an intensity of $2.5 \times 10^{13}\,\mathrm{W/cm^2}$.

3.4.2 Asymmetry parameters

In this work two methods for visualizing the CEP dependence of the photoemission process were used. Figure (3.9) a) illustrates how these parameters were obtained. The most fundamental is to extract the CEP dependence of each point in the momentum map individually. The modulation S of the signal at a point (p_x, p_y) (indicated by the red box in the figure) can be assumed to be dominated by a harmonic dependence on the CEP ϕ_{ce} as higher order oscillations can be neglected [81]. Therefore S can be written as:

$$S(p_x, p_y, \phi_{\mathrm{ce}}) = A(p_x, p_y)\cos(\phi_{\mathrm{ce}} + \Delta\phi(p_x, p_y)) + C(p_x, p_y). \tag{3.10}$$

Here $A(p_x, p_y)$ is the modulation amplitude, while $\Delta\phi(p_x, p_y)$ is the phase offset to ϕ_{ce}. $C(p_x, p_y)$ is the offset which accounts for the contributions that are not phase dependent. This CEP analysis requires high-quality scans with a sufficient signal at all positions in the map.

The CEP-averaged momentum projections are symmetric with respect to the laser propagation axis p_x. For a single fixed CEP it can happen that more electrons are emitted to a region p_y as compared to the opposite emission direction $-p_y$. The relative ratio will change sign if the CEP changes by π. It is therefore intuitive to visualize the CEP dependence by a radial asymmetry map. Here the signal is integrated in radial segments within a given angular range θ centered around the p_y axis (polarization axis). This is done on both sides of the p_x axis (indicated in Fig. 3.9 a)) and the relative difference is calculated by:

$$A(p_r, \phi_{\mathrm{ce}}) = \frac{S_{\mathrm{up}}(p_r, \phi_{\mathrm{ce}}) - S_{\mathrm{down}}(p_r, \phi_{\mathrm{ce}})}{S_{\mathrm{up}}(p_r, \phi_{\mathrm{ce}}) + S_{\mathrm{down}}(p_r, \phi_{\mathrm{ce}})} \tag{3.11}$$

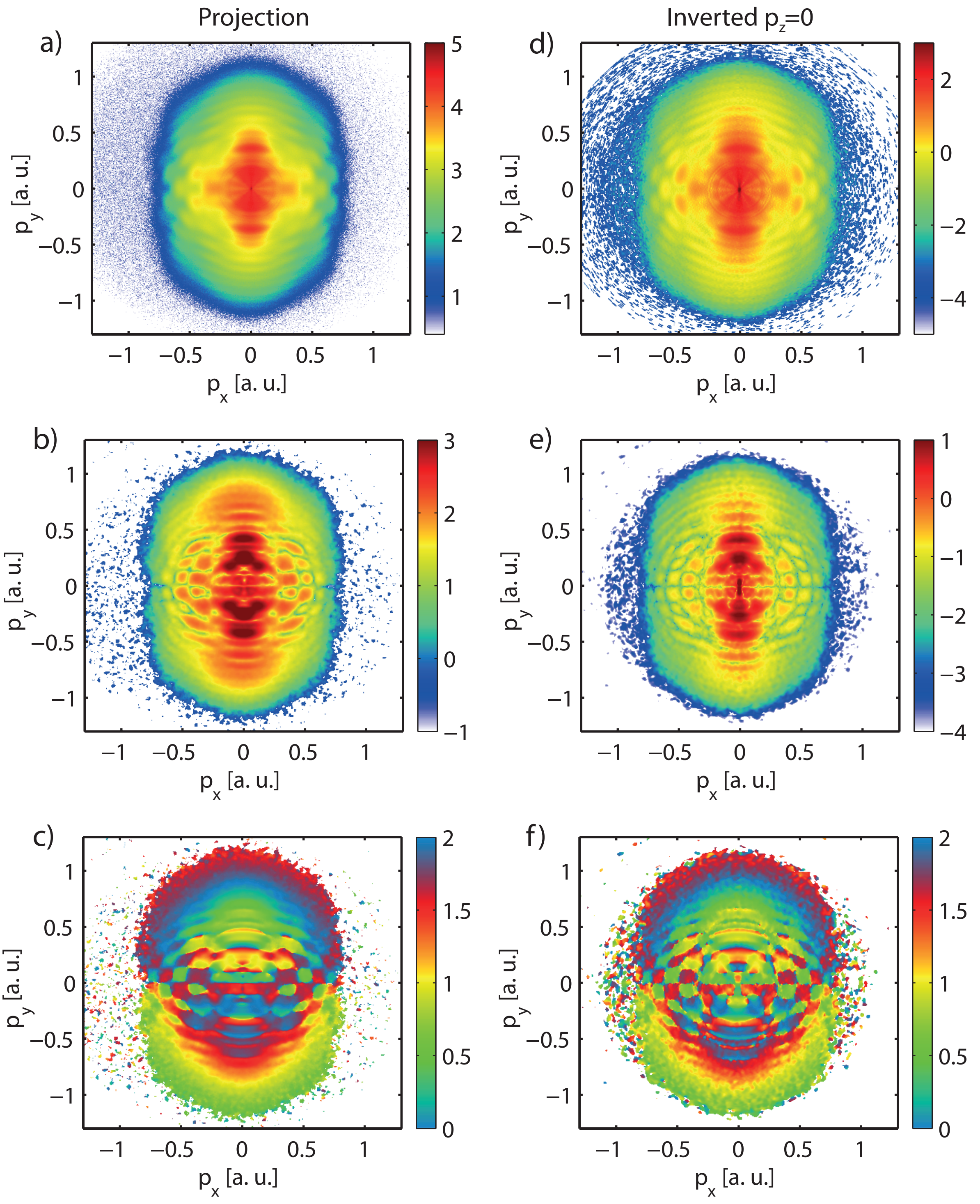

Figure 3.10: VMI measurements from Xe atoms at an intensity of $2.5 \times 10^{13}\,\mathrm{W/cm^2}$. a) Full VMI projection (logarithmic color scale). b) CEP modulation amplitude $A(p_x, p_y)$ (logarithmic color scale) and c) phase offset $\Delta\phi(p_x, p_y)$ of the full projection. d) Inverted momentum distribution ($p_z = 0$) of the same dataset. e) $A(p_x, p_y)$ and f) $\Delta\phi(p_x, p_y)$ for $p_z = 0$.

Figure (3.9) b) shows the radial asymmetry map for a VMI scan in Xe at an intensity of $2.5 \times 10^{13}\,\mathrm{W/cm^2}$.

3.4.3 CEP resolved photoemission from Xe gas

VMI measurements with Xe gas were a key element of the experiments on the nanoparticles. First they were used to calibrate the momentum map (see appendix A.1). The scans also served as a reference to determine the intensity and absolute phase of the individual measurements. At least one Xe reference scan was thus acquired for each nanoparticle scan set. The intensity was determined by using the modified ATI cutoff law given by equation (2.40), which agrees well in the intensity regime between 10^{13} and $10^{14}\,\mathrm{W/cm^2}$ [39, 82]. The Xe reference scan was also used to approximate the absolute phase. Comparison with TDSE calculations as well as classical trajectory integration predicts a phase shift of approximately 0.3π in the cutoff region [67]. As the Xe atoms can be assumed to have spherical symmetry, the full 3D momentum distributions can be calculated from the 2D momentum projections by iterative methods [79]. Figure 3.10 a) shows a summed image of 10^6 laser shots acquired at an intensity of $2.5 \times 10^{13}\,\mathrm{W/cm^2}$. The CEP modulation amplitude $A(p_x, p_y)$ and phase shift $\Delta\phi(p_x, p_y)$ as given by equation (3.10) are shown in b) and c), respectively. The inverted momentum distribution for $p_z = 0$ is shown in d) together with the modulation amplitude in e) and phase offset in f). The quality of the images presented in figure 3.10 demonstrate the power of the single-shot VMI approach with excellent signal-to-noise ratio and very high CEP accuracy.

3.4.4 VMI of nanoparticles - background suppression

A major advantage of single-shot VMI is that the data can be efficiently filtered during post-processing [74]. In general, care must be taken in such operations in order not to influence the physics under investigation.

As explained in section (3.3.2), the efficiency of aerodynamic lensing is limited and the average nanoparticle densities in the laser focus can be approximated to be below $10^6\,\mathrm{particles/cm^3}$. This implies that only a fraction of laser shots actually hit a nanoparticle. The relative nanoparticle signal is especially low for larger nanoparticles as here the aerodynamic lensing is less efficient. It was found that significantly more electrons are emitted from nanoparticles per single laser shot as compared to the background gas. This is evident when looking at the distribution of the number of events per shot. Such a histogram is plotted for a scan on 313 nm SiO_2 spheres in figure 3.11 a). The peak at low event numbers can be attributed to ATI background gas [74]. From the relative magnitude it is evident that the majority of laser shots do not show any nanoparticle signal. Figure 3.11 b) and c) show the full VMI projection as well as the radial asymmetry map for this scan taking all laser shots into account. d) and e) show the same plots, with the analysis limited to laser shots which have between 0 and 60 events per shot (indicated by the red shaded region in a)). One can see that the features resemble that of ATI with a well defined cutoff. This signal can be reproduced when running the aerodynamic lens just

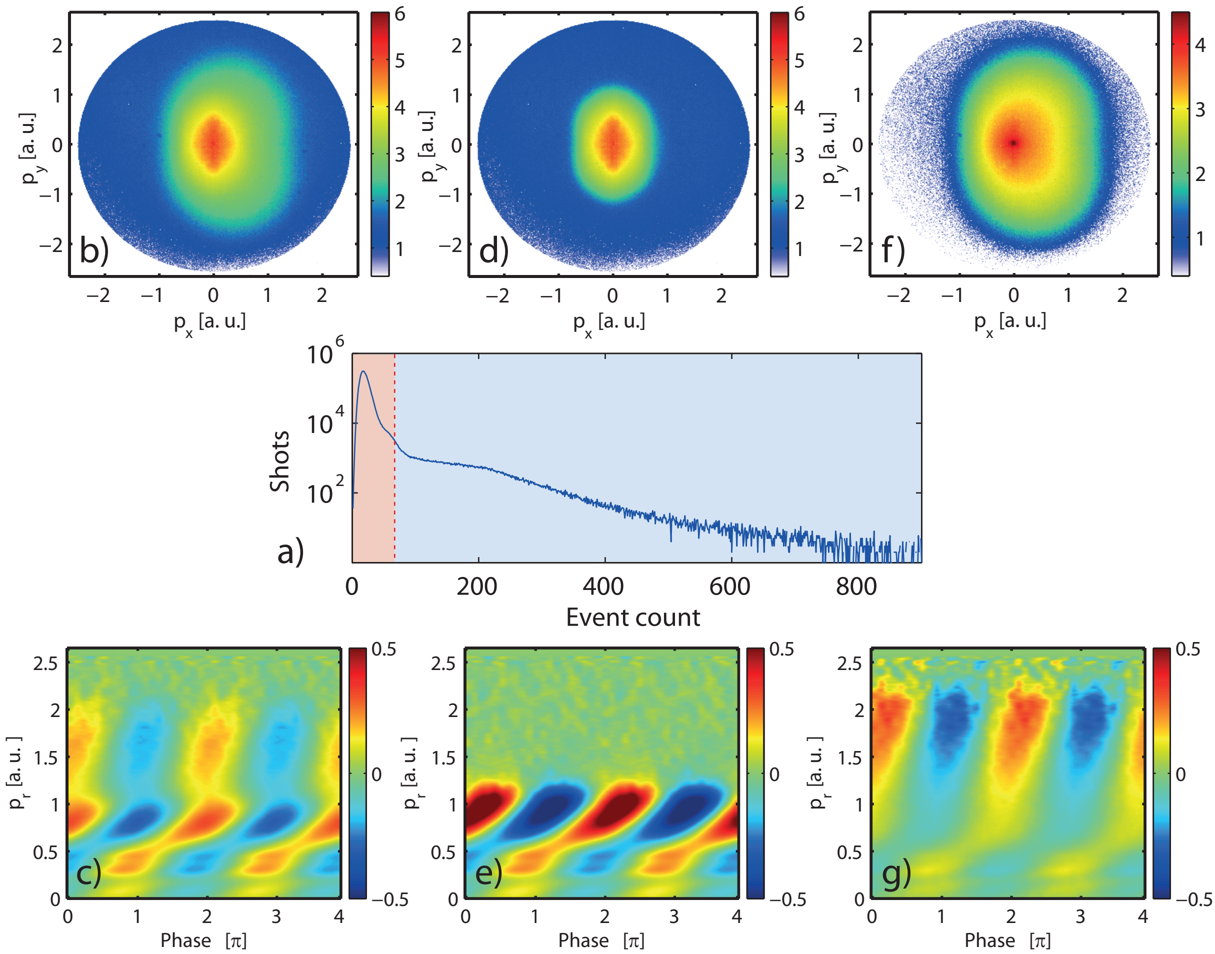

Figure 3.11: Illustration of the background suppression technique for a scan of 313 nm SiO_2 nanoparticles at an intensity of 2.7×10^{13} W/cm^2. a) shows the histogram of pixels above threshold. b) and c) show the full VMI projection and the radial asymmetry map for this scan. d) and e) show the same analysis only for 0 to 60 pixels per shot as indicated by the red area in a). f) and g) Same analysis for 60 to 1000 pixels per shot (blue region in a))

with pure solvent (ethanol). As this analysis covers around 90 % of laser shots, the background signal originating from dark counts has almost the same level as in b). Limiting the analysis to the laser shots with event numbers larger than 60 efficiently removes this undesired background contribution. This is shown in f) and g). The VMI projections are now nearly free from background and the nanoparticle signal is much clearer than in a). Also, the ATI contributions at lower momenta are also suppressed both in VMI projection as well as the radial asymmetry map, which makes it possible to (carefully) analyze the nanoparticle data in this momentum region.

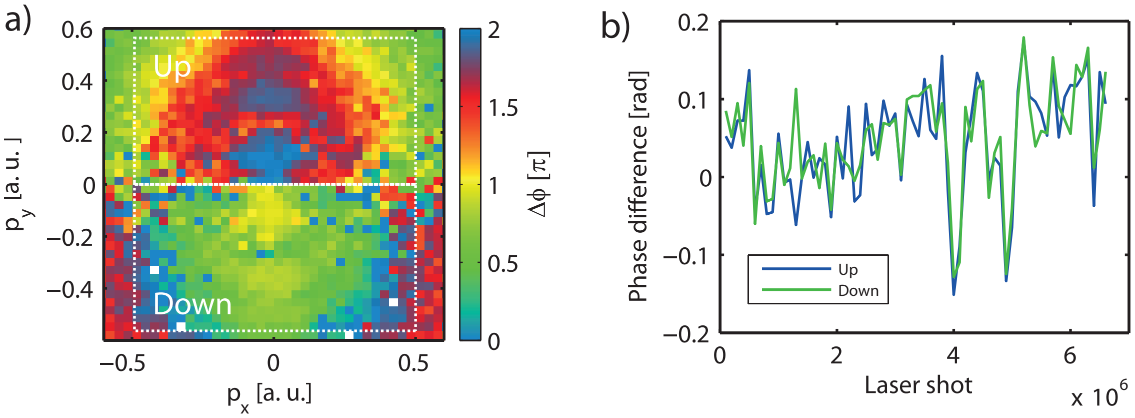

Figure 3.12: a) Phase offset in the central part of a single bin containing 10^5 laser shots. b) Retrieved phase drift between VMI and phasemeter for 6.7×10^6 laser shots with a bin size of 10^5 shots.

3.4.5 Stability of CEP tagging for long acquisition times

To test the accuracy of the setup during long measurements the correlation between the CEPs measured by the phasemeter and the VMI setup was investigated. A relative drift of CEP between phasemeter and experiment as well as intensity induced changes in the acquired asymmetry parameters might result in a reduced CEP dependence of the VMI data. It was theoretically shown by Kling *et al.* that at least 10^4 laser shots have to be acquired for an accurate CEP measurement by VMI due to the low count rates [83]. Taking this requirement into account, the VMI data was grouped into bins of 10^5 laser shots. The average phase shift from bin to bin was calculated from the $\Delta\phi$ map separately for positive and negative momenta p_y as indicated in Fig. 3.12 a). The average phase difference as compared to the first bin for an acquisition time of 7×10^6 shots (equivalent to 2 hours of acquisition time) is shown in Fig. 3.12 b). One can see a strong correlation of p_y and $-p_y$ phase evolution indicating a small error in this procedure. The phase drift between VMI and phasemeter is relatively small with a maximal excursion of 100 mrad and a standard deviation of 70 mrad. The error increases only slightly if the phasemeter rebinning function F is initialized only once with the first 10^5 frames (and not being periodically updated). From this finding, one can conclude that given sufficient laser stability the presented single-shot VMI approach gives highest accuracy in terms of CEP characterization.

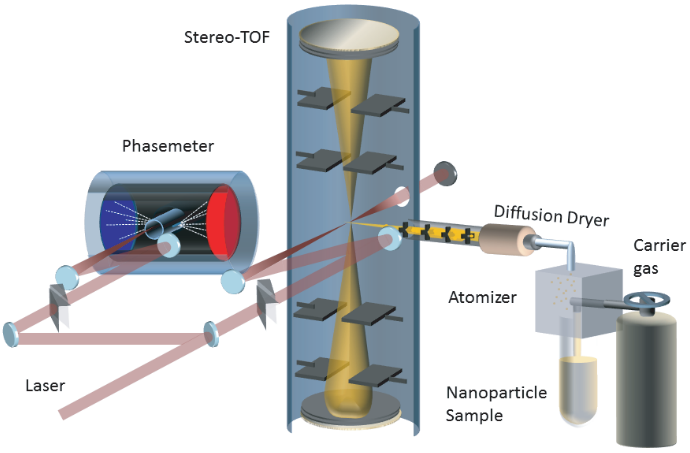

Figure 3.13: Overview of the stereo time-of-flight (sTOF) setup.

3.5 Stereo time-of-flight setup

3.5.1 Setup

For complimentary measurements, a stereo time-of-flight spectrometer provided by the group of Prof. Meiwes-Broer, Universität Rostock, was used. The machine is outlined in figure (3.13) a). Two symmetric, field-free drift tubes of 50 cm length detect the emitted photoelectrons along both sides of the laser polarization axis. Fully pumped the background pressure is at 2×10^{-8} mbar. Similar to the VMI, the aerodynamic lens system could be mounted perpendicular to both laser propagation and detection axes. For reference scans, gas (Ne, Xe) could be injected through a gas nozzle. The photoelectrons are detected by MCPs on each side of the drift tube. The single-event electron signals from the two MCPs were read out by a high-precision digitizer (Agilent Acquiris DC271) with a time resolution of 500 ps. In combination with approximately 300 ps trigger jitter originating from timing drifts of the delay generators, this results in an energy resolution of $E/\Delta E = 50$ at $E = 1$ keV. The maximum, resolvable electron energy was in practice limited by the appearance of a light peak emerging from scattered light and high energetic photons originating from the nanoparticles. In the experiments on nanoparticles, the highest measured cutoff energies are around 2.5 keV. The acquisition software handled the event detection as well as the phase-tagging. The peak detection algorithm uses a gate open and close threshold. The hit time was determined by the center-of-mass between the gate open and close time frames. Simultaneously, the two CEP asymmetry values were read from the phasemeter electronics box by an A/D-converter card. The rebinning for exact phase retrieval and phase tagging was handled by the acquisition software during running measurements enabling a live view of the phase dependent spectra.

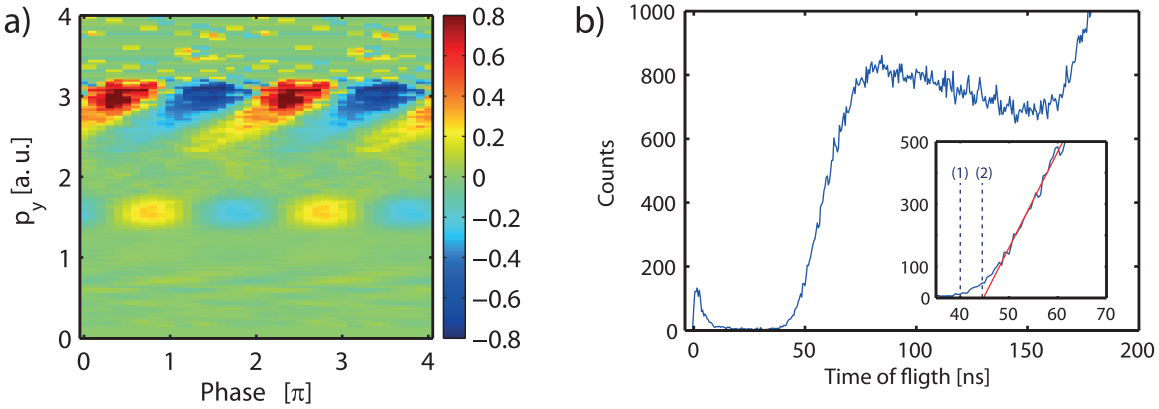

Figure 3.14: a) Asymmetry map measured on Ne gas at an intensity of $1.4 \times 10^{14}\,\mathrm{W/cm^2}$. b) Time-of-flight spectrum of a SiO_2 scan at an intensity of $1.5 \times 10^{14}\,\mathrm{W/cm^2}$. The first peak is produced by photons. The inset illustrates the two methods for determining the cutoff.

3.5.2 Data acquisition and analysis

To have an exact intensity calibration, a reference scan in N_2 and Ne was acquired for each nanoparticle scan. The intensity was calculated from the cutoff energy using equation (2.40). Due to the small acceptance angle, the count rates were significantly smaller as compared to the VMI measurements. The scans thus had to extend at least over 10^6 laser shots for a reliable determination of the cutoff energy. It was found that the spectra especially from the nanoparticles contain a strong light signal. On the one side, this makes the calibration of the instrument trivial. On the other side, the light signal exhibits a long exponential tail, which (depending on intensity) overlaps with the high-energy electron events. Unfortunately the STOF instrument does not offer the possibility to decelerate the electrons in order to separate light and electron signal.

The cutoff energy was obtained from the CEP-averaged spectra. Due to low signal in the cutoff region, contamination by the light peak signal determining this cutoff energy is not always unambiguously possible. It was found that the nanoparticle signal shows a nearly linear decay in the time-of-flight spectrum and an exponential decay in the energy spectrum. The background level could nevertheless be more easily identified in the time-of-flight spectrum, so this representation was used. Two methods were employed which are illustrated in Fig. 3.14 b) for a measurement on 95 nm SiO_2 spheres at $1.47 \times 10^{14}\,\mathrm{W/cm^2}$. First the cutoff was calculated from the manually determined position in the light-peak suppressed TOF spectra (indicated by (1) in the inset plot). Furthermore, the linear onset of the photoelectron signal was fitted and the intersection with the background level gave a second value (2). Throughout this work, the presented energy cutoff was always obtained by averaging the results of both methods. The systematic error originating from trigger jitter and digitizer resolution is always indicated in the plots for completeness.

The CEP dependence can be visualized in analogy to the VMI radial asymmetry maps.

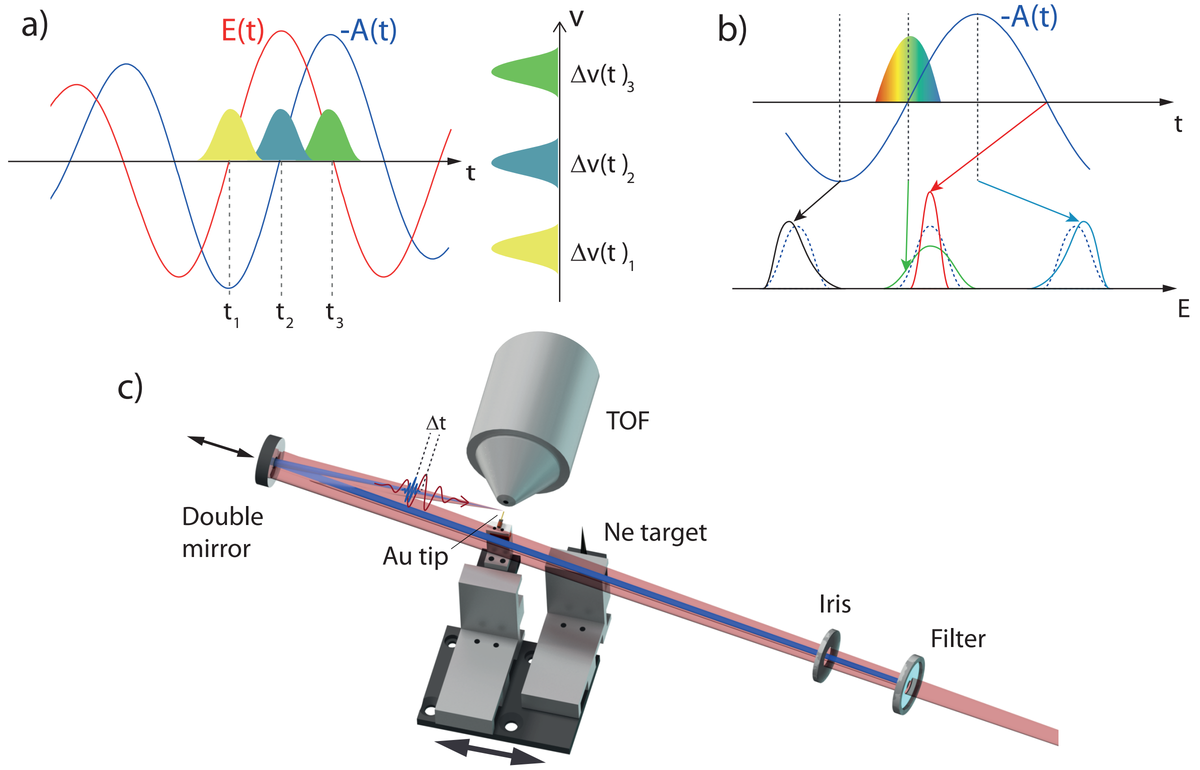

Figure 3.15: a) Working principle of the attosecond streak camera. The temporal overlap between IR field and attosecond pulse is indicated by yellow, blue and green areas. The acceleration of the XUV photoelectrons in the laser field results in an effective shift of their respective velocity distributions (indicated on the right). Adapted from [15]. b) Influence of positive chirp on final electron spectra for various IR phases. For a positive slope of $-A(t)$, this results in a broadening of the XUV spectrum, while it is narrowed for negative slopes. At the maxima of the vector potential, the chirp results in a asymmetric distortion. c) Experimental realization.

The relative asymmetry parameter is calculated from the phase tagged spectra:

$$A(p, \phi_{\mathrm{ce}}) = \frac{S_{\mathrm{up}}(p, \phi_{\mathrm{ce}}) - S_{\mathrm{down}}(p, \phi_{\mathrm{ce}})}{S_{\mathrm{up}}(p, \phi_{\mathrm{ce}}) + S_{\mathrm{down}}(p, \phi_{\mathrm{ce}})} \tag{3.12}$$

Fig. 3.14 a) shows the asymmetry map obtained from a scan with neon gas at an intensity of $1.4 \times 10^{14}\,\mathrm{W/cm^2}$.

3.6 AS-5 attosecond beamline

3.6.1 Attosecond streak camera

One of the most powerful techniques of modern attosecond science is the attosecond streak camera (also called attosecond transient recorder) [84]. The temporal structure of both initial NIR few-cycle laser field as well as the attosecond pulse can be retrieved with great accuracy. The principal mechanism is a pump-probe scheme in which photoelectrons are emitted by the XUV attosecond pulse and after emission accelerated by the superimposed NIR laser [85]. The IR laser pulse will be referred to as pump beam, while the XUV attosecond pulse is called the probe beam. This naming might differ from other studies, which focus on the structure of the XUV pulse. Given the fact that in this work the IR field is assumed to excite plasmonic oscillation, this convention is intuitive. The attosecond pulse can be considered here as a mere tool for a time-resolved measurement of the field oscillations. Figure 3.15 a) shows the working principle of the attosecond streaking technique. Pump and probe beam are focused into a target gas. The XUV pulse ionizes the medium creating fast photoelectrons with an average energy of $E_{\text{kin}} = \hbar\omega_{\text{XUV}} - I_p$. Here ω_{XUV} denotes the wavelength of the XUV radiation and I_p is the first ionization potential of the gas atoms. Electrons emitted by the XUV pulse will be accelerated by the IR laser field along its polarization direction. By varying the delay between fundamental IR field and attosecond pulse, the birth time of the photoelectrons with respect to the laser field are scanned. As the photoemission process can be assumed to happen instantaneously [86] this results in an experimental resolution only limited by the attosecond pulse length (and experimental stability). The emitted electrons can be detected by e.g. a time-of-flight spectrometer or VMI instrument. Assuming a homogeneous, linearly polarized light field $E(t)$, the final velocity v_f of an electron with charge $-e$ emitted at time t_e is according to Newton's classical law of motion:

$$v_f(t_e) = v_0 - \int_{t_e}^{\infty} \frac{e}{m_e} E(t)dt = v_0 - \frac{e}{m_e} A(t_e). \tag{3.13}$$

$A(t)$ is the vector potential of the electric field oscillation defined as $E(t) = -\frac{\partial}{\partial t}A(t)$ in the Coulomb gauge. This results in a final kinetic energy of :

$$E_{\text{kin}}(t_e) = \frac{1}{2} m_e v_0^2 - e v_0 A(t_e) + \frac{e^2}{2m_e} A^2(t_e). \tag{3.14}$$

In case of moderate laser fields, the quadratic term $A^2(t_e)$ can be neglected. One obtains a direct correlation of change in kinetic energy and laser vector potential

$$\Delta E_{\text{kin}}(t_e) \approx -e v_0 A(t_e) = -e A(t_e) \sqrt{\frac{2}{m_e} \big(\hbar\omega_{\text{XUV}} - I_p\big)}. \tag{3.15}$$

Plotting the photoelectron spectra as a function of delay time t_e between pump and probe pulse results in the streaking spectrogram. The XUV photoelectron features in such a spectrogram will according to equation (3.15) exhibit a direct imprint of the laser waveform, namely its negative vector potential.

In addition to the driving laser field, the spectrograms will also exhibit pronounced features that can directly be attributed to the spectro-temporal characteristic of the attosecond laser pulse [87]. Chirp of the XUV pulse will lead to pronounced broadening and narrowing of the features at positions $A(t_e) = 0$. For a positively chirped XUV pulse, the low frequencies of the XUV pulse arrive first. For a given delay setting this will lead to a compression of the spectral features if $A(t_e)$ has a negative slope, while it broadens the spectral features if the slope of $A(t_e)$ is positive, as illustrated in Fig. 3.15 b).

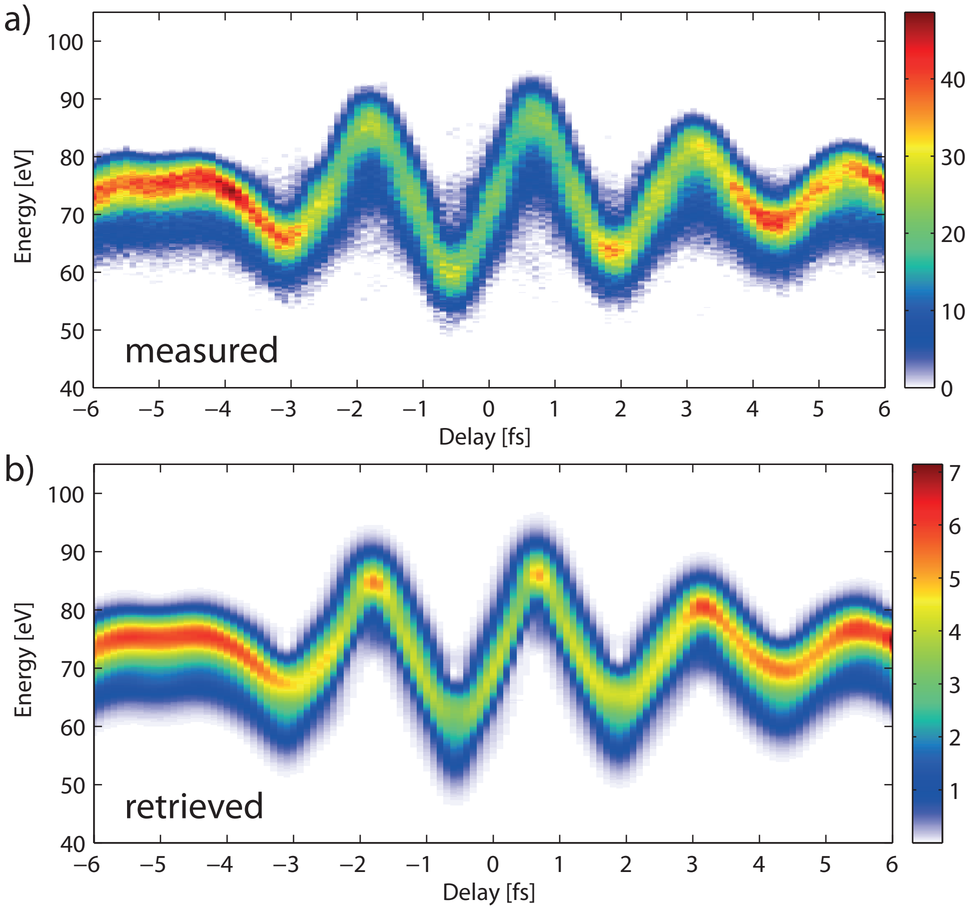

Figure 3.16: a) Attosecond streaking measurements in Ne gas at an intensity of 5 × $10^{12}\,\mathrm{W/cm^2}$. b) The same spectrogram as reconstructed by the ATTOGRAM retrieval algorithm [88].

Figure 3.16 a) shows a measured streaking spectrogram from neon gas. With the experimental streaking spectrum as input, an iterative FROG algorithm can be employed to reconstruct the temporal and spectral properties of the XUV and NIR pulses [89, 88]. The spectrogram retrieved by the ATTOGRAM software package is shown in b). From the

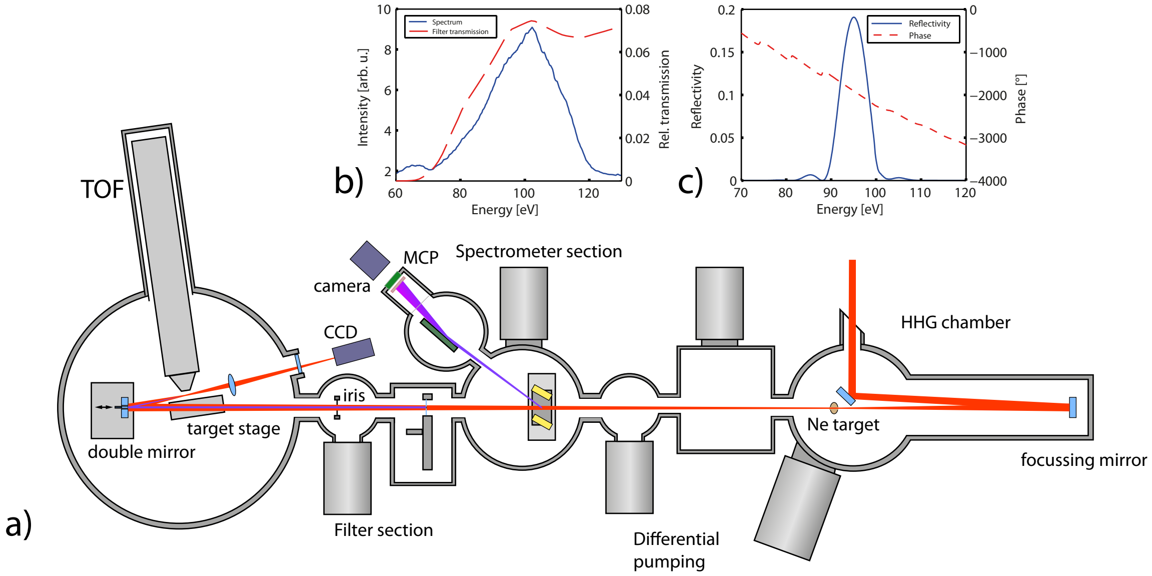
b)
Spectrum
Filter transmission
Intensity [arb. u.]
Rel. transmission
10
8
6
4
2
0.08
0.06
0.04
0.02
0
60
80
100
120
Energy [eV]
c)
Reflectivity
Phase
Reflectivity
Phase [°]
0.2
0.15
0.1
0.05
0
−1000
−2000
−3000
−4000
70
80
90
100
110
120
Energy [eV]
TOF
MCP
Spectrometer section
camera
CCD
HHG chamber
iris
target stage
double mirror
Ne target
focussing mirror
Filter section
Differential pumping
a)

Figure 3.17: a) Overview of the AS-5 beamline. b) Measured XUV spectrum (blue line) after the 0.8 μm Zr filter. The theoretical filter transmission is indicated by the red, dashed line with data from [90]. c) Reflectivity and GDD of the used XUV end mirror. (Courtesy of A. Guggenmoos.)

reconstruction, all pulse parameters can be retrieved. The temporal and spectral properties of the XUV pulse are shown in Fig. 3.18.

3.6.2 Beamline layout

The AS-5 attosecond beamline can be divided in four major components: High-harmonic generation chamber, beam characterization chamber, filter section and experimental chamber. Fig. 3.17 a) shows the layout of the beamline. The p-polarized laser beam is sent through a Brewster window into the HHG chamber. Here it is focused by a $f = 50$ cm spherical mirror onto a 3 mm diameter nickel tube (gas target). The laser-cut hole in the tube is approximately the size of the laser focus of 150 μm. Neon gas is injected by a gas feedthrough into the gas target tube. The optimal backing pressure for efficient HHG was found to lie between 150 and 200 mbar. In order to create a directed, intense XUV beam it is best to position the laser focus at the back of the gas target tube towards the propagation direction.

After traveling 1.5 m, the beam reaches the characterization section. Here the beam profile and the spectrum of the attosecond XUV pulse are monitored. Gold mirrors can be inserted into the beam to reflect the XUV beam either directly onto a MCP/phosphor screen or to first pass a flat-field corrected, grazing incidence grating which disperses the beam spectrally onto the MCP. To protect the imaging device from the strong contribution of low-order harmonics and the intense NIR part, an 800 nm thick zirconium (Zr) filter is installed in front of it. The image on the phosphor screen is recorded by a CCD camera. For calibration of the spectrometer, additional filters can be inserted into the beam. Though the resolution of the spectrometer is probably less than 2 eV and it is spectrally limited by the transmittance of the Zr filter, it proves to be a useful device for optimizing the HHG process. Imaging the beam profile enables the optimization of the NIR laser focus in the HHG target and phase matching conditions. The inset b) in figure 3.17 shows an experimental XUV spectrum along with the transmission through the 800 nm Zr filter.

The separation of NIR laser field and attosecond pulse is achieved with a small circular 150 nm zirconium filter mounted by thin metal rings on a 15 μm thick pellicle. The Zr filter efficiently blocks the NIR beam while it has a transmission of about 0.6 around 95 eV [90]. The outer part of the filter is opaque for XUV radiation and transmits only the fundamental NIR laser. The AS-5 is equipped with a filter wheel which can hold up to nine filters. It is thus possible to easily switch between a different set of filters. The intensity of the laser field can be adjusted by a motorized iris aligned with the central Zr filter mounted in a small chamber behind the filter section. For the experiments on the Au nanotips, usually much less laser intensity is required. To prevent damage to the sample and to have a better control over the intensity a special filter was made from a coated pellicle with only 20% transmission. This also ensures a good quality of the focus and less influence of misalignments.

In the experimental chamber the beams are focused by a spherical double mirror ($f = 125$ mm focal length) into the interaction region. The mirror stack can be moved and tilted in all three dimensions. The inner mirror reflecting the attosecond pulse is attached to a high precision piezo stage with position encoder. This piezo stage is used to adjust the delay between XUV and laser field. The outer mirror can be tilted independently by pico motors to optimize the spatial overlap between NIR and attosecond beam. The reflectivity for the XUV region is plotted in figure 3.17 c). The spectral width is 8 eV centered at 95 eV with a peak reflectivity of 20%.

In front of the TOF, a dual target stage is installed. On one mount is a gas nozzle made from a glass capillary with an opening diameter of less than 40 μm. The second target module carries the tips used for the streaking measurements described in chapter 6. Both targets are motorized and can be moved in all three dimensions (see Fig. 3.15 c)). The laser beam is refocused by a $f = 7$ cm lens onto a CCD camera located outside the vacuum chamber. This image of the focus serves as a guide for correct positioning of both gas and tip target in the laser focus. The streaked electrons are detected by a time-of-flight spectrometer. The spectrometer is equipped with an electrostatic lens to increase the acceptance angle of emitted electrons. This imaging of the electron trajectories onto the the MCP detector is energy selective and creates a window in the spectrum in which count rates are increased by approximately two orders of magnitude. After passing a 70 cm drift tube the electrons are post-accelerated to generate equal signals from the MCP. The signal is capacitively coupled out and digitized by a synchronized multiscaler card (FAST Comtec P7889) with 100 ps time resolution. The calibration of this TOF is described in appendix A.3. For the attosecond measurements, the active CEP stabilization system was used. For optimizing the generation of single attosecond pulses, streaking spectrograms

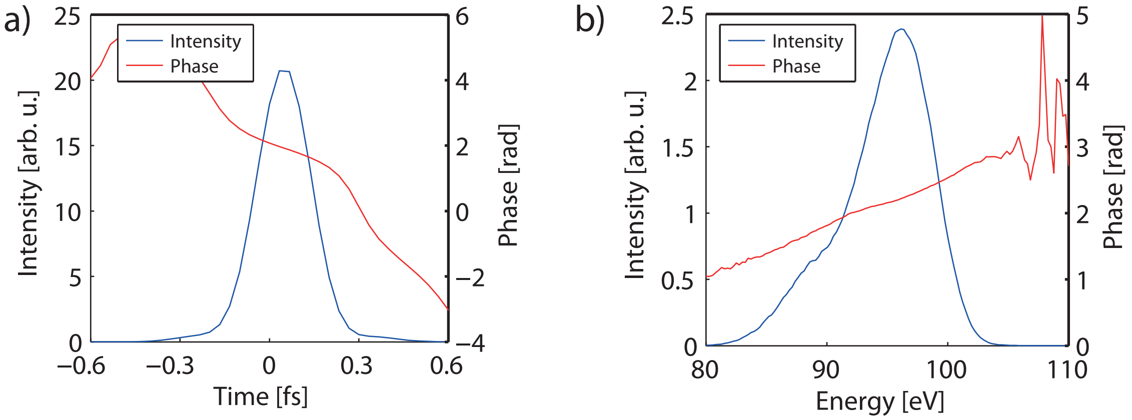

Figure 3.18: a) Reconstructed temporal XUV intensity and phase of the XUV attosecond pulse at the AS-5 beamline yielding a pulse length of 212 as. b) Spectral intensity and phase.

for various CEPs were acquired. The CEP with lowest satellite contributions was chosen and if necessary the HHG process was temporally further limited by a reduction of input intensity. The streaking spectrogram shown in Fig. 3.16 was obtained with the gas target in neon gas. The delay step was set to 100 as. The reconstruction of the attosecond pulse is shown in Fig. 3.18. The pulse length was found to be 212 as with a rather flat phase illustrating the good matching of mirror design and pulse generation.

Chapter 4

CEP resolved photoemission from dielectric nanospheres

4.1 Introduction

Only very recently, a carrier-envelope phase dependency of photoemission from a solid Au surface was experimentally observed [91]. The measured modulation was less than 1%. It was concluded that surface roughness and the large extent of the interaction volume was responsible for blurring the CEP effects. This was also concluded for the acceleration of photoelectrons in SPP fields at a metal surface [92]. First works on the CEP control of photoemission from nanosystems showed a much stronger CEP dependence [93, 94]. Krüger et al. measured a strong imprint of the CEP on photoelectron spectra from tungsten nanotips [94].

In this chapter the experimental and theoretical progress in CEP controlled photoemission from SiO_2 nanospheres by few cycle laser pulses will be reported [93, 95]. The experimental work was carried out using the combination of phase-tagged VMI with aerodynamic lensing as described in sections 3.3.2 and 3.4.

The choice for SiO_2 as a model system has several reasons. For once, this system is interesting due to its high damage threshold. The band gap is about 9 eV [96], which also assures there is no fundamental phase change induced during the interaction of the laser pulse with the particle for moderate intensities. The ionization dynamics will mostly occur in the highly non-linear tunneling regime. A second reason is that SiO_2 has a small index of refraction and exhibits only minimal dispersion and no (plasmonic) resonances. This ensures that the pulse duration will be only slightly altered such that CEP effects remain pronounced. From an experimental point of view, the high quality and stability of the samples is a major advantage. The SiO_2 spheres can be grown with high accuracy and smooth surfaces. These mono-disperse samples with size distributions of usually less than 5% guarantees no blurring or broadening due to a possible dependence of the photoelectron signal on size and shape.

For the interpretation of the experimental data, a simulation model (M^3C) was proposed by and developed in close collaboration with the group of Prof. Thomas Fennel, Universität Rostock. As this semi-classical model offers direct insight into the underlying physics, the key elements and findings of this model will be presented here first before comparing its predictions with the experimental results.

4.2 M^{3}C simulation model

4.2.1 Overview

Due to the size and complexity of the system, particle-in-cell (PIC) codes or ab-initio calculations by time-dependent density-functional theory (TDDFT) are not feasible. This is also not required for a moderate intensity regime of ultra-short laser pulses. In this regime it can be expected that the bulk optical properties are not altered during the laser pulse. As long as this assumption holds, the modeling can focus on the dynamics of electrons emitted from the surface. This is the realm of the M^{3}C model. The model implements the electromagnetic response of the nanoparticle to the external laser field, ionization from the surface and propagation of liberated electrons. The name stands for :

- Mean field: The interaction between free charges generated at the surface is taken into account by a mean field multipole expansion. This approximation allows to include many-particle effects.

- Mie theory: The optical near fields in and around the particle can be calculated using either the dipole approximation or the analytically correct Mie solution in order to account for propagation effects.

- Monte Carlo: A large number of electron trajectories is integrated. Each trajectory can be interpreted as the center-of-mass motion of individual electronic wavepackets. Collisional processes are modeled via Monte-Carlo sampling of rates for elastic and inelastic electron scattering.

One of the key elements is the Monte-Carlo sampling of electron trajectories. By integrating a large number of trajectories a self-consistent statistical ensemble is generated within a single run of the simulation. Each trajectory is weighted with respect to the absolute number of emitted electrons. The required number of electron trajectories can be determined from convergence tests. For a reliable outcome, typically 10^6 trajectories have to be integrated. To analyze the CEP dependence, the simulation is repeated for 40 different CE phases. The integration is performed by a velocity Verlet propagator with a time step of 5-10 as. Due to the short pulse length and the fact that all dynamics take place within tens of femtoseconds, ions and atoms are assumed to be frozen.

4.2.2 External laser field

The temporal evolution of the laser pulse is assumed to have a Gaussian envelope and is described by:

$$E_{\mathrm{las}}(t) = E_0 cos(\omega t + \phi_{\mathrm{ce}}) \exp\left[-2\ln 2\left(\frac{t}{\tau}\right)^2\right], \tag{4.1}$$

where E_0 is the peak laser field, ϕ_{ce} the carrier- envelope phase and τ is the pulse length (intensity full-width-half-maximum).

For materials that do not show strong dispersion and diameters smaller than 100 nm it is justified to use the quasistatic dipole approximation. The spatial distribution of the laser potential inside and around the sphere is thus given by:

$$\Phi^{\mathrm{ext}}(\mathbf{r}) = \begin{cases} -E_{\mathrm{las}}\left(1 - \frac{\epsilon_r - 1}{\epsilon_r + 2}\frac{R^3}{r^3}\right) y & r \geq R \\ -E_{\mathrm{las}}\left(\frac{3}{\epsilon_r + 2}\right) y & r < R. \end{cases} \tag{4.2}$$

For the simulations a constant relative permittivity of $\epsilon_r = 2.12$ was used [97]. For particle sizes where the dipole approximation cannot be used, a Mie solver was implemented in the model. As explained in section 2.1.4, Mie theory can be used to calculate the (complex) electric field distribution for a single wavelength. To reproduce the temporal waveform of the near-field, a discrete Fourier transform of the incident laser spectrum would be necessary. An implementation of the full spectrum of the used few-cycle laser field is nevertheless very inefficient. The limited computational resources require a reduction of the number of frequency components by usage of an artificial frequency comb. This computational trick corresponds to a high laser repetition rate which, however, does not interfere with the dynamics. A laser pulse with a repetition rate $f_{\mathrm{rep}} = 1/T_{\mathrm{rep}}$ can be represented by a superposition of a set of frequencies with a spacing of f_{rep}. Consequently the near field around the nanosphere can be written as

$$\mathbf{E}_{\mathrm{ext}}(\mathbf{r}, t) = \sum_{n=-N_{\mathrm{c}}}^{N_{\mathrm{c}}} A_n f_n(\mathbf{r}) e^{-i(\omega_n t + \phi_{\mathrm{ce}})}. \tag{4.3}$$

The frequencies ω_n are equally spaced around the carrier frequency ω_c: $\omega_n = \omega_c + 2\pi n f_{\mathrm{rep}}$. Furthermore $f_n(\mathbf{r})$ are the (complex) amplitudes obtained by Mie theory for the frequency ω_n. Note that each f_n includes the laser pulse propagation $e^{-ik_n x}$. A_n denotes the spectral amplitude for each component. For a Gaussian laser pulse, these also have a Gaussian distribution around the center frequency ω_c [98]. The artificial repetition f_{rep} rate can be chosen to be rather high as the simulation time window is usually less then 50 fs. This efficiently minimizes the number of calculated wavelength components and thus the computation time.

4.2.3 Modeling mutual electron interaction by mean field approach

As a large number of electrons will be created on the surface, electron-electron interactions as well as electron-ion interaction via the Coulomb force will have a strong influence on the dynamics of each individual electron. The total force acting on one electron is given by the sum of near-field $\mathbf{E}_{\text{ext}}$ generated by the laser field and the dielectric response of the sphere and the Coulomb field $\mathbf{E}_{\text{mf}}$ which is induced by free charges after ionization:

$$\mathbf{E}_{\text{eff}}(\mathbf{r}, t) = \mathbf{E}_{\text{ext}}(\mathbf{r}, t) + \mathbf{E}_{\text{mf}}(\mathbf{r}, t) \tag{4.4}$$

The potential created by the free charges can be written as:

$$\mathbf{\Phi}_{\text{mf}}(\mathbf{r}, t) = -\sum_i \frac{1}{4\pi\epsilon_0} \frac{e}{|\mathbf{r} - \mathbf{r}_i(t)|} + \sum_p \frac{1}{4\pi\epsilon_0} \frac{e}{|\mathbf{r} - \mathbf{r}_p(t)|} \tag{4.5}$$

Here the first sum extends over all electrons i at positions $\mathbf{r}_i$, while the second sum accounts for all positively charged parent ions p at $\mathbf{r}_p$.

In the most simple approach, the Coulomb field given by Eq. (4.5) could be individually summed for all electrons at all time steps. Considering that in a typical simulation at least 10^6 electrons are propagated, it is clear that such individual summing of the charge interaction is not feasible. For this reason, a mean field approach has to be employed. Given the spherical symmetry of the systems under considerations a multipole expansion of the charge distribution's potential as given by equations (2.36) and (2.37) is a good choice. Though these equations look very complicated, they can be efficiently implemented. This is due to the fact, that most of the terms have the same form for all four equations. By introducing a discrete radial grid the entries for individual r can be efficiently calculated by cumulative sums and saved for lookup. The mean field multipole expansion was implemented such, that at every time step the lookup tables are populated once for all free charges. Both liberated electrons as well as their parent ions are injected. Then the cumulative sums are created and can afterwards be retrieved for updating the fields acting on the individual electrons. With such a multipole expansion the computation time used for calculating the Coulomb field for all particles scales approximately linear with the number of particles $O(N)$. An important aspect one needs to consider is the order of the multipole expansion, which is equivalent to l in equations (2.36) and (2.37). The higher l, the more details of the potential landscape are preserved by the multipole expansion. Usually, a number of $l = 4 - 6$ is sufficient for particles in the dipolar size regime.

4.2.4 Electron emission, scattering and impact ionization

For the intensity regime that is under consideration ($> 10^{13}\,\text{W/cm}^2$), the dominant contribution to the creation of free charges is tunneling ionization. To calculate the photo ionization from the surface, the model employs the ADK ionization rate given by equation (2.39). The ionization potential of atomic Si is used which has a value of $I_p = 8.1\,\text{eV}$ [99].

It was found during this work, that using the band gap of SiO_2 ($I_p = 9\,\mathrm{eV}$) yields better agreement with respect to the momentum distribution maps.

Electrons are assumed to be ionized from the surface. At each time step a number of randomized points on the sphere's surface is probed. For calculating the ionization probability at a position $\mathbf{r}$, the local electric field $\mathbf{E}_{\mathrm{eff}}(\mathbf{r})$ is evaluated. The ionization only takes place, if the electric field points inside the sphere, so that an electron is pulled outwards. Note that the electric field used for the evaluation is the effective field. This implies that the ionization yield is dependent on the charge distribution around the sphere. In general this leads to a decrease of the ionization yield with time. Consequently, more electrons are created by tunnel ionization during the first cycles of the laser pulse on average. If an electron is ionized, it is placed at the tunnel exit given by a simple geometric approximation of $r_0 = R_{\mathrm{sphere}} + E_r/I_p$, where E_r is the radial electric field component.

A second mechanism for charge creation is impact ionization. Here a fast moving electron can inelastically scatter with electrons in the valence band of the nanoparticle and transfer energy to them. The simulation model accounts for this mechanism. If the electron is inside the sphere and has an energy above the ionization potential, it can create a second electron at rest. The kinetic energy of the scattered electron is reduced by the ionization potential $E_{\mathrm{kin}} = E^0_{\mathrm{kin}} - I_p$. The impact ionization rate is obtained by a modified version of the Lotz formula, which was originally developed for an isolated electron-ion/atom pair [100, 101]:

$$P_{\mathrm{ii}} = v n_{\mathrm{a}} 450\ \mathrm{eV}^2\ \mathrm{\mathring{A}}^2\ \frac{\ln(E_{\mathrm{kin}}/I_p)}{E_{\mathrm{kin}} I_p}. \tag{4.6}$$

Here v is the electron's velocity and n_{a} is the atomic density of bulk SiO_2.

Elastic scattering of electrons at atoms is assumed to only happen inside the nanoparticle. The probability for scattering is governed by the mean free path l_{mfp}. Synchrotron measurements show that this mean free path is on the order of 1 nm for SiO_2 [102] but also depends on the electron's kinetic energy E_{kin} [103]. In order to approximate the dispersive character of elastic scattering, l_{mfp} is expanded with respect to its energy E_{kin}:

$$l_{\mathrm{mfp}} = l_0 + l_1 E_{\mathrm{kin}} + l_2 E^2_{\mathrm{kin}} \tag{4.7}$$

The constants $l_0 = 0.2\,\mathrm{nm}$, $l_1 = 5.3 \times 10^{-3}\,\mathrm{nm/eV}$ and $l_2 = 1.8 \times 10^{-5}\,\mathrm{nm/eV^2}$ can be derived from a comparison with atomic scattering cross sections by fitting to the high energy behavior. In the model elastic scattering at atoms is assumed to be isotropic.

4.3 Microscopic analysis

Before we will turn to the experimental results we will first outline the dynamics of the electron photoemission and rescattering process with special emphasis on the collective effects that are included in the effective mean field. Figure 4.1 a) shows a simulated electron energy spectrum for 90 nm SiO_2 at an intensity of $3 \times 10^{13}\,\mathrm{W/cm^2}$ with the mean field contribution $\mathbf{E}_{\mathrm{mf}}$ turned off, i.e. the electrons are only accelerated by $\mathbf{E}_{\mathrm{ext}}$ which is

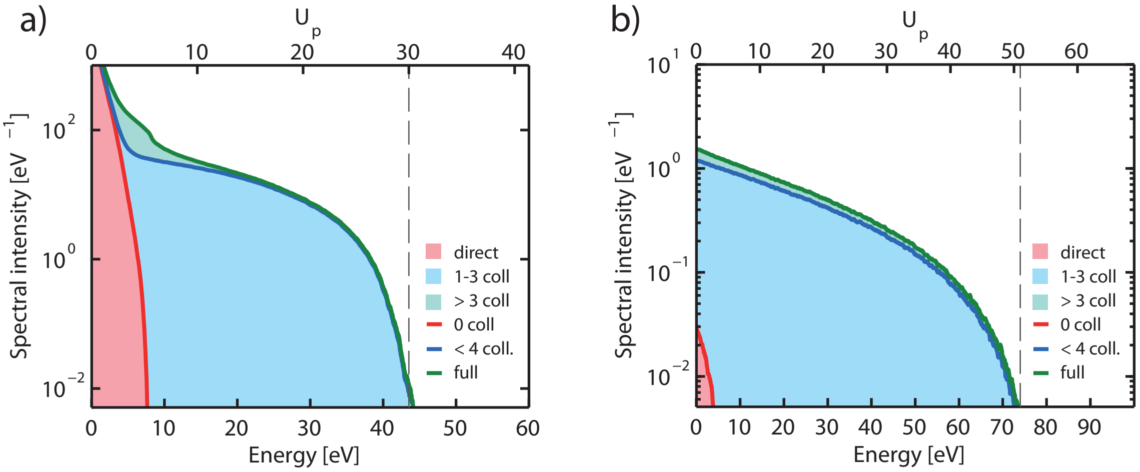

Figure 4.1: Electron energy spectra for the photoemission from 90 nm SiO_2 ($I = 3 \times 10^{13}\,\mathrm{W/cm^2}, \tau = 4\,\mathrm{fs}$). In a) the mean field contribution is turned off, while in b) it is taken into account. Each spectrum is decomposed into the contributions for unscattered electrons (red), trajectories with 1-3 scattering events (blue) and more than 3 scattering events (green).

the combination of laser field and dielectric response of the sphere. The spectrum extends to energies of 29 U_p. This value is close to the classical expectation. As discussed in section (2.1.5), the near-field enhancement for a 95 nm SiO_2 sphere is 1.5 resulting in an intensity enhancement factor of $\alpha = 2.25$. Including this enhancement factor in the cutoff formula, one obtains $E_c = 10.0007\alpha U_p \approx 23 U_p$ (see section 2.2.1). The discrepancy of 6 U_p originates in the derivation of the cutoff formula itself. Here, the laser field is assumed to be a continuous wave and the tunnel exit is not included [38]. The contributions of different kinds of trajectories, given by their number of scattering events, are highlighted. This number is an important characteristic and indication of its trajectory. Note, that such an analysis is not as simple as compared to gas ATI due to the high density of scattering centers. For example, an electron trajectory with two individual scattering events in short series can have the same characteristic compared to a trajectory with a single collision. Direct (unscatterd) electrons may only acquire a maximum energy of 4.5 U_p . Due to large number of trajectories these direct electrons thus dominate the lower energy region of the spectrum. The high energy part of the spectrum is created by electrons with only 1-3 scattering events. In overall, there is no qualitative difference to an energy spectrum from ATI in gases. Figure 4.2 a) shows the dependence of the final kinetic energy on the birth time of the electrons for the same intensity. Unscattered electrons are created during the first half of each half-cycle in the respective direction. The closer they are emitted with respect to the zero crossing of the electric field, the higher is their final kinetic energy. This reflects the integrating character of this process, as the vector potential of the light

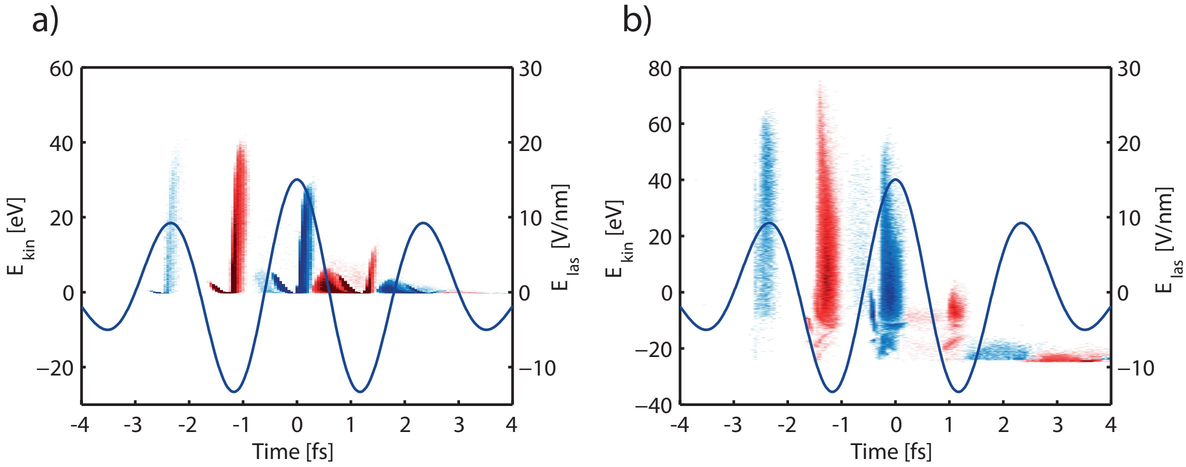

Figure 4.2: Dependence of the final kinetic energy (sampled at time $t = 50\,\mathrm{fs}$) on the birth time for simulations a) without mean field and b) with mean field contribution. The simulation parameters are $d = 90\,\mathrm{nm}, I = 3 \times 10^{13}\,\mathrm{W/cm^2}$ and $\tau = 4\,\mathrm{fs}$. The signal shown in red represents electrons emitted from the upper half sphere ($y > 0$), while the blue signal represents electrons from the lower half sphere ($y < 0$). For reference, the external laser field is also shown (blue line).

field is phase-offset by $\pi/2$. The electrons with the highest energies are emitted during the first half of the pulse between the peaks and zero crossings of the driving field well in accordance with the expectation of the simple men's model for ATI which expects the cutoff to occur at a phase of $\omega t = 14°$ [104].

Figure 4.1 b) shows the energy spectrum with mean field contribution turned on. Two major differences can be seen. First, the cutoff, which is still dominated by electrons with 1-3 scattering events, now lies at a value of around 52 U_p. The second observation is the almost complete suppression of direct electrons, resulting in a flat spectrum. The total number of emitted electrons also is drastically reduced by more than 1 order of magnitude. The birth time analysis for the mean field simulations is shown in figure 4.2 b). One can see, that the most energetic electrons are still born close to the peaks of the laser field but rather than after the peaks, they appear slightly in front of them. There are still features resembling the direct electrons as in a), but they now have negative energy meaning that they are trapped in the Coulomb mean field around the nanosphere. The blurring of these features can be explained by the now inevitable scattering of these trajectories. In overall, there is gradual decrease of energies up to a value of about $-25\,\mathrm{eV}$.

The observations at first seem a bit contradictory. The disappearance of the direct electron feature points to an attractive nature of the mean field potential exceeding 10 eV even at early times. On the other side, the increase in cutoff energy points to an additional acceleration for certain electron trajectories. A detailed phase space analysis gives insight

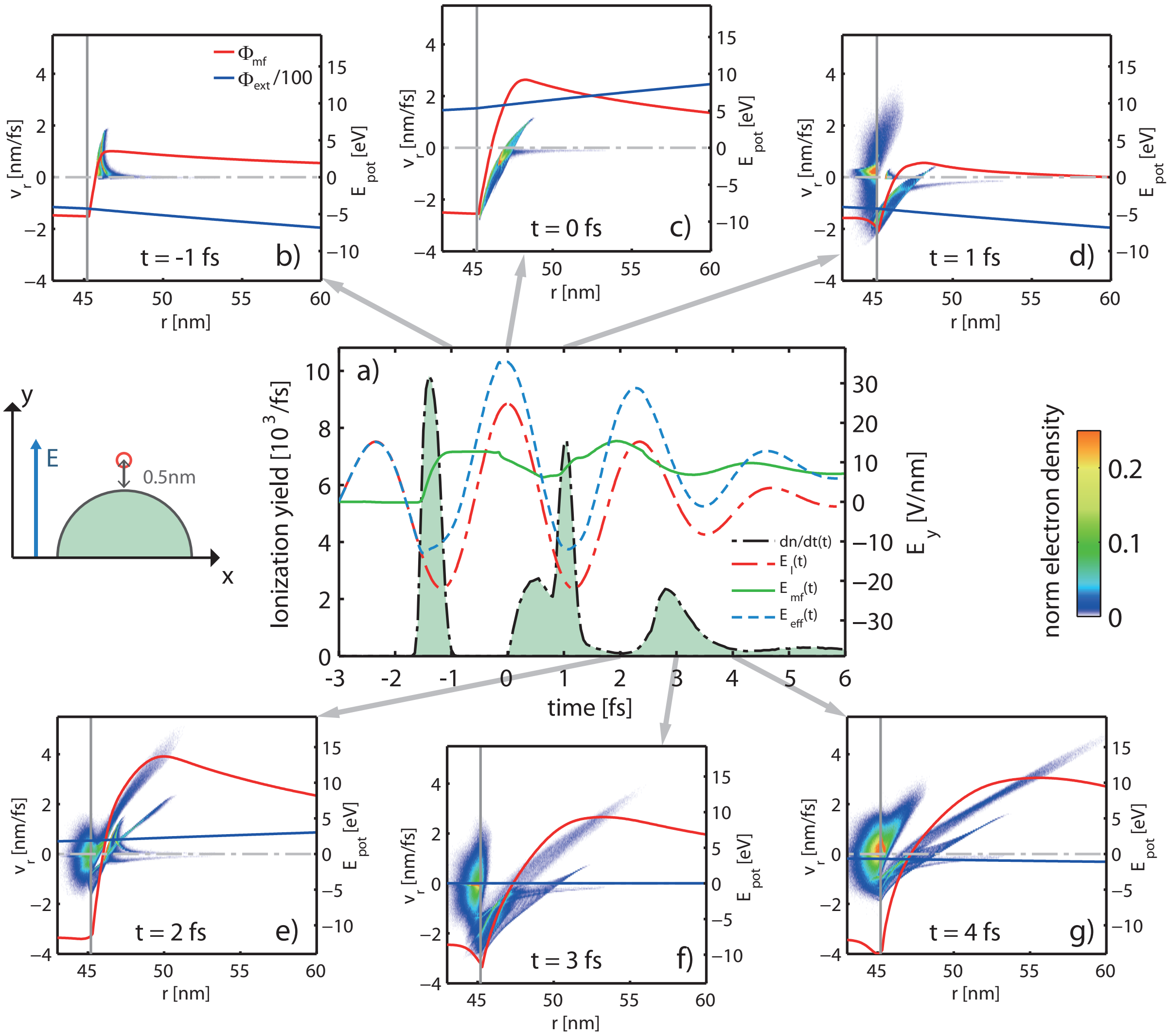

Figure 4.3: Phase space snapshots for simulations of SiO_2 spheres. a) Shows the evolution of the two contributions to the effective radial field sampled 0.5nm outside the pole of the sphere. The red dash-dotted line is the external laser field E_{las}. The solid, green line is the mean-field E_{mf}. The effective field $E_{\text{eff}} = E_{\text{las}} + E_{\text{mf}}$ is shown as dashed blue line. The black dash-dotted line shows the ionization yield per time summed over the full upper half-sphere. b)-g) show snapshot of the electron phase-space distribution for different delay times. The radial velocity v_r and the radial distance r are shown. The grey, vertical line indicates the particle surface. Also the potential induced by the laser field Φ_{ext} (blue line) and the mean-field Φ_{mf} (red line) are plotted. Note that Φ_{ext} is scaled (by 1/100) for better visibility.

into the processes leading to both effects. Figure 4.3 a) shows the evolution of the effective electric field E_{eff} as well as its two contributions E_{las} and E_{mf}. The fields were sampled at $y = R + 0.5\,\text{nm}$, i.e. just outside the pole of the sphere. The intensity is set to $3.5 \times 10^{13}\,\text{W/cm}^2$. The ionization yield from the surface of this half-sphere ($y > 0$) is also shown. The insets b)-g) show snapshots of the phase space distribution in radial direction for selected times. Here the electron motion is projected onto the velocity perpendicular to the sphere surface v_r as well as the distance r to the center. At early times, the effective field follows the laser field as no charges exist. The ionization starts at around $-2\,\text{fs}$. The liberated charges immediately create an electric field opposing the laser field. As this reduces the effective field E_{eff}, the ionization yield is reduced. The free charges are accelerated as can be seen in b) ($t = -1\,\text{fs}$). Now the laser and effective field reverse, thus the charges are accelerated back to the surface ($t = 0\,\text{fs}$). This acceleration is further enhanced by the mean field, which is still at high value. Now, electrons start to penetrate the surface of the sphere and scatter. The penetration of the sphere surface can also be observed in the ionization yield between $t = 0\,\text{fs}$ and $1\,\text{fs}$. The small spike here is caused by impact ionization of the returning electrons. An important observation with respect to the final energy of backscattered electrons is the dramatically enhanced acceleration in the effective field. As can be seen from the potentials shown in Fig. 4.3 c), both laser and mean field accelerate the electron back to the surface leading to a shortened trajectory, earlier recollision and in total a higher final momentum gain. This effect is further supported by the (slight) oscillatory character of the mean field. Because of the temporal dips of the trapping field rescattered electrons can leave the vicinity of the sphere with an effective net gain in momentum. Furthermore, as one can see in d) ($t = 1\,\text{fs}$), the outermost electrons have already passed the peak of the mean field potential, which leads to even further (space-charge like) acceleration. Figures 4.3 e)-g) show the further evolution of the phase phase. One can see that the process is repeating for the next laser cycle. As the laser is now already over its peak, the ionization yield and modulation of the trapping near fields become weaker. Thus, the described acceleration mechanism is less efficient. Also, due to the precedent removal of electrons, any new electron is born into the quite deep potential well of the mean field. This is also illustrated in figure 4.2 b). One can conclude, that the acceleration of rescattered electrons is heavily dependent on the time of birth as not only the laser field but also the mean field shows oscillatory character.

4.4 Comparison to experimental VMI data

VMI experiments were carried out for 95 nm SiO_2 using single-shot VMI. The data was CEP tagged as described in section 3.4 and distributed with a bin size of 18°. Background signal was suppressed by the method described in section 3.4.4. For laser intensities between $1 \times 10^{13}\,\text{W/cm}^2$ and $4 \times 10^{13}\,\text{W/cm}^2$ reliable data could be acquired. At low intensities there is no significant electron emission resulting in poor statistics despite long acquisition times. The limited energy range ($E < 100\,\text{eV}$) of the VMI setup imposes the upper limit.

Figure 4.4 a)-d) shows the VMI projections for four different intensities as presented

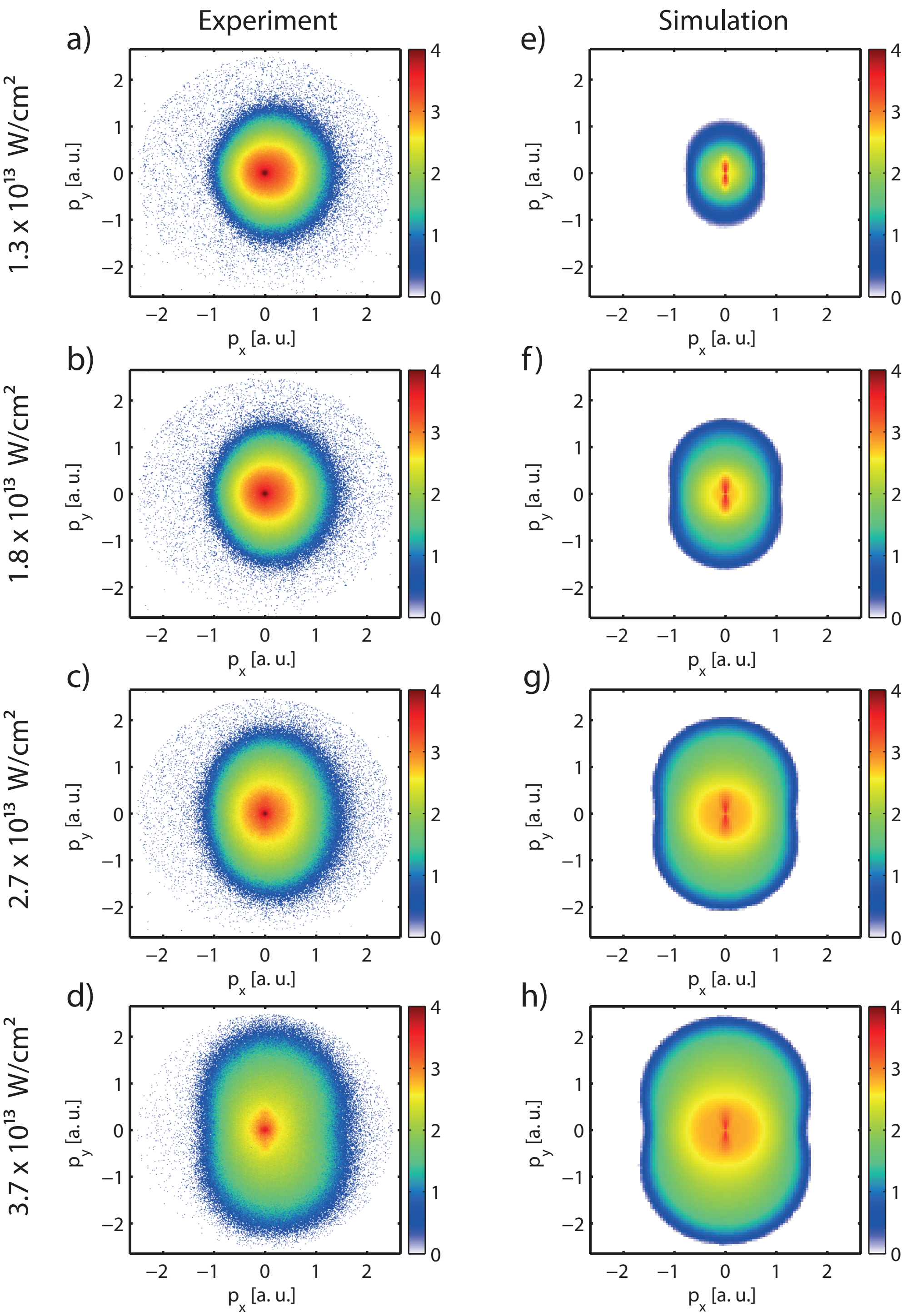

Figure 4.4: a)-d) Experimental VMI projections from 95nm SiO_2 spheres for four different intensities (logarithmic color scale). e)-h) Simulated VMI projections for the same parameters. As shown in [95].

in [95]. For the same intensities VMI projections from simulated data were created and are shown next to the experimental data e)-h). To simplify a direct comparison with the experiment, 2D focus averaging in the focal plane was taken into account by a weighted superposition. Due to the possible asymmetric emission with respect to the laser propagation axis, an inversion as described in section 3.4.3 was not carried out for the measurements for nanoparticles so all p_z are superimposed in the presented data.

The electron momentum maps of the SiO_2 nanospheres have a round to ellipse-like shape. Compared to atomic systems, the distributions are more homogeneous and do not exhibit the usual ATI features. In overall, there is good qualitative agreement between experimental and simulated VMI projections. The cutoff momenta along the laser polarization axis show a value of close to 50 U_p. At low intensities, the experiment shows a higher cutoff along the laser propagation axis resulting in a more round electron emission distribution. This can most likely be attributed to further contributions such as thermal emission from the hot electron gas, which are not included in the simulation model. These additional signals are likely to be most pronounced at low energies [105]. As the trapping potential becomes stronger with higher intensity, thermionic and incoherent emission will be further suppressed and limited to even lower energy regions, which can be observed in the disappearance of the central feature. The unknown magnitude of such secondary processes makes a quantitative comparison of the momentum and energy spectra difficult especially at the lower energies. Both in experiment and theory, the electron momentum distributions become elongated along the laser polarization axis with increasing intensities. This is a direct consequence of the dipolar field enhancement in combination with enhanced rescattering process.

Figure 4.5 shows the radial asymmetry plots, which were derived by equation 3.11. The opening angle θ here is set to 90°. The absolute CEP was determined from a comparison of the Xe reference scan with TDSE simulations. Both experiment and theory show a pronounced phase dependence up to the cutoff momentum. At low momenta, the experimentally observed relative asymmetry is not as strong as in the model calculations. This is to be expected as the additional signals from thermal emission and background ATI are likely to reduce the relative asymmetry. Thermal emission will not show CEP dependency, since the direct correlation between field-driven electron dynamics and electron emission momentum is lost. Background ATI is supposed to show CEP dependence, but it is likely to be phase offset, such that it may partially cancel with the nanoparticle signal. Similarly to atomic ATI, the asymmetry pattern shifts to higher CE phases with increasing momentum p_r of the rescattered electrons. This trend is apparent both in simulation and experiment. The asymmetry pattern is much steeper especially at high momenta as compared to Xe ATI measurements at similar intensities (see Fig. 3.9). Both experimental and theoretical asymmetry amplitudes increase towards the cutoff. The main reason is the decreasing contribution of trajectories with multiple scattering events and different emission times. The superposition of these long trajectories can be expected to be less coherent and thus leads to a decrease in relative asymmetry at lower momenta. Also focus averaging plays a role as for intermediate momenta, the contributions from different intensities and thus different phase offsets are superimposed. In general, the experimentally observed

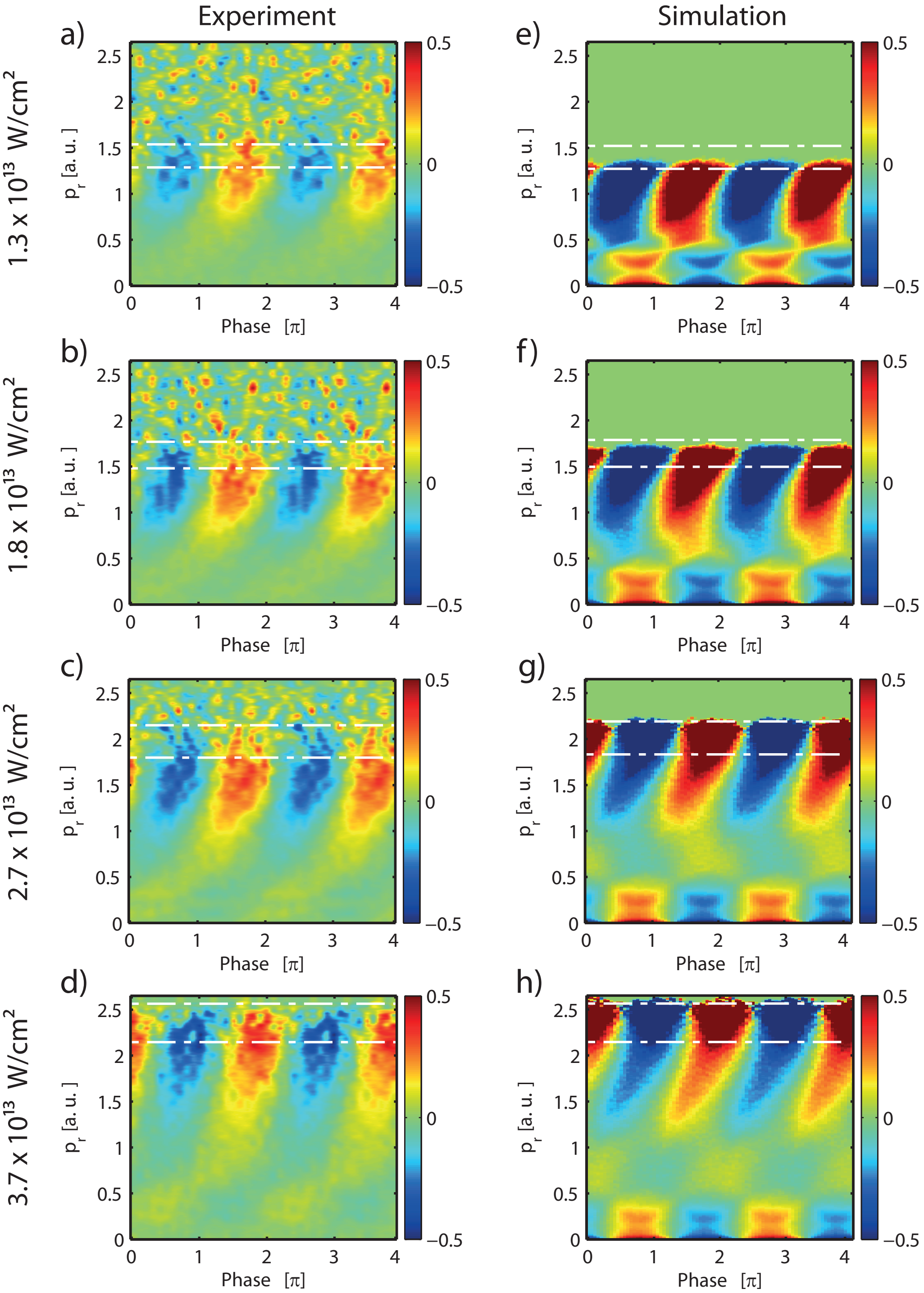

Figure 4.5: a)-d) Experimental radial asymmetry maps of 95 nm SiO_2 nanospheres at four intensities. e-h) Corresponding simulation results. As shown in [95].

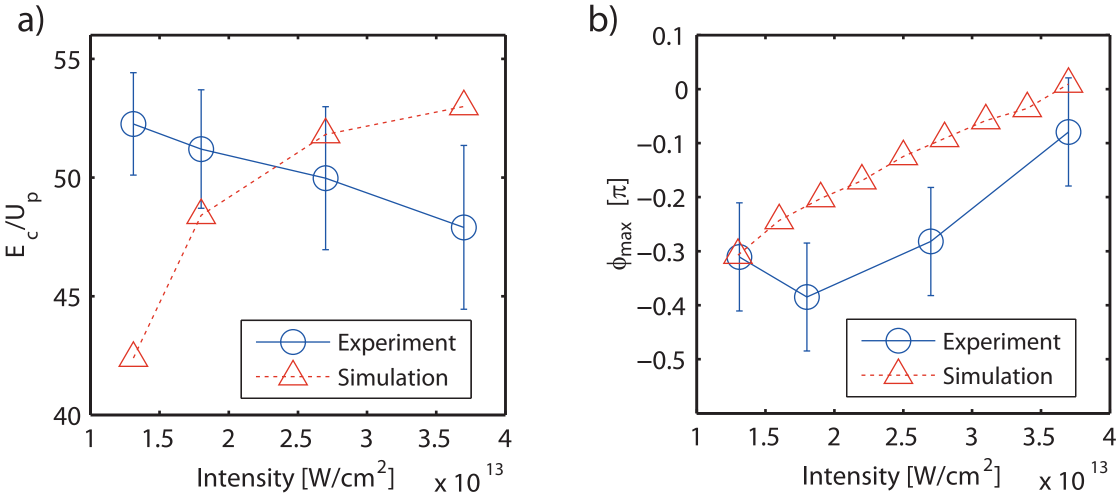

Figure 4.6: a) Cutoff energy divided by the ponderomotive potential plotted against intensity for the scans shown in Fig. 4.4 and 4.5. b) Phase shift in the cutoff region plotted against intensity.

asymmetry amplitude is slightly smaller than in the simulations which might result from additional background signal and dark counts.

Figure 4.6 a) shows the maximum kinetic energy from experiment and simulation. Due to the ambiguous definition of cutoff energy and possible contamination by background signal in the experimental energy spectra, the asymmetry plots were used to determine this value. The experimental curve lies close to 50 U_p with a slight decrease to higher intensities. The simulated data deviates from this especially at low intensities, where it approaches values of only 40 U_p. One possible reason for this deviation is the invalidity of the ionization model, which assumes tunnelling as the principal mechanism. With decreasing intensities approaching $1 \times 10^{13}\,\mathrm{W/cm^2}$, the Keldysh parameter becomes reasonably larger than 1. This implies, that the ADK approximation is not strictly valid, as the tunneling time becomes comparable to the laser period.

Fig. 4.6 b) shows a comparison of the cutoff CEP offset. This was calculated by averaging the asymmetry maps shown in figure 4.5 in the range between 35 and 50 U_p (as indicated by the white dashed lines). The resulting curve was fitted to a shifted cosine function:

$$f(\phi_{\mathrm{cep}}) = f_0 \cos(\phi_{\mathrm{cep}} - \phi_{\mathrm{max}}) \tag{4.8}$$

with f_0 and ϕ_{max} being the free parameters. Both experiment and simulation show an increase of ϕ_{max} with increasing intensity. This corresponds to the asymmetry pattern shifting to the right in figure 4.5. Comparing the magnitude of the shift, there is good agreement. The uncertainty in determining the absolute CEP offset from the Xe reference scan is most probably responsible for the vertical offset between the simulated and experimental data. The positive slope of ϕ_{max} indicates that for a certain half-cycle, electrons are ionized earlier as intensity increases. Due to the timing of the mean field with respect to the electron trajectory, these early born electrons experience the strongest acceleration.

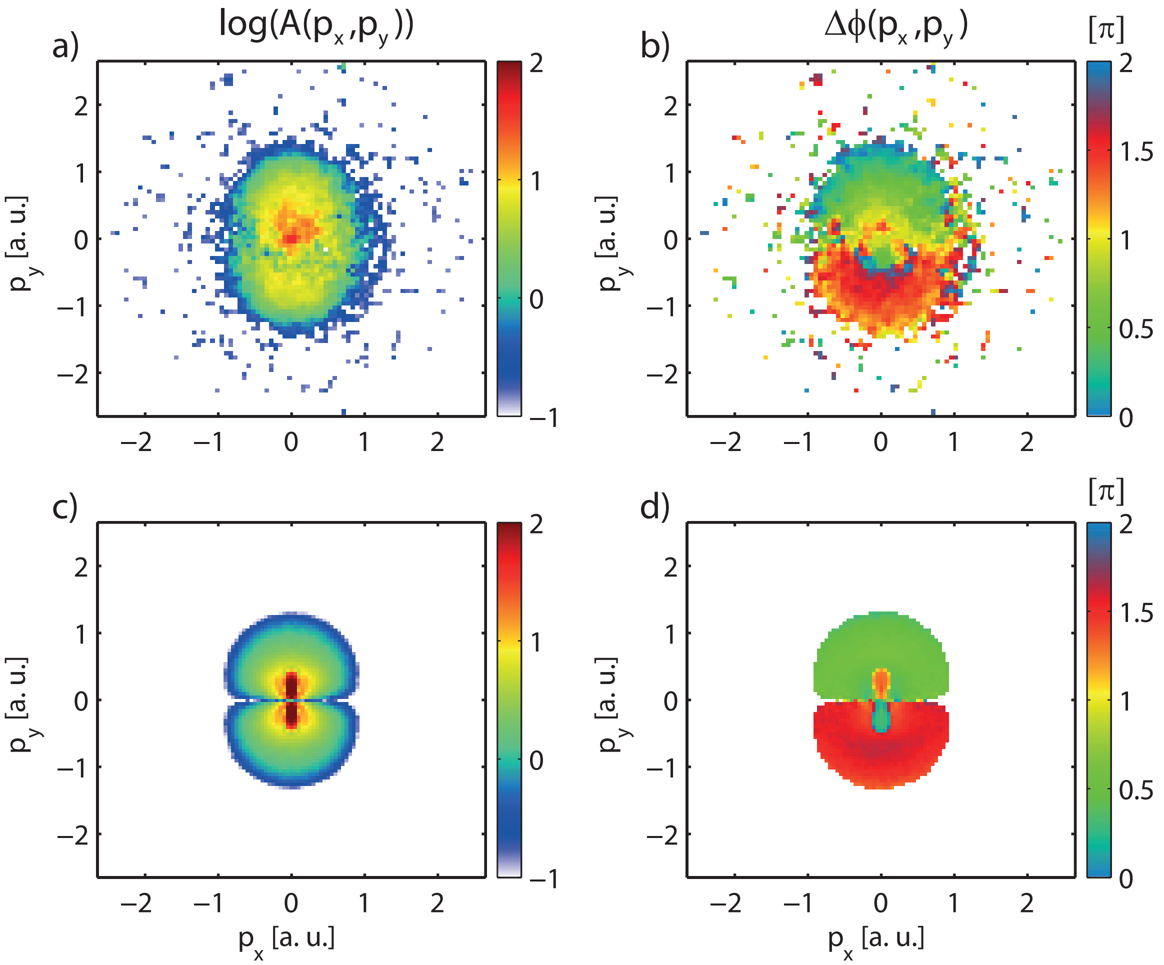

Figure 4.7: Fitted phase dependence of experimental and simulation data of 95 nm SiO_2 nanospheres at an intensity of $1.3 \times 10^{13}\,\mathrm{W/cm^2}$. a) Amplitude $A(p_x, p_y)$ (log color scale) b) Phase offset $\Delta\phi(p_x, p_y)$ of experimental data. c) and d) show the same result for the simulation.

For an even more detailed comparison, the CEP dependent part of the VMI projections were extracted by fitting the data with the harmonic phase dependence given by equation (3.10). Figure 4.8 a) and b) show the fit result of the experimentally observed CEP modulation amplitude $A(p_x, p_y)$ and phase $\Delta\phi(p_x, p_y)$, respectively. The intensity of this scan was $1.3 \times 10^{13}\,\mathrm{W/cm^2}$. In order to have sufficient statistics for the CEP analysis the scans extended over 10^6 laser shots. The experimental data was averaged in bins of 0.061 a.u. side length to increase the signal to noise ratio and visibility. Furthermore, a circular image filter of the same radius was applied. This can be justified, as the features of the nanoparticle electron momentum maps as well as its CEP dependence are usually quite extended. For comparison the fit results of the simulation (focus averaged) are shown in the same figure in c) and d). Again it has to be noted that though the VMI images were filtered to suppress the ATI background, it is still present at lower to intermediate momenta. Consequently, the analysis will focus more on the high energy part.

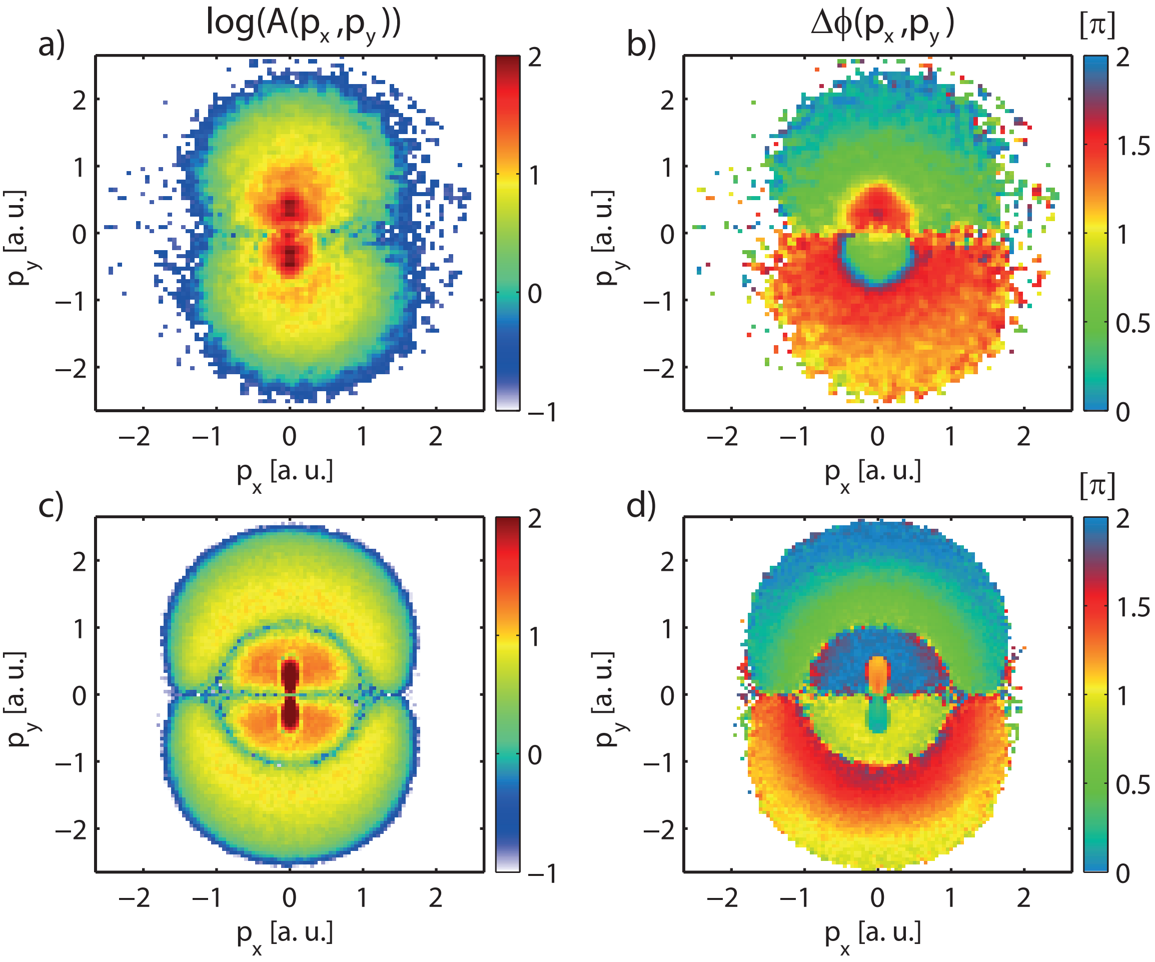

Figure 4.8: Fitted phase dependence of experimental and simulation data of 95 nm SiO_2 nanospheres at an intensity of $3.7 \times 10^{13}\,\mathrm{W/cm^2}$. a) Amplitude $A(p_x, p_y)$ (log color scale) b) Phase offset $\Delta\phi(p_x, p_y)$ of experimental data. c) and d) show the same result for the simulation.

In overall the shape and general trends of experiment and simulation agree well. As compared to the full projected VMI image shown in figure 4.4 a), the asymmetry amplitude at $1.3 \times 10^{13}\,\mathrm{W/cm^2}$ is more smooth. The M^3C simulations show a more pronounced asymmetry at low momenta. The phase shift $\Delta\phi$ jumps by π, when going from negative to positive momenta p_y. This reflects the symmetry of the electron emission with respect to the laser polarization axis. This symmetry also leads to the minimum of $A(p_x, p_y)$ at $p_y = 0$. Even if electrons from one side of the sphere are either accelerated or scattered such that their momentum points to the opposite direction, the two contributions will cancel out.

The same analysis for an intensity of $3.7 \times 10^{13}\,\mathrm{W/cm^2}$ is shown in figure 4.8. Here, one can see that the mentioned effects still persist and also become more apparent in the experimental data. Especially, the shape of the asymmetry amplitude resembles a lemniscate (two lobe structure). Such a behavior is known from ATI in gases [104]. In the simple men's model, the circular features arise as a direct consequence of the two acceleration stages: Emitted electrons are accelerated and gain a momentum Δp_1 before recollision. The scattering at the atomic potential is assumed to be isotropic, so Δp_1 can now be oriented in any direction. Additional acceleration Δp_2 after the scattering event occurs mostly into the p_y direction. The momentum maps thus exhibit two circular features with a radius of Δp_1 shifted to the origin by $\pm\Delta p_2$ along the p_y axis.

Such a simple explanation holds in parts true for the SiO_2 dynamics. Due to the high non-linearity of the emission process most electrons are created at the poles of the nanosphere as the field enhancement peaks here. At the poles both the laser and Coulomb field are perpendicular to the surface. A fundamental difference is that scattering is not isotropic. Also contributions from other parts of the sphere have to be considered. Under large angles from the poles, the laser field has a significant component parallel to the surface while scattering happens symmetric with respect to the surface normal. This will lead to a pronounced broadening of the observed features.

4.5 Propagation effects at large SiO_2 nanospheres

4.5.1 Spatial reconstruction of the near-fields

It will now be investigated to what extend the VMI projections carry signatures of the near-field distribution around the sphere. Such an analysis has to focus on the question to what extend the features observed in momentum space can be traced back to the birth positions. Figure 4.9 a) illustrates the important parameters in the rescattering process. For simplicity only the $z = 0$ and $p_z = 0$ plane is considered. The birth angle θ_b is the angle between propagation axis and emission position of the electron. After the electron has returned to the surface it will scatter at a position given by θ_s. The maximum excursion of the electron during a single field oscillation is typically less than 5 nm, such that the point where it penetrates the sphere will lie close to the emission point. One can thus assume that $\theta_\mathrm{s} \approx \theta_\mathrm{b}$. After backscattering the electron will leave the sphere under an angle γ which is defined relative to the surface normal. Scattering must of course take place out of the surface, efficiently limiting the possible values of γ to a maximum of 90°. Due to the non-zero mean free path in the nanoparticle, the distributions of γ will be further non-isotropic with a preference for the radial direction. A third contribution that leads to a narrowing of the backscattering is the mean field. Only trajectories with a sufficiently small γ can leave the sphere. If γ is too large, the trajectory will be captured by the attractive trapping field resulting in further surface collisions and therefore loss of final

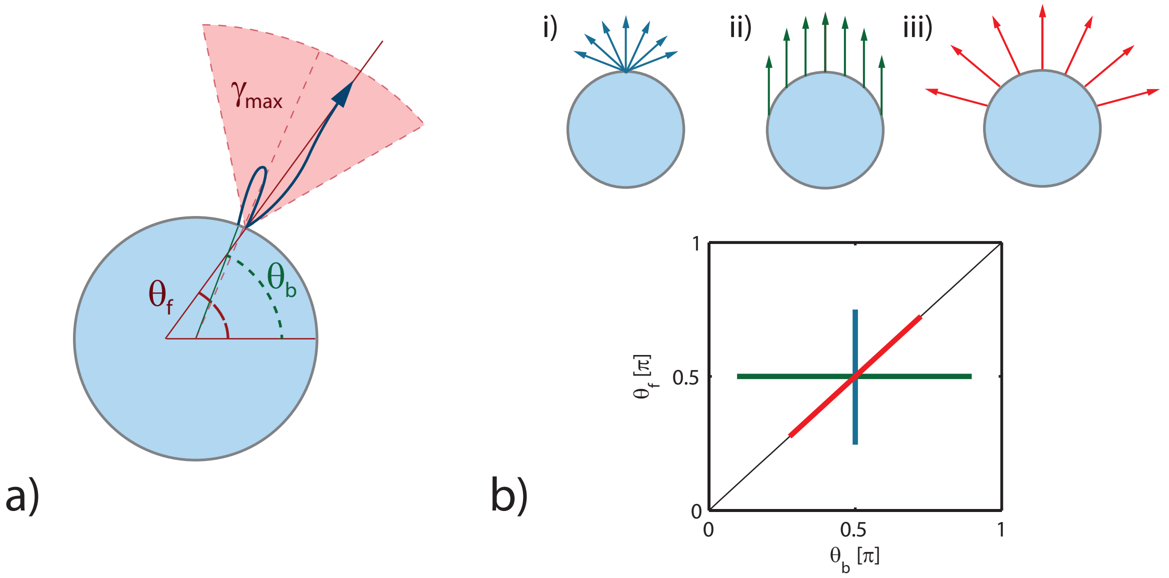

Figure 4.9: a) Illustration of the important angles involved in the rescattering process. The electron is ionized at θ_b, rescattered under an angle γ to the surface normal and detected under a final angle θ_f. b) Three particular natures of the overall photoemission from the sphere. i) uni-directional from a single emission position ii) emission from all positions in a single direction iii) emission normal to the surface. The three emission patterns show a different characteristic relation between θ_b and θ_f as indicated in the lower plot (Courtesy of L. Seiffert).

momentum and coherence.

After rescattering the electron will be further accelerated and hit the detector. The direction and magnitude of the final velocity will determine the electron's position on the detector. The hit angle is also defined with respect to the positive laser propagation axis and denoted as θ_{f}. For a single trajectory, θ_{f} can be decomposed into the three distinct processes of emission θ_{b}, rescattering γ and post-collision acceleration β:

$$\theta_{\mathrm{f}} = \theta_{\mathrm{b}} + \gamma + \beta \tag{4.9}$$

The final distribution of θ_{f} for a given birth position is determined mostly by the spread of γ. The additional acceleration by β will lead to a distortion and bending towards the laser polarization axis.

Figure (4.9) b) illustrates some special cases in the relation between θ_{f} and θ_{b}, which will exhibit distinctive features when projecting the distribution of emitted electrons on θ_{f} and θ_{b}.

1. Emission takes place at a single position but with a large distribution of rescattering angles γ. This will create a vertical feature in the correlation plot (blue line).

2. An extended emission for multiple birth positions into one single direction, will appear as a horizontal feature (green line).
3. Electrons emitted from different birth positions have a unique final angle θ_f. The special case $\theta_\mathrm{f} = \theta_\mathrm{b}$ results in the red line.

It is obvious that for case 3) the velocity-map image will contain information about the local field evolution. For such a case, a local reconstruction of e.g. field strength, mean field strength and phase should be possible.

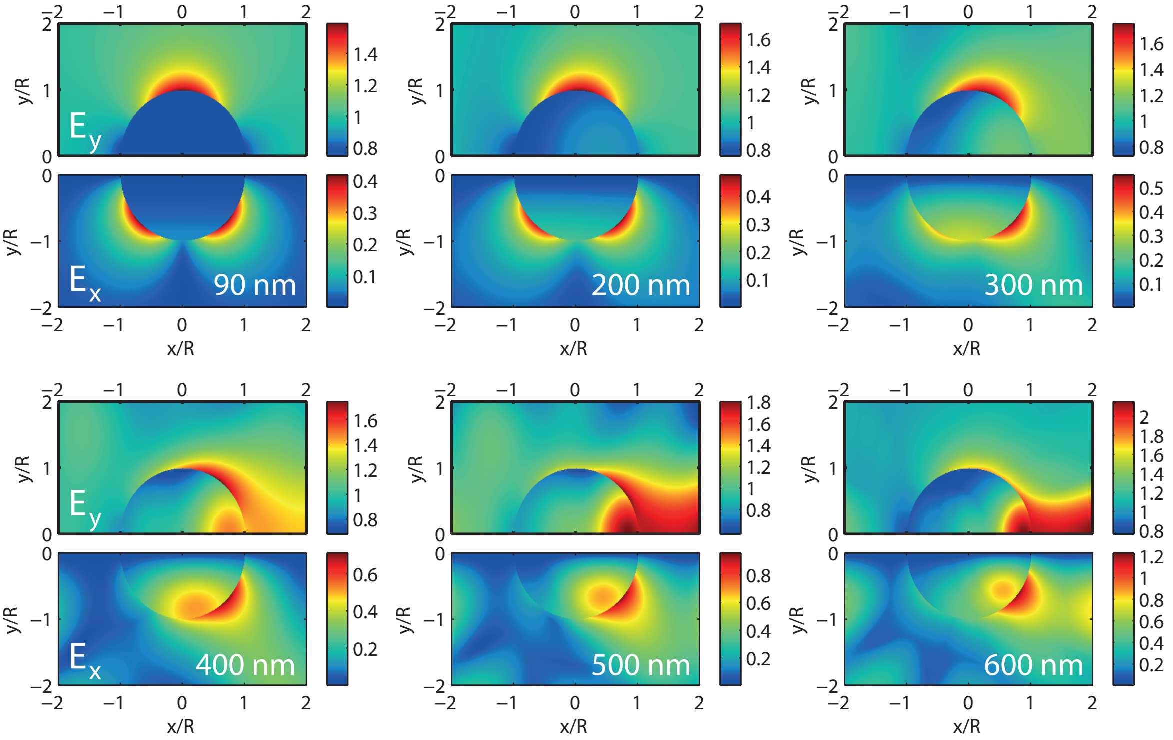

Figure 4.10: Maximum, relative field enhancement maps for SiO_2 for various diameters calculated by Mie theory. For each size the upper plot shows the E_y component (laser polarization axis) while the lower plot shows the E_x component (laser propagation axis).

4.5.2 Field distribution at large SiO_2 nanospheres

A system with a known field inhomogeneity would represent an ideal test system to unambiguously identify the strength and character of the correlation between birth and detection angle. One possibility would be to use asymmetric system like nanocylinders but this is experimentally challenging as such particles would need to be aligned with great precision. Fortunately, a very simple solution is to use SiO_2 spheres with larger sizes.

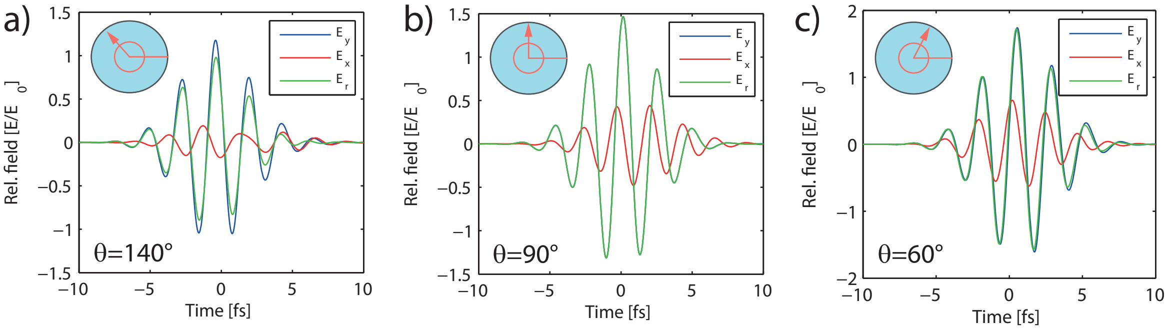

Figure 4.11: Electric field transients at different positions of the sphere.

As explained in 2.1.5, for sphere diameters exceeding 100 nm, the dipole approximation is not valid any more. Now, Mie theory has to be employed to calculate the electric near-fields. Figure 4.10 shows the maximum field relative to the incident field for various sizes for a 4.5 fs pulse. Both E_x (polarization axis) and E_y (propagation axis) components are shown. For 95 nm, the E_y field is as expected from a dipole symmetric with respect to the $x = 0$ axis both for the E_x and E_y component. At around 200 nm, the E_y field distribution is slightly bent in positive x-direction. This effect grows stronger for larger spheres. Also E_x shows a noticeable asymmetry. For sphere diameters beyond 550 nm, the maximum field enhancement can be found on the rear side of the sphere. From such sizes on, the nanosphere efficiently behaves like a miniature lens [106]. Besides the asymmetry in the field distributions, one also observes an increase in field enhancement from about 1.5 for 95 nm to 1.9 for 400 nm. This increase is even stronger pronounced for the E_x component. It has to be noted that the phase relation between E_x and E_y is strongly dependent on position.

Another important aspect are dispersive effects imprinted on the temporal evolution. These do not result from the material properties (dispersion) but have a geometric origin. For large spheres (above 300 nm), the small wavelength components of the laser field are comparable to the particle diameter (see the experimental laser spectrum in Fig. 3.2). As the laser pulse spectrum extends over a whole octave the scattered fields of the spectral components will strongly differ both in amplitude and phase. When reconstructing the temporal field evolution for different points on the surface, an effective change of the carrier-envelope phase is noticeable. Figure 4.11 shows the temporal evolution of the electric field on different positions on the sphere. E_x, E_y and the radial field component $E_r = \sin\theta E_y - \cos\theta E_x$ are shown. The CEP of the incident pulse was set to $\phi_{\mathrm{ce}} = 0$. On the front side of the sphere ($\theta = 140°$), there is an effectively negative local CEP. At the pole of the sphere ($\theta = 90°$) the radial field is of course equal to E_y. Here the effective CEP is still slightly negative. On the position of maximum field enhancement of E_y ($\theta = 60°$), E_x also noticeably grows. Nevertheless, E_r is mostly dominated by the E_y-component. On this side of the sphere the CEP changes to positive values. Comparing all three positions, one finds that the pulse is not noticeable prolonged such that CEP effects should be as pronounced as in the measurements on small SiO$_2$ spheres. The local variations in the effective CEP due to the propagation effects should be apparent in the $\Delta\phi$ phase offset maps.

4.5.3 Size-dependent VMI data

To confirm whether the predicted asymmetry can be observed experimentally, VMI measurements were taken for sphere sizes of 95, 188, 313, 400 and 550 nm. The acquisition times were chosen such that a reconstruction of the CEP asymmetry amplitude and phase offset maps could be obtained. As the aerodynamic lens is designed to give best performance at 100 nm particle size a strong decrease in efficiency could be observed for larger sizes. Thus acquisition times had to be prolonged to about 10^7 laser shots. Figure 4.12 shows the full VMI projections (left column) and CEP-modulation amplitude maps $A(p_x, p_y)$ (right column) for a number of sphere diameters. The result for $d = 95\,\mathrm{nm}$ ($I = 3.7 \times 10^{13}\,\mathrm{W/cm^2}$) are presented in a) and b). The corresponding maps for 188 nm diameter ($I = 4.6 \times 10^{13}\,\mathrm{W/cm^2}$) are shown in c) and d). Note, that (in this particular data set) the vertical feature close to the origin results from a worn-out MCP. The shape of $A(p_x, p_y)$ is as expected similar to the 95 nm results without a noticeable asymmetry around $p_x = 0$. Figure 4.12 e) and f) show the results for $d = 313\,\mathrm{nm}$ for an intensity of $I = 2.7 \times 10^{13}\,\mathrm{W/cm^2}$. Here a bending of the momentum distribution towards the laser propagation axis can be observed. This distortion is even more obvious in the modulation map. As can be seen in g) and h) the asymmetry with respect to $p_x = 0$ further grows for $d = 400\,\mathrm{nm}$ ($I = 2.8 \times 10^{13}\,\mathrm{W/cm^2}$). Scans at lower intensities were also taken. These are not shown here, but it can be noted that they exhibit a very similar change in distribution with increasing sphere size as in Fig. 4.12. Very similar to the observation made in section 4.4, the modulation and phase maps acquired at low intensity are more homogeneous and the lemniscate features (two lobe structure) are not as pronounced as compared to the high intensity scans.

The experimental modulation amplitude and phase offset for the 400 nm sphere ($I = 2.8 \times 10^{13}\,\mathrm{W/cm^2}$) are shown in figure 4.13 a) and b), respectively. Besides the tilt to positive p_x direction in the modulation map, the phase shift $\Delta\phi$ also exhibits a pronounced asymmetry. For a given radius one observes an increase in $\Delta\phi$ when going from the front to the back side. Simulations by the M^{3}C model were performed using mean field multipole expansion up to the 10th order and $n_{\max} = 4$ Mie coefficients for the same peak intensity with focal averaging. The results are shown in Fig. 4.13 c) and d). Comparing the overall distribution there is good agreement both in shape and relative magnitudes especially for the amplitude map. The simulated data exhibit a very similar asymmetry towards the laser propagation axis. The phase shift maps $\Delta\phi$ show some deviations at low momenta where the simulated map have a slightly different profile when going from the center to the cutoff. This might be attributed to a too coarse focus averaging in the simulations. To quantify the agreement between experiment and simulation model, the phase shift $\Delta\phi$ was evaluated in the cutoff region. A mask was created from the modulation amplitude map accepting 1 to 4 % of the peak modulation. This mask is shown in e) for the experimental data. In Fig. 4.13 f), the phase shift $\Delta\phi$ is plotted against its angle to the origin (equivalent

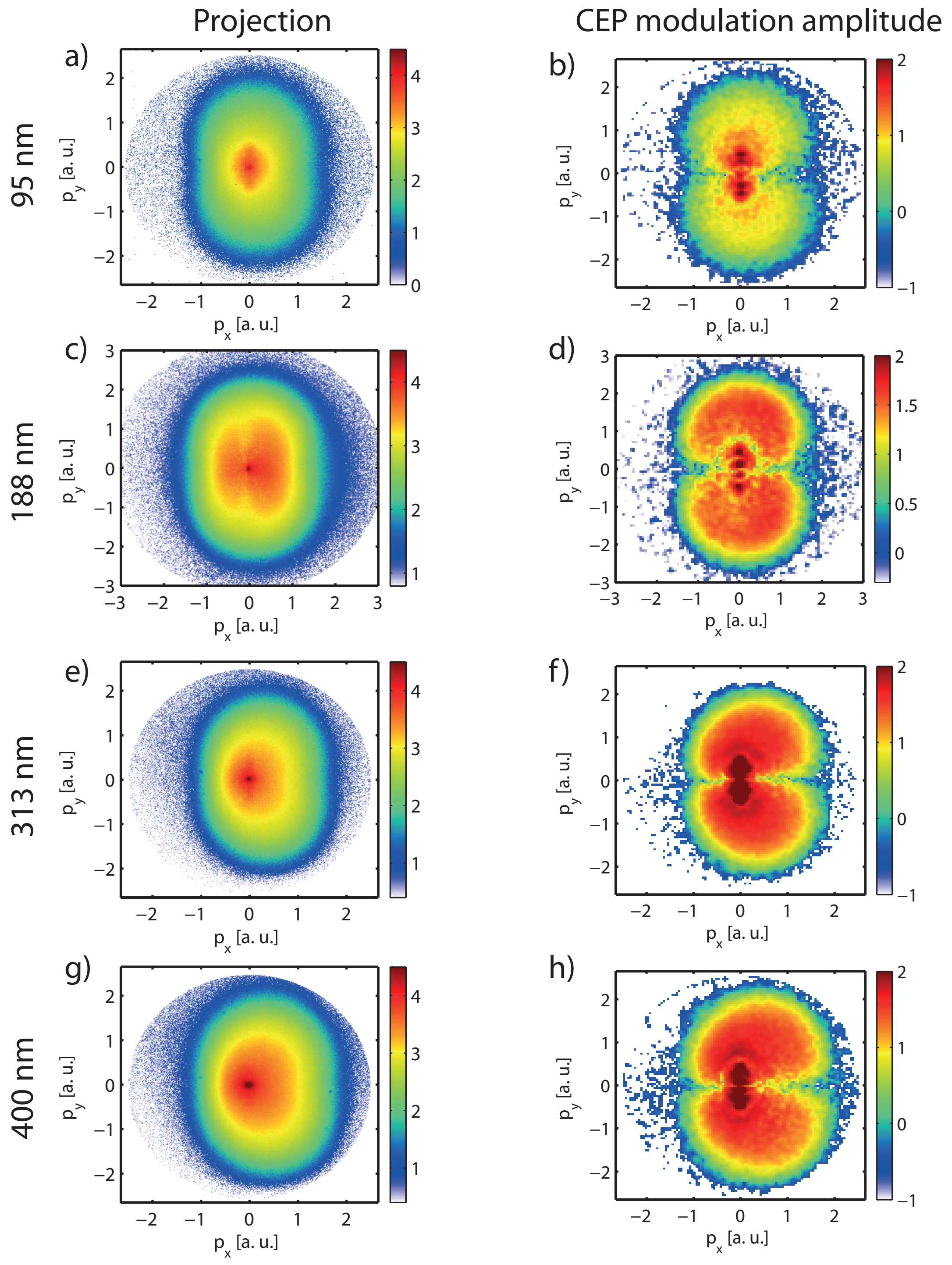

Figure 4.12: VMI projections (left column) and CEP modulation amplitudes (right column) for SiO_2 spheres of different diameters. a), b) 95 nm at $3.7 \times 10^{13}\,\mathrm{W/cm^2}$. c), d) 188 nm at $4.6 \times 10^{13}\,\mathrm{W/cm^2}$. e), f) 313 nm at $2.8 \times 10^{13}\,\mathrm{W/cm^2}$. g), h) 400 nm at $2.8 \times 10^{13}\,\mathrm{W/cm^2}$.

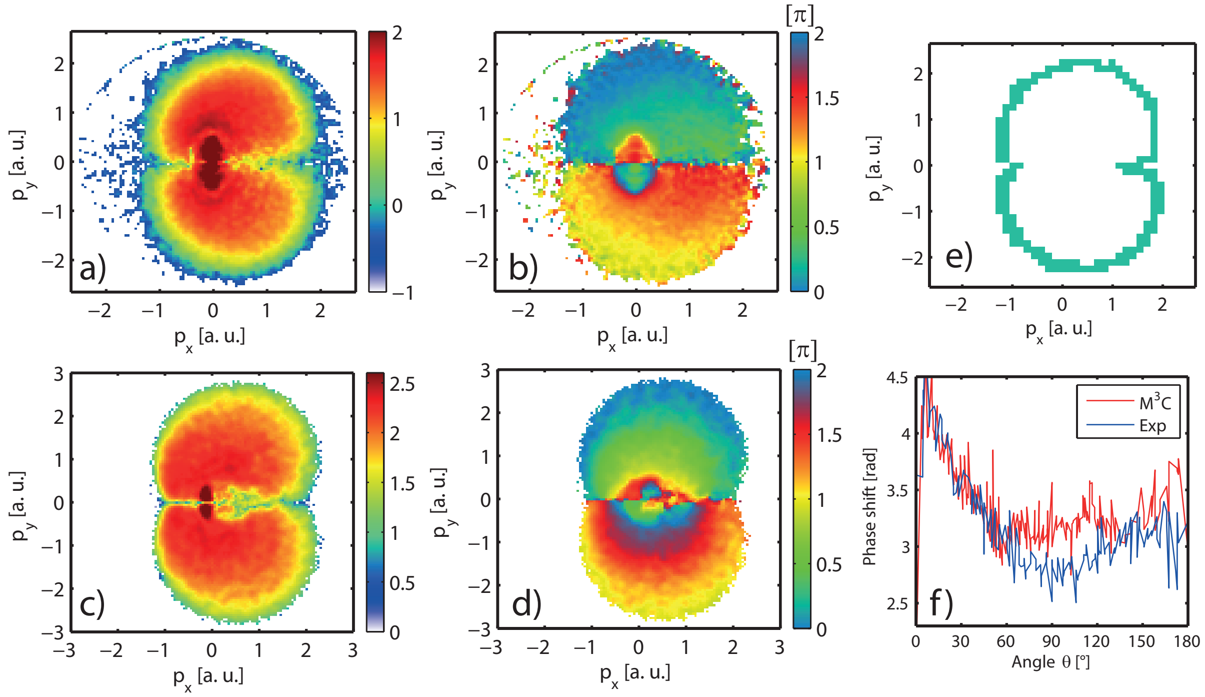

Figure 4.13: a),b) CEP modulation amplitude $A(p_x, p_y)$ (logarithmic color scale) and phase shift $\Delta\phi$ for $d = 400\,\mathrm{nm}$ at $2.8 \times 10^{13}\,\mathrm{W/cm^2}$, respectively. c,d) Results from M^{3}C simulation with a peak intensity of $3 \times 10^{13}\,\mathrm{W/cm^2}$. e) Filter mask for the cutoff momentum part. f) Phase shift in the cutoff region for the experimental (blue line) and simulated data (red line).

to θ_f) for all points that lie within the cutoff mask. The same was done for the simulated data. The M^{3}C result agrees very well with the experimental data. Only in the region around 90° the simulated $\Delta\phi$ deviates from the experimental data by about 0.4 rad. To some extent this asymmetric phase offset is caused by the propagation effects (shown in Fig. 4.11), which lead to a constant variation of the effective laser CEP over the sphere surface. Furthermore, as was described in section 4.4 also the rescattering/acceleration process exhibits an intensity dependent phase offset. One can therefore conclude that the data shown in Fig. 4.13 f) contains a superposition of these two local effects on the surface convoluted with the scattering angle distribution.

4.5.4 Correlation analysis and reconstruction of field profiles

The good agreement between experiment and M^{3}C model both for large and small spheres motivates a further analysis of the correlation between of birth angle θ_b and final detection angle θ_f. As the birth position and the final velocity is known for all trajectories a direct comparison is very easily obtained from the simulations. In Fig. 4.14 the distributions of

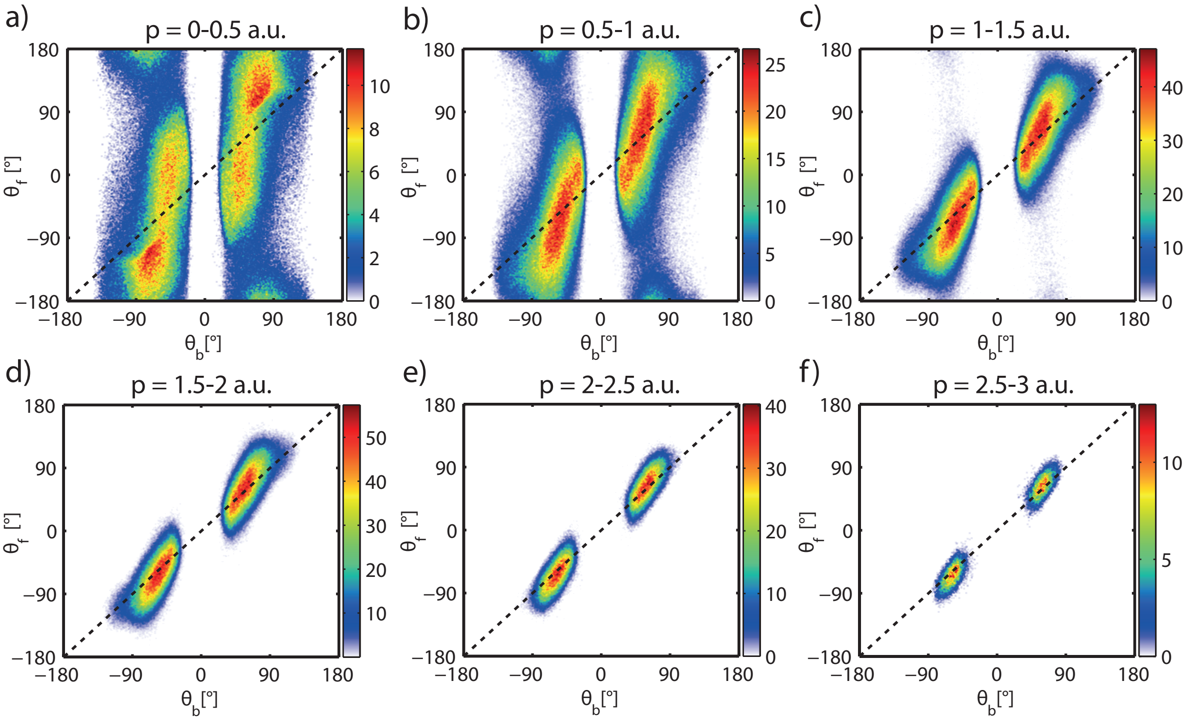

Figure 4.14: Correlation of birth θ_b and detection angles θ_f for a 400 nm SiO$_2$ nanosphere at peak intensity of 3×10^{13} W/cm^2 including focus averaging. The electron distributions were filtered with respect to the final momentum. a) $0-0.5$ a.u., b) $0.5-1$ a.u., c) $1-1.5$ a.u., d) $1.5-2$ a.u., e) $2-2.5$ a.u. and f) $2.5-3$ a.u..

emitted electrons are plotted as a function of birth angle θ_b and final momentum angle θ_f for different final momentum regions. The data is focus averaged with a peak intensity of 3×10^{13} W/cm^2 and the sphere size was chosen to be 400 nm. One can see in a) and b), that low energetic electrons ($p < 1$ a.u.) are mostly emitted at regions of high field enhancement located at the back of the sphere, while the final angle is almost homogeneously distributed. This is similar to case 1) in figure (4.9). It was found, that low intensities contribute stronger to the broad distribution of final angles, which results from a less efficient filtering of rescattering angles γ by the Coulomb mean field. For increasing electron momentum, the correlation between birth and final angle becomes stronger. From 4.14 e) and f), it can be concluded that for momenta above 2 a.u., the distributions of birth and final angles are very similar both in position as well as width. The characteristics are here very similar to case 3) in figure (4.9), i.e. a direct mapping of birth and detection angle $\theta_b \approx \theta_f$.

These findings indicate that the reconstruction of field profiles should be possible, when only the highest energetic electrons in the respective emission directions are used. The error should be further minimized when considering only the center of mass of the distributions. To test this assumption, the experimental data was now used to determine the angle of maximum field enhancement. From the previously made conclusion the angle under which the maximum momentum can be observed should well coincide with the birth angle of these electrons. The modulation maps were converted to polar coordinates. Fig. 4.15 shows these plots for the 95 nm and 400 nm data. The center of mass angle is indicated by the black, dotted line. The cutoff momentum p_c was determined manually. The angle θ_{com} was determined by calculating the center of mass of the modulation map averaged between $0.8p_c$ and p_c. The resulting center-of-mass angles θ_{com} for the different sphere sizes are plotted in figure 4.16 a). The M^{3}C prediction for various sizes is also shown (green triangles) along with the angles of maximum radial field enhancement that were calculated by Mie theory (red line). In overall, one can see good agreement. For smaller sphere sizes the experimentally observed θ_{com} is lower than the Mie prediction. Including radiation pressure effects by the magnetic field components in the M^{3}C simulations and increasing the number of multipole moments to $l = 10$ reproduces this behavior. The field enhancement factors were also qualitatively obtained from the experimental data. To do so the cutoff energies at θ_{com} were rescaled assuming a linear dependence on laser intensity of $E_c = 50U_p$. The data point at 95 nm was assumed to lie on the curve given by Mie theory and serves as a normalization for the other sizes. An increase of the relative field enhancement with sphere size is clearly visible. The error bars reflect errors in intensity calibration and cutoff determination. Within these margins, there is good agreement with Mie theory.

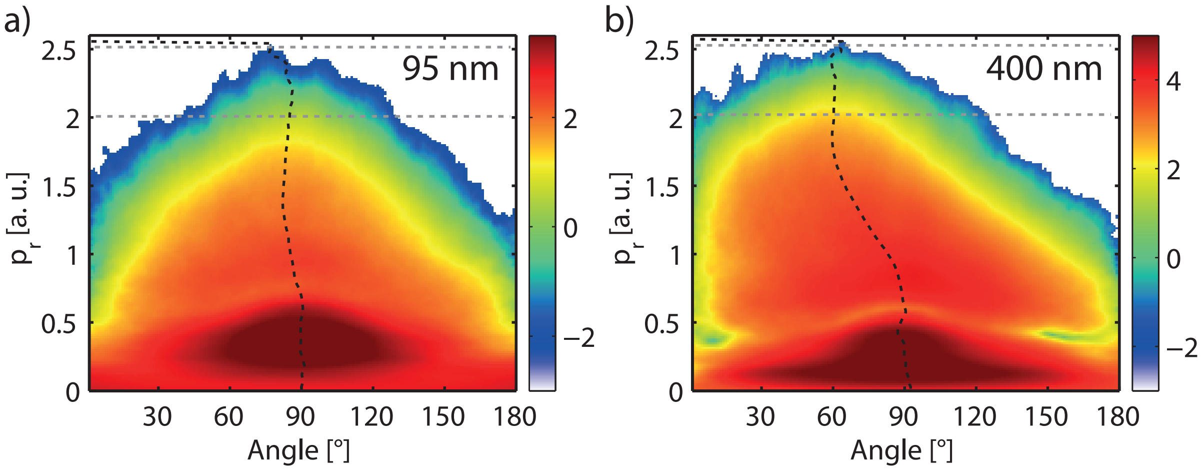

Figure 4.15: Plot of the modulation amplitude in polar coordinates $A(p_r, \theta)$ for a) 95 nm at 3.7×10^{13} W/cm^2 and b) for 400 nm at 2.8×10^{13} W/cm^2. The black, dotted line represents the center-of-mass angle θ_{com} as a function of radial momentum. The grey, dotted lines indicate the region from $0.8p_c$ to p_c used for obtaining the averaged center-of-mass angles.

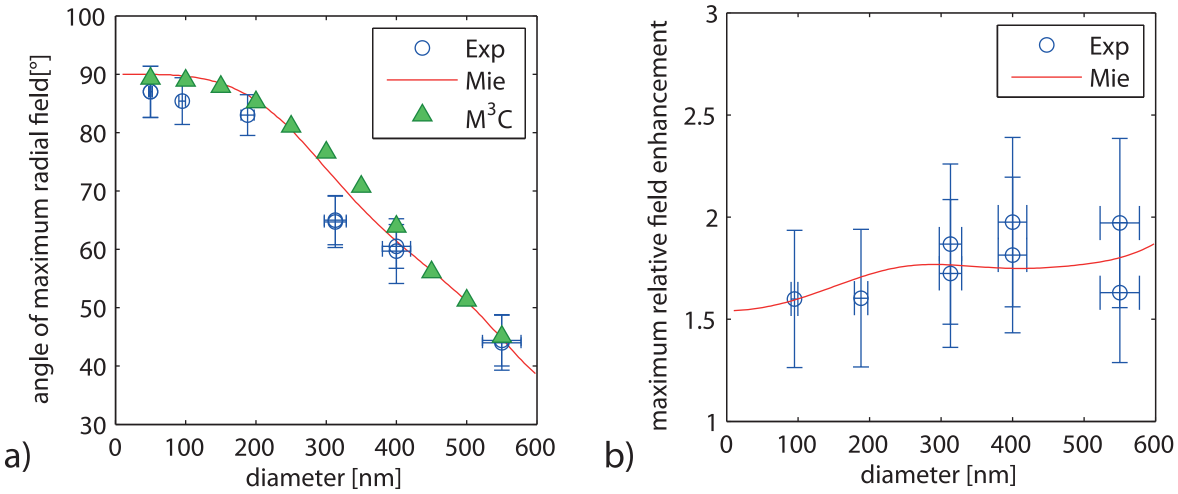

Figure 4.16: a) Comparison of θ_{com} (center of mass obtained between 0.8 p_c - p_c) with the angle of maximum field θ_{mie} enhancement as obtained by Mie theory. b) Retrieved field enhancement values.

4.6 Conclusions and outlook

The presented experimental results illustrate that the ionization dynamics of dielectric nanoparticles is strongly dependent on the driving laser field. Electrons can efficiently be controlled by means of the carrier-envelope phase. It could be shown that charge interaction is highly time-dependent for such short driving fields. The mean field was identified as an additional acceleration mechanism leading to an increase in final kinetic energies of emitted electrons. The full potential of the VMI technique is revealed especially when investigating isolated SiO_2 nanospheres as it provides high signal-to-noise ratio and means to suppress background signal. In combination with phase-tagging, the full CEP dependence can easily be obtained even for long acquisition times. The strong CEP dependence of SiO_2 nanosystems gives the possibility to focus the analysis on the CEP dependent portion of the signal. This has the advantage that any detector background and thermal emission is not taken into account. Only the dynamics of the rescattered electrons remain, which carry strong signatures of the field transient they were accelerated by. The huge amount of information contained in the velocity map images for a single measurements makes it possible to image the propagation effects of the laser field which lead to a pronounced asymmetry in the observed momentum distributions. The analysis of M^{3}C simulations indicate that there is a strong correlation between momentum and real space for the highest energetic electrons at the intensities under consideration.

More insight into the interplay between ionization dynamics and near-field acceleration might be obtained by using tailored light fields [107]. For such an approach, further technical progress such as an increased nanoparticle density will result in a considerably shortened acquisition times. These developments might also help to overcome the lack of full 3D momentum information, e.g. by multiple rotating the laser polarization and appropriate inverting algorithms. This will enable the complete reconstruction of the near fields in time and space. From there on, non-spherical system can be studied given they can be orientated in the interaction volume with the necessary precision.

Chapter 5

Nonlinear regime of photoemission near optical breakdown

The experiments presented in the previous chapter focused on a moderate intensity regime. Here, the system can be still be assumed to be unperturbed at least for the duration of the few-cycle laser pulse, i.e. the optical properties are not altered. Above a certain intensity this situation is likely to change and the large number of ionized electrons inside the sphere will also alter its optical response.

The field of optical breakdown has been studied extensively with respect to laser ablation and the damage thresholds of bulk dielectrics. For laser pulse lengths above 20 ps the melting process directly follows the deposition of energy, while for sub-picosecond laser pulses the coupling of the hot electron system to the lattice is too slow such that the scaling of damage fluence differs for short pulses [48]. The now very local distribution of energy leads to a local Coulomb explosion of ions (laser ablation). The creation of free electrons is attributed mainly to avalanche ionization for pulses longer than 100 fs [48, 29]. A further study by Lenzner *et al.* employed pulse lengths down to 5 fs [47]. It was found that for such short pulses the ionization process is not dominated by the avalanche process any more, but rather by multi-photon and tunnel ionization and peak intensities exceeding $10^{14}\,\mathrm{W/cm^2}$ are necessary to induce optical breakdown.

As the measurement of ablation depths and efficiencies is a rather indirect method, it is desirable to have a more direct experimental access to the processes involving charge carrier creation. Recently, Schultze *et al.* could observe a reversible 10 % increase of the XUV transmittance through a bulk SiO_2 sample at an NIR field strength of $2.5\,\mathrm{V\AA^{-1}}$ [108]. At very similar intensities, Schiffrin *et al.* could measure a CEP dependent current across a bulk SiO_2 sample [19]. It was concluded that charge carrier injection happens on a time scale shorter than an optical half-cycle.

To extend the photoemission studies to intensities above the thresholds for optical breakdown, experiments using the stereo time-of-flight apparatus in conjunction with the phasemeter were carried out. The data gathered with this technique of course offers much less information as compared to VMI. Nevertheless, the energy spectra and its CEP dependence offers first insight into a now even higher complex sub-cycle dynamics. Here, one

Nr.	Material	Diameter	Size distribution	ϵ_r'	ϵ_r''	α	Δ_g [eV] (direct)
2	SiO_2	95 nm	$< 5\%$	2.12 [97]	≈ 0	1.5	9 [96]
4	ZrO_2	60 nm	$\approx 20\%$	4.6 [109]	≈ 0	2.1	3.65 [110]
3	TiO_2	60 nm	$\approx 20\%$	6.47 [111]	≈ 0	2.3	3.7 [112]
5	Si	60 nm	$\approx 20\%$	14.2 [113]	0.08	2.63	3.42
6	Au	15 nm	$> 25\%$	-17.9 [22]	1.12	3.4	-

Table 5.1: List of samples used for the STOF experiments.

major advantage of studying isolated nanoparticles delivered by the aerodynamic lens is apparent. As the sample is always refreshed between consecutive laser shots, damage to the sample does not have to be considered unlike studies in bulk samples.

5.1 STOF measurements

5.1.1 Samples

A list of the samples used for the STOF experiments is shown in table 5.1.1. The same 95 nm SiO_2 sample as for the VMI experiments was used. Furthermore a variety of other materials with different band gaps and dielectric constants were used. The ZrO_2 , TiO_2 and Si samples were obtained by a commercial supplier (Particular GmbH, Hannover). For these samples, the size deviation was around 20% as communicated by the manufacturer. As the fabrication of large Au spheres requires several filtering steps which is tedious and expensive for large quantities, a sample with an average diameter of 16 nm was prepared by the group of Prof. Feldmann (LMU, München).

The index of refraction and the (direct) band gaps Δ_g are also listed in table 5.1.1. The field enhancement at the sphere poles can be calculated by the dipole approximation (2.23) as $\alpha = 1 + (\epsilon_r - 1)/(\epsilon_r + 2)$. The field enhancement varies from around 1.5 for SiO_2 to 3.4 for the Au particles.

5.1.2 Intensity dependence of spectral cutoffs

Measurements with the nanoparticles were carried out using the stereo time-of-flight spectrometer described in section 3.5 and CEP tagging. Figure 5.1 a) shows electron energy spectra for various intensities for 95 nm SiO_2 nanospheres. Each scan typically extended over 10^6 laser shots. In the figure, the sum of all CEPs and both detectors is shown. The intensity was calibrated using an ATI background gas scan with exactly the same filter wheel setting acquired in direct consecution.

For the 95 nm SiO_2 spheres, the spectra show a strong signal at low energies which is mostly composed of ATI from background gas. As in the VMI experiments, the signal at high energies exclusively originates from nanoparticles. The rescattered electron signal shows an exponential-like distribution up to the cutoff. The shape does not change

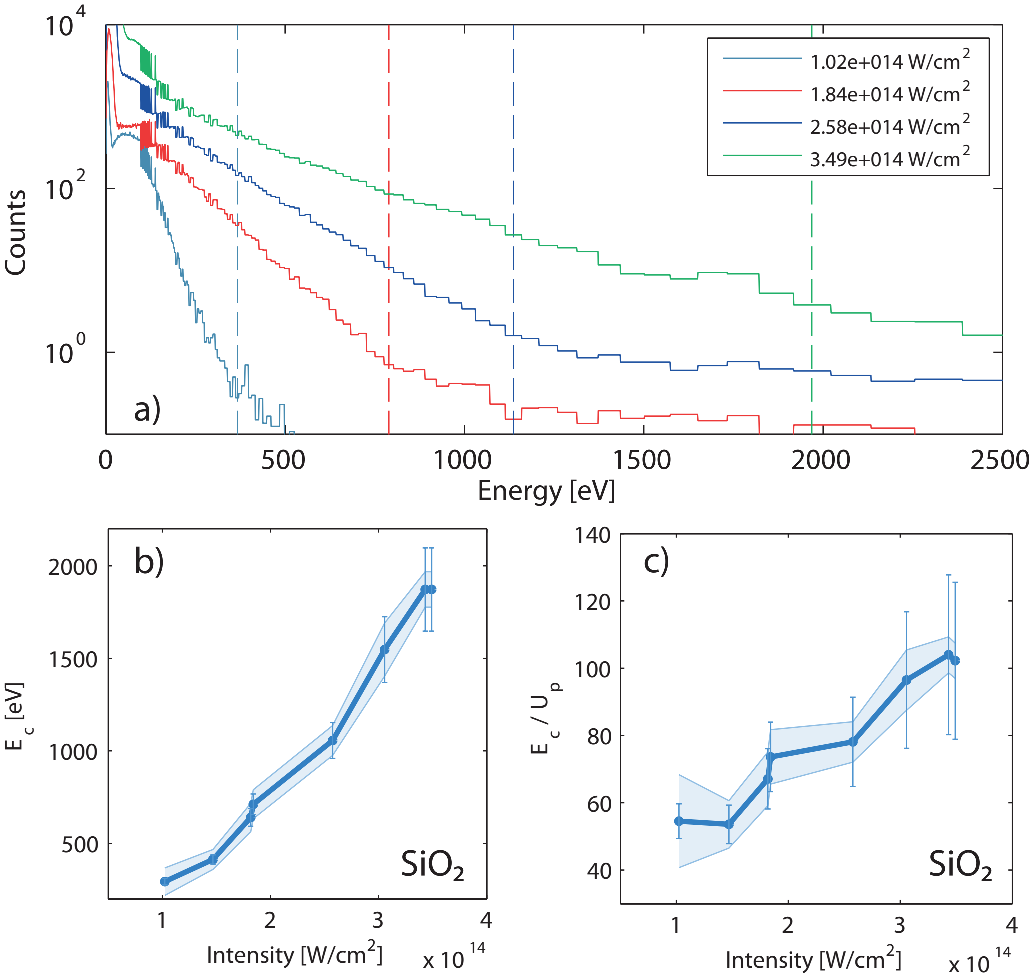

Figure 5.1: a) Photoelectron energy spectra from 95 nm SiO_2 nanospheres for four different intensities. b) Cutoff energies for 95 nm SiO_2 plotted against intensity. c) Rescaled cutoff dependence E_c/U_p as a function of intensity.

noticeably for the various intensities. The cutoff value was determined by the procedure described in section 3.5.2. Figure 5.1 b) shows the cutoff energy as a function of peak laser intensity. The solid error bars denote the experimental error caused by trigger jitter, the limited resolution of the TOF setup and data acquisition system. The shaded area illustrates the systematic uncertainty in determining the cutoff. The energy cutoff is monotonically increasing with intensity. There is an obvious increase in slope. This slope is illustrated in figure 5.1 c), which shows the cutoff energy E_c divided by the ponderomotive potential U_p. Between $1 \times 10^{14}\,\mathrm{W/cm^2}$ and $1.5 \times 10^{14}\,\mathrm{W/cm^2}$ the value of E_c/U_p lies around 53. This is comparable to the observations made with the VMI setup at lower intensities (see section 4.4). For stronger pulses, E_c/U_p increases, reaching values close to 100 at around $3.5 \times 10^{14}\,\mathrm{W/cm^2}$.

The results for ZrO_2 and TiO_2 are shown in figure 5.2. A similar behavior as for SiO_2

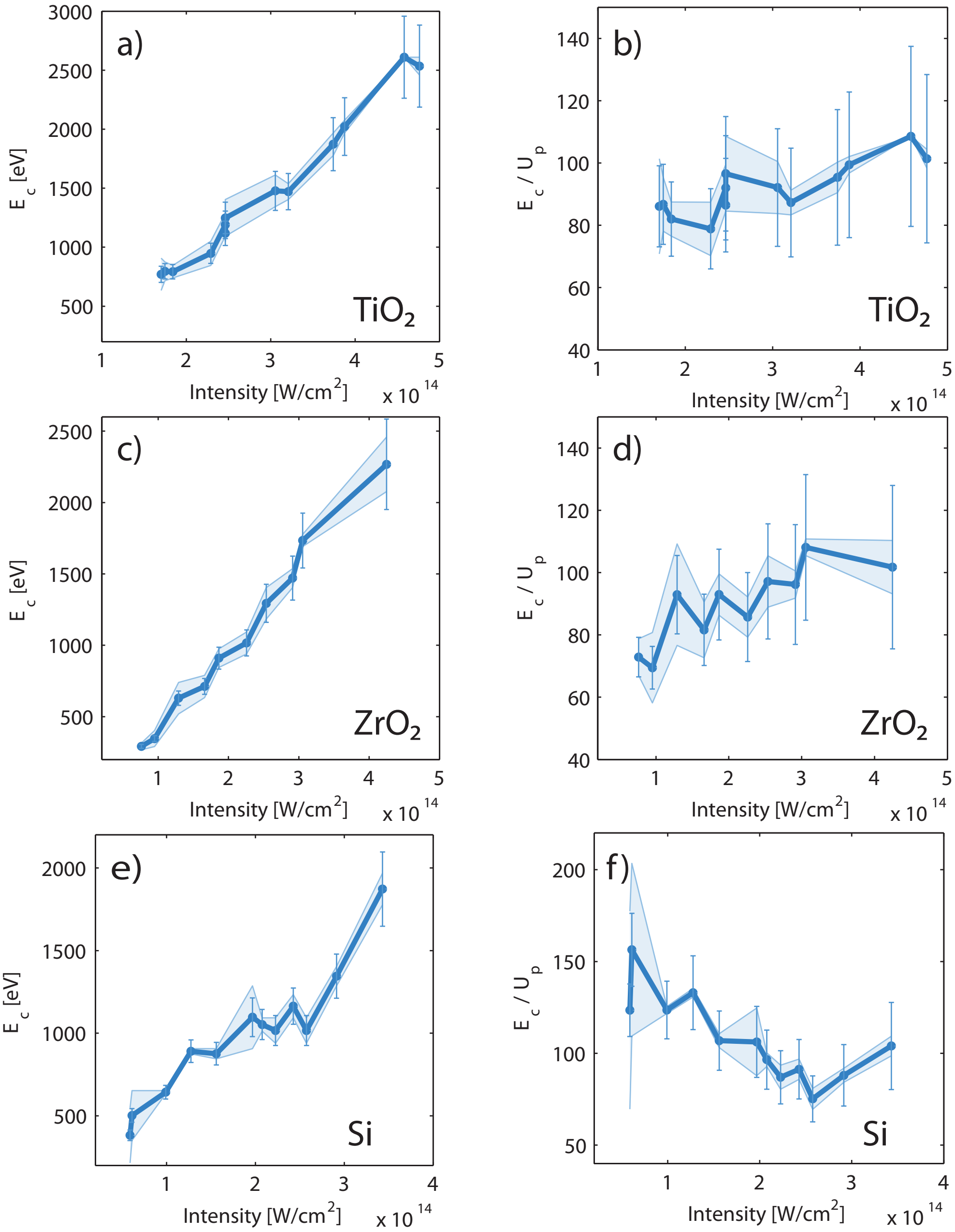

Figure 5.2: a) Cutoff energies for 60 nm TiO_2 nanospheres plotted against intensity. b) Rescaled cutoff dependence E_c/U_p as a function of intensity. c) and d) show the same plots for 60 nm ZrO_2 particles. e) and f) show the same plots for 60 nm Si particles.

can be observed here. As the count rate from the TiO_2 sample was not as high as for the other materials, the scans start at a higher intensity. The cutoff energy E_c is shown in figure 5.2 a) and shows an increase as well. E_c/U_p has a value of around 83 at 1.7×10^{14} W/cm^2

and exhibits a slight increase. The data of the ZrO_2 sample is very similar to this (see figure 5.2 c) and d)). Here, E_c/U_p starts slightly lower with an average value of 75 U_p. Both ZrO_2 and TiO_2 again reach values of $E_c/U_p \approx 100$ for intensities between 3 and $4 \times 10^{14}\,\mathrm{W/cm^2}$.

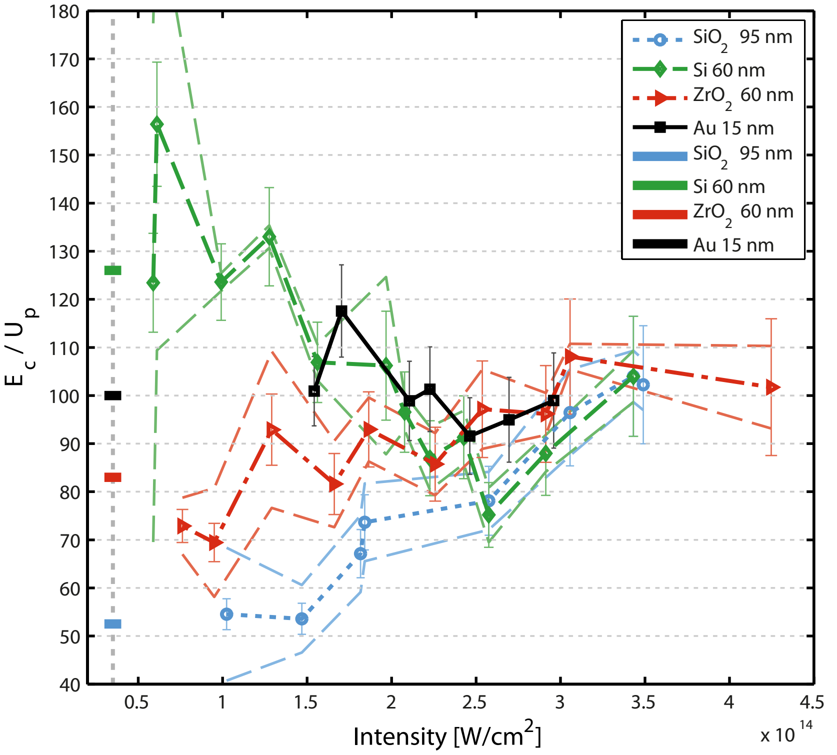

Figure 5.3: Rescaled cutoff energies E_c/U_p as a function of intensity for SiO_2, Si, ZrO_2 and Au nanoparticles. The results of M^3C simulations for each material at an intensity of $3.5 \times 10^{13}\,\mathrm{W/cm^2}$ are also shown.

For 60 nm Si, one observes a different trend. As indicated in figure 5.2 e) E_c is still rising with intensity. But the slope is decreasing as shown in figure 5.2 f). For low intensities around $5 \times 10^{13}\,\mathrm{W/cm^2}$ one obverses high ratios of E_c and U_p exceeding 150. This value decreases to around 85 at $2.7 \times 10^{14}\,\mathrm{W/cm^2}$ after which it shows a slight increase.

Figure 5.3 shows a comparison of all obtained cutoff values for SiO_2, ZrO_2, Si and Au sample. The Au sample shows values of E_c between 90 and 120 U_p. It must be noted that this sample shows only a weak signal due to its small size. The number of electrons emitted per nanoparticle is lower, at the same time the aerodynamic lens does not work as efficiently for this size. Nevertheless the observed cutoffs are comparable to those of measurements on Ag clusters (1-7 nm) using the same s-TOF device, where cutoff values of around 100 U_p were observed [18].

In overall, one finds that the E_c/U_p curves of all materials converge. Above $2.5 \times 10^{14}\,\mathrm{W/cm^2}$ all cutoff energies show a similar value between 90 and 110 U_p within their respective error bars. The predicted values by M^{3}C simulations for an intensity of $3.5 \times 10^{13}\,\mathrm{W/cm^2}$ are indicated in the figure. There is good agreement when extrapolating the individual lines within the experimental error.

5.1.3 CEP dependence at high intensities

Figure 5.4 shows the asymmetry maps for various intensities of 95 nm SiO_2 nanospheres. The asymmetry as a function of momentum p is given by the relative difference of the two detector signals:

$$A(p) = \frac{S_{\mathrm{up}}(p) - S_{\mathrm{down}}(p)}{S_{\mathrm{up}}(p) + S_{\mathrm{down}}(p)} \tag{5.1}$$

The cutoff momentum as determined by the time-flight-spectrum is indicated by the white dashed line. In the same way, the cutoff of the reference scan is marked by the red, dashed line. The phase dependence of the background gas ATI is usually still well visible in the nanoparticle scans. Choosing the momentum scale serves for a better visualization of the features.

The strongest and clearest CEP dependence could be observed for the SiO_2 nanospheres. For an intensity of $1.5 \times 10^{14}\,\mathrm{W/cm^2}$, the asymmetry pattern shifts towards higher CE phases with increasing momentum. This resembles the observation made for lower intensities as discussed in section 4.4. Going to higher intensities, a substantial change is noticeable in the asymmetry maps. In the region between 1.7×10^{14} to $2 \times 10^{14}\,\mathrm{W/cm^2}$, one generally observes a decrease of the effective asymmetry especially in the cutoff region. An experimental observation is that the exact shape of the asymmetry maps could not be reproduced from day to day. Obviously, a critical point is reached and slight changes in the driving laser pulse waveform yield different outcome. This is consistent with the expectation of a high non-linearity. For higher intensities above $2 \times 10^{14}\,\mathrm{W/cm^2}$, the asymmetry patterns is more apparent and more reproducible. As can be seen in figure 5.4 c) and d), from this point on the asymmetry evolution is completely different and shows a homogeneous, almost linear trend in the opposite direction.

It was found, that the other materials show much less pronounced asymmetry patterns. This can most likely be attributed to their size distribution in combination with the high non-linearity of the involved processes. The asymmetry maps of ZrO_2 exhibit characteristics similar to SiO_2 at the higher intensities. The asymmetry maps for $7.63 \times 10^{13}\,\mathrm{W/cm^2}$ and $2.5 \times 10^{14}\,\mathrm{W/cm^2}$ are shown in Fig. 5.5 a) an b), respectively. One can see that the features in the asymmetry maps are not well pronounced. Nevertheless, there is also a distinct change in evolution along the momentum axis when comparing the two intensities. The directionality is consistent to the observations made for SiO_2. In Fig. 5.5 c) and d), two typical asymmetry maps for Si and TiO_2 are presented for intensities of $2.47 \times 10^{14}\,\mathrm{W/cm^2}$ and $3.05 \times 10^{14}\,\mathrm{W/cm^2}$, respectively. At these high intensities, a similar trend as compared to SiO_2 and ZrO_2 is observable, but the data definitely lacks quality for a quantitative analysis.

An analysis of the light peak signal revealed no clear and reproducible dependency of the light peak amplitude on the CEP for any of the studied materials. This is a strong

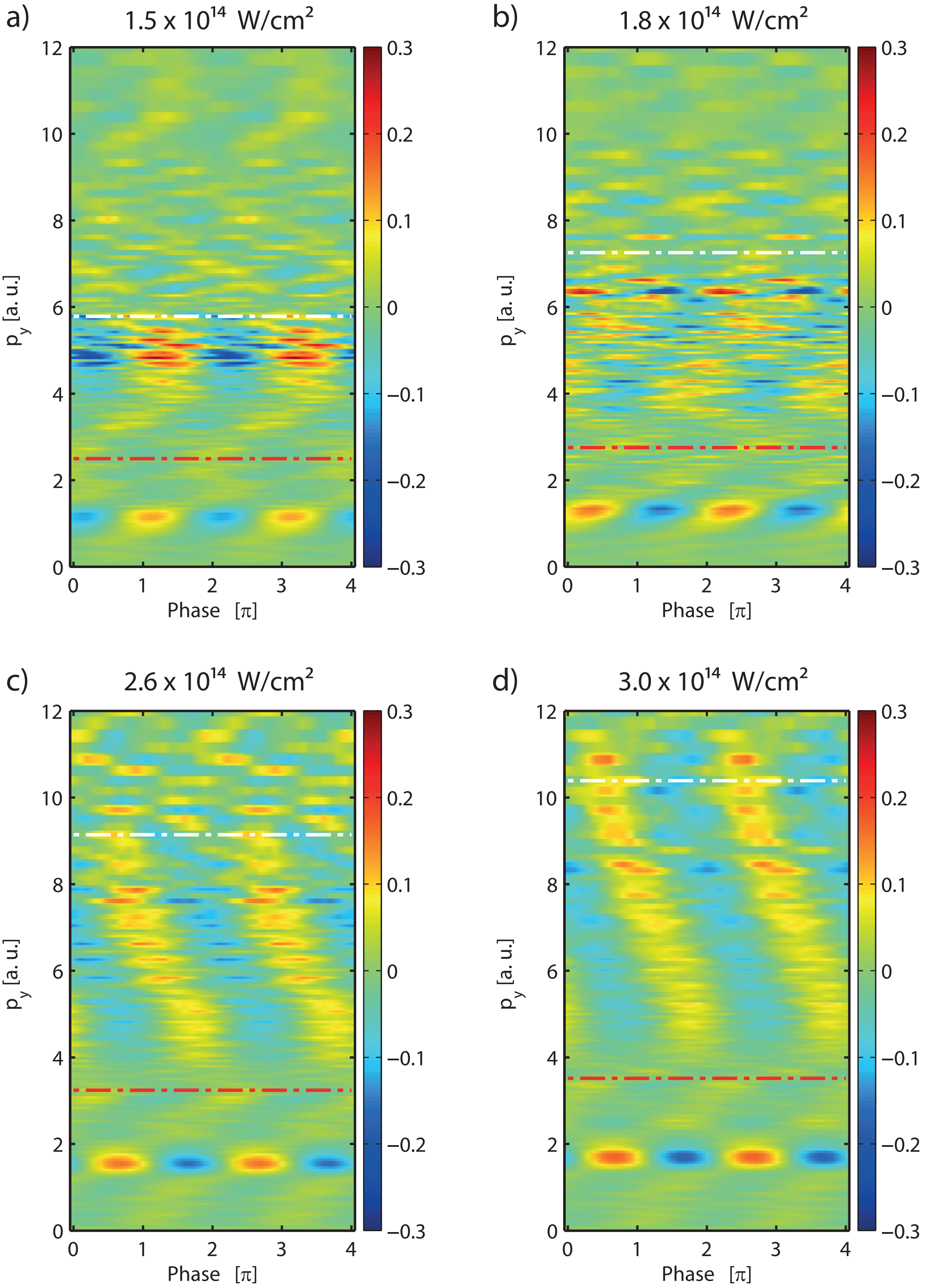

Figure 5.4: CEP asymmetry map (momentum scale) for 95 nm SiO_2 nanospheres for four different intensities. The cutoff momentum obtained from the time-of-flight spectrum is indicated for the nanoparticles (white, dashed line) as well as for the reference scan (red, dashed line).

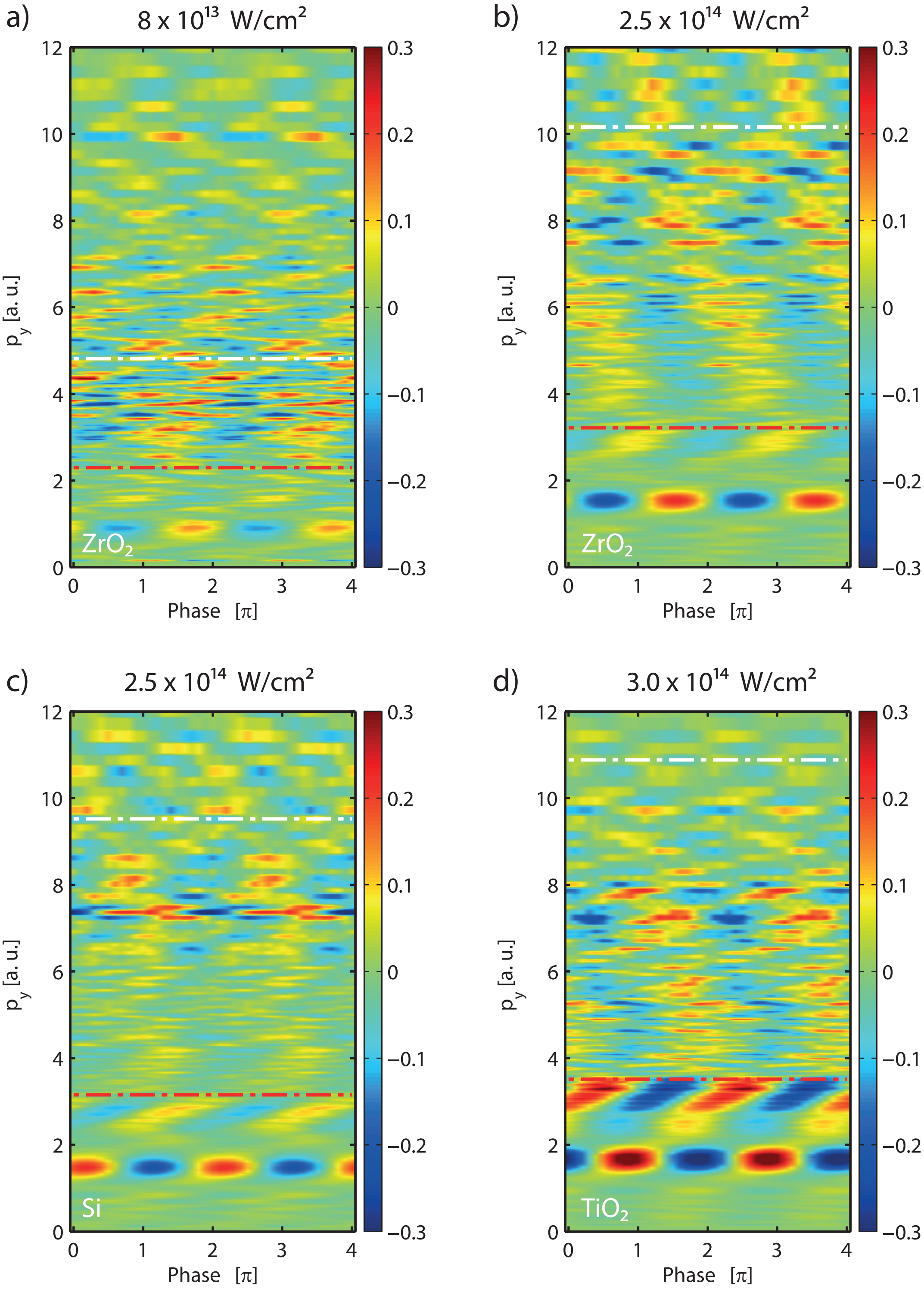

Figure 5.5: CEP asymmetry map (momentum scale) for a) 60 nm ZrO_2 at $8 \times 10^{13}\,\mathrm{W/cm^2}$. b) 60 nm ZrO_2 at $2.5 \times 10^{14}\,\mathrm{W/cm^2}$. c) 60 nm Si at $2.5 \times 10^{14}\,\mathrm{W/cm^2}$. d) 60 nm TiO_2 at $3.0 \times 10^{14}\,\mathrm{W/cm^2}$.

indication that a substantial portion of the emitted photons are incoherent and stem from e.g. Bremsstrahlung and/or recombination processes in the nanoparticle. It should also to be mentioned, that most probably a very broad spectrum contributes to the light signal as was observed in a study on HHG from Ag nanoparticle plumes [114]. In combination with the focus averaging effect, the CEP dependence of various spectral regions and laser intensities might cancel out in this integrated measurement of the emitted light.

5.2 Theoretical predictions

5.2.1 M^{3}C model

The results for M^{3}C simulations for each material at $3.5 \times 10^{13}\,\mathrm{W/cm^2}$ are shown in Fig. 5.3 (solid bars). The results agree well with experimental data at the lowest intensities for each material. The differences in E_c/U_p can be attributed mostly to the different field enhancement factors.

Tests with the M^{3}C simulation model for intensities above $1 \times 10^{14}\,\mathrm{W/cm^2}$ show a decrease in E_c/U_p. This can be attributed to a less efficient mean field acceleration mechanism in combination with a strong increase in the trapping potential. Due to the much higher kinetic energy of the electrons, the time for leaving the near-field after rescattering is drastically reduced and the tunnel exit is much closer to the sphere surface. This leads to a decreased influence of the mean-field potential. It has to be mentioned, that these calculations have to be taken with care as no reliable convergence tests could be carried out due to very large number of integrated electron trajectories. The question arises whether ionization is still modeled correctly for the intensities under consideration as no saturation effects are taken into account. Also, it has to be noted that the M^{3}C model does not include electron-electron scattering and possible recombination mechanisms. Most important, the optical properties are assumed to be constant which is questionable at such field strengths close to the damage threshold.

5.2.2 Free charge density approximations

According to the dipole approximation, the electric field inside the sphere is homogeneous and given by:

$$\mathbf{E}_{\mathrm{i}}(t) = \frac{3}{\epsilon + 2}\mathbf{E}_{\mathrm{l}}(t). \tag{5.2}$$

For materials with large values of $|\epsilon|$, the particle efficiently shields the electric field inside the sphere. In the following, it will be assumed that the mean-field potential can be neglected as it does not play a major role for most parts of the particles interior. The evolution of the population can be expressed by a rate equation (2.46):

$$\frac{dn_e}{dt} = (W_\gamma + \beta n_e I)\left(1 - \frac{n_e}{n_0}\right) - \frac{n_e}{\tau_r} \approx W_\gamma \left(1 - \frac{n_e}{n_0}\right). \tag{5.3}$$

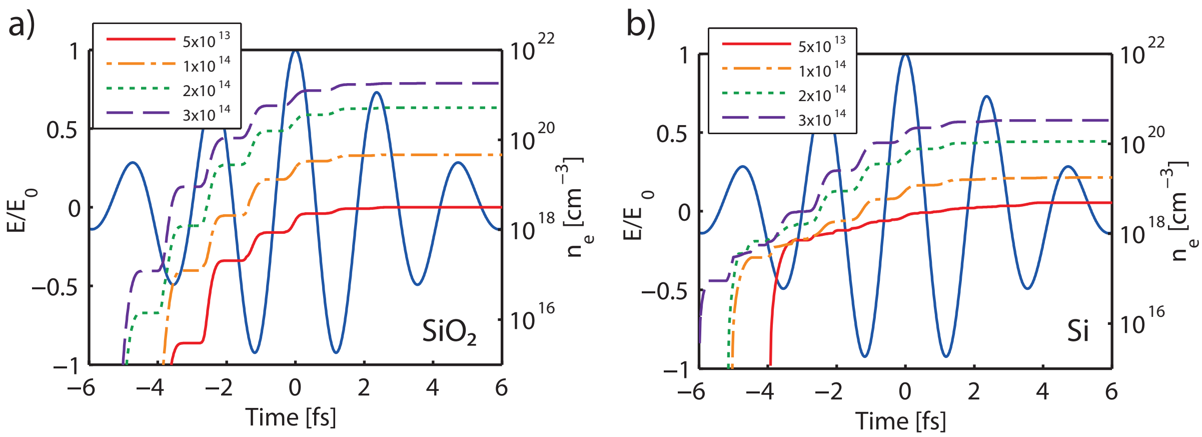

Figure 5.6: a) Valence band population according to the Keldysh model for SiO_2 nanospheres at different peak intensities. The blue line represents the normalized electric fields. b) Valence band population according to the Keldysh model for Si nanospheres at different intensities

W_γ describes the charge creation by tunnel and multi photon ionization given by equation (2.42), while the term $\beta n_e I$ models the electron avalanche process. To take saturation into account, it is assumed that at most one electron per atom can be promoted to the conduction band. This is reflected by the scaling term $n_e/n_0 - 1$. The relaxation term n_e/τ_r accounts for recombination of free charge carriers. According to Chimier *et al.*, impact ionization is very inefficient compared to photoionization at pulse lengths shorter than 10 fs [50]. Therefore it will be neglected here, $\beta \approx 0$. The free electron decay constant is on the order of $\tau_r \approx 150\,\mathrm{fs}$ [115] and consequently this term will also be neglected. This leaves only the pure photoionization yield W_γ given by the Keldysh formula (2.42). The condition for optical breakdown is reached when $\omega_p \approx \omega$ which is equivalent to an electron density of $n_e \approx 2 \times 10^{21}\,\mathrm{cm}^{-3}$ for a wavelength of 750 nm.

The transient electron density in the conduction band was calculated by integrating equation (5.3) with the electric field given by (5.2) for SiO_2 and Si nanospheres. The effective band gap was chosen to be $\Delta = 9\,\mathrm{eV}$ for SiO_2 whereas for Si the direct band gap value of $\Delta = 3.4\,\mathrm{eV}$ was used. The pulse length was set to 5 fs. Fig. 5.6 a) shows the results for SiO_2 nanospheres at four different intensities between $5 \times 10^{13}\,\mathrm{W/cm^2}$ and $3 \times 10^{14}\,\mathrm{W/cm^2}$. As one can see, the charge density reaches $10^{21}\,\mathrm{cm}^{-3}$ for peak intensities above $1 \times 10^{14}\,\mathrm{W/cm^2}$. The critical charge density is reached for intensities around $3 \times 10^{14}\,\mathrm{W/cm^2}$. The results for Si are shown in Fig. 5.6 b). A much higher final electron population is expected for this material due to the lower band gap. Instead one obtains values even below the SiO_2 final charge densities, which is caused by the more effective shielding of the sphere interior. This effect could explain the convergence of the rescaled cutoff energies in Fig. 5.3 for all materials at a similar intensity.

Such a simple model can of course only give a rough approximation of the threshold intensity. First of all impact ionization is not taken into account. Especially for such high intensities, the laser pulse length and its exact waveform will play a major role. Already a few seed electrons will create a reasonable population in the conduction band during the onset of the pulse. This effect will be even more pronounced if the laser pulse exhibits significant satellite pulses. A second problem, that needs to be considered are changes in the electromagnetic response during the pulse, which will in turn modify the ionization rates. A significant increase of charge carrier density will lead to a pronounced change in optical properties, i.e. enhanced absorption and different field distributions.

According to Apalkov *et al.*, a strong non-linear optical response is adiabatically driven by the external electric field in dielectrics [54]. The adiabatic band gap shall collapse when the electric field overcomes a value of $E_{\mathrm{crit}} = \Delta/ea$ where a is the lattice constant. This corresponds to a field strength of $2.5\,\mathrm{V\AA^{-1}}$ for a lattice constant of $5\,\mathrm{\AA}$. Translating this to the nanosphere, an external laser intensity of $1 \times 10^{14}\,\mathrm{W/cm^2}$ is required. Optical breakdown shall occur at a field strength of $2.5\,\mathrm{V\AA^{-1}}$ which corresponds to $1.6 \times 10^{14}\,\mathrm{W/cm^2}$.

5.2.3 Interpretation

The approximations made in the last section indicate that the conditions for optical breakdown are reached for all materials. Therefore it is tempting to relate the experimental observations directly to this transient (semi-)metallization. Nevertheless, one has to consider, that the data presented here is not a direct measure of the material properties. As explained in the last chapter, the near-fields are strongly dependent on the temporal evolution of the charge distribution created by ionization from the surface. Therefore the possible reasons for the increase in cutoff energies can be divided in those intrinsic to the rescattering process and those that are related to transient change in optical properties. Three possible effects with respect to the mean field acceleration process can be found

1. A stronger sub-cycle acceleration, i.e. a stronger modulation of the effective mean field. This might be caused by saturation effect in the ionization yield.
2. An enhanced post-acceleration by a dramatically increased Coulomb repulsion (space-charge like broadening of the electron energy distribution).
3. Fast electrons created during the Coulomb explosion of the nanoparticle.

As there is still a CEP dependence noticeable even in the cutoff region, process 3) can most likely be ruled out. Similarly, pure Coulomb repulsion cannot explain the pronounced change in characteristics in CEP dependence above a critical intensity. In combination with a drastically increased trapping potential, the emission could of course be transferred to different half-cycles. Here, one has to conclude that the exact influence of mutual charge interactions can only be resolved by simulations. Therefore, one has to consider that the mean field acceleration process and its intensity dependence will definitely have a strong influence on the observed spectra.

A comparison with the theoretical predictions and the electron densities shown in Fig. 5.6 indicates, that the conditions for optical breakdown are reached even for such short pulses. This could result in a drastically non-linear evolution of the optical response. The critical intensities lie around $2 \times 10^{14}\,\mathrm{W/cm^2}$ for all materials, but no clear threshold is visible. This could either be intrinsic to the process i.e. a gradual change of the electromagnetic response in good agreement with the recent theoretical prediction by Apalkov for SiO_2 or the threshold could be obscured within the experimental error. Assuming the applicability of a Drude type model, it is obvious that the most severe changes are found at the end of the pulse and probably result in a stronger enhancement. This could explain the reversal of features in the CEP asymmetry maps, as electrons born later during the pulse are accelerated stronger. Furthermore, the obvious convergence of the rescaled cutoff energies of all materials shown in Fig. 5.3 are in accordance with this explanation. The essential message of this interpretation is that the individual material properties are lost or at least are not of importance to the optical response any more. The material state is comparable to that of a dense plasma. A system in such a highly non-equilibrium state will of course experience a redistribution of the absorbed energy leading to Coulomb explosion. But as the CEP dependence indicates, only the dynamics of a few femtoseconds are contributing to the experimentally observed electron spectra (especially in the cutoff region). The cutoff energies converge to a value of around 100 U_p for all materials which would point to a field enhancement factor of about 3 when neglecting the mean field. This is in accordance with a Drude-like index of refraction of the plasma [32].

In addition, the perceived poor quality of the CEP asymmetry maps may be attributed not only to a poor sample quality but also to the metallization process. The charge generation process depends on the temporal evolution of the electric field strength and therefore on the CEP. In combination with the CEP dependence of the acceleration/rescattering process, complicated features and cancellation can arise. As the intensities become higher, the charge density and therefore the material properties might have reached a steady state even before the intensity peak arrives at the sample, which would lead to more stable CEP asymmetry maps. A direct analysis of course is hampered by the focus averaging intrinsic to the experiment. The strong dependence on waveform and exact intensity profile of the laser pulse could also explain the difficulties in reproducing the asymmetry map characteristics.

5.3 Conclusions and outlook

The photoemission energy spectra and CEP asymmetry maps for intensities exceeding $10^{14}\,\mathrm{W/cm^2}$ were presented for different nanoparticle compositions in the dipolar size range. The rescaled cutoff energies of all materials converge to values slightly below 100 U_p for intensities above $2.5 \times 10^{14}\,\mathrm{W/cm^2}$. Also the CEP asymmetry maps exhibit a distinct intensity dependence. As the laser intensities agree well with the theoretically predicted breakdown thresholds, it is most likely that the measured energy spectra carry significant traces of the sub-cycle conduction band electron populations and the associated change in optical properties.

The experimental implementation so far suffers from the uncertainty about the exact laser waveform of the laser field and influence of satellite pulses. Also the contribution of the Coulomb mean field at these intensities has to be investigated. Nevertheless the experimental approach has advantages over studies in bulk samples, as intensities above the damage threshold can be applied. Also a reconstruction of charge carrier dynamics is less complicated than the rather indirect method of measuring ablation depths. Therefore, the presented experimental findings can serve as a benchmark for existing and future theoretical models. Using nanoparticles limits the system's size and simplifies a theoretical approach such as MicPIC [51].

An exact knowledge of the laser waveform (e.g. by attosecond streaking spectroscopy) and an optimization of the intensity contrast would enable the exact characterization of charge carrier dynamics by pulse-length variation and pump-probe techniques. Such pump-probe experiments could even be pushed to the ultimate limit of shaped few-cycle waveforms [107]. A single-shot detection system for light scattered from the nanospheres could enable a combination of CEP and intensity tagging. For once this approach would make best use of the sample and acquisition time. Furthermore, the suppression of focus averaging effects would simplify the interpretation of the CEP asymmetry maps.

A further possibility is to study the light emitted from the particles in more detail. A spectral decomposition might show CEP dependent regions. This coherent signal would give additional information about the rescattering process and the state of the system during recollision.

Chapter 6

Direct measurement of near-fields by attosecond streaking

6.1 Introduction

In chapter 3 it was concluded that the photoelectron momentum distribution carries significant information about the near-field evolution of the SiO_2 nanospheres. Reconstruction of the temporal and spatial field profiles with this technique is of course dependent on comparison to reference simulations to a large extent. Therefore a more direct experimental access to the temporal evolution of plasmonic near-fields would be of great use. Two-pulse pump-probe measurements can be employed to obtain further insight into the temporal dynamics. Auto-correlation experiments by Hanke *et al.* with few-cycle laser fields showed evidence that the plasmon decay times of Au antennas depend on antenna geometry [116]. Local phase and polarization of near-fields at bowtie gap antennas were measured with interferometric scattering-type near-field optical microscopy (s-SNOM) experiments [117].

Attosecond streaking spectroscopy is a promising candidate for a time-resolved and non-invasive measurement of plasmonic fields offering sub-cycle time resolution. A major advantage concerning plasmonic resonant systems is the large spectral separation of pump and probe beam as the probe pulse lies in the XUV spectral region. It was shown by Cavalieri *et al.* that attosecond streaking spectroscopy can be applied on tungsten surfaces with a similar precision as compared to gas-phase streaking experiments [118]. In another study, it could be shown that the near-field of carbon nanotubes excited by a sub-ps laser pulse is imprinted on the spectrum of a short electron bunch which could be delayed in time and also spatially imaged [119]. Therefore the application of attosecond streaking for measuring (plasmonic) near-field field oscillations should be feasible, which is supported by a number of theoretical studies [120, 121, 122, 123, 124, 125]. The concept of attosecond plasmonic streaking is depicted in Fig. 6.1. Electrons are emitted by the attosecond XUV pulse which can be time delayed to a driving laser field in the optical region. On their way to the detector, the photoelectrons are accelerated by the near-field resulting in an effective change of their kinetic energy. The major difference to the streaking technique presented in section 3.6.1 is the exchange of gas atoms with either isolated nanoparticles or systems of nanoantennas.

Due to the extent of plasmonic systems such as antenna arrays and the possibility to observe traveling surface plasmons, an experimental realization would greatly benefit from spatial resolution in the nanometer regime. Photoemission electron microscopy (PEEM) can reconstruct the emission position of a photoelectron with high accuracy. With such a PEEM, Bauer *et al.* could measure the phase propagation of plasmons over small silver disks with an interferometric two-photon-photoemission (2PPE) approach [126]. The spatio-temporal evolution of traveling SPP fields was shown by Lemke *et al.* using essentially the same technique [127]. Not surprisingly, PEEM was proposed as a tool for full spatial and temporal reconstruction using attosecond XUV pulses by Stockman *et al.* [120]. This study theoretically investigated the imprint of highly localized electric field oscillations on rough silver surfaces (so called "hot spots") on the XUV photoelectron spectrum. Several attempts were made to experimentally realize this approach [128, 129]. These studies focused on the characterization of the PEEM imaging capabilities of fast photoelectrons emitted by attosecond XUV pulses. Mikkelsen *et al.* concluded that space-charge effects can be minimized with an appropriate XUV flux and a resolution of less than 300 nm could be obtained [128] without energy discrimination. Chew *et al.* conducted experiments with a time-of-flight-PEEM that also offers the electron energy information. Here it was shown that the images are predominantly formed by secondary photo-electrons [129]. Imaging of the direct photo-electrons could not be achieved in this study mainly due to the low effective count rate which was limited by the low repetition rate of the XUV source and dead times of the employed delay line detector.

In this chapter the efforts for realizing the combination of attosecond streaking with nanosystems will be presented. As the efforts on a combined spatio-temporal measurement approach needs to be postponed until higher repetition rate XUV sources are available, the work concentrates on the measurement of plasmonic fields at isolated nanosystems. It will be demonstrated that the combination of attosecond and nano-technology poses both experimental challenges as well as systematic peculiarities that need to be considered. At first, the streaking process from Au spheres will be considered theoretically as a sort of feasibility study [27] from which important characteristics of nanoplasmonic streaking can be derived. Then the first experimental evidence on streaking spectroscopy from Au nanotips will be presented and discussed.

6.2 General considerations

With respect to the emitted XUV photoelectron spectrum, one has to consider that nanoplasmonic streaking has to be treated in analogy to surface streaking experiments. The main difference between surface and (noble) gas streaking is that instead of emission from a single state, the XUV photoelectron spectrum will be a convolution of the density of states (DOS) of the bulk material and the XUV spectrum [130]. Experimentally this was observed in the streaking experiments from a tungsten surface [118]. For attosecond

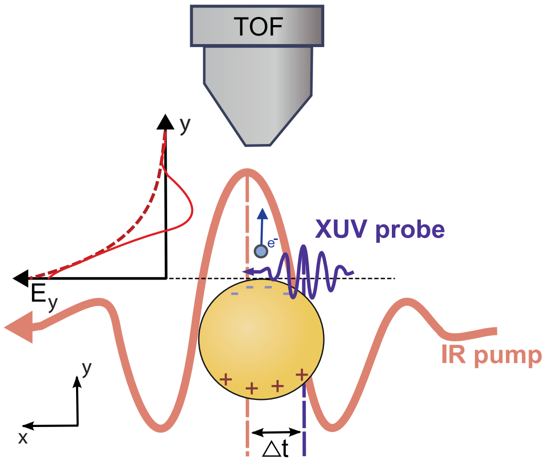

Figure 6.1: Working principle of nanoplasmonic streaking.

streaking measurements, a clear and sharp photoline is required for an accurate measurement of field evolution and amplitude. Therefore very clean samples are needed. Surface contamination will lead a further blurring of the spectral features, as the contaminant's ionization potential will most likely differ from the bulk material's work function.

Another complication might arise from the fact that the penetration depth of XUV light into the material is usually higher than tens of nanometers [90]. Therefore photoelectrons can also be set free rather deep in the material. As the mean free path of these electrons also lies around at least a few Angstroms, one needs to carefully analyze the field profiles inside the system [131].

Special peculiarities arise from the inhomogeneous field distribution at nanosystems. A key requirement for the quality of an attosecond streaking measurement is a homogeneous laser field in the interaction region. This is usually achieved by the use of relatively large focal lengths resulting in a sufficiently large Rayleigh length and a careful alignment. Only then the direct relation between streaking amplitude and vector potential given by equation (3.15) is valid. Turning to nanosystems it is obvious that the assumption of a spatially homogeneous laser field no longer holds.

For once, nanosystems can exhibit vastly different field profiles across its surface. As was discussed in chapter 4 even dielectric nanospheres exhibit large differences in field strength across their surfaces (see Fig. 4.10). In general, the gradients will depend on the effective radius of curvature and be more pronounced for complicated, resonant antenna geometries. A second mechanism leading to an effective inhomogeneity is the travel of the streaked electron in combination with the localized character of the plasmonic fields. After its emission the electron will depart from the surface, traveling to the detector. For fields with a strong localization at the surface, the electron will leave this field even before the end of the light oscillations. This effect was also observed by Herink *et al.* when studying photoemission from nanotips with different driving wavelengths [132].

6.2.1 The regimes of near-field streaking

The coordinate conventions are indicated in Fig. 6.1 and 6.2 a). The laser field is assumed to propagate along the x-axis with a linear polarization along the y-axis which is also the detection axis. For light waveforms with arbitrary spatial distribution $\mathbf{E}(\mathbf{r},t)$, the change in final velocity of the electron v_f as a function of its emission time t_e is given by

$$\mathbf{v}_\mathrm{f}(t_\mathrm{e}) = \mathbf{v}_0 - \int_{t_\mathrm{e}}^{\infty} \frac{e\mathbf{E}(\mathbf{r},t)}{m} dt. \tag{6.1}$$

Here e denotes the elementary charge. v_0 is the initial velocity of the electron, which is in general dominated by the XUV attosecond pulse spectrum and the work function. The kinetic energy of a released electron can be approximated by $E_\mathrm{kin} = \hbar\omega_\mathrm{XUV} - \Delta$, where ω_XUV is the center wavelength of the attosecond pulse and Δ is the work function of the material.

The form of $\mathbf{E}(\mathbf{r},t)$ of course strongly depends on the system geometry and material. It was shown that the evolution of plasmonic near-fields from the surface into free space can well be approximated by an exponential function [133]. Introducing the spatial decay constant χ, the decay can be written as

$$\mathbf{E}(y,t) \approx E_\mathrm{l}(t) \exp\left(\frac{-y(t)}{\chi}\right). \tag{6.2}$$

Here it is assumed that the surface is normal to the y-axis and the electron shall be emitted in the y-direction (see Fig. 6.2 a)). Note that χ is in fact not a constant, meaning that it has to be defined at every point under consideration and is also dependent on the emission angle of the electron.

A second approximation concerns the velocity of the XUV electron. Usually the change in velocity Δv that is imposed by the acceleration in the laser field is much smaller than the initial velocity v_0. For example an electron with E_kin of 100 eV and a streaking amplitude of 10 eV only leads to a relative change in velocity $(v_0 + \Delta v)/v_0 \approx 5\%$. The electron's distance from the surface can thus be approximated by

$$y(t) \approx y_0 + v_0(t - t_e). \tag{6.3}$$

Using this approximation, equation (6.2) turns into

$$\mathbf{E}(y,t) \approx E_\mathrm{l}(t) \exp\left(\frac{-v_0(t-t_e)}{\chi}\right) = E_\mathrm{l}(t) \exp\left(\frac{-(t-t_e)}{\tau_s}\right), \tag{6.4}$$

where the spatial decay time constant $\tau_s = \chi/v_0$ was introduced.

A sharp plasmonic resonance can be treated in analogy to a damped, driven oscillator [21]. Therefore the oscillations $E_l(t)$ will also show an exponential decay after its excitation at time $t = 0$:

$$E_\mathrm{l}(t) = E_0 \cos(\omega t + \phi_\mathrm{ce}) \exp\left(-\frac{t}{\tau_p}\right), \tag{6.5}$$

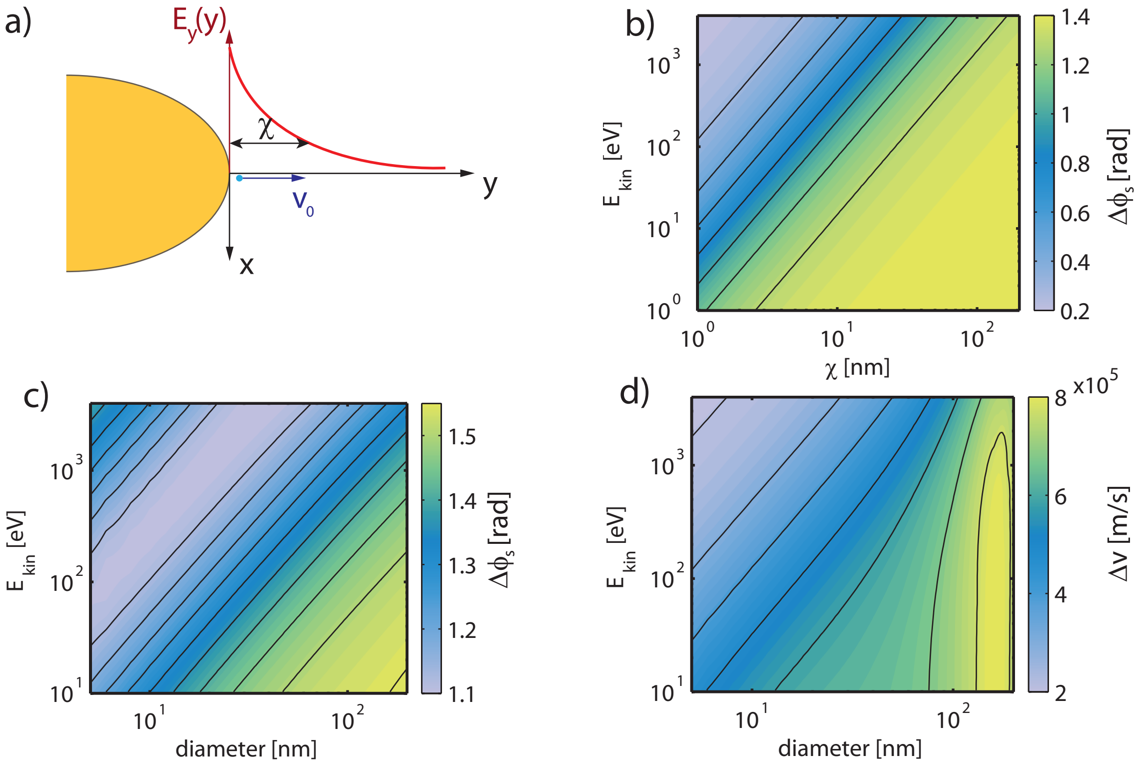

Figure 6.2: a) Illustration of the streaking geometry: The electron leaves at $y = 0$ in positive y-direction. The near-field is assumed to decay exponentially along its trajectory. b) Phase shift $\Delta\phi_s$ between streaking waveform and near-field oscillation obtained from the analytic approximation (6.8) as a function of spatial decay constant χ and electron kinetic energy E_{kin}. c) and d) Phase shift $\Delta\phi_s$ and streaking amplitude Δv for streaking from the pole of an Au nanosphere as a function of sphere diameter and electron kinetic energy.

where E_0 is the peak field amplitude, ϕ_{ce} the effective carrier-envelope phase and τ_p is the temporal decay constant. Inserting equations (6.3), (6.4) and (6.5) into (6.1) yields

$$\Delta v(t_{\mathrm{e}}) = v_0 - v(t_e) = -\int_{t_{\mathrm{e}}}^{\infty} \frac{e}{m} E_0 \cos(\omega t + \phi_{\mathrm{ce}}) \exp\left[-\frac{t}{\tau_p} - \frac{(t-t_e)}{\tau_s}\right] dt. \tag{6.6}$$

With the simplifications made, equation (6.6) is integrable. The change in final photoelectron velocity as a function of emission time is:

$$\Delta v(t_{\mathrm{e}}) = -\frac{eE_0}{m} \frac{\tau_p \tau_s e^{-\frac{t_e}{\tau_p}}}{(\tau_s+\tau_p)^2 + \tau_p^2 \tau_s^2 \omega^2} \Big[(\tau_p+\tau_s)\cos(\omega t_e + \phi_{\mathrm{ce}}) - \tau_p \tau_s \omega \sin(\omega t_e + \phi_{\mathrm{ce}})\Big]. \tag{6.7}$$

Note, that this equation only holds for probing the field after its excitation when the plasmon is decaying. Analyzing the rather complicated expression of Eq. (6.7) shows that the streaking amplitude will also exhibit an exponential decay $\exp(-t_e/\tau_p)$ directly reflecting the temporal decay of the near field. The complex form of the oscillating terms originate from the interplay between spatial and temporal decay of the light field. The phase of the oscillation in the streaking spectrogram is:

$$\Delta\phi_s = \arctan\left(\frac{\tau_p \tau_s \omega}{\tau_p + \tau_s}\right). \tag{6.8}$$

As the near-field was defined such that it peaks (or is instantaneously excited) at $t = 0$, $\Delta\phi_s$ is the phase shift between the streaking waveform and the local near-field oscillation. It is thus a direct measure of the streaking regime. For spatially extended fields and relative small temporal decay time $\tau_p \ll \tau_s$, the phase shift is $\Delta\phi_s \approx \arctan(\tau_p\omega)$. In this case $\Delta\phi_s$ is close to $\pi/2$, as for any oscillating light pulse the period is shorter than its envelope $\omega^{-1} < \tau_p$. The situation is equivalent to conventional streaking, where Δv is proportional to the vector potential and will be referred to as the ponderomotive streaking regime.

In the opposite limiting case, the electron will leave the surface during a fraction of a half-cycle of the laser field. Then the spatial decay is small compared to both temporal decay constant and oscillation period. Here $\tau_p \gg \tau_s$ and $\tau_s \ll \omega^{-1}$, which results in a phase shift close to zero $\Delta\phi_s \approx \arctan(\tau_s\omega) \approx 0$. The measured streaking waveform will thus directly reflect the electric field of the plasmonic oscillation. Note, that in the field probing regime, the streaking amplitude will significantly decrease for a fixed electric field amplitude E_0. Figure 6.2 b) shows the phase shift $\Delta\phi_s$ as a function of initial electron energy E_{kin} and spatial decay constant χ for a fixed temporal decay of $\tau_p = 10\,\mathrm{fs}$ and a laser wavelength of $\lambda = 720\,\mathrm{nm}$. Keeping χ at a fixed value, increasing E_{kin} leads to a transition from ponderomotive to the field probing regime.

6.2.2 Simulated streaking spectrograms for Au spheres

Today, typical attosecond XUV sources operate in the region around $\hbar\omega_{\mathrm{XUV}} \approx 100\,\mathrm{eV}$. Plasmonic systems of interest have sizes between tens and hundreds of nanometers. From Fig. 6.2 b) it is thus obvious, that an experiment with these parameters will take place in an intermediate regime between ponderomotive and instantaneous field probing. Furthermore, the spatial inhomogeneity across the surface of the nanoparticle was so far completely neglected. To get more insight into the possible outcome of an attosecond nanoplasmonic streaking experiment, numerical simulations have to be performed. This has been done for rectangular Au antennas [121, 123] and spherical Au [122, 123, 124] and Ag particles [125].

The key results for streaking from spherical Au particles will be outlined here with special emphasis on the dependence on the emission position of the XUV photoelectrons [122]. Figure 6.3 a) and b) show the maximum field enhancement patterns for Au spheres of 10 and 100 nm diameter. The polarization is along the y-axis. For moderate sizes the field enhancement rises as the particles become more resonant with the laser field (compare to Fig. 2.5 b)). As the most pronounced mode is the dipolar mode, the distribution of the relative field enhancement does not differ for sizes between 10 nm and 100 nm. Due

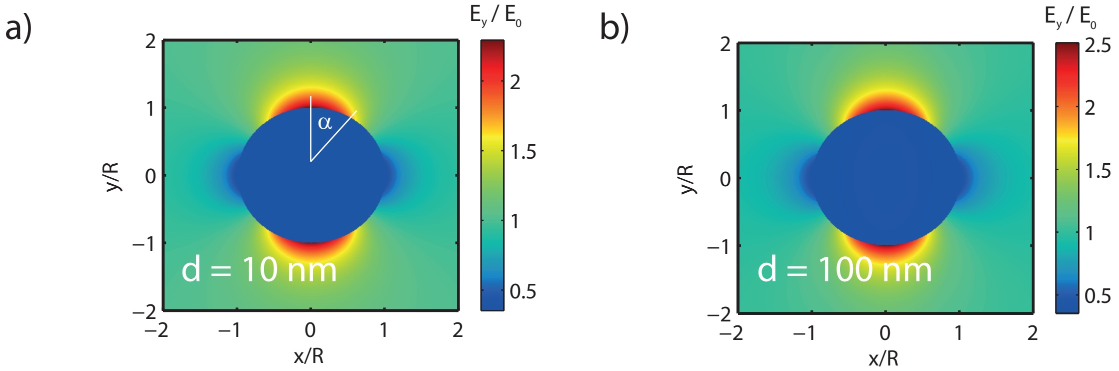

Figure 6.3: a) Field distribution (E_y) at an Au sphere with a diameter of $d = 10\,\mathrm{nm}$ for a wavelength of 720 nm. b) Same map for $d = 100\,\mathrm{nm}$.

to the symmetry of the system the emission position of an XUV photoelectron can be characterized by a single parameter, namely the angle α to the laser polarization axis.

The equations of motion (6.1) were integrated for different emission times t_e to obtain a complete streaking waveform. The integration was done by a fourth order Runge-Kutta algorithm with a time step of 10 as. The laser field was assumed to have a Gaussian envelope with 5 fs (FWHM of electric field), a center wavelength of λ =720 nm and a peak intensity of $1 \times 10^{12}\,\mathrm{W/cm^2}$. The local field was calculated by Mie theory using the SPlaC package [134]. The enhancement leads to a maximum near-field intensity of close to $1 \times 10^{13}\,\mathrm{W/cm^2}$, which should be below the damage threshold of the particle. Only the Mie solution for the center wavelength was considered, which is well justified for the considered sizes between 10 nm and 100 nm. The kinetic energy of the electrons was fixed to $E_{\mathrm{kin}} = 100\,\mathrm{eV}$ corresponding to an XUV photon energy of $\hbar\omega = E_{\mathrm{kin}} + I_p \approx 105\,\mathrm{eV}$.

Fixing the emission angle to $\alpha = 0°$, one can examine the dependence of the streaking regime on sphere diameter d and initial electron energy E_{kin} emitted along the y-axis. The results for $\Delta\phi_s$ are shown in figure 6.2 c). Despite the fact that the spatial decay for this dipolar system follows an approximately $1/r^3$ behavior, the characteristics are strikingly similar to the results of the analytic approximation given by equation (6.8). For higher kinetic energies, the phase shift decreases as the field probing regime is entered. The major difference is that for high kinetic energies and small sphere diameters, $\Delta\phi_s$ increases again. This results from the homogeneous laser field surrounding the particle, that was not accounted for in the derivation of equation (6.8). As the fast electrons leave the near-field within a fraction of an optical period, their effective acceleration is small compared to the acceleration that results from ponderomotive streaking in the driving laser field. Under these conditions the imprint of the near-field is determined by its relative strength as compared to the driving field, which is just the field enhancement factor. One can thus conclude that the direct field-probing regime is only achievable with extremely high field enhancement factors. For the Au spheres under consideration, this is obviously not the case. These findings are also reflected for the streaking amplitude, which is shown in figure

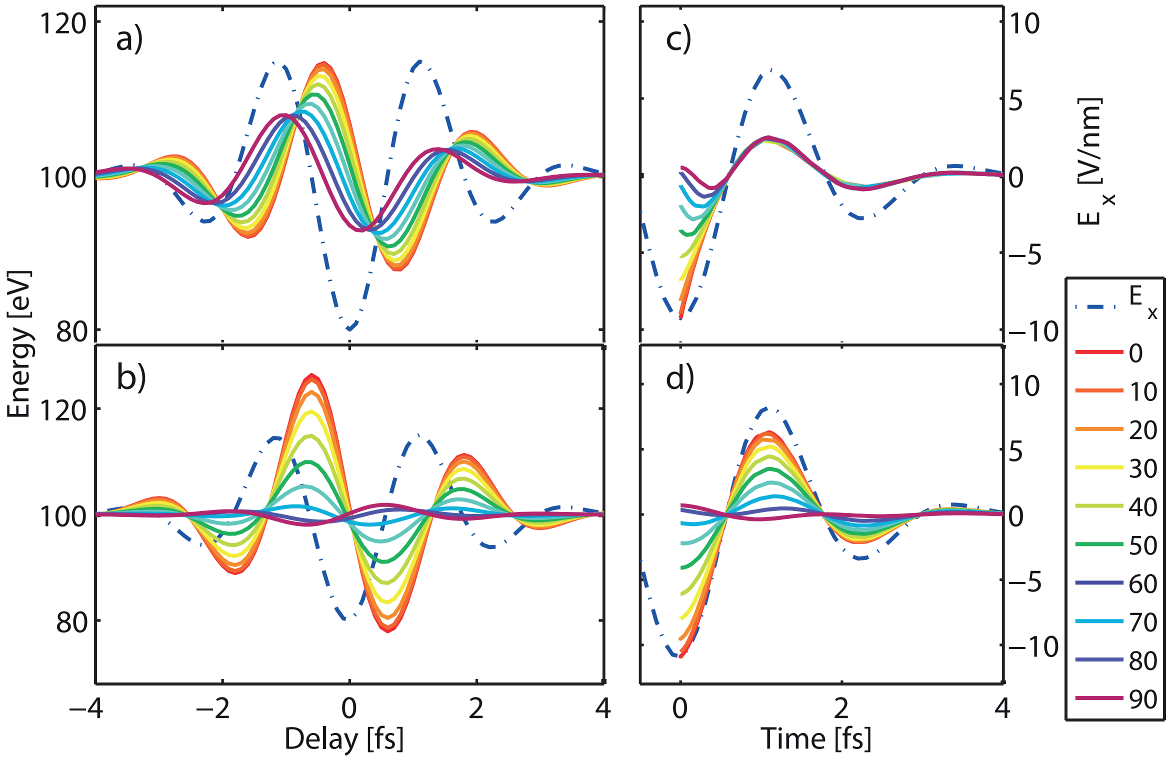

Figure 6.4: a) and b) show simulated streaking waveforms for electrons emitted at different positions (defined by the angle α) on the sphere for $d = 10$ and 100 nm, respectively. The blue dash-dotted line indicates the driving laser field. c) and d) shows the effective field for electrons launched at $t_e = 0$ for the same emission positions for both sphere sizes. As shown in [122].

6.8 d). Here one finds a decrease when approaching the field probing regime converging to the amplitude for conventional homogeneous field streaking. For larger sphere diameters the amplitude becomes larger. This can be attributed to more efficient acceleration in the near-field but also to the fact that the enhancement factor rises with increasing diameter.

Figure 6.4 a) and b) shows simulated streaking curves for different emission positions (defined by α) for a diameter $d = 10$ nm and 100 nm, respectively. Here initial velocity of the photoelectrons was set parallel to the y-axis and the kinetic energy was kept fixed at 100 eV. The accelerating fields for electrons emitted at $t_e = 0$ is shown in c) and d) for the same emission positions. The driving laser field is depicted by the blue dashed-dotted line in all plots. For the 10 nm spheres, emission at the pole leads to phase shift of about 0.3 π with respect to the driving field indicating that the streaking process is in an intermediate regime. Emission at larger angles α leads to a larger phase shift $\Delta\phi_s$. This results from the fact that these electrons are born in a region with lower electric field amplitude (compare to Fig. 6.3). The influence of the dipolar pattern is also reflected in figure 6.4 c), where one

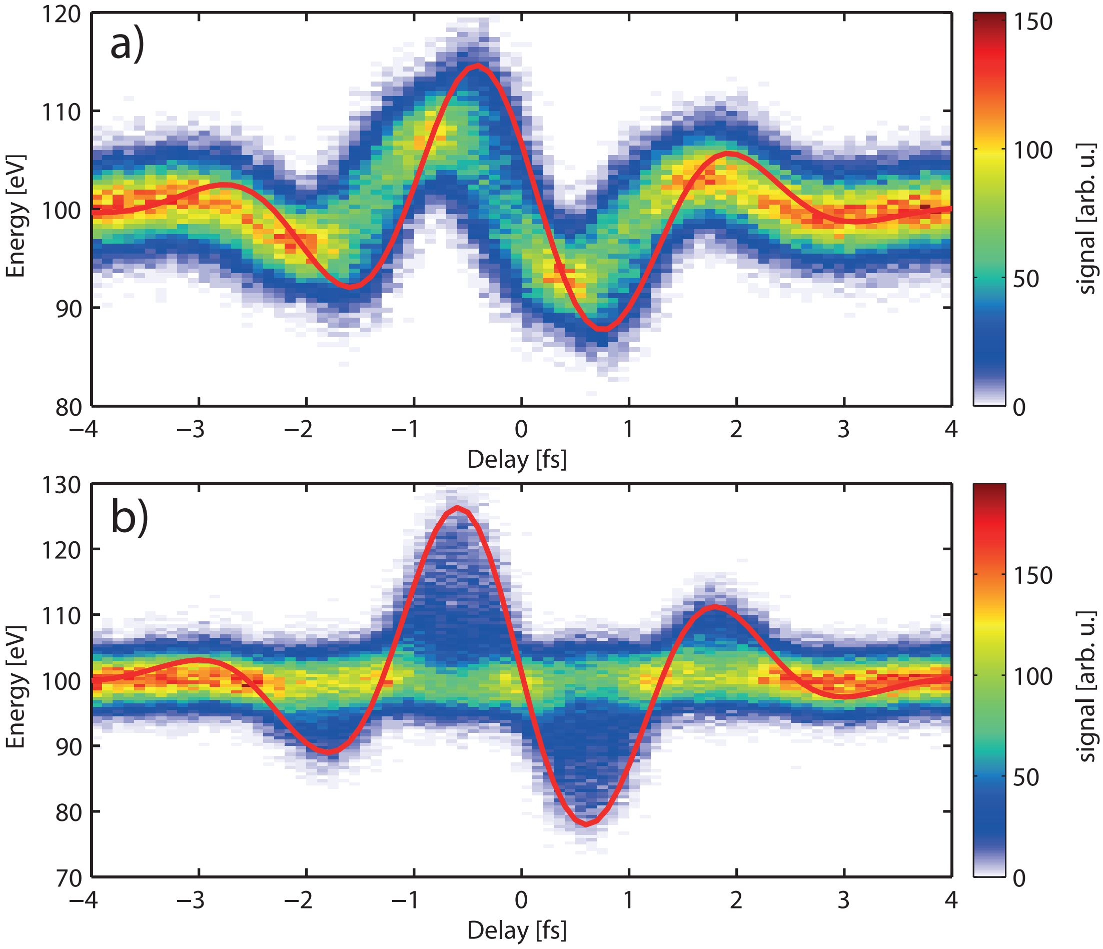

Figure 6.5: Simulated streaking spectrograms for Au spheres for different diameters. a) shows the result for$d$ = 10 nm and b) for 100 nm. The laser pulse is centered at $t = 0$ with a peak intensity of 1×10^{12} W/cm^2, pulse length of 5 fs and central wavelength of 720 nm. The red line indicates the streaking curve for electrons emitted at the particle pole ($\alpha = 0°$). As shown in [122].

can see that trajectories with large α start at almost zero fields and then travel into the dipolar field pattern. After about one half-cycle, the accelerating fields of all trajectories have converged.

For a sphere diameter of 100 nm, the dependence on emission position is even stronger pronounced. Here electrons emitted at $\alpha = 0°$ show a streaking waveform which is phase-offset by $\pi/2$ to the driving near-field indicating that the pulse has decayed temporally before the electron has left the near-field region (ponderomotive character). Going to larger angles α, one finds a rapidly decreasing amplitude but only a minor phase shift. At very large α the amplitude is close to zero while the phase shift abruptly changes to almost π. This reflects the fact, that electrons emitted here probe the dipolar field which is has opposite sign as compared to the driving field.

Assuming the experiment does not have the capability of discriminating the emission position (e.g. a conventional TOF setup), the outcome of a nanoplasmonic experiment will be the superposition of all contributions. This is due to the fact that XUV photoemission is a single photon process which will take place homogeneously over the nanoparticle. In order to simulate the implications of this superposition, a large number of 1.5×10^5 trajectories were integrated for 10 nm and 100 nm spherical gold particles. All experimental parameters that influence the appearance of a streaking spectrogram were taken into account. The attosecond probe pulse was assumed to have a pulse length of 250 as with a spectrum centered at 105 eV and a bandwidth of 7 eV. The emission was assumed to occur from a well defined, narrow valence band. The relative emission probability from the back-side of the sphere was modeled by calculating the transmission of the XUV through the sphere from tabulated data [90].

The results are shown in figure 6.5 a) and b) for $d = 10\,\mathrm{nm}$ and 100 nm, respectively. The smaller Au sphere exhibits a streaking spectrogram with relatively high contrast resembling streaking from a gas target. The contributions from different emission positions on the sphere cause a distortion of the waveform. As expected, the spectrogram from the large 100 nm sphere is drastically different. The streaking features are blurred and the spectrogram has lost its waveform-like character. The initial spectrum is still dominant for all delay times. In overall, the findings are in good agreement with another study on spherical gold particles [123], which takes the plasmon decay time into account.

The question now arises to what extent the information about the plasmonic field can be retrieved from an experimental spectrogram. In the considered case of a single TOF detector, the streaking spectrograms are not easy to interpret if the system is not well known. Nevertheless, major properties of the plasmonic oscillation can still be recovered. Comparing figures 6.4 and 6.5, one finds that the streaking curves of all trajectories cross almost at the same time for each half-cycle. This results in the characteristic periodic spots in the streaking spectrogram. From the period one can directly deduce the frequency of the plasmonic oscillation as proposed by Borisov *et al.* [123]. Also the envelope and thus the lifetime can be recovered from the spectrogram by analyzing the maximum streaking amplitudes at each delay step. Prell *et al.* proposed using the breathing of the XUV features measured by VMI to reconstruct the dipole moment of Ag nanospheres [125].

6.2.3 Target density and count rate approximations

Besides the systematic particularities described above, nano-plasmonic streaking also poses another experimental challenge. This is simply related to the small size and surface areas of nanosystems. The number of electrons emitted per area during one XUV pulse is directly proportional to the atomic absorption cross section σ_a, the number of Au atoms n and the photon flux of the XUV beam I_{xuv}:

$$c_e = n\sigma_a I_{\mathrm{xuv}} = \rho h \sigma_a I_{\mathrm{xuv}}, \tag{6.9}$$

where $\rho = 58.4\,\mathrm{nm}^{-3}$ is atomic density of Au atoms and h is the depth of the emission which is on the order of $h \approx 0.5\,\mathrm{nm}$ for gold [135]. I_{xuv} is dependent on the number of photons in the beam N and the focal spot size r_f : $I_{\mathrm{xuv}} = N\pi^{-1}r_f^{-2}$. The number of photons is usually around 10^5 for a table-top attosecond beamline while the focus size is on the order of a few micrometer [136]. The number of electrons recorded from a spherical particle with radius R is:

$$n_e = c_e R^2 \pi P_d, \tag{6.10}$$

where P_d is the detection efficiency. For a TOF with a full acceptance angle of 45° as used at the AS-5 beamline, this efficiency is roughly $P_d \approx 1\%$. If isolated nanoparticles are used, the overall electron count rate j_e can be written as:

$$j_e = V_i n_e f \rho_{\mathrm{np}}, \tag{6.11}$$

where V_i is the interaction volume, ρ_{np} the density of nanoparticles in the focus and $f = 1\,\mathrm{kHz}$ the laser repetition rate. Assuming one nanoparticle in the focus per laser shot, this gives an average count rate of $j_e \approx 10\,\mathrm{cts/s}$ for an Au sphere with a radius of $R = 50\,\mathrm{nm}$ and assuming a focus radius of $r_f = 3\,\mu\mathrm{m}$.

Count rate tests were carried out by attaching an aerodynamic lens to the AS-5 experimental chamber. SiO_2 spheres with a diameter of 95 nm were injected at the highest possible concentration providing an estimated density of $10^5 - 10^6\,\mathrm{cm}^{-3}$ in the focus. While the nanoparticle ATI photoelectron signal was clearly visible, a scan using only the XUV probe beam showed no significant signal above the background level. As was learned from the VMI measurements, only around 20% of the shots contain a nanoparticle. Considering that the XUV focus at the AS-5 beamline is much smaller as compared to the IR focus in the VMI by approximately two orders of magnitude, the lack of nanoparticle XUV signal is not surprising as the average number of nanoparticles in the XUV focus is accordingly less than 10^{-3}. To improve the effective target density it was therefore decided to use an Au nanotip, which can be kept fixed in the focus, instead of isolated particles. A further advantage is that focus averaging does not need to be taken into account.

6.3 Attosecond streaking from Au nano-tips

6.3.1 Plasmonic properties

In order to know what to expect from a tip streaking experiment, the field distributions were calculated using a commercial FDTD solver (Lumerical FDTD). The incident laser light was modeled as a 4.5 fs (intensity FWHM) pulse centered at 750 nm. Figure 6.6 a) shows the coordinate conventions. The light field was polarized along the y-axis, traveling in x-direction. The tip was oriented along the y-axis with an apex radius of 100 nm. It was assumed that the shaft is a perfect cylinder. The maximum field enhancement maps are shown for the xz-plane in Fig. 6.6 b), the xz-plane in c) and the yz-plane in d). The maximum field enhancement at the tip apex is 2.5. Field bending towards the back

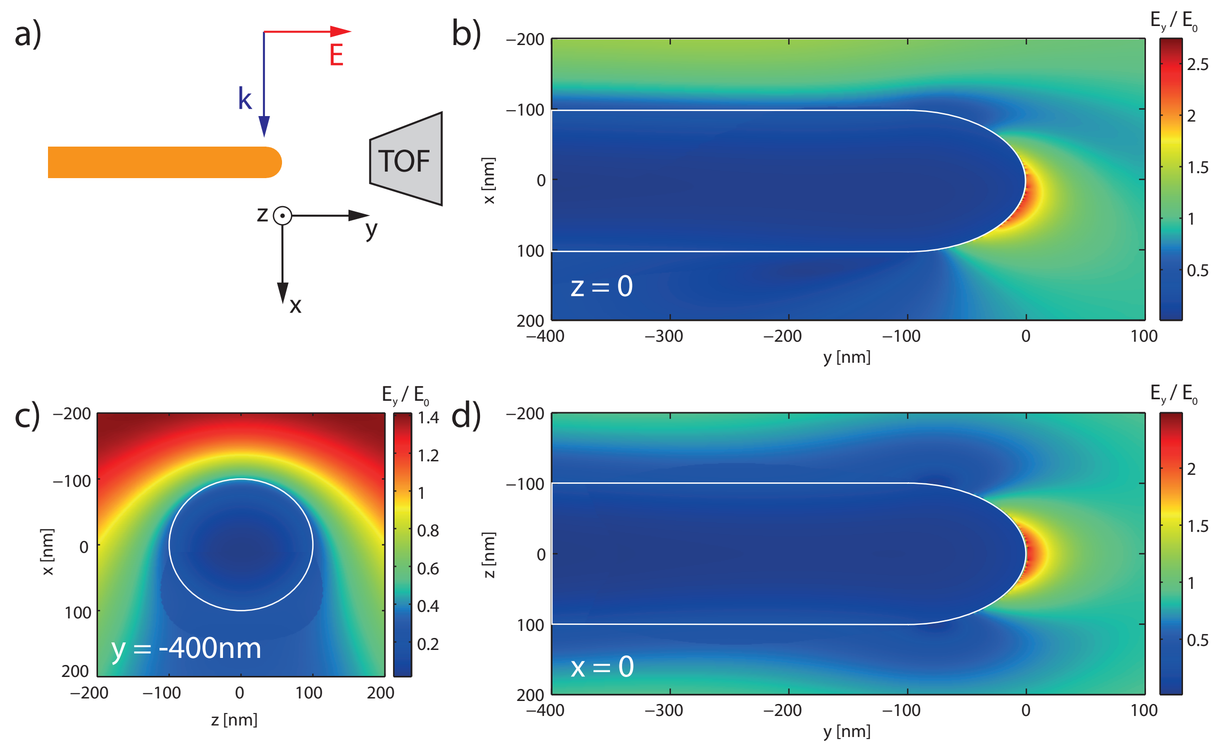

Figure 6.6: a) Coordinate conventions for Au tip simulations and experiments. The tip is oriented along the y-axis. The incident field is traveling along the x-axis and polarized along the y-axis. b) Maximum relative field enhancement of E_y in the xz-plane calculated by FDTD for a 4.5 fs pulse. c) Same plot for the xz plane at $y = -400\,\text{nm}$ and d) for the yz-plane ($x = 0$).

of the tip similar to the large SiO_2 nanoparticles can be observed in a). The effect is slightly more pronounced as compared to the 200 nm diameter SiO_2 spheres which can be attributed to the material properties. As can be seen in Fig. 6.6, the tip effectively shields its backside. Note, that also the fields at the front side of the cylindrical part are significantly suppressed. This can be attributed to the superposition of the incoming wave with the reflected (scattered) wave, which is phase shifted by almost π. Leaving the tip apex along the y-axis, there is only a slight variation of field strength and temporal profile. The FDTD simulations show however that a traveling surface plasmon is excited by the interaction with the laser pulse. Therefore a slight distortion (especially on the back side) appears. Concerning the timing of the fields, one finds a slight delay of the oscillations at the tip apex with respect to the incident field of roughly 300 as. At the "side" of the tip ($x = -101\,\text{nm}, y = 300\,\text{nm}$), the oscillations are effectively advanced by about 350 as. This phase shift is quite homogeneous around the front side of cylinder ($x < 0$). The FDTD results for large y-values agree with Mie theory predictions for an infinitive long cylinder (when neglecting the SPP). Using the Mie code by Schäfer *et al.* [137] to calculate the near-field profile a similar phase shift of 340 as is observed for a 4.5 fs laser pulse.

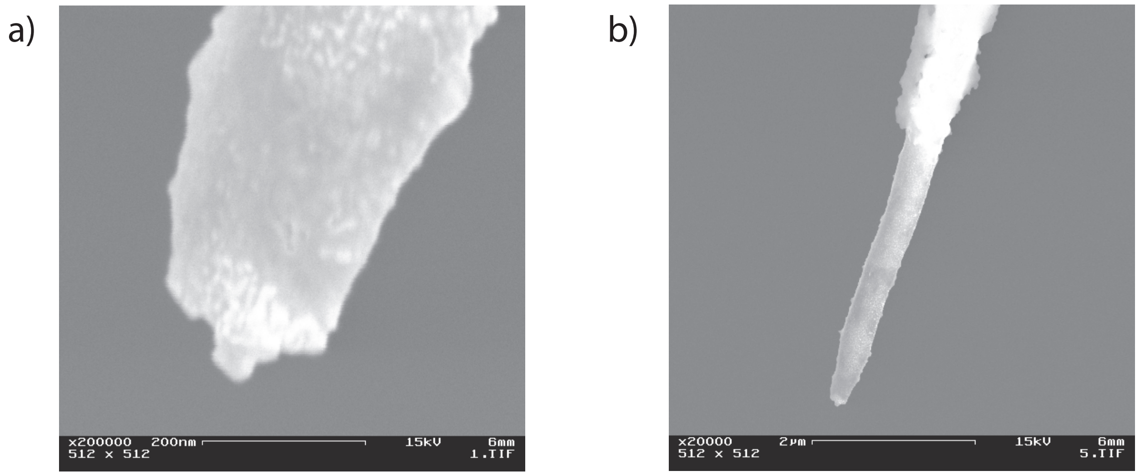

Figure 6.7: a) and b) Scanning electron microscope images of the Au tip used for the streaking measurements. (Courtesy of M. Förster)

6.3.2 Streaking experiments

Streaking experiments using a gold nanotip were carried out. The tips were fabricated by electrochemical etching by the group of Prof. Peter Hommelhoff (Max-Planck-Institut für Quantenoptik, Garching) [138]. Fig. 6.7 shows scanning electron microscope (SEM) images of the Au tip. The tip radius was chosen to lie around 100 nm in order to obtain sufficient count rates. As can be seen this requirement is met and the tip apex radius is close to this value. The cylindrical shank of the tip exhibits a very uniform shape which extends at least $3\,\mu$m from the apex with an approximate radius between 100 and 150 nm. This assures a very homogeneous response of the tip. The SEM images were taken after the streaking measurements, such that excessive laser induced damage during the streaking experiments can be ruled out. One can see some surface contamination (white spots) on the tip which most likely are leftovers from the fabrication process. The constituents of this contamination could not be determined.

The tip was oriented along the laser polarization axis in front of the TOF and could be moved by open-loop piezo stages in all three dimensions. The achieved count rates illuminating the tip shown in figure 6.7 only with the XUV attosecond pulse varied between 0.04 and 0.1 cts/shot (full spectrum) depending on the XUV flux. A typical electron energy spectrum with both NIR and XUV light incident on the tip is shown in figure 6.8 a). The NIR intensity was set to values of $5-10\times10^{11}\,\mathrm{W/cm^2}$. The resulting photoelectron energy cutoff was correspondingly around $13-15\,$eV. Unlike streaking in Ne, the XUV part of the spectrum shows a broad distribution starting around 93 eV and peaking at 80 eV. The lack of features is in parts the result of the solid state target. Streaking experiments from clean tungsten surfaces shows broadened spectral lines due to the width of the density of states [139] and secondary electrons. A further contribution to the broadening are

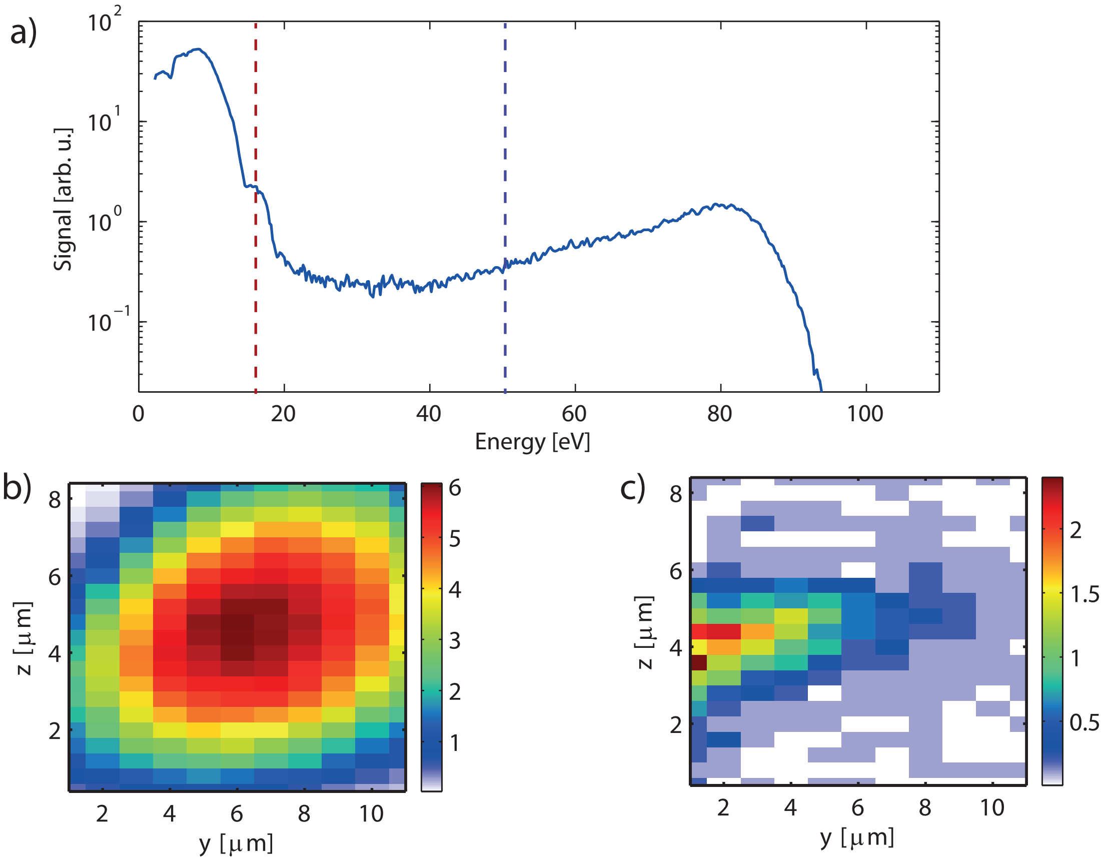

Figure 6.8: a) Typical photoelectron electron spectrum from the Au tip under both NIR and XUV irradiation. The NIR photoelectron cutoff is indicated by the red dashed line. b),c) Position scan of the tip in the sample along y- and z-axis. The signal in b) contains energies up the photoelectron cutoff indicted by the red line dashed line in a). c) contains of electrons with energies higher than 56 eV as indicated by the blue dashed line in a).

surface contaminations originating from the fabrication process or deposited background gas. The pressure in the experimental chamber was 10^{-7} mbar during the experiments. As the illumination with the NIR beam and the effective heating is likely to remove parts of this contamination, its exact influence is not known. With the higher ionization potential of the additional materials, the Au valence band which is to be expected at around 90 eV is likely to be blurred especially towards lower energies. It has to emphasized here, that a thin contamination layer will only slightly alter the plasmonic response.

Due to the low XUV count rates from the Au tip, usage of the TOF lens system was essential for the experiments. The overall observation is that the scaling of lens voltage to transmission window was still comparable to photoemission from Ne gas. Nevertheless, the field bending character (lightning rod effect) of the tip apex might result in a further broadening of the spectrum caused by a slight dependence of the acceptance angle and/or

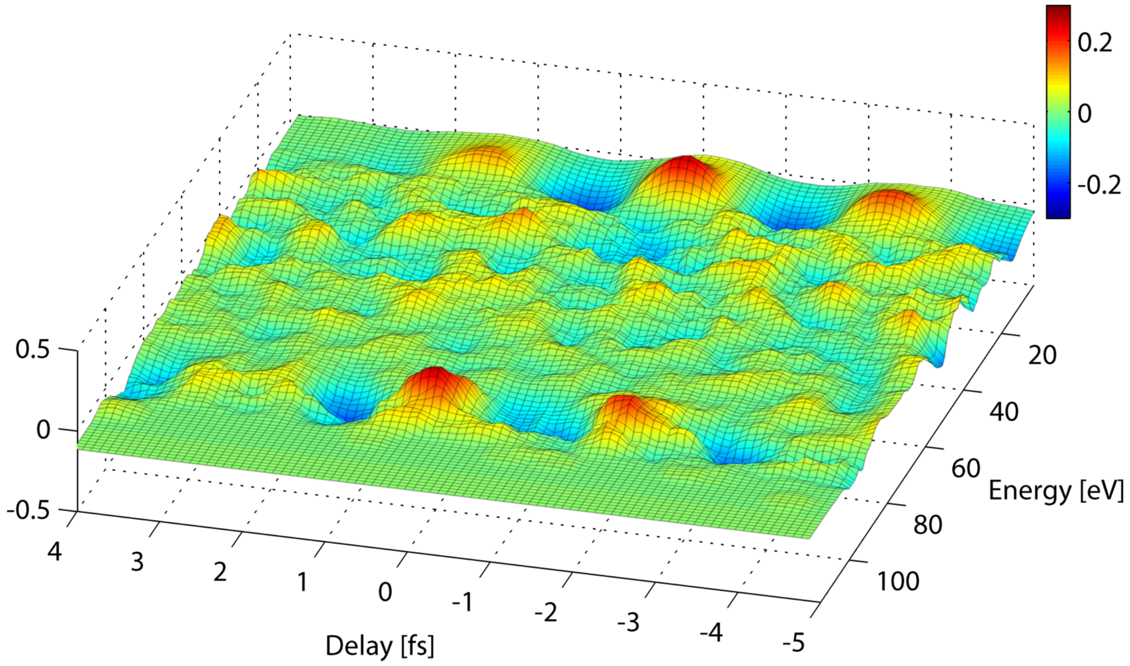

Figure 6.9: Relative difference streaking spectrogram measured from the Au tip at $I \approx 7 \times 10^{11}\,\mathrm{W/cm^2}$. The modulation at low energies originates from the interference of pump and leakage NIR beam. The features at high energies is created by XUV electrons streaked to higher energies.

time-of-flight on the emission position.

A crucial aspect in the tip streaking experiment is the correct positioning of the tip in the focus. Along the laser propagation axis, this poses no major problem. Here the tip could be positioned by eye in the center of the TOF with an estimated accuracy of better than 0.5 mm and further be optimized with the help of the electron count rates to find the focus of the electrostatic TOF lens. The correct alignment in the laser polarization plane was more difficult. Due to its small size, the front part of the tip only caused some minor interferences in the focus imaging system. The rear part could well be observed, which served for rough positioning. For fine alignment the strong enhancement of the NIR field at the tip apex could be utilized. The NIR laser field intensity was set to values around $1 \times 10^{12}\,\mathrm{W/cm^2}$. The tip apex could now be moved into the laser focus by simply optimizing the NIR photoelectron count rates. Figure 6.8 b) and c) shows the integrated signal of different spectral regions while scanning the tip through the focus in the yz-plane. The image in b) was obtained from the low energy part of the spectrum (indicated in a)) which is mostly composed of NIR photoemission. The high energy region is shown in c) which exclusively originates from XUV induced photoelectrons. Both images result from a single scan. The figures show clearly, that the tip is not resonant with the XUV attosecond pulse in any form and photoemission is a single photon process. This results in direct imaging of the tip shape comparable to a knife-edge measurement. The NIR photoemission on the other side shows the hot-spot nature of the tip apex. Here count rates are drastically increased due to the local field enhancement. The images indicate that the NIR spot is (as expected) significantly larger than the XUV focus. Note however, that the scales are only approximated with the step size of the open-loop stages (Mechonics MS-30) as communicated by the manufacturer.

Due to the low count rates, the acquisition of pump-probe streaking measurements was challenging. This is of course mainly due to laser and CEP stability. For each scan set, the tip was exchanged with the gas target at least once and a reference scan was acquired with the same intensity and CE phase. Measurements on the tip were then done by acquiring spectrograms with delay step of 100 as and acquisition time of 4000 shots per time step until the CEP stabilization failed and the system had to be restarted. All acquired scans were then superimposed to obtain a single spectrogram. Note, that the full intensity of the IR beam was sent to the HHG target to maximize the XUV flux. This resulted in an XUV spectrum that extended up to 110 eV. Despite this high cutoff, the reference scans still do not show noticeable satellite pulses. Even with long acquisition times ($> 10^5$ shots per delay step), the signal-to-noise ratio is quite low due to the vanishingly small count rate and a possible unstreaked background. Consequently, the streaking features are not very pronounced in the resulting streaking spectrograms. A better visualization of the spectral features is provided by the relative difference spectrogram which is defined as

$$R(E, t_d) = \frac{S(E, t_d) - \langle S(E) \rangle}{\langle S(E) \rangle + \beta}. \tag{6.12}$$

Here, $\langle S(E) \rangle$ denotes the average (of all delay steps) of the streaking spectrogram for an energy bin E. To assure finiteness, a small number β is added in the denominator. Figure 6.9 shows the relative difference spectrogram for an intensity of 7×10^{11} W/cm^2. One can see a strong modulation in the NIR photoelectron part of the spectrum at low energies. This can be attributed to the cross-correlation of the NIR beam from the outer mirror and the NIR leakage through the Zr filter. Such an interference is usually not visible in streaking spectrograms in Neon. Due to the much higher NIR intensities used for streaking in gases, the relative strength of this modulation is much lower here. The nature of the correlation seen in Fig. 6.9 is rather complicated. First of all the 15 μm thick pellicle filter induces an effective CEP shift of about 100° in the outer NIR beam. The beam leaked through the Zr suffers from spectral narrowing especially at wavelengths lower than 900 nm. A distortion of the waveform is the consequence. As the position of the peaks of such a cross-correlation is dependent on the individual CEPs of both pulses, the features can thus not be used for the calibration of the timing. In the high energy region starting from 84 eV, the relative difference spectrogram exhibits another modulation which is caused by streaking in the near-fields. The features are different from a usual streaking spectrogram as they do not show a clear shift of a photoline. This is due to the broad and undefined XUV photoelectron spectrum. Electrons streaked to lower energies (positive vector potential) are likely to disappear in the strong background (and possibly a phase offset) signal. If the electrons are streaked to higher energies, they will appear in a region with low signal,

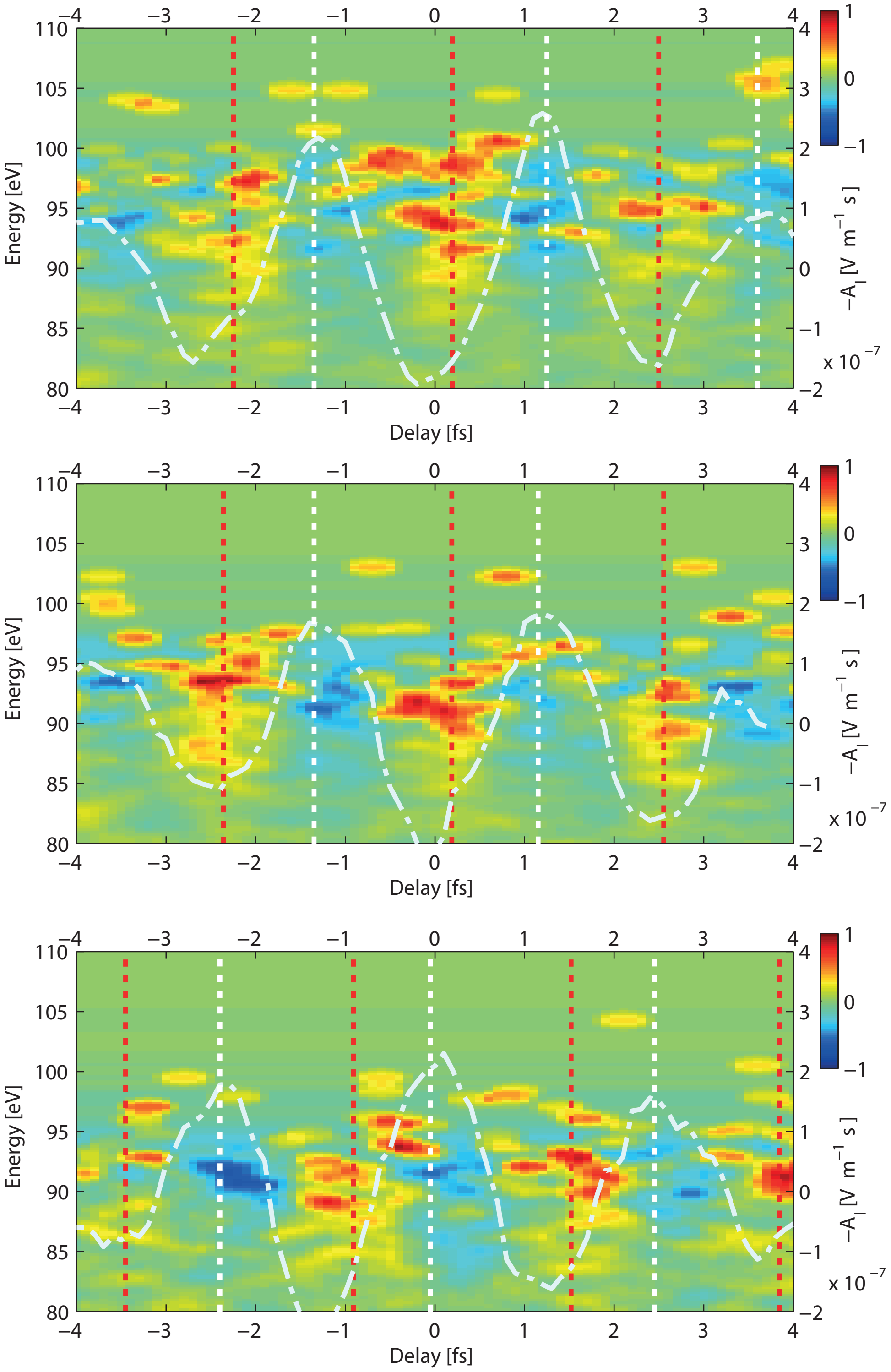

Figure 6.10: Three relative difference spectrograms obtained at a peak NIR intensity of 7×10^{11} W/cm^2. The negative vector potential of the reference scans are overlayed (white dash-dotted line). The timing of the central tip streaking features are indicated by the vertical red dotted line. The corresponding times for the reference scans is shown by the vertical white dashed line. a) and b) had a CE phase of $\phi_{\text{ce}} \approx -\pi$ while in c) $\phi_{\text{ce}} \approx 0$.

Scan name	CE phase ϕ_{ce}	Δt	Shots per delay	XUV Counts per delay
506to513	0	-1.1024	16000	470
540to547	$-\pi$	-0.98654	28000	1520
550to554	0	-0.94686	20000	570
562to565	0	-0.94118	16000	540
569to571	0	-1.0509	12000	430
577to599	$-\pi$	-1.0181	68000	2010
sum		-1.0076	160000	5540

Table 6.1: List of tip streaking measurements with obtained shift of reference scan to streaking features.

so this contribution shows a higher contrast. It was found that only the streaking features to higher energies (negative vector potential) are visible in the experiment. Note, that parts of the relative difference spectrogram also can be negative as the average $\langle S(E) \rangle$ is composed of all delay steps.

Figure 6.10 shows the high energy part of three scans at the Au tip. For each set of tip scans, at least one reference scan with the same laser parameters was taken using Neon. The negative vector potential from these Ne scans is plotted for comparison (white dash-dotted line). One can see that there is a delay of the (negative) vector potential with respect to the streaking features of the tip. This temporal shift has an average value of $\Delta t \approx 1 \pm 0.06\,\mathrm{fs}$ and is consistently reproduced in all scans regardless of the phase of the driving laser field (see table 6.1). Due to the low contrast in the experimental data, it could not be determined to what extent this temporal shift of the oscillations is caused by an effective CEP shift of the near-field streaking features or by a true temporal shift of the near-field envelope. Compared to the reference scan, the tip streaking features do not show noticeable prolongation of the pulse. Also, the period is exactly that of the reference measurement. Some counts are apparent at higher energies exceeding 95 eV, but the signal strength is barely above the average count rate without NIR pump beam applied.

In order to obtain better statistics all scan sets were superimposed. For this superposition, the individual spectrograms were shifted along the delay axis to align all central streaking features. Note, that this results in a mixing of measurements with different CE phases such that the overall envelope is not necessarily preserved and therefore cannot be used in the analysis. It is nevertheless to be assumed that the streaking signal of the individual half-cycles does not differ for different CEPs. The summed streaking spectrogram is shown in figure 6.11 a). Due to the much higher signal-to-noise ratio the streaking pattern can also be observed in the traditional streaking spectrogram. The corresponding relative difference spectrogram is shown in b).

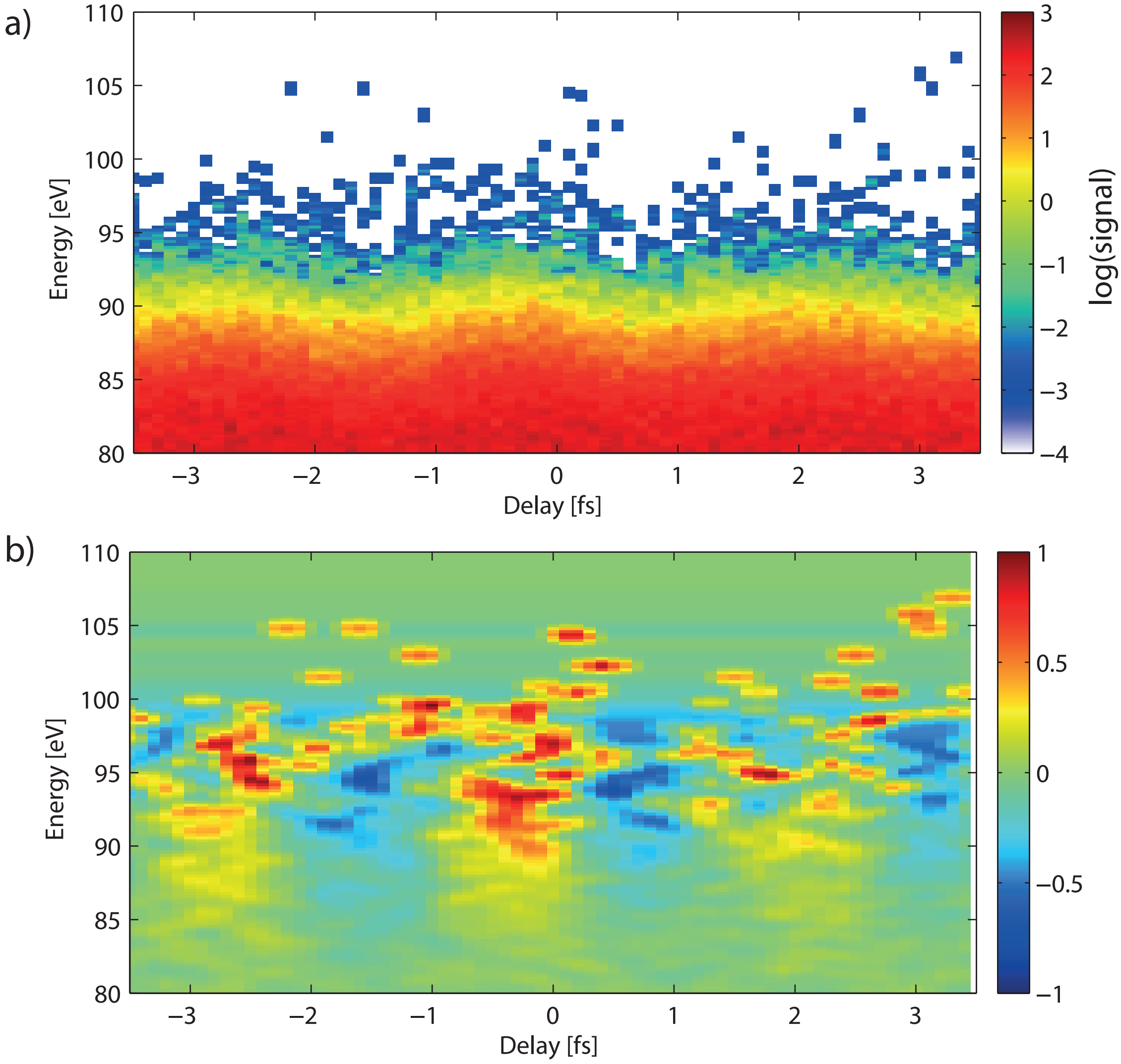

Figure 6.11: a) Streaking spectrogram (logarithmic color scale) of all experimental scan sets superimposed. b) Relative difference spectrogram for the data shown in a).

6.3.3 Interpretation

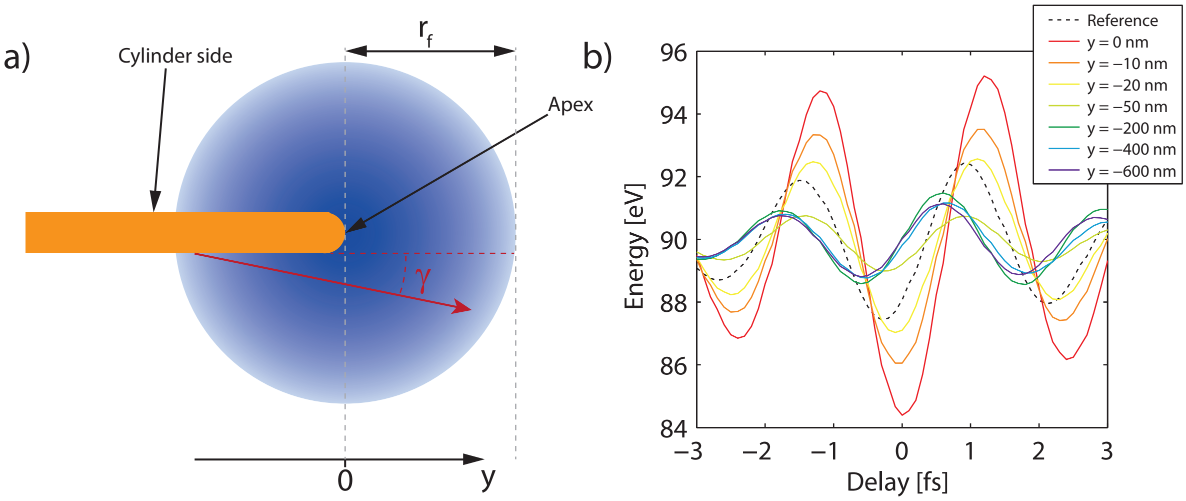

Figure 6.12: a) Illustration of the size of XUV probe pulse relative to the Au tip. b) Simulated streaking curves for various emission positions for $E_{\mathrm{kin}} = 90\,\mathrm{eV}$ and a peak laser intensity of $I = 7 \times 10^{11}\,\mathrm{W/cm^2}$. The emission angle was set to $\gamma = 4°$.

Fig. 6.12 a) shows the assumed geometry of the experiment. As the probe XUV beam diameter is in the range of a few micrometer, it will significantly illuminate the side of the tip. In the following, the ”side” of the tip refers to all positions with $y < -100\,\mathrm{nm}$. For geometric reasons and the fact that XUV photoemission is a single photon process, most electrons will be emitted from this cylindrical shank. Assuming a $2\,\mu\mathrm{m}$ probe beam diameter, the cross section of the tip apex is less than 1% as compared to the side. As was mentioned before, the local electric fields on the cylinder surface are comparable both in strength as well as temporal evolution. Therefore it is most probable that the observed streaking features originate from the side of the tip. This is supported by the unchanged period of the oscillation and no noticeable prolongation, which indicates that no resonant behaviour is observed.

In order to find more proof about the origin of the experimentally observed streaking features, streaking from the Au tip was numerically simulated in analogy to the Au spheres presented in section 6.2.2. The temporal field distribution was obtained from FDTD simulations. Due to large amount of data, the emission and trajectory integration was limited to the xz-plane. The intensity was chosen to be $7 \times 10^{11}\,\mathrm{W/cm^2}$. The electron's initial kinetic energy was set to $E_{\mathrm{kin}} = 90\,\mathrm{eV}$ and the angle of emission γ (to the y-axis) was fixed at 4°. Note, that no strong dependence on this emission angle could be found for any emission position indicating that streaking takes place in the ponderomotive regime. Streaking from selected positions for these parameters is shown in Fig. 6.12 b). A reference streaking waveform was acquired from a second run without the tip in the simulation volume (black, dashed curve). As expected, emission from the tip apex ($y = 0$) results in the highest streaking amplitude. The phase shift with respect to the reference is equivalent to 300 as. A similar observation as with the large Au spheres is made when turning to the cylindrical shaft $y < -100\,\mathrm{nm}$. Here the amplitude is decreased and a shift to earlier delay times is observed. The time/phase shift converges to a value equivalent to -350 as as compared to the reference. As can be seen all streaking curves for $y < -100\,\mathrm{nm}$ are quite similar. This is a direct consequence of the homogeneous field evolution at the side of the sphere. Tests for different planes (xz , yz) showed that the streaking signal from the cylinder region does not change significantly over the whole surface of the cylinder. The general observation is that streaking takes place mostly in the ponderomotive regime, due to the very extended fields (compare to Fig. 6.6).

For comparison with the experimental spectrograms, 10^7 trajectories with randomized birth position y between 0 and $-400\,\mathrm{nm}$ were integrated. The launch angle γ was uniformly distributed between 2 to 40° with respect to the y-axis. The initial energy was randomized such that on average the experimentally observed distribution was reproduced. A comparison between experimental and simulated data is shown in Fig. 6.13. For reference, the experimental data is shown in a) and b) in an absolute and relative difference form, respectively. Note that these plots are a just slightly smoothed versions of the data shown in Fig. 6.11. The simulated data is shown in the same form in c) and d). This simulated streaking spectrogram was shifted along the time axis for best overlap with the experimental data.

In overall, there is good agreement between experiment and simulation. As expected, the analysis of birth position shows, that the pronounced streaking features in the simulated spectrograms are caused by electrons emitted from the cylindrical region ($y < -100\,\mathrm{nm}$). The contributions from the tip apex cause the small signal streaked to higher energies (indicated in the figure). This is especially visible in the relative difference spectrogram. The temporal shift of the tip apex contribution with respect to the cylinder region streaking signal is in agreement with the results from Fig. 6.12 to be around 700 as. Similar features at higher energies are also observable in the experimental data especially in the relative difference spectrogram. Nevertheless one has to mention that the signal in this region is just above the background level. To obtain the amplitude of the streaking features, the average spectrum was fitted to both experimental and simulated streaking spectrogram with an energy shift ΔE as free parameter. The results are shown Fig. 6.13 in e). In overall, there is good agreement. The experimental curve extends less to negative energies which is caused by the strong unstreaked background. Despite the agreement in amplitude and even some traces of the tip apex signal, the phase/temporal shifts do not match. As explained before, the experiment shows a reproducible average shift of $\Delta t \approx -1\,\mathrm{fs}$ while the principal streaking features of the simulations yields $\Delta t \approx -350\,\mathrm{as}$.

Systematic errors might result from an incorrect alignment, which is not surprising as a time span of 700 as correspond to a distance of only 200 nm. One possible systematic error is a slightly different position along the laser axis when switching from the gas target to the gold tip. This is very unlikely though, as all scans show about the same temporal shift. Also, by taking streaking spectrograms with the gas target at different positions along the whole opening of the TOF detector of $\Delta x = 3\,\mathrm{mm}$ through the focus it was found that the streaking traces are delayed by at most 200 as. Another possible reason for an observed

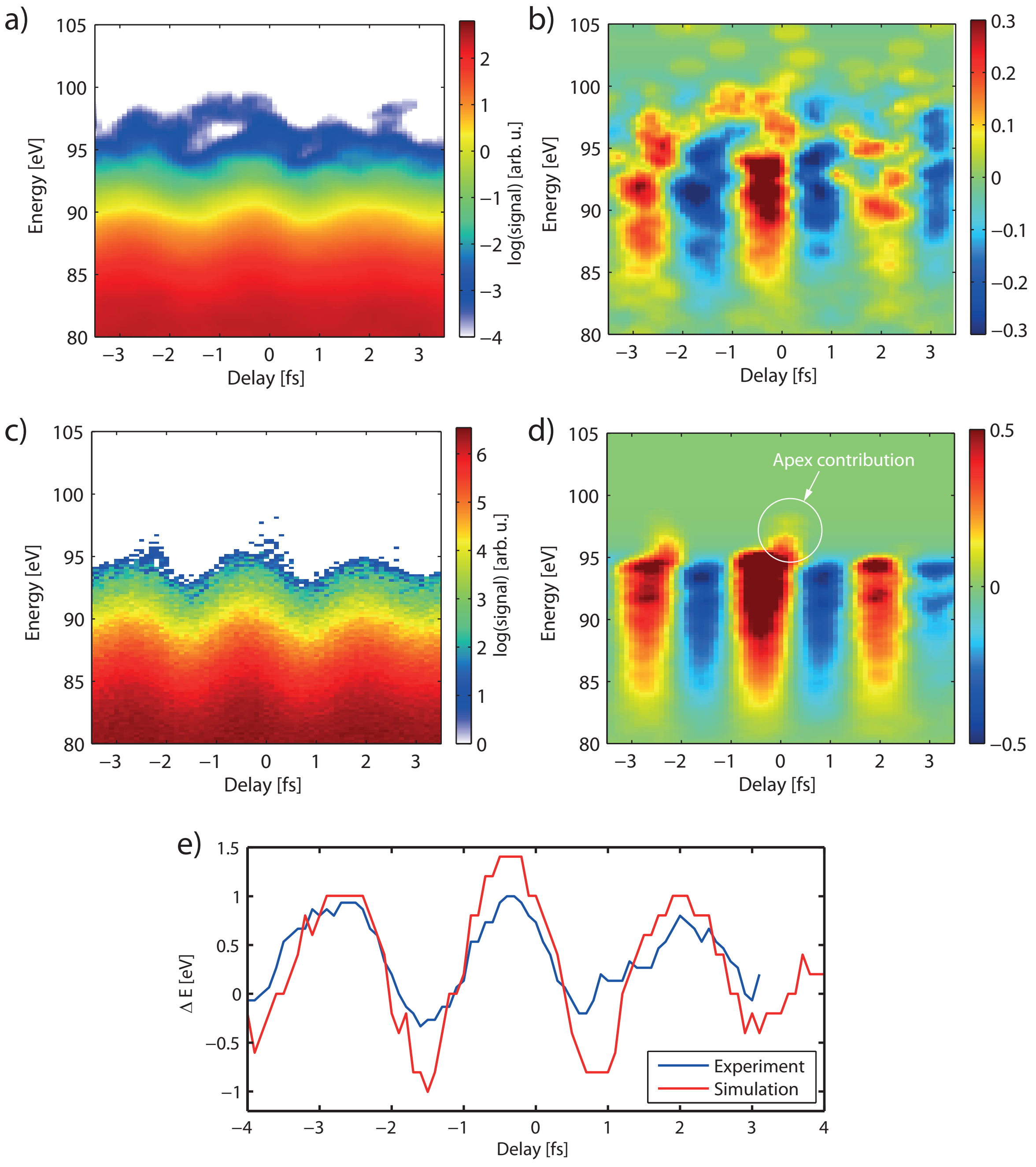

Figure 6.13: a) Smoothed, experimental streaking spectrogram (logarithmic color scale). b) Relative difference streaking spectrogram of a). c) Simulated streaking spectrogram and d) corresponding relative difference streaking spectrogram. e) Retrieved streaking amplitude for experiment and simulation.

shift of the streaking features are wavefront distortions, as the tip mainly samples the fields at the edge of the NIR focus. As mentioned in chapter 3.6.2, the XUV focus lies in front of the IR focus along the laser propagation axis. Therefore one can expect the wavefronts to be slightly spherical. As the NIR beam is likely to show inhomogeneities especially at its tails and suffers from astigmatism the sampled waveform might further be disturbed. A major contribution to the temporal shift can be found in the propagation of the pump beam through the Ne gas cloud will affect the relative timing. For taking the reference scan, the backing pressure to the gas target was set to 1.5 bar and the pressure in the experimental chamber rose from 1.1×10^{-7} mbar to 7.3×10^{-5} mbar. Despite the small index of refraction of Ne of $n_{\mathrm{Ne}} \approx 1.0006$ in the optical [140], a travel distance of 1 mm through Ne ($p = 1$ bar) will cause an effective delay of -200 as between pump and probe. The probe will be not affected as the index of refraction in the XUV region can be assumed to be much closer to unity [90]. A more quantitative analysis would of course require knowledge of the exact pressure distribution around the gas target.

Further delay shifts are to be expected from to the surface streaking process. Here, it must be noted that there is so far no systematic study on a possible delay in photoemission between single atoms and the delocalized valence electrons of a metal surface. The photoemission characteristics from Au are likely to be comparable to that observed in Mg [139, 135]. Due to the bulk nature of the sample, electrons can be emitted up to a few Angstroms into the material. Assuming a strong shielding of the electric field in the material, this would lead to an effective temporal shift as electrons emitted deep inside the material need to travel to the surface first before being streaked. For $E_{\mathrm{kin}} = 90$ eV and $d = 0.6$ nm [135], this results in a temporal shift of about 100 as. The superposition of all emission depths will reduce this value. The question here of course also lies in the geometry. The detected electrons are emitted under a small angle to the surface, so the effective time shift is hard to approximate with classical means. Also, the undefined XUV photoelectron spectrum might be related to this special experimental geometry. XUV photoemission is likely to be directed dominantly normal to the surface, because emission is not limited to the surface. As the detector axis is parallel to the surface for the cylindrical tip structure, the detection efficiency for electrons scattered near the surface might be increased. Such an effect will also contribute to the broadening and blurring of the XUV photoelectron spectrum.

The last possible source for deviations is the possibly incorrect modeling by the FDTD approach. A simulation of a tip with a conical shaped shaft yields questionable results, as numerical artifacts (”hotspots”) appear on the surface which are caused by the misalignment of surface and (rectangular) simulation grid. In reality, it is of course possible that tip shape and local imperfections of the tip will also influence the near-field evolution (compare to Fig. 6.7). A misalignment of the tip with respect to the polarization axis will also influence the plasmonic response as now a field component normal to the surface appears.

6.4 Conclusions and outlook

In this chapter it was shown that attosecond streaking from nanosystems can differ strongly from the tradition gas-phase streaking due to the localized nature of near-fields and inhomogeneous distributions. First experimental evidence using Au tips measured at the AS-5 beamline shows features of sub-micrometer near-fields imprinted on the XUV electron spectra. A phase/time shift relative to reference scans was observed, which deviates from (classically) simulated streaking spectrograms obtained in combination with FDTD simulations. The experimental data shows traces of the tip apex field enhancement.

Due to the low count rate, nanoplasmonic streaking will benefit from further developments in attosecond science in terms of XUV photon flux and repetition rate. Using fixed nanosystems such as the Au tips as targets liberates from the requirement of long focal lengths, as the XUV photoemission is highly localized along the laser propagation axis and Gouy phase shifts do not play a role. This would enable a much tighter focusing of the probe beam resulting in higher count rates.

Due to the unknown spatial and temporal properties of the pump NIR focus and some uncertainty of the emission distribution of photoelectrons the interpretation of the presented streaking results remains difficult. It can thus be concluded, that an improved experiment needs to target on resolving these issues. This requires a highly localized probe XUV beam with good focus quality such that photoemission can be limited to a small area on the sample. In addition, a homogeneous, extended NIR pump beam would also be beneficial to prevent any ambiguities caused by a possible NIR waveform distortion. The localization of the XUV beam will also help in increasing count rates and the relative signal strength of regions of (resonant) field enhancement. Such an approach could also target on the spatial scanning of e.g. a tip sample with a fixed NIR beam position. This could enable the observation of traveling surface plasmons. Progress in fabrication of tip structures as shown in [141] will enable a further tailoring of the plasmonic properties, which in a first step could be used to answer the question of the photoelectron's origin. Once characterized, a specially designed tip might serve as a probe for measuring the light field transient in sub-micron spatial dimensions. Using simple, isolated systems such as Au spheres would also eliminate contributions from the cylindrical part of the sample. An experimental realization nevertheless requires high target densities and/or a strong XUV source. Also techniques like VMI which offer more information about the photoelectrons origin could be used to bridge the gap until true spatial imaging by e.g. PEEM can be achieved.

Appendix A

Data analysis

A.1 Calibration of velocity map images

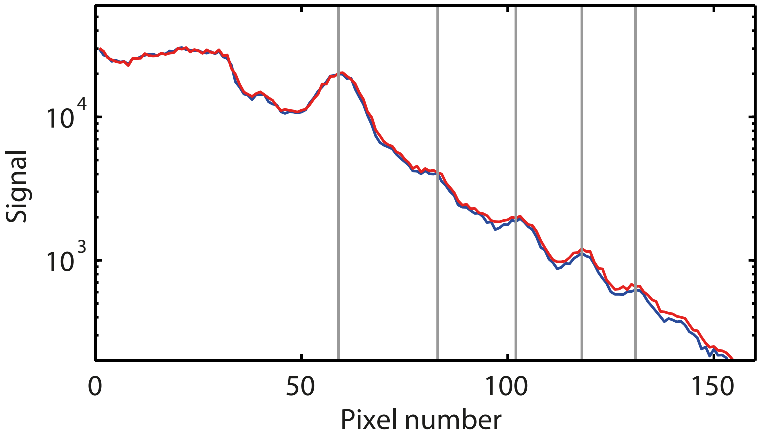

Figure A.1: Illustration of the VMI calibration (Xe scan at 2.5×10^{13} W/cm^2). The signal on both sides of the polarization axis is shown by the blue and red line. The periodic above-threshold-ionization pattern is marked by the grey lines.

The position of the electron event on the VMI detector screen is proportional to its momentum. As the device records an image, a scaling parameter $c = p/x$ between pixel number x and physical momentum p has to be determined. Typical ATI spectra exhibit a modulation with a spacing of $\Delta E = \hbar\omega$ (especially for longer pulse durations), where ω is the laser frequency. This pattern can be used for calibration of the device if the central laser wavelength is known. Fig. A.1 shows the signal on both sides of the laser polarization as a function of pixel number to the center. The scan was acquired from Xe gas at an intensity of 2.5×10^{13} W/cm^2. The grey lines indicate the periodic features. Assuming a central wavelength of 720 nm, the spacing between two peaks should be equal to $\Delta E = (p_n^2 - p_{n-1}^2)/2m_e = c^2(x_n^2 - x_{n-1}^2)/2m_e \approx 1.72\,\mathrm{eV}$. The scaling factor between pixel distance and momentum (in atomic units) can therefore be obtained as $c_n = \sqrt{1.72/(13.6055(x_n^2 - x_{n-1}^2))}$, where x_n and x_{n-1} are the positions of the features in pixels. The final calibration factor is obtained by averaging all observable features: $c = \langle c_n \rangle$.

A.2 Statistical rebinning of single shot CE measurements

In order to retrieve accurate CEP measurements, the rebinning algorithm proposed by Sayler *et al.* was used [68]. The directly measured angle θ in the parametric asymmetry plot as a function of the two asymmetry values A_1 and A_2 (see equation (3.6)) is

$$\theta = \arctan(\frac{A_1}{A_2}), \tag{A.1}$$

which is not homogeneously distributed. This is evident in the angular density of laser shots $\rho(\theta)$. The number of shots in an infinitesimal small angular bin is $\rho(\theta)d\theta$. For an uniformly distributed distribution $\phi(\theta)$ this would be $\langle\rho\rangle\, d\phi$, where $\langle\rho\rangle$ is the average density. As the two must be equal, this enables the derivation of the mapping $\phi(\theta)$:

$$d\phi = \frac{\rho(\theta)}{\langle\rho\rangle} d\theta \Rightarrow \phi(\theta) = \phi_0 + \int_0^\theta \frac{\rho(\theta')}{\langle\rho\rangle} d\theta'. \tag{A.2}$$

The offset ϕ_0 can be chosen to be zero, as there is also another global offset between phasemeter and main experiment. The integration in equation (A.2) needs to be done numerically. To do so, the θ values of 10^5 laser shots are distributed in typically 360 bins. After normalization, the integration can readily be done creating a direct mapping which utilizes linear interpolation. The *vmi_analysis* program contains the C-routines for the whole operation.

A.3 Calibration of the AS-5 TOF

For calibrating of the time-of-flight instrument at the AS-5 beamline and the conversion from TOF to energy spectra, the following steps were performed:

- The zero time was determined by moving the gas target into the laser beam at a relatively high intensity. Doing so, the signal contained a strong light peak from which the electron birth time could be deduced.
- The TOF flight spectra was converted into the energy domain. Simulated flight times obtained from the manufacturer (Käsdorf, Geräte für Forschung und Industrie) were used for the mapping between time and energy. As these mappings only contain a

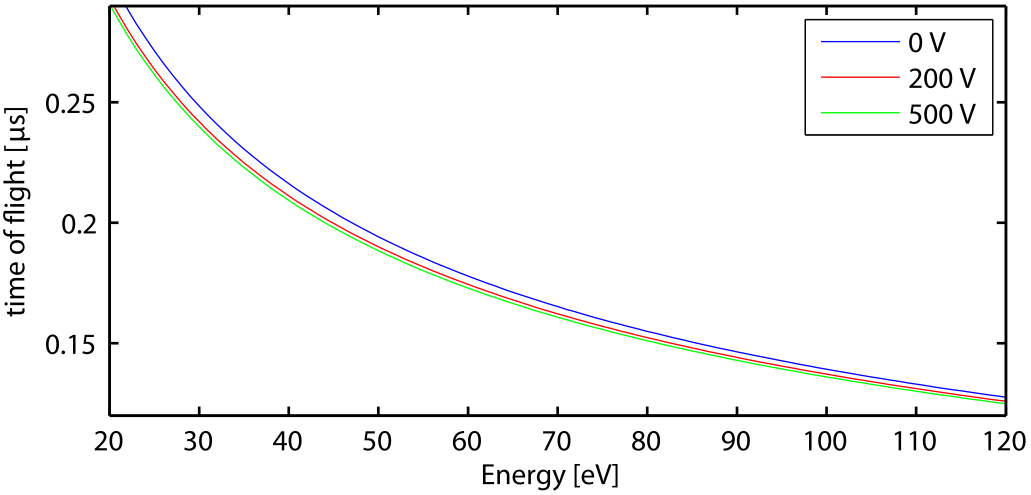

Figure A.2: TOF calibration curves for various lens voltages.

certain set of lens voltages, the kinetic energy was obtained by 2D interpolation (lens voltage and time of flight). Fig. A.2 shows the mappings for various lens voltages. Outside the tabulated TOF energy region, a fit to the tabulated data was used.

- The obtained spectrum $S(E)$ was rescaled by the derivative of the time-energy relationship $|dt/dE|$ to obtain the correct distribution.

Appendix B

Data Archiving

The experimental raw data, evaluation files, and original figures can be found on the Data Archive Server of the Laboratory for Attosecond Physics at the Max Planck Institute of Quantum Optics:
`/afs/rzg/mpq/lap/publication_archive`

Refer to `ReadMe.txt` for an overview and instructions how the codes are used. Note, that due to size constraints only preprocessed data is archived here. The complete raw data is available from Prof. Matthias Kling. The list below contains paths to all the relevant files given with respect to the root folder of the thesis.

Figure 2.2

▶ plot script	`chapter2\plotEpsAu_drude.m`

Figure 2.5 a)

▶ Data	`chapter2\fieldMaps\`
▶ C Program	`software\fieldMaps\`
▶ plot script	`chapter2\plotMaps_ex.m`

Figure 2.5 b)

Data obtained by SPlaC Mie Code

▶ plot script	`chapter6\sphere_simulations_prb\plotAllFigures.m`

Figure 3.2

▶ Laser spectra	`chapter3\laser_spectra\`
▶ Spectra plot script	`chapter3\plotSpectra.m`
▶ Waveform script	`chapter6\streaking_data\auswertung_493.m`

Figure 3.5

▶ PAP plot script	`chapter4\analysis_scripts\plotPhasePotato.m`

Figure 3.9 and 3.10

Experimental data from Xe

▶ Experimental data	`chapter3\Xenon_25e12\`
▶ Scripts for plots	`chapter3\plotFig_Xe_25e12_cog.m` `chapter3\plotFig_Xe_25e12_inverted_cog.m`

Figure 3.11

Experimental data

▶ Full scan	`chapter4\experimental data\313nm\SiO2_313nm_24uJ_final\full\`
▶ Background	`chapter4\experimental data\313nm\SiO2_313nm_24uJ_final\0_to_60\`
▶ NP signal	`chapter4\experimental data\313nm\SiO2_313nm_24uJ_final\60_to_1000\`
▶ Plot scripts	`chapter4\analysis_scripts\plot_sio2_313nm_3e13_bg.m`

Figure 3.12

The data was obtained by a combination of a MatLab script with the vmi_analysis_advanced software.

▶ Raw exp. data	`chapter4\experimental data\400nm\SiO2_400nm_24uJ_final\`
▶ Processed exp. data	`chapter3\phase_drift_analysis\`
▶ Matlab script	`chapter3\phaseDriftAnalysis.m`

Figure 3.14

▶ Ne Raw exp. data	`chapter5\data\2012-12-12\Neon_85uJ\`
▶ SiO_2 Raw exp. data	`chapter5\data\2012-12-18\SiO2_90nm_60uJ\`
▶ Plot script	`chapter5\plotExpChapt.m`

Figure 3.16 and 3.18

▶ Experimental data	`chapter6\streaking_data\2013-02-13\0493_ne_streak\`
▶ Analysis script	`chapter6\streaking_data\auswertung_493.m`

Figure 4.1 and 4.2

As the amount of data from the M^3C model is too large only the parameter files and executables are stored.

▶ Parameters MF off	`chapter4\m3c data\95nm\3e13_mie_off_meanfield_off\`
▶ Parameters MF on	`chapter4\m3c data\95nm\3e13_mie_off_meanfield_on\`

Figure 4.3

As the amount of data from the M^{3}C model is too large only the parameter files and executables are stored.

▶ Parameters MF on	`chapter4\m3c data\95nm\3.5e13_mie_off_meanfield_on\`

Figure 4.4, 4.5, 4.7 and 4.8

Experimental data:

▶ 1.3×10^{13} W/cm^2	`chapter4\experimental data\95nm\SiO2_95nm_9uJ_hv_final\`
Plot script	`chapter4\analysis_scripts\plot_sio2_95nm_13e12.m`
▶ 1.8×10^{13} W/cm^2	`chapter4\experimental data\95nm\SiO2_95nm_12uJ_hv_final\`
Plot script	`chapter4\analysis_scripts\plot_sio2_95nm_18e12.m`
▶ 2.7×10^{13} W/cm^2	`chapter4\experimental data\95nm\SiO2_95nm_18uJ_hv_final\`
Plot script	`chapter4\analysis_scripts\plot_sio2_95nm_27e12.m`
▶ 3.7×10^{13} W/cm^2	`chapter4\experimental data\95nm\SiO2_95nm_25uJ_hv_final\`
Plot script	`chapter4\analysis_scripts\plot_sio2_95nm_37e12.m`

M^{3}C model results obtained by the group of Th. Fennel:

▶ Plots	`chapter4\m3c data\95nm\rostock\`

Figure 4.6

▶ Data and plot script	`chapter4\analysis_scripts\sio2_95nm_plot_cutoff_laws.m`

Figure 4.10 and 4.11

▶ Field distributions	`chapter2\plotMaps_ex_and_ez.m`
▶ Temporal profiles	`chapter2\plot_E_vs_t_400nm.m`

Figure 4.12 and 4.13

▶ 95nm	`chapter4\analysis_scripts\plot_sio2_95nm_37e12.m`
▶ 188nm	`chapter4\analysis_scripts\plot_sio2_188nm_46e12.m`
▶ 313nm	`chapter4\analysis_scripts\plot_sio2_313nm_3e13.m`
▶ 400nm	`chapter4\analysis_scripts\plot_sio2_400nm_3e13.m`

Simulated data for 400nm obtained from Th. Fennel:

▶ M^{3}C 400nm	`chapter4\analysis_scripts\plot_sio2_400nm_M3C.m`
▶ Cutoff comparison	`chapter4\analysis_scripts\plot_dphi_400nm.m`

Figure 4.14

Simulated data for 400nm obtained from Th. Fennel:

▶ Figures	`chapter4\m3c data\400nm\angle\`

Figure 4.15

- 95nm `chapter4\analysis_scripts\plot_sio2_95nm_37e12_radial.m`
- 400nm `chapter4\analysis_scripts\plot_sio2_400nm_3e13_radial.m`

Figure 4.16

- Plot script `chapter4\analysis_scripts\com_analysis.m`

Figure 5.1, 5.2 and 5.3

The experimental data is stored in `chapter5\data`.
See `chapter5\readme.txt` for details about the format.

- SiO_2 plot script `chapter5\figure_scripts\createCutoffPlotsSiO2.m`
- TiO_2 plot script `chapter5\figure_scripts\createCutoffPlotsTiO2.m`
- ZrO_2 plot script `chapter5\figure_scripts\createCutoffPlotsZrO2.m`
- Si plot script `chapter5\figure_scripts\createCutoffPlotsSi.m`
- E_c/U_p comparison `chapter5\figure_scripts\plotEcUpcomparison.m`

Figure 5.4 and 5.5

- Plot script `chapter5\figure_scripts\plot_asymmetry_maps.m`

Figure 5.6

- Plot script `chapter5\ioni_yield\plot_e_densities.m`

Figure 6.2, 6.4 and 6.5

Data as presented in [122].

- Simulation scripts `chapter6\sphere_simulations_prb\streaking code\`
- Final data `chapter6\sphere_simulations_prb\data\`

For plotting scripts refer to:
`chapter6\sphere_simulations_prb\plotAllFigures.m`

- Figure 6.2 scripts: `chapter6\sim_streaking\plot_sim_dphi_formula.m`, `chapter6\sim_streaking\plot_sim_sphere_dphi_dv.m`
- Figure 6.5 scripts: `chapter6\plot_Au_simulated_streaking.m`

Figure 6.6

Due to the very extended size of the FDTD simulation result, only the planar cuts are saved.

- Plot script `chapter6\fdtd_tip\plotTipFields.m\`

Figure 6.7

SEM images of the Au tips can be found in

▶ Experimental data	`chapter6\sem_images_tips\`

Figure 6.8

▶ Plot script	`chapter6\exp_tip_scan\plot_exp_tip_scan.m`

Figure 6.9

▶ Plot script	`chapter6\streaking_data\plotSingleScanComp.m`

Figure 6.10

▶ Experimental data 1	`chapter6\streaking_data\Tip_0550to0554_fred.mat`
▶ Analysis script 1	`chapter6\streaking_data\Tip_0550to0554_fred.m`
▶ Experimental data 2	`chapter6\streaking_data\Tip_0577to0599_fred.mat`
▶ Analysis script 2	`chapter6\streaking_data\Tip_0577to0599_fred.m`
▶ Experimental data 3	`chapter6\streaking_data\Tip_0540to0547_fred.mat`
▶ Analysis script 3	`chapter6\streaking_data\Tip_0540to0547_fred.m`

Figure 6.11 and 6.13 a), b) and e)

▶ Analysis script	`chapter6\streaking_data\all_scans.m`
▶ Plot script	`chapter6\streaking_data\plotAllScans2.m`

Figure 6.12 b) and 6.13 c), d) and e)

▶ Single streaking data	`chapter6\fdtd_tip\streak_r100nm_single_streaks.m`
▶ Random streaking	`chapter6\fdtd_tip\streak_1e7_r100nm_50_to94_z-400nm_comp.m`
▶ Plot script	`chapter6\fdtd_tip\plotTipStreaking.m`

Bibliography

[1] G. Mie, “Beiträge zur optik trüber medien, speziell kolloidaler metallösungen,” *Annalen der Physik*, vol. 330, no. 3, pp. 377–445, 1908.

[2] R. W. Wood, “On a remarkable case of uneven distribution of light in a diffraction grating spectrum,” *Proceedings of the Physical Society of London*, vol. 18, no. 1, pp. 269–275, 1902.

[3] R. Ritchie, “Plasma losses by fast electrons in thin films,” *Physical Review*, vol. 106, no. 5, pp. 874–881, 1957.

[4] A. Frank, E. Arakawa, and R. Birkhoff, “Optical emission from irradiated foils. II,” *Physical Review*, vol. 126, no. 6, pp. 1947–1952, 1962.

[5] M. Moskovits, “Surface-enhanced spectroscopy,” *Reviews of Modern Physics*, vol. 57, no. 3, pp. 783–826, 1985.

[6] R. F. Oulton, V. J. Sorger, T. Zentgraf, R. Ma, C. Gladden, L. Dai, G. Bartal, and X. Zhang, “Plasmon lasers at deep subwavelength scale,” *Nature*, vol. 461, no. 7264, pp. 629–632, 2009.

[7] K. Nakayama, K. Tanabe, and H. A. Atwater, “Plasmonic nanoparticle enhanced light absorption in GaAs solar cells,” *Applied Physics Letters*, vol. 93, no. 12, p. 121904, 2008.

[8] S. Lal, S. E. Clare, and N. J. Halas, “Nanoshell-Enabled photothermal cancer therapy: Impending clinical impact,” *Accounts of Chemical Research*, vol. 41, no. 12, pp. 1842–1851, 2008.

[9] A. J. DeMaria, “Self mode-locking of lasers with saturable absorbers,” *Applied Physics Letters*, vol. 8, no. 7, p. 174, 1966.

[10] G. Eesley, “Generation of nonequilibrium electron and lattice temperatures in copper by picosecond laser pulses,” *Physical Review B*, vol. 33, no. 4, pp. 2144–2151, 1986.

[11] E. Beaurepaire, J. Merle, A. Daunois, and J. Bigot, “Ultrafast spin dynamics in ferromagnetic nickel,” *Physical Review Letters*, vol. 76, no. 22, pp. 4250–4253, 1996.

[12] A. Wirth, R. Santra, and E. Goulielmakis, “Real time tracing of valence-shell electronic coherences with attosecond transient absorption spectroscopy,” *Chemical Physics*, vol. 414, pp. 149–159, 2013.

[13] E. Goulielmakis, M. Schultze, M. Hofstetter, V. S. Yakovlev, J. Gagnon, M. Uiberacker, A. L. Aquila, E. M. Gullikson, D. T. Attwood, R. Kienberger, F. Krausz, and U. Kleineberg, “Single-Cycle nonlinear optics,” *Science*, vol. 320, no. 5883, pp. 1614–1617, 2008.

[14] K. Zhao, Q. Zhang, M. Chini, Y. Wu, X. Wang, and Z. Chang, “Tailoring a 67 attosecond pulse through advantageous phase-mismatch,” *Optics Letters*, vol. 37, no. 18, p. 3891, 2012.

[15] F. Krausz and M. Ivanov, “Attosecond physics,” *Reviews of Modern Physics*, vol. 81, no. 1, pp. 163–234, 2009.

[16] K. J. Betsch, N. G. Johnson, B. Bergues, M. Kübel, O. Herrwerth, A. Senftleben, I. Ben-Itzhak, G. G. Paulus, R. Moshammer, J. Ullrich, M. F. Kling, and R. R. Jones, “Controlled directional ion emission from several fragmentation channels of CO driven by a few-cycle laser field,” *Physical Review A*, vol. 86, no. 6, p. 063403, 2012.

[17] T. Fennel, K. Meiwes-Broer, J. Tiggesbäumker, P. Reinhard, P. M. Dinh, and E. Suraud, “Laser-driven nonlinear cluster dynamics,” *Reviews of Modern Physics*, vol. 82, no. 2, pp. 1793–1842, 2010.

[18] J. Passig, R. Irsig, N. X. Truong, T. Fennel, J. Tiggesbäumker, and K. H. Meiwes-Broer, “Nanoplasmonic electron acceleration in silver clusters studied by angular-resolved electron spectroscopy,” *New Journal of Physics*, vol. 14, no. 8, p. 085020, 2012.

[19] A. Schiffrin, T. Paasch-Colberg, N. Karpowicz, V. Apalkov, D. Gerster, S. Mühlbrandt, M. Korbman, J. Reichert, M. Schultze, S. Holzner, J. V. Barth, R. Kienberger, R. Ernstorfer, V. S. Yakovlev, M. I. Stockman, and F. Krausz, “Optical-field-induced current in dielectrics,” *Nature*, vol. 493, no. 7430, pp. 70–74, 2012.

[20] J. D. Jackson, *Classical electrodynamics.* New York: Wiley, 3rd ed., 1999.

[21] S. A. Maier, *Plasmonics: fundamentals and applications.* New York: Springer, 2007.

[22] P. B. Johnson and R. W. Christy, “Optical constants of the noble metals,” *Physical Review B*, vol. 6, no. 12, pp. 4370–4379, 1972.

[23] N. Grady, N. Halas, and P. Nordlander, “Influence of dielectric function properties on the optical response of plasmon resonant metallic nanoparticles,” *Chemical Physics Letters*, vol. 399, no. 1-3, pp. 167–171, 2004.

[24] C. Ciraci, R. T. Hill, J. J. Mock, Y. Urzhumov, A. I. Fernandez-Dominguez, S. A. Maier, J. B. Pendry, A. Chilkoti, and D. R. Smith, "Probing the ultimate limits of plasmonic enhancement," *Science*, vol. 337, no. 6098, pp. 1072–1074, 2012.

[25] M. Durach, A. Rusina, M. F. Kling, and M. I. Stockman, "Metallization of nanofilms in strong adiabatic electric fields," *Physical Review Letters*, vol. 105, no. 8, p. 086803, 2010.

[26] P. Biagioni, J. Huang, L. Duò, M. Finazzi, and B. Hecht, "Cross resonant optical antenna," *Physical Review Letters*, vol. 102, no. 25, p. 256801, 2009.

[27] F. Süßmann, S. L. Stebbings, S. Zherebtsov, S. H. Chew, M. I. Stockman, E. Rühl, U. Kleineberg, T. Fennel, and M. F. Kling, "Attosecond control and tracing of collective electron motion in nanostructures," in *Attosecond and XUV Physics: Ultrafast Dynamics and Spectroscopy*, Berlin: Wiley-VCH, 2013.

[28] C. Sönnichsen, T. Franzl, T. Wilk, G. von Plessen, and J. Feldmann, "Drastic reduction of plasmon damping in gold nanorods," *Physical Review Letters*, vol. 88, no. 7, p. 077402, 2002.

[29] E. Gamaly, *Femtosecond Laser-Matter Interaction: theory, experiments and applications.* Singapore: Pan Stanford, 2011.

[30] R. L. Olmon and M. B. Raschke, "Antenna–load interactions at optical frequencies: impedance matching to quantum systems," *Nanotechnology*, vol. 23, no. 44, p. 444001, 2012.

[31] C. Bohren, *Absorption and scattering of light by small particles.* New York: Wiley, 1983.

[32] T. Brabec, *Strong field laser physics.* New York: Springer, 2008.

[33] H. Fröhlich and H. Pelzer, "Plasma oscillations and energy loss of charged particles in solids," *Proc. Phys. Soc.*, vol. A68, no. 525, 1955.

[34] A. Taflove and S. C. Hagness, *Computational electrodynamics: the finite-difference time-domain method.* Boston: Artech House, 3rd ed., 2005.

[35] L. V. Keldysh, "Ionization in the field of a strong electromagnetic wave," *Sov. Phys. JETP*, vol. 20, no. 5, 1965.

[36] M. V. Ammosov, N. B. Delone, and V. P. Krainov, "Tunnel ionization of complex atoms and of atomic ions in an alternating electromagnetic field," *Sov. Phys. JETP*, vol. 64, no. 6, 1986.

[37] P. Corkum, "Plasma perspective on strong field multiphoton ionization," *Physical Review Letters*, vol. 71, no. 13, pp. 1994–1997, 1993.

[38] G. G. Paulus, W. Becker, W. Nicklich, and H. Walther, "Rescattering effects in above-threshold ionization: a classical model," *Journal of Physics B: Atomic, Molecular and Optical Physics*, vol. 27, no. 21, pp. L703–L708, 1994.

[39] M. Busuladžić, A. Gazibegović-Busuladžić, and D. B. Milošević, "High-order above-threshold ionization in a laser field: Influence of the ionization potential on the high-energy cutoff," *Laser Physics*, vol. 16, no. 2, pp. 289–293, 2006.

[40] J. Krause, K. Schafer, and K. Kulander, "High-order harmonic generation from atoms and ions in the high intensity regime," *Physical Review Letters*, vol. 68, no. 24, pp. 3535–3538, 1992.

[41] M. Lewenstein, P. Balcou, M. Ivanov, A. L'Huillier, and P. Corkum, "Theory of high-harmonic generation by low-frequency laser fields," *Physical Review A*, vol. 49, no. 3, pp. 2117–2132, 1994.

[42] M. Hentschel, R. Kienberger, C. Spielmann, G. A. Reider, N. Milosevic, T. Brabec, P. Corkum, U. Heinzmann, M. Drescher, and F. Krausz, "Attosecond metrology," *Nature*, vol. 414, no. 6863, pp. 509–513, 2001.

[43] P. Antoine, A. L'Huillier, and M. Lewenstein, "Attosecond pulse trains using High–Order harmonics," *Physical Review Letters*, vol. 77, no. 7, pp. 1234–1237, 1996.

[44] P. B. Corkum and F. Krausz, "Attosecond science," *Nature Physics*, vol. 3, no. 6, pp. 381–387, 2007.

[45] V. E. Gruzdev, "Laser-induced ionization of solids: back to keldysh," pp. 480–492, 2005.

[46] E. Gamaly, "The physics of ultra-short laser interaction with solids at non-relativistic intensities," *Physics Reports*, vol. 508, no. 4-5, pp. 91–243, 2011.

[47] M. Lenzner, J. Krüger, S. Sartania, Z. Cheng, C. Spielmann, G. Mourou, W. Kautek, and F. Krausz, "Femtosecond optical breakdown in dielectrics," *Physical Review Letters*, vol. 80, no. 18, pp. 4076–4079, 1998.

[48] B. Stuart, M. Feit, S. Herman, A. Rubenchik, B. Shore, and M. Perry, "Nanosecond-to-femtosecond laser-induced breakdown in dielectrics," *Physical Review B*, vol. 53, no. 4, pp. 1749–1761, 1996.

[49] S. Winkler, I. Burakov, R. Stoian, N. Bulgakova, A. Husakou, A. Mermillod-Blondin, A. Rosenfeld, D. Ashkenasi, and I. Hertel, "Transient response of dielectric materials exposed to ultrafast laser radiation," *Applied Physics A*, vol. 84, no. 4, pp. 413–422, 2006.

[50] B. Chimier, O. Utéza, N. Sanner, M. Sentis, T. Itina, P. Lassonde, F. Légaré, F. Vidal, and J. C. Kieffer, "Damage and ablation thresholds of fused-silica in femtosecond regime," *Physical Review B*, vol. 84, no. 9, p. 094104, 2011.

[51] C. Peltz, C. Varin, T. Brabec, and T. Fennel, "Fully microscopic analysis of laser-driven finite plasmas using the example of clusters," *New Journal of Physics*, vol. 14, no. 6, p. 065011, 2012.

[52] C. Varin, C. Peltz, T. Brabec, and T. Fennel, "Attosecond plasma wave dynamics in Laser-Driven cluster nanoplasmas," *Physical Review Letters*, vol. 108, no. 17, p. 175007, 2012.

[53] T. Otobe, K. Yabana, and J. Iwata, "First-principles calculation of the electron dynamics in crystalline SiO2," *Journal of Physics: Condensed Matter*, vol. 21, no. 6, p. 064224, 2009.

[54] V. Apalkov and M. I. Stockman, "Theory of dielectric nanofilms in strong ultrafast optical fields," *Physical Review B*, vol. 86, no. 16, p. 165118, 2012.

[55] I. Ahmad, S. A. Trushin, Z. Major, C. Wandt, S. Klingebiel, T. Wang, V. Pervak, A. Popp, M. Siebold, F. Krausz, and S. Karsch, "Frontend light source for short-pulse pumped OPCPA system," *Applied Physics B*, vol. 97, no. 3, pp. 529–536, 2009.

[56] I. Ahmad, L. Bergé, Z. Major, F. Krausz, S. Karsch, and S. A. Trushin, "Redshift of few-cycle infrared pulses in the filamentation regime," *New Journal of Physics*, vol. 13, no. 9, p. 093005, 2011.

[57] V. Pervak, C. Teisset, A. Sugita, S. Naumov, F. Krausz, and A. Apolonski, "High-dispersive mirrors for femtosecond lasers," *Optics Express*, vol. 16, no. 14, p. 10220, 2008.

[58] T. Brabec and F. Krausz, "Nonlinear optical pulse propagation in the Single-Cycle regime," *Physical Review Letters*, vol. 78, no. 17, pp. 3282–3285, 1997.

[59] V. Pervak, I. Ahmad, M. K. Trubetskov, A. V. Tikhonravov, and F. Krausz, "Double-angle multilayer mirrors with smooth dispersion characteristics," *Optics Express*, vol. 17, no. 10, p. 7943, 2009.

[60] J. Reichert, R. Holzwarth, T. Udem, and T. Hänsch, "Measuring the frequency of light with mode-locked lasers," *Optics Communications*, vol. 172, no. 1-6, pp. 59–68, 1999.

[61] A. Poppe, R. Holzwarth, A. Apolonski, G. Tempea, C. Spielmann, T. Hänsch, and F. Krausz, "Few-cycle optical waveform synthesis," *Applied Physics B*, vol. 72, no. 3, pp. 373–376, 2001.

[62] L. Xu, C. Spielmann, A. Poppe, T. Brabec, F. Krausz, and T. W. Hänsch, "Route to phase control of ultrashort light pulses," *Optics Letters*, vol. 21, no. 24, p. 2008, 1996.

[63] A. Baltuska, M. Uiberacker, E. Goulielmakis, R. Kienberger, V. Yakovlev, T. Udem, T. Hansch, and F. Krausz, "Phase-controlled amplification of few-cycle laser pulses," *IEEE Journal of Selected Topics in Quantum Electronics*, vol. 9, no. 4, pp. 972–989, 2003.

[64] M. Schultze, A. Wirth, I. Grguras, M. Uiberacker, T. Uphues, A. Verhoef, J. Gagnon, M. Hofstetter, U. Kleineberg, E. Goulielmakis, and F. Krausz, "State-of-the-art attosecond metrology," *Journal of Electron Spectroscopy and Related Phenomena*, vol. 184, no. 3-6, pp. 68–77, 2011.

[65] T. Rathje, N. G. Johnson, M. Möller, F. Süßmann, D. Adolph, M. Kübel, R. Kienberger, M. F. Kling, G. G. Paulus, and A. M. Sayler, "Review of attosecond resolved measurement and control via carrier–envelope phase tagging with above-threshold ionization," *Journal of Physics B: Atomic, Molecular and Optical Physics*, vol. 45, no. 7, p. 074003, 2012.

[66] G. G. Paulus, F. Grasbon, H. Walther, P. Villoresi, M. Nisoli, S. Stagira, E. Priori, and S. De Silvestri, "Absolute-phase phenomena in photoionization with few-cycle laser pulses," *Nature*, vol. 414, no. 6860, pp. 182–184, 2001.

[67] G. Paulus, F. Lindner, H. Walther, A. Baltuška, E. Goulielmakis, M. Lezius, and F. Krausz, "Measurement of the phase of Few-Cycle laser pulses," *Physical Review Letters*, vol. 91, no. 25, p. 253004, 2003.

[68] A. M. Sayler, T. Rathje, W. Müller, K. Rühle, R. Kienberger, and G. G. Paulus, "Precise, real-time, every-single-shot, carrier-envelope phase measurement of ultrashort laser pulses," *Optics Letters*, vol. 36, no. 1, p. 1, 2010.

[69] M. Kübel, K. J. Betsch, N. G. Johnson, U. Kleineberg, R. Moshammer, J. Ullrich, G. G. Paulus, M. F. Kling, and B. Bergues, "Carrier-envelope-phase tagging in measurements with long acquisition times," *New Journal of Physics*, vol. 14, no. 9, p. 093027, 2012.

[70] P. Liu, P. J. Ziemann, D. B. Kittelson, and P. H. McMurry, "Generating particle beams of controlled dimensions and divergence: I. theory of particle motion in aerodynamic lenses and nozzle expansions," *Aerosol Science and Technology*, vol. 22, no. 3, pp. 293–313, 1995.

[71] W. Stöber, A. Fink, and E. Bohn, "Controlled growth of monodisperse silica spheres in the micron size range," *Journal of Colloid and Interface Science*, vol. 26, no. 1, pp. 62–69, 1968.

[72] X. Wang and P. H. McMurry, "A design tool for aerodynamic lens systems," *Aerosol Science and Technology*, vol. 40, no. 5, pp. 320–334, 2006.

[73] H. Bresch, *Photoionisation von freien Aerosolpartikeln mit Synchrotronstrahlung.* PhD thesis, Freie Universität Berlin, 2007.

[74] F. Süßmann, S. Zherebtsov, J. Plenge, N. G. Johnson, M. Kübel, A. M. Sayler, V. Mondes, C. Graf, E. Rühl, G. G. Paulus, D. Schmischke, P. Swrschek, and M. F. Kling, "Single-shot velocity-map imaging of attosecond light-field control at kilohertz rate," *Review of Scientific Instruments*, vol. 82, no. 9, p. 093109, 2011.

[75] J. Ullrich, R. Moshammer, A. Dorn, R. Dörner, L. P. H. Schmidt, and H. Schmidt-Böcking, "Recoil-ion and electron momentum spectroscopy: reaction-microscopes," *Reports on Progress in Physics*, vol. 66, no. 9, pp. 1463–1545, 2003.

[76] C. J. Dasch, "One-dimensional tomography: a comparison of abel, onion-peeling, and filtered backprojection methods," *Applied Optics*, vol. 31, no. 8, p. 1146, 1992.

[77] A. T. J. B. Eppink and D. H. Parker, "Velocity map imaging of ions and electrons using electrostatic lenses: Application in photoelectron and photofragment ion imaging of molecular oxygen," *Review of Scientific Instruments*, vol. 68, no. 9, p. 3477, 1997.

[78] C. Bordas, F. Paulig, H. Helm, and D. L. Huestis, "Photoelectron imaging spectrometry: Principle and inversion method," *Review of Scientific Instruments*, vol. 67, no. 6, p. 2257, 1996.

[79] M. J. J. Vrakking, "An iterative procedure for the inversion of two-dimensional ion/photoelectron imaging experiments," *Review of Scientific Instruments*, vol. 72, p. 4084, 2001.

[80] T. Horio and T. Suzuki, "Multihit two-dimensional charged-particle imaging system with real-time image processing at 1000 frames/s," *Review of Scientific Instruments*, vol. 80, no. 1, p. 013706, 2009.

[81] V. Roudnev and B. Esry, "General theory of Carrier-Envelope phase effects," *Physical Review Letters*, vol. 99, no. 22, p. 220406, 2007.

[82] M. J. Nandor, M. A. Walker, and L. D. V. Woerkom, "Angular distributions of high-intensity ATI and the onset of the plateau," *Journal of Physics B: Atomic, Molecular and Optical Physics*, vol. 31, no. 20, pp. 4617–4629, 1998.

[83] M. F. Kling, J. Rauschenberger, A. J. Verhoef, E. Hasović, T. Uphues, D. B. Milošević, H. G. Muller, and M. J. J. Vrakking, "Imaging of carrier-envelope phase effects in above-threshold ionization with intense few-cycle laser fields," *New Journal of Physics*, vol. 10, no. 2, p. 025024, 2008.

[84] R. Kienberger, E. Goulielmakis, M. Uiberacker, A. Baltuska, V. Yakovlev, F. Bammer, A. Scrinzi, T. Westerwalbesloh, U. Kleineberg, U. Heinzmann, M. Drescher, and F. Krausz, "Atomic transient recorder," *Nature*, vol. 427, no. 6977, pp. 817–821, 2004.

[85] J. Itatani, F. Quéré, G. Yudin, M. Ivanov, F. Krausz, and P. Corkum, "Attosecond streak camera," *Physical Review Letters*, vol. 88, no. 17, p. 173903, 2002.

[86] M. Schultze, M. Fiess, N. Karpowicz, J. Gagnon, M. Korbman, M. Hofstetter, S. Neppl, A. L. Cavalieri, Y. Komninos, T. Mercouris, C. A. Nicolaides, R. Pazourek, S. Nagele, J. Feist, J. Burgdorfer, A. M. Azzeer, R. Ernstorfer, R. Kienberger, U. Kleineberg, E. Goulielmakis, F. Krausz, and V. S. Yakovlev, "Delay in photoemission," *Science*, vol. 328, no. 5986, pp. 1658–1662, 2010.

[87] M. Hofstetter, M. Schultze, M. Fieß, B. Dennhardt, A. Guggenmos, J. Gagnon, V. S. Yakovlev, E. Goulielmakis, R. Kienberger, E. M. Gullikson, F. Krausz, and U. Kleineberg, "Attosecond dispersion control by extreme ultraviolet multilayer mirrors," *Optics Express*, vol. 19, no. 3, p. 1767, 2011.

[88] J. Gagnon and V. S. Yakovlev, "The robustness of attosecond streaking measurements," *Optics Express*, vol. 17, no. 20, p. 17678, 2009.

[89] Y. Mairesse and F. Quéré, "Frequency-resolved optical gating for complete reconstruction of attosecond bursts," *Physical Review A*, vol. 71, no. 1, p. 011401(R), 2005.

[90] B. Henke, E. M. Gullikson, and J. C. Davis, "X-Ray interactions: Photoabsorption, scattering, transmission, and reflection at e = 50-30,000 eV, z = 1-92," *Atomic Data and Nuclear Data Tables*, vol. 54, pp. 181–342, 1993.

[91] A. Apolonski, P. Dombi, G. Paulus, M. Kakehata, R. Holzwarth, T. Udem, C. Lemell, K. Torizuka, J. Burgdörfer, T. Hänsch, and F. Krausz, "Observation of Light-Phase-Sensitive photoemission from a metal," *Physical Review Letters*, vol. 92, no. 7, p. 073902, 2004.

[92] P. Rácz, S. E. Irvine, M. Lenner, A. Mitrofanov, A. Baltuška, A. Y. Elezzabi, and P. Dombi, "Strong-field plasmonic electron acceleration with few-cycle, phase-stabilized laser pulses," *Applied Physics Letters*, vol. 98, no. 11, p. 111116, 2011.

[93] S. Zherebtsov, T. Fennel, J. Plenge, E. Antonsson, I. Znakovskaya, A. Wirth, O. Herrwerth, F. Süßmann, C. Peltz, I. Ahmad, S. A. Trushin, V. Pervak, S. Karsch, M. J. J. Vrakking, B. Langer, C. Graf, M. I. Stockman, F. Krausz, E. Rühl, and M. F. Kling, "Controlled near-field enhanced electron acceleration from dielectric nanospheres with intense few-cycle laser fields," *Nature Physics*, vol. 7, pp. 656–662, 2011.

[94] M. Krüger, M. Schenk, and P. Hommelhoff, “Attosecond control of electrons emitted from a nanoscale metal tip,” *Nature*, vol. 475, no. 7354, pp. 78–81, 2011.

[95] S. Zherebtsov, F. Süßmann, C. Peltz, J. Plenge, K. J. Betsch, I. Znakovskaya, A. S. Alnaser, N. G. Johnson, M. Kübel, A. Horn, V. Mondes, C. Graf, S. A. Trushin, A. Azzeer, M. J. J. Vrakking, G. G. Paulus, F. Krausz, E. Rühl, T. Fennel, and M. F. Kling, “Carrier–envelope phase-tagged imaging of the controlled electron acceleration from SiO2 nanospheres in intense few-cycle laser fields,” *New Journal of Physics*, vol. 14, no. 7, p. 075010, 2012.

[96] Y. Li and W. Ching, “Band structures of all polycrystalline forms of silicon dioxide,” *Physical Review B*, vol. 31, no. 4, pp. 2172–2179, 1985.

[97] B. N. Khlebtsov, V. A. Khanadeev, and N. G. Khlebtsov, “Determination of the size, concentration, and refractive index of silica nanoparticles from turbidity spectra,” *Langmuir*, vol. 24, no. 16, pp. 8964–8970, 2008.

[98] B. E. A. Saleh and M. C. Teich, *Fundamentals of photonics*. Hoboken: Wiley Interscience, 2nd ed., 2007.

[99] W. C. Martin and R. Zalubas, “Energy levels of silicon, si i through si XIV,” *Journal of Physical and Chemical Reference Data*, vol. 12, no. 2, p. 323, 1983.

[100] W. Lotz, “An empirical formula for the electron-impact ionization cross-section,” *Zeitschrift für Physik*, vol. 206, no. 2, pp. 205–211, 1967.

[101] T. Fennel, L. Ramunno, and T. Brabec, “Highly charged ions from Laser-Cluster interactions: Local-Field-Enhanced impact ionization and frustrated Electron-Ion recombination,” *Physical Review Letters*, vol. 99, no. 23, p. 233401, 2007.

[102] M. Suzuki, H. Ando, Y. Higashi, H. Takenaka, H. Shimada, N. Matsubayashi, M. Imamura, S. Kurosawa, S. Tanuma, and C. J. Powell, “Experimental determination of electron effective attenuation lengths in silicon dioxide thin films using synchrotron radiation i. data analysis and comparisons,” *Surface and Interface Analysis*, vol. 29, no. 5, pp. 330–335, 2000.

[103] J. Kuhr and H. Fitting, “Monte carlo simulation of electron emission from solids,” *Journal of Electron Spectroscopy and Related Phenomena*, vol. 105, no. 2-3, pp. 257–273, 1999.

[104] Z. Chen, A. Le, T. Morishita, and C. Lin, “Quantitative rescattering theory for laser-induced high-energy plateau photoelectron spectra,” *Physical Review A*, vol. 79, no. 3, p. 033409, 2009.

[105] B. Concina, B. Baguenard, F. Calvo, and C. Bordas, “Kinetic energy spectra in thermionic emission from small tungsten cluster anions: Evidence for nonclassical

electron capture," *The Journal of Chemical Physics*, vol. 132, no. 10, p. 104307, 2010.

[106] M. J. Mendes, I. Tobías, A. Martí, and A. Luque, "Light concentration in the near-field of dielectric spheroidal particles with mesoscopic sizes," *Optics Express*, vol. 19, no. 17, p. 16207, 2011.

[107] M. T. Hassan, A. Wirth, I. Grguras?, A. Moulet, T. T. Luu, J. Gagnon, V. Pervak, and E. Goulielmakis, "Invited article: Attosecond photonics: Synthesis and control of light transients," *Review of Scientific Instruments*, vol. 83, no. 11, p. 111301, 2012.

[108] M. Schultze, E. M. Bothschafter, A. Sommer, S. Holzner, W. Schweinberger, M. Fiess, M. Hofstetter, R. Kienberger, V. Apalkov, V. S. Yakovlev, M. I. Stockman, and F. Krausz, "Controlling dielectrics with the electric field of light," *Nature*, vol. 493, no. 7430, pp. 75–78, 2012.

[109] D. L. Wood and K. Nassau, "Refractive index of cubic zirconia stabilized with yttria," *Applied Optics*, vol. 21, no. 16, p. 2978, 1982.

[110] J. C. Garcia, L. M. R. Scolfaro, A. T. Lino, V. N. Freire, G. A. Farias, C. C. Silva, H. W. L. Alves, S. C. P. Rodrigues, and E. F. da Silva, "Structural, electronic, and optical properties of ZrO[sub 2] from ab initio calculations," *Journal of Applied Physics*, vol. 100, no. 10, p. 104103, 2006.

[111] J. R. Devore, "Refractive indices of rutile and sphalerite," *Journal of the Optical Society of America*, vol. 41, no. 6, p. 416, 1951.

[112] M. Landmann, E. Rauls, and W. G. Schmidt, "The electronic structure and optical response of rutile, anatase and brookite TiO2," *Journal of Physics: Condensed Matter*, vol. 24, no. 19, p. 195503, 2012.

[113] E. D. Palik and G. Ghosh, *Handbook of optical constants of solids.* San Diego: Academic Press, 1998.

[114] R. A. Ganeev, M. Suzuki, M. Baba, M. Ichihara, and H. Kuroda, "High-order harmonic generation in ag nanoparticle-containing plasma," *Journal of Physics B: Atomic, Molecular and Optical Physics*, vol. 41, no. 4, p. 045603, 2008.

[115] P. Audebert, P. Daguzan, A. Dos Santos, J. Gauthier, J. Geindre, S. Guizard, G. Hamoniaux, K. Krastev, P. Martin, G. Petite, and A. Antonetti, "Space-Time observation of an electron gas in SiO2," *Physical Review Letters*, vol. 73, no. 14, pp. 1990–1993, 1994.

[116] T. Hanke, J. Cesar, V. Knittel, A. Trügler, U. Hohenester, A. Leitenstorfer, and R. Bratschitsch, "Tailoring spatiotemporal light confinement in single plasmonic nanoantennas," *Nano Letters*, vol. 12, no. 2, pp. 992–996, 2012.

[117] M. Schnell, A. Garcia-Etxarri, J. Alkorta, J. Aizpurua, and R. Hillenbrand, "Phase-Resolved mapping of the Near-Field vector and polarization state in nanoscale antenna gaps," *Nano Letters*, vol. 10, no. 9, pp. 3524–3528, 2010.

[118] A. L. Cavalieri, N. Müller, T. Uphues, V. S. Yakovlev, A. Baltuška, B. Horvath, B. Schmidt, L. Blümel, R. Holzwarth, S. Hendel, M. Drescher, U. Kleineberg, P. M. Echenique, R. Kienberger, F. Krausz, and U. Heinzmann, "Attosecond spectroscopy in condensed matter," *Nature*, vol. 449, no. 7165, pp. 1029–1032, 2007.

[119] B. Barwick, D. J. Flannigan, and A. H. Zewail, "Photon-induced near-field electron microscopy," *Nature*, vol. 462, no. 7275, pp. 902–906, 2009.

[120] M. I. Stockman, M. F. Kling, U. Kleineberg, and F. Krausz, "Attosecond nanoplasmonic-field microscope," *Nature Photonics*, vol. 1, no. 9, pp. 539–544, 2007.

[121] E. Skopalová, D. Y. Lei, T. Witting, C. Arrell, F. Frank, Y. Sonnefraud, S. A. Maier, J. W. G. Tisch, and J. P. Marangos, "Numerical simulation of attosecond nanoplasmonic streaking," *New Journal of Physics*, vol. 13, no. 8, p. 083003, 2011.

[122] F. Süßmann and M. Kling, "Attosecond nanoplasmonic streaking of localized fields near metal nanospheres," *Physical Review B*, vol. 84, no. 12, p. 121406(R), 2011.

[123] A. G. Borisov, P. M. Echenique, and A. K. Kazansky, "Attostreaking with metallic nano-objects," *New Journal of Physics*, vol. 14, no. 2, p. 023036, 2012.

[124] F. Kelkensberg, A. F. Koenderink, and M. J. J. Vrakking, "Attosecond streaking in a nano-plasmonic field," *New Journal of Physics*, vol. 14, no. 9, p. 093034, 2012.

[125] J. S. Prell, L. J. Borja, D. M. Neumark, and S. R. Leone, "Simulation of attosecond-resolved imaging of the plasmon electric field in metallic nanoparticles," *Annalen der Physik*, vol. 525, no. 1-2, pp. 151–161, 2013.

[126] M. Bauer, C. Wiemann, J. Lange, D. Bayer, M. Rohmer, and M. Aeschlimann, "Phase propagation of localized surface plasmons probed by time-resolved photoemission electron microscopy," *Applied Physics A*, vol. 88, no. 3, pp. 473–480, 2007.

[127] C. Lemke, C. Schneider, T. Leißner, D. Bayer, J. W. Radke, A. Fischer, P. Melchior, A. B. Evlyukhin, B. N. Chichkov, C. Reinhardt, M. Bauer, and M. Aeschlimann, "Spatiotemporal characterization of SPP pulse propagation in Two-Dimensional plasmonic focusing devices," *Nano Letters*, vol. 13, no. 3, pp. 1053–1058, 2013.

[128] A. Mikkelsen, J. Schwenke, T. Fordell, G. Luo, K. Kluender, E. Hilner, N. Anttu, A. A. Zakharov, E. Lundgren, J. Mauritsson, J. N. Andersen, H. Q. Xu, and A. L'Huillier, "Photoemission electron microscopy using extreme ultraviolet attosecond pulse trains," *Review of Scientific Instruments*, vol. 80, no. 12, p. 123703, 2009.

[129] S. H. Chew, F. Süßmann, C. Späth, A. Wirth, J. Schmidt, S. Zherebtsov, A. Guggenmos, A. Oelsner, N. Weber, J. Kapaldo, A. Gliserin, M. I. Stockman, M. F. Kling, and U. Kleineberg, "Time-of-flight-photoelectron emission microscopy on plasmonic structures using attosecond extreme ultraviolet pulses," *Applied Physics Letters*, vol. 100, no. 5, p. 051904, 2012.

[130] C. Lemell, B. Solleder, K. Tőkési, and J. Burgdörfer, "Simulation of attosecond streaking of electrons emitted from a tungsten surface," *Physical Review A*, vol. 79, no. 6, p. 062901, 2009.

[131] C. Zhang and U. Thumm, "Attosecond photoelectron spectroscopy of metal surfaces," *Physical Review Letters*, vol. 102, no. 12, p. 123601, 2009.

[132] G. Herink, D. R. Solli, M. Gulde, and C. Ropers, "Field-driven photoemission from nanostructures quenches the quiver motion," *Nature*, vol. 483, no. 7388, pp. 190–193, 2012.

[133] S. Lal, N. K. Grady, G. P. Goodrich, and N. J. Halas, "Profiling the near field of a plasmonic nanoparticle with Raman-Based molecular rulers," *Nano Letters*, vol. 6, no. 10, pp. 2338–2343, 2006.

[134] E. C. Le Ru and P. G. Etchegoin, *Principles of surface-enhanced Raman spectroscopy: and related plasmonic effects.* Amsterdam: Elsevier, 1st ed., 2009.

[135] S. Tanuma, C. J. Powell, and D. R. Penn, "Calculations of electron inelastic mean free paths. IX. data for 41 elemental solids over the 50 eV to 30 keV range," *Surface and Interface Analysis*, vol. 43, no. 3, pp. 689–713, 2011.

[136] M. Schultze, E. Goulielmakis, M. Uiberacker, M. Hofstetter, J. Kim, D. Kim, F. Krausz, and U. Kleineberg, "Powerful 170-attosecond XUV pulses generated with few-cycle laser pulses and broadband multilayer optics," *New Journal of Physics*, vol. 9, no. 7, pp. 243–243, 2007.

[137] J. Schäfer, S. Lee, and A. Kienle, "Calculation of the near fields for the scattering of electromagnetic waves by multiple infinite cylinders at perpendicular incidence," *Journal of Quantitative Spectroscopy and Radiative Transfer*, vol. 113, no. 16, pp. 2113–2123, 2012.

[138] M. Eisele, M. Krüger, M. Schenk, A. Ziegler, and P. Hommelhoff, "Note: Production of sharp gold tips with high surface quality," *Review of Scientific Instruments*, vol. 82, no. 2, p. 026101, 2011.

[139] S. Neppl, R. Ernstorfer, E. M. Bothschafter, A. L. Cavalieri, D. Menzel, J. V. Barth, F. Krausz, R. Kienberger, and P. Feulner, "Attosecond Time-Resolved photoemission from core and valence states of magnesium," *Physical Review Letters*, vol. 109, no. 8, p. 087401, 2012.

[140] M. J. Weber, *Handbook of optical materials.* Boca Raton: CRC Press, 2003.

[141] S. S. Kharintsev, G. G. Hoffmann, A. I. Fishman, and M. K. Salakhov, "Plasmonic optical antenna design for performing tip-enhanced raman spectroscopy and microscopy," *Journal of Physics D: Applied Physics*, vol. 46, no. 14, p. 145501, 2013.

Acknowledgements

Special thanks goes to Prof. Matthias Kling for giving me the possibility to pursue my PhD thesis. I could always count on his experience and prompt support. Prof. Thomas Fennel supervised many theoretical aspects of this work. I am indebted to Prof. Ferenc Krausz for giving me the possibilty to work in his group and being able to access its wealth of knowledge.

I am very grateful to have been part of a great team and want to thank Sergey Zherebtsov, Johannes Stierle, Johannes Schötz, Benjamin Förg, Sarah Stebbings, Matthias Kübel, Nora Kling, Irina Znakovskaya, Kelsie Betsch, Waldemar Schneider, Lauryna Lötscher, Yingying Yang for great collegiality, their support and knowledge.

As this thesis covers a broad set of topics and experimental techniques, i am indebted to many people without whom this work would definitely have been impossible. I am thankful to the whole PFS team, namely Sergei Trushin, Alexander Kessel, Christoph Skrobol, Sandro Klingebiel, Christoph Wandt for always supplying a high-quality laser beam and the great cooperation. The good collaboration with Lennart Seiffert and Christoph Peltz is appreciated as without such support expimentalists are left in the dark. The supply of high-quality samples and the knowledge about the aerodynamic lensing by Jürgen Plenge, Eckart Rühl, Valerie Mondes and Christina Graf was essential for most parts of this work. The STOF setup was provided by Karl-Heinz Meiwes-Broer, Johannes Passig and Slawomir Skruszewicz along with a lot of support. I am deeply thankful to Adrian Wirth, Thorsten Uphues, Simon Watson, James Kapaldo, Oliver Herrwerth and Chenchao Liu for the great work they have done in designing and implementing the AS5-beamline. Thanks to Prof. Peter Hommelhoff, Michael Krüger and Michael Förster for supply of the Au nanotips and many fruitful discussions. Support by Byungnam Ahn, Prof. Dong-Eon Kim and Peter Baum is appreciated. Special optics were supplied by Vladimir Pervak and Olga Razskazovskaya. I am also thankful to Alexander Guggenmoos, Michael Hofstätter and Prof. Ulf Kleineberg for the outstanding XUV optics, Soo Hoon Chew for the good cooperation during the PEEM campaign and Alexander Weber-Bargioni for providing samples and insight into nanoantenna physics.

A lot of support, the essential motivation and leisure was provided by Vanessa Knittel. Thank you very much!

Our technicians Karl Bauer, Manuel Fischer, Harald Haas, Anton Horn, Alois Böswald and the team of the MPQ workshop deserve special acknowledgement for their prompt support and unending patience.

I want to thank all fellow IMPRS students, the IMPRS coordinators and Mrs. Wild for the nice events. The SPP 1391 Ultrafast Nanooptics program not only gave financial support but also the opportunity for exchanging knowledge of various fields in plasmonic research.

Many more people contributed to this work by discussions or just creating a very pleasant atmosphere at the institute: Agustin Schiffrin, Hartmut Schröder, Yunpei Deng, Ralph Ernstdorfer, Boris Bergues, Eleftherios Goulielmakis, Antoine Moulet, Mohammed Hassan, Tran Trung Luu, Stefan Neppl, Martin Schultze, Wolfram Helml, Elisabeth Bothschafter, Wolfgang Schweinberger, Michael Jobst, Johannes Wenz, Matthias Heigoldt, Konstantin Khrennikov, Jürgen Schmidt, Christan Späth, Vadislav Yakovlev, Ali Alnaser and Tim Paasch-Colberg and many more.